Functional Dextran-Based Hydrogels

Synthesis and Biomedical Applications

Dissertation

zur Erlangung des Grades
"Doktor der Naturwissenschaften"
im Promotionsfach Chemie

am Fachbereich Chemie, Pharmazie und Geowissenschaften
der Johannes Gutenberg-Universität in Mainz

vorgelegt von

Annette Brunsen
geboren in Haselünne

Mainz, 2010

Die vorliegende Arbeit wurde in der Zeit von Januar 2007 bis Januar 2010 in der Materialforschungsgruppe am Max-Planck-Institut für Polymerforschung in Mainz angefertigt.

Dekan:

1. Berichterstatter:
2. Berichterstatter:

Übrige Mitglieder der Prüfungskommission:

Tag der mündlichen Prüfung: 15. März 2010

„Du bist zeitlebens für das verantwortlich,
was du dir vertraut gemacht hast.“

Antoine de Saint-Exupéry
(Werk: Der kleine Prinz)

ABSTRACT

Dextran-based polymers are versatile hydrophilic materials which can provide functionalized surfaces in various areas including biological and medical applications. Functional, responsive, dextran-based hydrogels are crosslinked, dextran-based polymers allowing the modulation of response towards external stimuli. The controlled modulation of hydrogel properties towards specific applications and the detailed characterization of the optical, mechanical, and chemical properties are of strong interest in science and for further applications. Especially, the structural characteristics of swollen hydrogel matrices and the characterization of their variations upon environmental changes are challenging. Depending on their properties hydrogels are applied as actuators, biosensors, in drug delivery, tissue engineering, or for medical coatings. However, the field of possible applications still shows potential to be expanded.

Surface attached hydrogel films with a thickness of several micrometers can serve as waveguiding matrix for leaky optical waveguide modes. On the basis of highly swelling and waveguiding dextran-based hydrogel films an optical biosensor concept was developed. The synthesis of a dextran-based hydrogel matrix, its functionalization to modulate its response towards external stimuli, and the characterization of the swollen hydrogel films were main interests within this biosensor project. A second focus was the optimization of the hydrogel characteristics for cell growth with the aim of creating scaffolds for bone regeneration. Matrix modification towards successful cell growth experiments with endothelial cells and osteoblasts was achieved.

A photo-crosslinkable, carboxymethylated dextran-based hydrogel (PCMD) was synthesized and characterized in terms of swelling behaviour and structural properties. Further functionalization was carried out before and after crosslinking. This functionalization aimed towards external manipulation of the swelling degree and the charge of the hydrogel matrix important for biosensor experiments as well as for cell adhesion. The modulation of functionalized PCMD hydrogel responses to pH, ion concentration, electrochemical switching, or a magnetic force was investigated.

The PCMD hydrogel films were optically characterized by combining surface plasmon resonance (SPR) and optical waveguide mode spectroscopy (OWS). This technique allows a detailed analysis of the refractive index profile perpendicular to the substrate surface by applying the Wentzel-Kramers-Brillouin (WKB) approximation.

In order to perform biosensor experiments, analyte capturing units such as proteins or antibodies were covalently coupled to the crosslinked hydrogel backbone by applying active ester chemistry. Consequently, target analytes are located inside the waveguiding matrix. By using labeled analytes, fluorescence enhancement was achieved by fluorescence excitation with the electromagnetic field in the center of the optical waveguide modes. The fluorescence excited by the evanescent electromagnetic field of the surface plasmon was 2-3 orders of magnitude lower. Furthermore, the signal to noise ratio was improved by the fluorescence excitation with leaky optical waveguide modes.

The applicability of the PCMD hydrogel sensor matrix for clinically relevant samples was proofed in a cooperation project with Yi Wang and Jakub Dostálek for the detection of PSA in serum with long range surface plasmon spectroscopy (LRSP) and fluorescence excitation by LRSP (LR-SPFS).

TABLE OF CONTENTS

Abbreviations

ACT	acetate buffer
AF-FFF	asymmetric flow field-flow fractionation
AFM	atomic force microscopy
BPTES	benzophenonetriethoxysilane
BSA	bovine serum albumine
c-Ab	capturing antibody
CMD	carboxymethylated dextran
CQ	collisional quenching
CV	cyclic voltammetry
D	diffusion coefficient
2D	two-dimensional
3D	three-dimensional
d-Ab	detection antibody
DLS	dynamic light scattering
DMF	dimethylformamide
DMIAAm	2-dimethylmaleinimido ethylacrylamide
DMSO	dimethylsulfoxide
d_s	degree of substitution
ε	dielectric constant
EDC	1-ethyl-3-(3-dimethylaminopropyl
ELISA	enzyme linked immunosorbend assay
E_{ox}	oxidation potential
E_{red}	reduction potential
FCS	fluorescence correlation spectroscopy
FIB	focused ion beam
f-PSA	free prostate specific antigen
FRET	fluorescence resonance energy transfer
HEPES	(4-(2-hydroxyethyl)-1-piperazineethanesulfonic acid)
HMDS	hexamethyldisilazane
HOMO	highest occupied molecular orbital
I	intensity
IC	internal conversion
IPN	interpenetrating networks
ISC	inter system crossing
LCST	lower critical solution temperature
LOD	limit of detection
LRSP	long range surface plasmon spectroscopy
LR-SPFS	long range surface plasmon fluorescence spectroscopy
LUMO	lowest unoccupied molecular orbital
M_r	relative molecular mass
n	refractive index
NHS	N-hydroxysuccinimide
NMR	nuclear magnetic resonance
NP	nanoparticle
NR_4^+	N-(trimethoxysilylpropyl)-N,N,N-trimethylammonium chloride
OWFS	optical waveguide mode fluorescence spectroscoy

OWS	optical waveguide mode spectroscopy
PBS	phosphate buffered saline
PCMD	benzophenone photo-crosslinkable carboxymethylated dextran
PDMS	poly(dimethylsiloxane)
PEEK	poly(ether etherketone)
PEG	poly-ethylene glycol
P(HEMA)	poly(2-hydroxyethyl methacrylate)
PLA	poly(lactic acid)
PMMA	poly(methylmethacrylate)
PNIPAAm	poly(N-isopropylacrylamide)
PTFE	polytetrafluoroethylene
PVA	poly(vinyl alcohol)
S_0	electronic ground state
S_1	electronic excited state
SAM	self-assembled monolayer
SEM	scanning electron microscopy
sIPN	semi-interpenetrating networks
SPFS	surface plasmon fluorescence spectroscopy
SPR	surface plasmon resonance
SQUID	superconducting quantum interference device
T	temperature
T_E	transversal electric mode (s-polarized light)
TEM	transmission electron microscopy
TEMED	N,N,N’,N’-tetramethylene-diamine
TFA-NHS	N-hydroxysuccinimide trifluoroacetate
TFA-PFP	pentafluorophenyl trifluoroacetate
TFPS	para-tetrafluorophenol sulfonate
TIR	angle of total internal reflection
T_M	transversal magnetic mode (p-polarized light)
UCST	upper critical solution temperature
UV	ultraviolet
VIS	visible
WKB	Wentzel-Kramers-Brillouin (approximation)

1 Introduction

This work describes functional dextran-based hydrogels and their applications. One focus was the synthesis, functionalization, and further processing of dextran for hydrogel preparation. A second focus was the matrix characterization and the implementation of the developed hydrogel into a surface plasmon resonance- and optical waveguide mode enhanced fluorescence-based biosensor platform. Furthermore, the application of the dextran-based hydrogel as scaffold for tissue engineering was investigated.

1.1 Hydrogels – Highly Swelling Polymer Networks

Polymers are versatile materials used in many different fields from medicine to engineeering due to their manifold structures and properties. Continuously, new polymers are developed and the understanding of structure and properties is improved. They can have a purely synthetic origin but polymers are generated in nature as well. Popular natural polymers are the DNA, proteins, gelatin or cellulose for example. A famous synthetic polymer is polytetrafluoroethylene (PTFE) well known as Teflon. Polymers are the starting material for gels. Gels are composed of 3-dimensionally crosslinked polymer chains building up networks that swell upon contact with appropriate liquids. Different classes of gels such as hydrogels, organogels, and xerogels were devoloped. Hydrogels are crosslinked, hydrophilic, upon contact with water highly swelling polymer networks. The ability to take up a multiple of their own weight of water makes them interesting materials in a broad variety of applications. Their applications include a wide range from medicine to analytics corresponding to the manifold structures and functionalities that exist. Hydrogels can be classified as neutral or ionic based on the nature of functional groups. Additionally, they can be classified based on the method of preparation as homo- or copolymers, based on the physical structure as amorphous, semicristalline or hydrocolloidal aggregates or regarding to their origin as synthetic or natural polymers for example.[1]

1.1.1 Functional Hydrogels and Applications

The insertion of different functional groups can be achieved by mixing of various polymers or the copolymerization of different segments in the polymer chain. Additionally, polymers that allow further functionalization, so called functional hydrogels, provide access to a large range of applications.

Functionalization of hydrogel structures can be performed by active ester chemistry, click chemistry, polymeric anhydrides, epoxides, aldehydes and ketones. Including Michael-type and Friedel-Crafts reactions as well as methylations, polymer analogous reactions involve almost all high yield organic reactions.[2-4] Reactive sites allow the modification with a variety of molecules including biomolecules for biosensor applications and affinity binding.[5-7] Furthermore, attaching molecular recognition sites creates further possibilities in cell culturing[8] and polymer assisted drug delivery advanced medication especially by using environmentally responsive hydrogels.[9]

In general, hydrogels are implemented in many fields of applications from medical or pharmaceutical applications[1, 10] like drug delivery[9, 11-13], wound healing[14, 15], and tissue engineering[16-18] as well as for actuators[19-22], separation,[23, 24] industrial coatings,[25, 26] or binding studies.[27]

Hydrogels synthesized as carriers are supposed to interact with the mucosa or other parts of the body. They are preferentially functionalized with a high density of carboxyl- or hydroxyl groups because the mucosa-glycoprotein interaction is thought to occur primarily via hydrogen bonding.[28] Monomers frequently used for such hydrogels include acrylic and methacrylic acid.

For drug delivery applications temperature sensitive swelling behaviour as observed for poly(N-isopropylacrylamide)[29] and poly-*N,N*-diethylacrylamide.[30] are useful.

For tissue engineering biocompatible hydrogels are required. Often natural polymers are preferable such as collagene or chitosan.[16] But as well synthetic polymers such as poly-ethylene glycol (PEG) show good properties for tissue engineering.[16, 31]

1.1.2 Crosslinking and Swelling Affecting Diffusion and Surface Properties.

Crosslinking can be achieved by physical or chemical bonds. Physical crosslinks can be entanglements, crystallites, or weak associations such as hydrogen bonds or van der

Waals interactions[32-35] These gels are usually stable but can easily be reliquified for example by heating as in the case of gelatine. In contrast, chemically, covalently crosslinked hydrogels do not reliquify. Chemical crosslinking can be achieved by chemical reactions such as [2+2]cycloadditions, nucleophilic substitutions, addition-, and condensation reactions, high energy irradiation, radical reactions, or enzymes.[32, 36]

The structure of hydrogels is defined by three parameters: the polymer volume fraction in the swollen state, the number of average molecular weight between crosslinks and the correlation lenghts meaning the pore size. Analyzing the network structure is extremely difficult and can be done either by applying theoretical models or by indirect experimental techniques. Three distinct models were used to examine network structure formation by theoretical simulations:

- kinetic models take into account the mass balances on the species.[37, 38]
- statistical models[39] and
- Monte Carlo models[40] were developed to provide more insight into the network formation process and the heterogeneities of the network.

The ultimate goal of all theoretical models is the prediction of the hydrogel swelling behavior which can be described by a variety of nonideal thermodynamic frameworks. Due to the highly nonideal thermodynamic behavior of polymer networks in electrolyte solutions, no theory can predict exact behavior. The most successful theory describing the hydrogel swelling characteristics is the Flory Rhener Theory and its manifold modifications.[41, 42] The thermodynamical force of mixing (osmosis of the hydrogel into the solution) resulting in swelling is thereby counterbalanced by the retractive force induced by the crosslinks of the network. Are these two forces equal an equilibrium state is reached. The limitation of this description is the limitation to neutral polymeric networks. The thermodynamic swelling force for ionic polymer networks is much higher than for neutral ones. The swelling kinetics of hydrogels can be classified as diffusion-controlled (Fickian) or relaxation-controlled (non-Fickian).[43]

The swelling and crosslinking influences the diffusion through the hydrogel network. The diffusion is determined by the structure and pore size, the chemical characteristics and thus the polymer composition, the water content, and the nature and size of the solutes. The interaction among solutes, gel polymers, and solvents has an important effect on the diffusion. Diffusion is thereby best described by Fick’s equation or by Maxwell’s equations which correlate the solute’s flux with its chemical potential gradient in the system.[35]

Besides the diffusion inside the hydrogel matrix the surface properties of the hydrogel matrix are affected by the crosslinking and swelling characteristics. Hydrogels have a complex surface structure with single polymer chains extending into the solution. At the hydrogel/solution interface the structure changes gradually[44] and the extended polymer chains behave like polymer brushes.[45] The surface properties are highly influencing matrix/cell interactions and with this determine the hydrogel potential for cell adhesion.

1.1.3 Stimuli Responsive and Hybrid Hydrogels

Hydrogels that are responsive to special environmental stimuli or respond to certain molecules present a huge class of extremely useful materials for example for drug delivery. Brief examples are response to changes in temperature, pH, pressure, irradiation, electric fields and chemical stimuli. This response ranges from a small change in the degree of swelling to the complete collapse and total inversion of their properties.

The response to pH is a widely found stimulus originating from the electrostatic repulsion between ionized groups in the polymer network. Suitable acidic functionalities are carboxyl groups and sulfonic acids. Pendant basic functionalities are ammonium salts for example. Considering the different pH values in the digestive organs these responsive hydrogels mainly found applications in drug delivery.[9]

The response to temperature can be a transition into the collapsed state below an upper critical solution temperature (UCST) as well as a transition into the collapsed state above a lower critical solution temperature (LCST). It depends foremost on the ratio of hydrophilic and hydrophobic segments within the polymer but effects like crosslinking density and grafting are important, too. A famous example for a hydrogel with LCST behaviour is poly(N-isopropylacrylamide) (PNIPAAm).

The response to irradiation with light can be assigned to an effect of either osmotic pressure due to the generation of charges upon irradiation or to local temperature changes affecting the LCST behavior. In polymers modified with leuco derivatives, UV-light creates ion pairs, causing a swelling due to the increase in osmotic pressure.[46] Whereas chlorophyll transforms visible or IR light into local heat.[47] Light can be used as a defined stimulus, in terms of localisation and intensity, which led to to the application of these hydrogels in microfluidics.

Another defined trigger is the electrical stimulus. Electro sensitive hydrogels swell and collapse due to the movement of ions because of an osmotic gradient induced by an applied potential. Additionally, electroactive functionalities such as ruthenium complexes[48] can be coupled into the polymer network creating redox active hydrogels. Electro sensitive hydrogels can be applied as actuators and are promising candidates for the development for artificial muscles.[49, 50]

Besides, the introduction of functional monomers and functional groups into the polymer backbone of a hydrogel network, hybrid systems, using different components, can be used to create hydrogels with specific properties. Hybrid materials can be prepared by combining two or more different polymers or by introducing completely different materials such as nanoparticles.

Pure polymer hybrid systems can be used for adjusting pH-sensitivity by modifying a pH-sensitive polyelectrolyte hydrogel with a second neutral polymer such as 2-hydroxyethyl methacrylate or maleic anhydrate with varying ratio.[9] Another versatile combination is the mixing of a temperature-sensitive polymer such as NIPAAm and a pH-sensitive polymer such as acrylic acid resulting in a double responsive hydrogel.[51]

In addition polymeric nanoparticles as well as inorganic nanoparticles facilitate the generation of functional and responsive hybrid materials. The combination of responsive behaviour and functionality allows the preparation of matrices for numerous applications especially in the field of drug delivery and sensing.

1.1.4 Dextran and Water-Based Chemistry

Dextran consists of a 1,6-linked glucose backbone. Every glucose unit in the dextran backbone carries three hydroxyl groups which can be used for chemical modification. Dextran shows a high biocompatibility and is degradable by the enzyme dextranase. Therefore, it is a good candidate for medical applications such as drug delivery.[12] Natural dextran exists with a molecular weight between 15.000 and 50.000.000 Da and is synthesized extracellular by the bacteria Leuconostoc mesenteroides from sucrose.

The chemical processability of dextran is limited by its solubility. It is highly soluble in water. It can be dissolved in DMSO and has a low solubility in DMF whereby its solubility increases with decreasing molecular weight and increasing temperature. Consequently, for the modification of dextran water-based organic chemistry is the ideal method. There has been a considerable interest in the development of organic reactions in water since it was reported, that Diels-Alder reactions could be greatly accelerated by using water as a solvent.[52] Nowadays, different examples are know even reaction that involve water sensitive compounds.[53] Chemical reactions that are reported to be performed in water belong to the class of pericyclic reactions, reactions of carbanion and carbocation equivalents, reactions of radicals and carbenes, oxidations and reductions, and to the field of transition metal catalysis.[54] Problems in water-based organic chemistry can be the insolubility of organic compounds and the performance of dehydration reactions because the water directly leads to re-hydration. Consequently, water-based organic chemistry is an interesting tool for future research. Especially, carbohydrate chemistry and the chemical modification of biomolecules benefit from classical chemistry that can be performed in water.

1.2 Optical Biosensors

According to IUPAC a biosensor is defined as a "device that used specific biochemical reactions mediated by isolated enzymes, immunosystems, tissue, organelles or whole cells to detect chemical compounds usually by electric, thermal, or optical signals.[55] Thus, two components are of importance: first the recognition chemistry or biology and second the read out mechanism. Both have to be optimized to create a sensitive and selective biosensor device. Thereby, the recognition chemistry determines the selectivity whereas the read out system is mainly responsible for the sensitivity. The most widespread commercial biosensor is the blood glucose biosensor. The enzyme glucose oxidase is used to oxidize blood glucose. Thereby, the enzyme component FAD is reduced to $FADH_2$ triggering an electric current.[56] Generally, biosensor devices are used for environmental monitoring, trace gas detection or water treatment facilities. Detected target analytes are bacteria,[56] organophosphates and pesticides,[57] cells,[58] or drug residues in food such as antibiotics.[56]

1.2.1 Analyte Recognition

The bioelement in the sensor may be an enzyme, antibody, a living cell or tissue for example. Generally, analyte recognition can be performed

- on the basis of a capturing mechanism,
- by catalysis or

- cell based.

Commonly applied coupling strategies for various analyte recognition units are summarized in Figure 1.2.1.[63] Organic reactions are used for coupling as well as protein-antibody interactions. In principle, every method leading to a stable bound analyte capturing unit can be used.

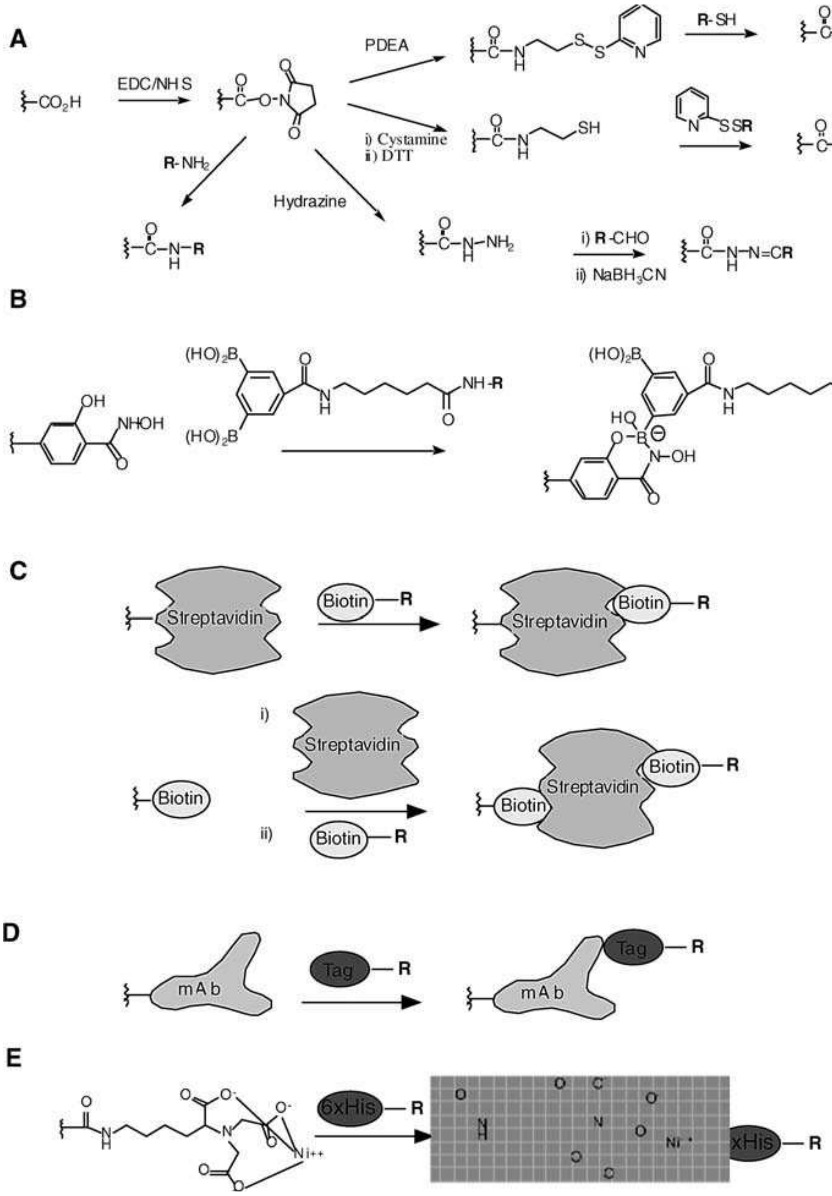

***Figure 1.2.1:** Commonly employed coupling strategies for the immobilisation of analyte recognition receptors in the field of biosensing.[63] Thereby EDC/NHS represents ethylenediamine/ N-hydroxysuccinimide, PDEA 2-(pyridinyldithio)ethane amine, and DTT dithiothreitol.*

Cell-based[59] recognition is based on the analyte coupling to a cell surface receptor which triggers a detecable signal or starts a signaling cascade that can be detected. Recognition by catalysis is usually based on an enzymatic reaction that generates a detectable product.[60] Examples are the change in proton concentration, the release of oxygen or CO_2, the release of metals or halides, an ion- or electron transfer and the change in optical properties due to the production of a colored product. One idea is based on receptor proteins that trigger signal transduction through a membrane for example by influencing the ion transport of channels. Sensor concepts based on artificial membranes attached to an electrode with incorporated proteins or engineered channels try to simulate these natural sensing systems.[61] Finally, the most important mechanism for this work is the analyte recognition on the basis of a capturing mechanism. Thereby, the binding of an analyte or a labeled analyte triggers a detectable signal. Specificity is achieved by using detection units occurring in nature for specific capturing of a certain analyte.

The capturing element[62] applied depends on the detection format such as direct, sandwich, and competitive detection. In the direct detection the binding of an antibody is recorded. For the sandwich assay and for the competitive detection an antigen is the target analyte. In both methods an antibody serves as capturing unit. In a competitive assay the binding of a labeled antigen to the analyte free capturing units is detected whereas in a sandwich assay a labeled secondary antibody binding to the captured analyte is recorded. The choice of an appropriate biorecognition element and the appropriate immobilization method is of critical importance with direct impact on the performance of a sensor device. A plethora of biorecognition elements has been employed. The most popular and most frequently used ones are antibodies. They offer a high specifity and their affinity to the corresponding target analyte is usually very high.

Besides, single-chain antibody fragments and biotinylated fragments have been used as biorecognition element as well.[64-66] A cheaper and usually more stable alternative is the use of smaller peptides. A disadvantage of peptides can be seen in their lower specificity compared to antibodies. Nevertheless, they are good candidates for the recognition of antibodies such as antibodies against hepatitis G,[67] herpes simplex virus type 1 and 2,[68] and for the detection of heavy metals.[69] A versatile approach is the use of DNA or RNA aptamers, which are single-stranded oligonucleotide sequences, as recognition units for proteins, nucleic acids, and cells.[70, 71]

1.2.2 Surface Attachment of the Analyte Recognition Unit

To create a biosensor device the analyte recognition units have to be coupled to a surface. Surfaces suitable for biosensing are mainly metal, glass or polymers. Usually, the surface is functionalized in order to covalently couple recognition units. Functionalization in case of metal or glass surface is mostly carried out by adhesion of a self-assembled monolayer (Figure 1.2.2).[72-74]

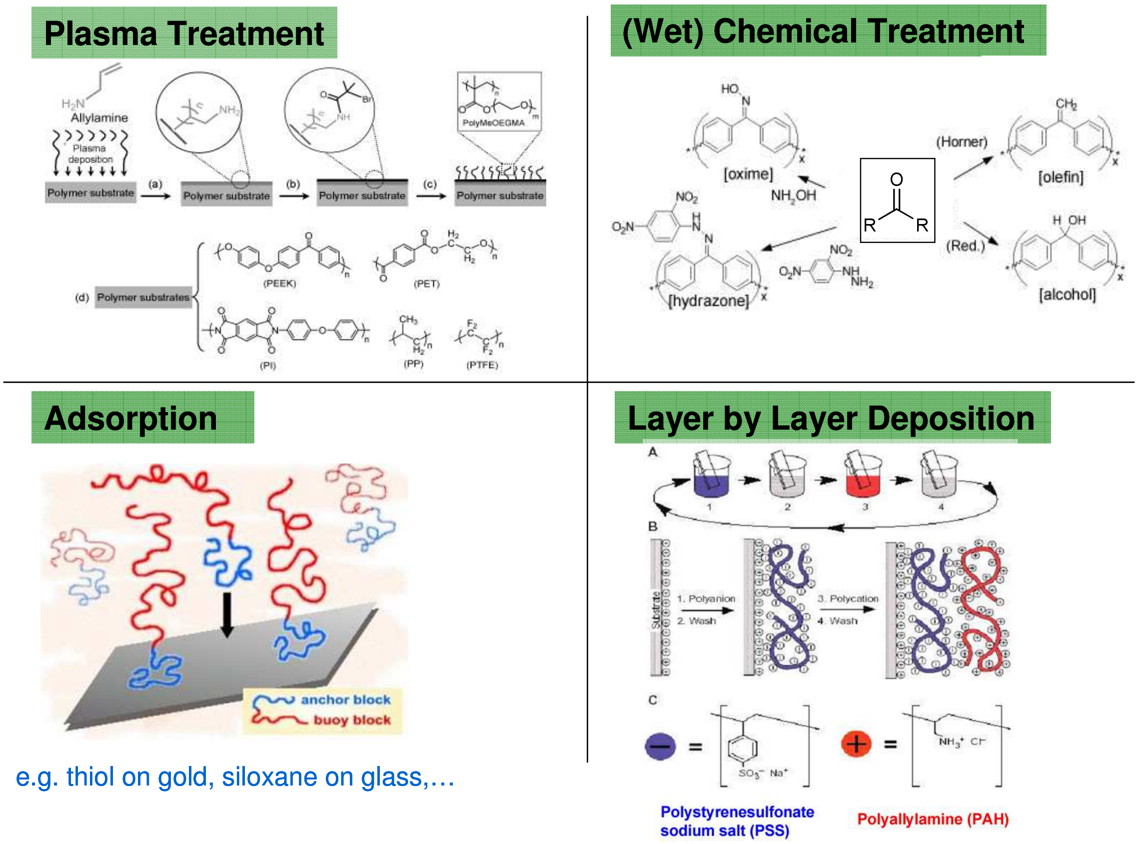

Figure 1.2.2: Common surface modification strategies including plasma treatment, chemical surface modification, adsorption of molecules and layer-by-layer deposition.[75, 76]

These monolayers can be used directly for covalent coupling of an analyte capturing unit or they can serve as foundation for further coupling of chemical structures such as polymer brushes or hydrogels.[51, 77] These structures subsequently serve as two- or three-dimensional scaffold for coupling of recognition units. Surface modification of polymers is performed by plasma techniques or by using wet chemistry (Figure 1.2.3).[76] A versatile example of polymer surface modification is the surface modification of poly(ether etherketone) (PEEK) which is used in many fields from medicine to aerospace due to its high temperature stability. Recently, the manifold modification of PEEK surfaces by various polymer brushes was reported.[77]

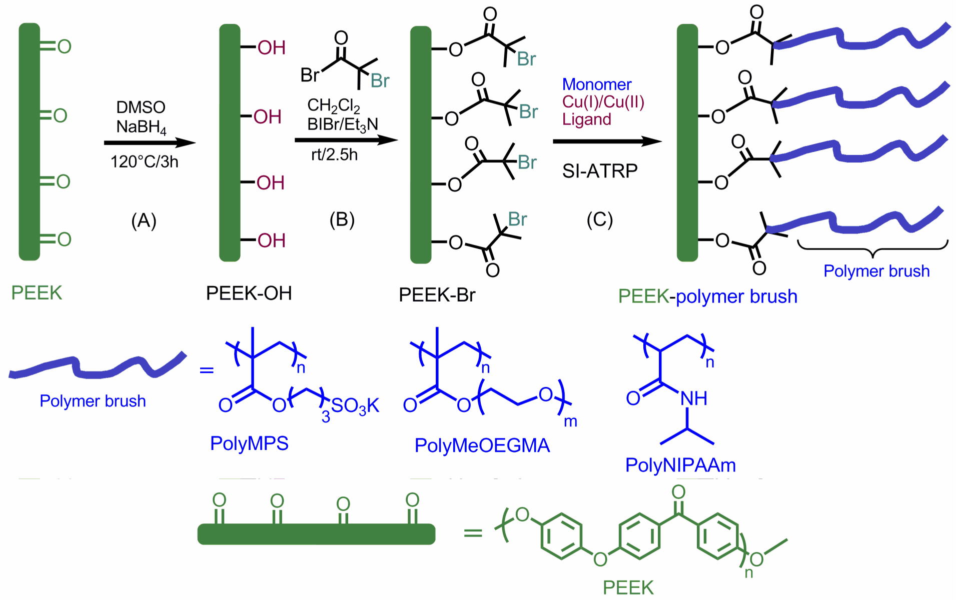

***Figure 1.2.3**: Surface modification of poly(ether etherketone) (PEEK) by grafting polymer brushes (C) to a monolayer of initiator molecules (B). Surface activation was carried out by organic chemistry in this case.*[77]

With this strategy of surface modification the advantages of the substrate material are totally preserved whereas the surface properties can be changed

1.2.3 Read-out Mechanisms

The signal read out is mostly performed optically, electrochemically, or by a quartz crystal microbalance (piezoelectric).

Optical signal read out is based on changes of light. Many optical biosensors are based on evanescent wave techniques such as surface plasmon resonance[78] or on the evanescent field of optical waveguide modes.[79] Other optical techniques are based on fluorescence- or absorbance detection depending on the possibility of using label-free sensing concept or of using fluorescent labels. Surface plasmon resonance requires a metal surface. Thereby, changes in the electric permittivity (dielectric constant) at the metal-dielectric interface are detected. For example, the analysis of casein in milk has been performed by the detection of changes in the absorption on gold.[80]

Electrochemical biosensor concepts[81] are based on reactions that produces or consumes electrons mostly redox-enzyme catalysed ones. The target analyte is thereby involved in a reaction occuring on the active electrode surface. The produced ions create a potential resulting in a measurable signal. Either the potential at zero current or the current at a fixed potential can be recorded. The advantage of the electrochemical detection can be seen in the label-free and direct analysis of small molecules such as peptides for example by applying biofunctionalized ion-sensitive field-effect transistors.[82]

A third sensor concept is the quartz crystal microbalance belonging to a class of surface wave acoustic biosensors. Thereby, the mass per unit area is detected by recording the change in frequency of a quartz crystal resonator. Addition or removal of a small mass upon oxidation growth/decay or film deposition at the surface of the acoustic resonator leads to a change of the resonance frequency.[83, 84]

A last read out concept to be mentioned here is the thermometric sensor. The heat produced or absorbed by a reaction is proportional to the molar enthalpy and thus to the overall number of molecules involved. Thermal sensors do not need frequent recalibration and are investigated for example to detect pesticides.

1.2.4 Biosensors – State of the Art

Recent developments of biosensors aim for miniaturized, smart, and integrated systems for analytical and therapeutic treatments to enable the simultaneous description and monitoring of gene and protein expression or metabolic states. A lot of challenging problems have to be overcome: monitoring of physical parameters is well established whereas chemo- and biosensors are available for only a few parameters and mainly as *in vitro* devices. Gene arrays are under development in the field of research but are not used in clinical practice. Protein arrays are in an advanced state with promising results but not yet mature reproducible state.[56] The most common example of a frequently used biosensor is the already mentioned glucose sensor which exists as integrated multi-array device.[85, 86] The miniaturization of this sensor faced a great interest due to monitoring of diabetics at home with an inexpensive diagnostic instrument resulting in a more precise adjustment of insulin. An important field in biosensor development is the continuous monitoring of analytes for example to control the degree of anesthesia. Furthermore, sensors for *in vivo* applications are of high interest.[56] Therefore, microminiaturization is unavoidable. Expectations are raised to significantly improve analytical performance by merging sophisticated micro- and nanotechnologies with hybrid biosystems. A very versatile approach for *in vivo* applications is the combination of a sensor response with drug delivery. For this purpose, responsive hydrogels are useful materials because they can be tuned to respond to certain molecules by volume changes. A biodegradable, insulin-carrying, glucose-sensitive hydrogel is a perfect candidate for insulin delivery. Up to now *in vitro* optimization of such systems are reported.[87] The volume change is applied for sensing devices, too. Swelling of biosensitive poly(2-hydroxyethyl methacrylate) (p-HEMA) hydrogels upon contact with analytes can be detected by a capacitance change produced by a deformed conducting diaphragm.[88] Such new developments are still under investigation but they show exciting possibilities for biosensing in the future.

For high-throughput detection of analytes biochip arrays were developed. This is of critical importance for genetic-screening in order to detect point mutations that can lead to tumors in an early-stage.[56] To analyze proteins, microarrays based on immunochemical assays were developed. Basically, four types of immunoassays exist: enzyme immunoassay, radioimmunoassay, fluorescent immunoassay, and enzyme linked immunosorbend assay (ELISA). Their major difference can be seen in the type of label used. As already briefly mentioned microarray technology has currently been expanded beyond DNA detection to the field of proteomics for the analysis of protein function in system biology.[56] Antibody array chips on the basis of microsystem technology allow protein analysis for known proteins.[89, 90] The drawback of proteins is their enhanced instability compared to DNA and they must be immobilized while preserving their functionality. Immunoassays are for example combined with surface plasmon resonance based techniques. Besides, the commercially available SPR-detection systems,[78, 91-93] frequently new sensor concepts based on optical read out[94] especially based on evanescent wave techniques are developed.[95-98] Thereby, either the recognition process or the optical detection principle is optimized to improve sensitivity and the range of detectable species.[62, 99-101] Detection limits in the femtomolar or even attomolar range are reported.[102, 103]

With the knowledge of DNA and protein-based biology a multitude of metabolites have been investigated.[104] The monitoring of metabolic parameters gains increasing importance especially in the field of tissue engineering. To create metabolic sensors the combination of biological sensing elements with microtransducer arrays is necessary to produce a multi-biosensor device. Cells can be grown and monitored for example on chips that record pH and pO_2 simultaneously.[105] Such devices are commercially available and can be used for cytotoxicity testing as well.[106] Further research is necessary for the parallel detection of an increasing number of parameters. Furthermore, the cell-culture monitoring by analyzing extracellular fluids is advanced and new sensor principles have to be developed.[56]

Another trend is the development of nanobiosensors. A relatively new immobilization strategy uses the phenomenon of spontaneous assembly of phospholipids at planar interfaces between thermotropic liquid crystals. The patterned orientation of the liquid crystals reflects the spatial and temporal organization of the phospholipids. This provides a principle for label-free monitoring of molecular and biomolecular species without complex instrumentation.[107, 108] Detection limits of down to single molecule detection can be achieved with cantilever based sensors. Especially, multifunctional cantilevers have a great potential in biodiagnostics because they permit label-free, non-amplified analysis for example in gene-expression or proteomics.[109, 110]

Despite the new nanotechnologies in the field of biosensors nanomaterials are applied for example in array type assays or used for *in vivo* monitoring replacing organic dyes as labels. Nanocrystals show a high brilliance with tuneable emission maxima and narrow spectral width with typical full width half maxima (FWHM) of 25 nm and do not show photobleaching.[111] Besides optical labeling nanoparticles allow the read out by completely different techniques for example by conjugating magnetic nanoparticles commonly applied in the production of MRI contrast agents.

Finally, the ultimate goal would be the development of arrays of many different detector molecules to create a miniaturized, high-throughput, integrated “electronic nose”.

1.3 Aim and Outline

The aim of this work was to combine the field of hydrogel synthesis and functionalization as well as optical surface plasmon resonance and waveguide mode spectroscopy to create a functional hydrogel matrix for applications in optical biosensing and biomedicine.

The development and characterization of a material suitable for these applications requires the understanding of its chemical, mechanical, and optical properties and the exploration of its interactions with biomolecules and cells. In order to use the advantage of biocompatibility, especially for further biomedical applications, it was decided to employ a “natural” polymer present in nature, namely dextran. Dextran is very hydrophilic. Thus, 3-dimensional dextran networks are expected to show high swelling degrees in aqueous environments. Highly swelling hydrogels as 3-dimensional polymer networks facilitate the uptake of biomolecules and are consequently desired for biosensor and biomedical applications.

The chemical synthesis of a highly swelling detran hydrogel was based on preparation of a benzophenone photo-crosslinkable, carboxymethylated dextran-based (PCMD) polymer. The carboxyl groups serve as binding units for biomolecules such as proteins or antibodies in biosensor and biomedical applications. With active ester chemistry molecules carrying primary amino groups were covalently coupled to carboxyl groups even under aqueous conditions. Furthermore, the carboxyl groups introduce a responsivity towards pH- and ionic strength, allowing modulation of the hydrogel's swelling degree. Further functionalization of the dextran backbone aimed towards external manipulation of swelling degree and charge of the hydrogel. The hydrogel response to pH, ion concentration, electrochemical switching, and a magnetic force was studied.

Hydrogel formation by photo-crosslinking allowed simultaneous surface attachment of hydrogel films to substrates modified with a benzophenone-terminated adhesion layer. This molecular design allowing post-synthetical hydrogel network formation by photo-crosslinking and simultaneous surface attachment is advantageous in terms of easier functionalization and characterization of the soluble pre-polymer. In addition it provides the possibility to accurately control the crosslinking density by the applied light energy dose which grants facile tunability of the hydrogel properties.

Hydrogel films of a certain thickness can serve as waveguide. This feature allowed the optical characterization of the hydrogel's swelling properties by combining surface plasmon resonance (SPR) with optical waveguide mode spectroscopy (OWS). Based on these optical methods a biosensor concept applying a sandwich assay was developed. The idea was to use the electromagnetic field of the optical waveguide modes for fluorescence excitation of labeled analytes. The preparation of a highly swelling, waveguiding hydrogel matrix which allows analyte diffusion and binding inside the waveguide was expected to provide new sensor matrices. The coupling of labeled analytes inside the waveguiding medium should enable fluorescence excitation by the electromagnetic field in the center of the optical waveguide modes. This is expected to result in an enhanced fluorescence as compared to the fluorescence excited by an evanescent field such as the evanescent field of a surface plasmon. Thereby, the increased penetration depth and the higher field intensity of the optical waveguide modes as well as the increased amount of analyte capturing units due to the thicker sensor matrix were expected to contribute to a fluorescence enhancement. To investigate the potential of this sensor concept the well studied affinity binding of streptavidin-Cy5 to immobilized biotin was studied as model system. The optimization of the sensor concept towards biomolecule-detection was carried out with the tumor suppressor protein-antibody system p53-p53Ab6 under ideal conditions such as buffer environment. Subsequent fluorescence detection was performed with a labeled secondary antibody. Furthermore, the sensor matrix was successfully tested for prostate specific antigen (PSA) detection in clinically relevant samples like serum. For this purpose long range surface plasmon spectroscopy (LRSP) and fluorescence detection with LRSP (LR-SPFS) were applied in a cooperation project with Y. Wang and J. Dostálek at the Max Planck Institute for Polymer Research. Additionally, cooperation projects in the field of neutron scattering with A. Falk and fluorescence correlation spectroscopy with R. Raccis and Prof. G. Fytas were initiated at the Max Planck Institute for Polymer Research for further characterization of the hydrated hydrogel matrix in terms of surface structure, pore size, and diffusion.

Apart from the bio-related application in the field of sensing, the dextran-based hydrogel matrix was optimized towards the incorporation of even bigger species than proteins or antibodies, namely cells. Cell growth of endothelial cells and osteoblasts with the aim of applications in bone regeneration, are investigated in a cooperation project with Dr. U. Ritz and Dr. A. Hofmann at the University Hospital in Mainz. Especially, dextran's biocompatibility, hydrophilicity, and its degradability in the presence of dextranase were expected to make the dextran-based hydrogel a versatile material for cell growth.

1.4 Bibliography

[1] N. A. Peppas, P. Bures, W. Leobandung, H. Ichikawa, *European Journal of Pharmaceuticals and Biopharmaceuticals* **2000**, *50*, 27.
[2] M. A. Gauthier, M. I. Gibson, H. A. Klok, *Angew. Chem. Int. Ed.* **2009**, *48*, 48.
[3] A. D. Fuchs, J. C. Tiller, *Angew. Chem. Int. Ed.* **2006**, *45*, 6759.
[4] M. G. Zolotukhin, H. M. Colquhoun, L. G. Sestiaa, D. R. Rueda, D. Flot, *Macromolecules* **2003**, *36*, 4766.
[5] B. H. Schneider, E. L. Dickinson, M. D. Vach, J. V. Hoijer, L. V. Howard, *Biosens. Bioelectron.* **2000**, *15*, 13.
[6] H. Vaisocherova, W. Yang, Z. Zhang, Z. Q. Cao, G. Cheng, M. Piliarik, J. Homola, S. Jiang, *Anal. Chem.* **2008**, *80*, 7894.
[7] A. W. Wark, H. J. Lee, R. M. Corn, *Anal. Chem.* **2005**, *77*, 3904.
[8] M. Gumusderelioglu, H. Turkoglu, *Biomaterials* **2002**, *23*, 3927.
[9] Y. Qiu, K. Park, *Advanced Drug Delivery Reviews* **2001**, *53*, 321.
[10] N. A. Peppas, J. Z. Hilt, A. Khademhosseini, R. Langer, *Advanced Materials* **2006**, *18*, 1345.
[11] V. Ravaine, C. Ancla, B. Catargi, *J. Contr. Release* **2008**, *132*, 2.

[12] T. Coviello, P. Matricardi, C. Marianecci, F. Alhaique, *Jounal of Controlled Release* **2007**, *119*, 5.

[13] H. Zhang, H. Wu, L. Fan, F. Li, C.-H. Gu, M. Jia, *Polymer Composites* **2009**, *30*, 1243.

[14] J. S. Bateng, K. H. Matthews, H. N. E. Stevens, G. M. Ecclestone, *Journal of Pharmaceutical Science* **2008**, *97*, 2892.

[15] R. A. F. Clark, K. Ghosh, M. G. Tonnesen, *Journal of Investigative Dermatology* **2007**, *127*, 1018.

[16] K. Y. Lee, D. J. Mooney, *Chem. Rev.* **2001**, *101*, 1869.

[17] F. Rosso, G. Marino, A. Giordano, M. Barbarisi, D. Parmeggiani, A. Barbarisi, *Journal of Cellular Physiology* **2005**, *203*, 465.

[18] J. L. Ifkovits, J. A. Burdick, *Tissue Engineering* **2007**, *13*, 2369.

[19] J. M. G. Swann, A. J. Ryan, *Polym. Int.* **2009**, *58*, 285.

[20] S. Chaterji, I. K. Kwon, K. Park, *Prog. Polym. Sci.* **2007**, *32*, 1083.

[21] J. F. Mano, *Advanced Engineering Materials* **2008**, *10*, 515.

[22] B. Jeong, A. Gutowska, *Trends in Biotechnology* **2002**, *20*, 305.

[23] O. Okay, *Prog. Polym. Sci.* **2000**, *25*, 711.

[24] I. Galaev, B. Mattiasson, *Enzyme and Microbial Technology* **1993**, *15*, 354.

[25] R. Landers, U. Hubner, R. Schmelzeisen, R. Mülhaupt, *Biomaterials* **2002**, *23*, 4437.

[26] S. Liu, J. Niu, Z. Gu, *J. Appl. Polym. Sci.* **2009**, *112*, 2656.

[27] V. Chegel, Y. Shirshov, S. Avilov, M. Demchenko, M. Mustafaev, *J. Biochem. Biophys. Methods* **2002**, *50*, 201.

[28] Y. Huang, W. Leobandung, A. Foss, N. A. Peppas, *J. Contr. Release* **2000**, *65*, 63.

[29] Schild, *Progr. Polym. Sci.* **1992**, *17*, 163.

[30] Idziak, e. al., *Macromolecules* **1999**, *32*, 1260.

[31] B. D. Ratner, S. J. Bryant, *Annu. Rev. Biomed. Eng.* **2004**, *6*, 41.

[32] W. E. Hennink, C. F. v. Nostrum, *Advanced Drug Delivery Reviews* **2002**, *54*, 13.

[33] J. Berger, M. Reist, J. M. Mayer, O. Felt, N. A. Peppas, R. Gurny, *Europ. J. Pharmaceutics Biompharmaceutics* **2004**, *57*, 19.

[34] S. R. V. Tomme, W. E. Hennink, *Expert Reviews of Medical Devices* **2007**, *4*, 147.

[35] N. A. Peppas, Y. Huang, M. Torres-Lugo, J. H. Ward, J. Zhang, *Annu. Rev. Biomed. Eng* **2000**, *2*, 9.

[36] M. Hamidi, A. Azadi, P. Rafiei, *Adv. Drug Deliv. Rev.* **2008**, *60*, 1638.

[37] S. Zhu, A. E. Hamielec, R. H. Pelton, *Macromol. Chem. Theor. Simul.* **1993**, *2*, 587.

[38] O. Okay, *J. Appl. Polym. Sci.* **1999**, *74*, 2181.

[39] A. B. Kinney, A. B. Scranton, in *Superabsorbent Polymers, Vol. 480* (Eds.: F. L. Buchholz, N. A. Peppas), ACS Symp. Ser., Washington, DC. Am. Chem. Soc., **1994**, pp. 2.

[40] K. S. Anseth, C. N. Bowman, *Chem. Eng. Sci.* **1994**, *47*, 2207.

[41] P. J. Flory, B. D. Rehner, *J. Chem. Phys.* **1943**, *11*, 521.

[42] P. Flory, *Principles of Polymer Chemistry, Vol. Chapter XIII*, Cornell University Press, Ithaca, **1953**.

[43] N. A. Peppas, P. Colombo, *J. Contr. Release* **1997**, *45*, 35.

[44] B. D. Ratner, in *Hydrogels in Medicine and Pharmacy, Vol. 1* (Ed.: N. A. Peppas), Boca Raton FL: CRC, **1986**, pp. 85.

[45] A. Halperin, M. Tirell, T. P. Lodge, *Adv. Polym. Sci.* **1992**, *100*, 31.

[46] A. Mamada, T. Tanaka, D. Kungwachakun, M. Irie, *Macromolecules* **1990**, *23*, 1517.

[47] A. Suzuki, T. Tanaka, *Nature* **1990**, *346*, 345.

[48] A. Heller, *Current Opinion in Chemical Biology* **2006**, *10*, 664.

[49] Y. Osada, H. Okuzaki, H. Hori, *Nature* **1992**, *355*, 242.

[50] K. Kajiwara, S. B. Rossmurphy, *Nature* **1992**, *355*, 208.

[51] P. W. Beines, I. Klosterkamp, B. Menges, U. Jonas, W. Knoll, *Langmuir* **2007**, *23*, 2231.

[52] R. Breslow, *Acc. Chem. Res.* **2004**, *37*, 471.

[53] L. Chen, C.-J. Li, *Org. Lett.* **2004**, *6*, 3151.

[54] C.-J. Li, L. Chen, *Chem. Soc. Rev.* **2006**, *35*, 68.

[55] M. W. G. d. Bolster, R. Cammack, D. R. Coucouvanis, J. Reedijk, C. Veeger, *Pure Appl. Chem.* **1997**, *69*, 1251.

[56] G. A. Urban, *Meas.Sci. Technol.* **2009**, *20*, 012001.

[57] M. Zourob, A. Simonian, J. Wild, S. Mohr, X. Fan, I. Abdulhalim, N. J. Goddard, *The Analyst* **2007**, *132*, 114.

[58] M. Pescheck, J. Schrader, D. Sell, *Bioelectrochemistry* **2005**, *67*, 47.

[59] J. Shah, E. Wilkins, *Electroanalysis* **2003**, *15*, 157.

[60] M. Chaplin, C. Bucke, *Enzyme Technology*, Cambridge University Press, New York, **1990**.

[61] H. M. Keizer, B. R. Dorvel, M. Andersson, D. Fine, R. B. Price, J. R. Long, A. Dodabalapur, I. Köper, W. Knoll, P. A. V. Anderson, R. S. Duran, *ChemBioChem* **2007**, *8*, 1246.

[62] J. Homola, *Chem. Rev.* **2008**, *108*, 462.

[63] M. A. Cooper, *Anal. Bioanal. Chem.* **2003**, *377*, 834.

[64] K. Y. Tomizaki, K. Usui, H. Mihara, *ChemBioChem* **2005**, *6*, 782.

[65] L. Dunne, S. Daly, A. Baxter, S. Haughey, R. O'Kennedy, *Spectrosc. Lett.* **2005**, *38*, 229.

[66] N. Scholler, B. Garvik, T. Quarles, S. Jiang, N. J. Urban, *J. Immunol. Methods* **2006**, *317*, 132.

[67] N. Rojo, G. Ercilla, I. Haro, *Curr. Protein Pept. Sci.* **2003**, *4*, 291.

[68] C. Wittekindt, B. Fleckenstein, K. Wiesmuller, B. R. Eing, J. E. Kuhn, *Virol. J. Methods* **2000**, *87*, 133.

[69] E. S. Forzani, H. Q. Zhang, W. Chen, N. J. Tao, *Environ. Sci. Technol.* **2005**, *39*, 1257.

[70] M. N. Win, J. S. Klein, C. D. Smolke, *Nucleic Acids Res.* **2006**, *34*, 5670.

[71] Z. Wang, T. Wilkop, D. Xu, Y. Dong, G. MA, Q. Cheng, *Bioanal. Chem.* **2007**, *389*, 819.

[72] S. Flink, C. J. M. v. V. Frank, D. N. Reinhoudt, *Adv. Mater.* **2000**, *12*, 1315.

[73] R. G. Nuzzo, D. L. Allara, *J. Am. Chem. Soc.* **1983**, *105*, 4481.

[74] J. P. Folkers, P. E. Laibinis, G. M. Whitesides, *J. Phys. Chem.* **1994**, *98*, 563.

[75] http://esperia.iesl.forth.gr/~ujonas/Master_Surf_Chem/lecture_IntroSurfChem_3c.pdf.

[76] B. Yameen, *Dissertation* **2009**, *Johannes Gutenberg-Universität Mainz.*

[77] B. Yameen, M. Alvarez, O. Azzaroni, U. Jonas, W. Knoll, *Langmuir* **2009**, *25*, 6214.

[78] S. Löfas, M. Malmqvist, I. Roennberg, E. Stenberg, B. Liedberg, I. Lundstroem, *Sensors and Actuators B* **1991**, *5*, 79.

[79] W. Knoll, *Annu. Rev. Phys. Chem* **1998**, *49*, 569.

[80] H. M. Hiep, e. al., *Sci. Technol. Adv. Mater.* **2007**, *8*, 331.

[81] D. Grieshaber, R. MacKenzie, J. Vörös, E. Reimhult, *Sensors* **2008**, *8*, 1400.

[82] S. Q. Lud, M. G. Nikolaides, I. Haase, M. Fischer, A. R. Bausch, *Chem. Phys. Chem.* **2006**, *7*, 379.

[83] M. D. Ward, D. A. Buttry, *Science* **1990**, *249*, 1000.

[84] D. Johannsmann, *Phys. Chem. Chem. Phys.* **2008**, *10*, 4516.

[85] Y. Hamazato, M. Nakako, S. Satorus, M. Mitsuo, *IEEE Trans. Electron Devices* **1989**, *36*, 1303.

[86] A. Heller, B. Feldmann, *Chem. Rev.* **2008**, *108*, 2482.

[87] N. Kashyapa, B. Viswanadb, G. Sharmaa, V. Bhardwaja, P. Ramaraob, M. N. V. R. Kumar, *Biomaterials* **2007**, *28*, 2051.

[88] Z. A. Strong, A. W. Wang, C. McConnagh, *Biomed. Microdevices* **2002**, *4*, 97.

[89] T. Joos, e. al., *Electrophoresis* **2000**, *21*, 2641.

[90] T. O. Joos, D. Stoll, M. F. Templin, J. Bachmann, *Curr. Opin. Drug. Discov. Dev.* **2005**, *8*, 239.

[91] S. Löfas, B. Johnsson, *J. Chem. Soc., Chem. Commun.* **1990**, *21*, 1526.

[92] B. Johnsson, S. Löfas, G. Lindquist, *Anal. Biochem.* **1991**, *198*, 268.

[93] D. R. Hall, D. J. Winzor, *J. Chromatrogr. B* **1998**, *715*, 163.

[94] S. M. Borisov, O. S. Wolfbeis, *Chem. Rev.* **2008**, *108*, 423.

[95] R. Slavik, J. Homola, H. Vaisocherova, *Meas. Sci. Technol.* **2006**, *17*, 932.

[96] A. Sato, B. Menges, W. Knoll, *J. Appl. Phys.* **2009**, *105*, 014701.

[97] J. Dostálek, A. Kasry, W. Knoll, *Plasmonics* **2007**, *2*, 97.

[98] W. Knoll, A. Karsy, F. Yu, Y. Wang, A. Brunsen, J. Dostálek, *Journal of Nonlinear Optical Physics & Materials* **2008**, *17*, 121.

[99] Y. Wang, A. Brunsen, U. Jonas, J. Dostalek, W. Knoll, *Analytical Chemistry* **2009**, *81*, 9625.

[100] D. R. Shankaran, K. V. Gobi, N. Miura, *Sensors and Actuators B* **2007**, *121*, 158.

[101] X. D. Hoa, A. G. Kirk, M. Tabrizian, *Biosensors and Bioelectronics* **2007**, *23*, 151.

[102] F. Yu, B. Persson, S. Loefas, W. Knoll, *Anal. Chem.* **2004**, *76*, 6765.

[103] F. Yu, B. Persson, S. Löfas, W. Knoll, *J. Am. Chem. Soc.* **2004**, *126*, 8902.

[104] B. Daviss, *The Scientist* **2005**, *19*, 25.

[105] R. Ehret, e. al., *Fresenius' J. Anal. Chem.* **2001**, *369*, 30.

[106] L. Cerotti, J. Ponti, P. Colpo, E. Sabbioi, F. Rossi, *Biosens. Bioelectron.* **2007**, *22*, 3057.

[107] J. M. Brake, M. K. Dachner, Y.-Y. Luk, N. L. Abbott, *Science* **2003**, *302*, 2094.

[108] S. J. woltman, G. D. Jay, G. P. Crawford, *Nat. Mater.* **2007**, *6*, 929.

[109] F. Huber, M. Hegner, C. Gerber, H. J. Güntherodt, H. P. Lang, *Biosens. Bioelectron.* **2005**, *2*, 1599.

[110] C. Ziegler, *Anal. Bioanal. Chem.* **2004**, *379*, 946.

[111] H. Fernandes, K. Bingham, I. Chambers, A. Mendelow, *Acta Neuorchir. Suppl.* **1998**, *71*, 44.

2 *Methods*

2.1 Surface Plasmon Resonance (SPR) and Optical Waveguide Mode Spectroscopy (OWS)

For surface plasmon resonance (SPR) and optical waveguide mode spectroscopy (OWS) the same setup can be used, only the sample configuration is different. A top view of an SPR/OWS setup with all its components is schematically depicted in Figure 2.1.1.[1] The setup allows simultaneous fluorescence detection with the photomultiplier that is located at the backside of the sample cell.

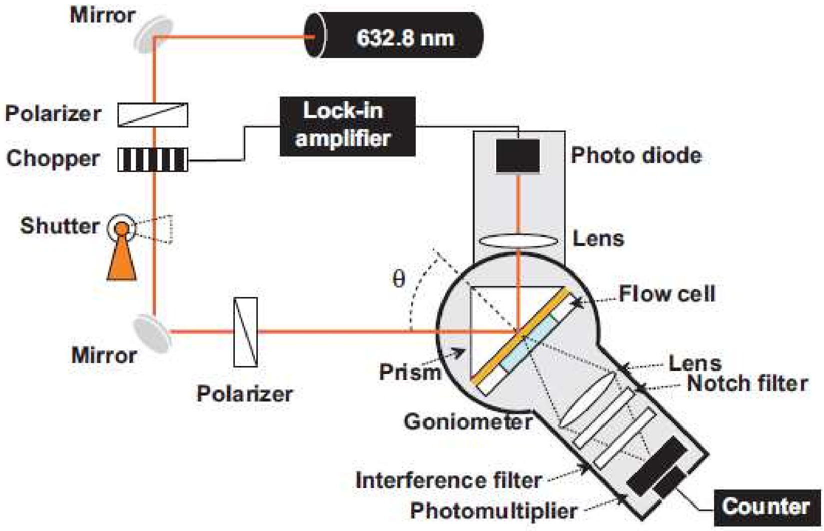

Figure 2.1.1: *Schematic view of a SPR setup with an additional photomultiplier that allows fluorescence detection at the backside of the sample cell.*[1]

The theoretical background of SPR and OWS is summarized in the subsequent chapters. Especially, the combination of both techniques, facilitate the characterization of hydrogel matrices. Additionally, they are versatile techniques for application in optical biosensorsing.

2.1.1 Surface Plasmon Resonance Spectroscopy (SPR)

A surface plasmon is a surface electromagnetic wave that propagates in a direction parallel to the metal/dielectric interface. The surface plasmon is located on the boundary of the metal and the external medium (air or water), with an exponentially decaying electromagnetic field perpendicular to the metal surface. The penetration depth of the surface plasmon is smaller than the wavelength of the incident beam (λ) and is around 200 nm.[2] In case of total internal reflection of the exponentially decaying electromagentic field can be calculated with Equation 2.1.1.[2] With $d_{1/e}$ as the penetration depth, λ as the wavelength of the incident beam, n_1 as the refractive index of the optically denser media, n_2 as the refractive index of the optically thinner media, and Θ_i as the angle of the incident beam.

$$d_{\frac{1}{e}} = \frac{\lambda}{2\pi}\left[\frac{n_1^2}{n_2^2}\sin^2\Theta_i - 1\right]^{-\frac{1}{2}} \tag{2.1.1}$$

While a laser beam is coupled to the interface of tow media with different optical density, going from the optically denser n_1 (glass) to the optically thinner (water) medium, a part of the beam is refracted following Snells law (Equation 2.1.2) whereas the other part is reflected with the same angle than the incident wave ($\theta_r = \theta_i$).

$$\sin\Theta_t = \frac{n_1}{n_2}\sin\Theta_i \tag{2.1.2}$$

The angle of total internal reflection (TIR) can be calculated with Equation 2.1.2 by setting the transmitted angle (Θ_t) to 90°. This corresponds to the situation depicted in orange in Figure 2.1.2.

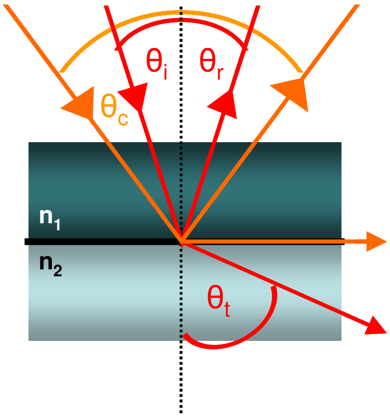

Figure 2.1.2: Schematic view of the optical refraction and reflection occurring at an interface based on Snells law. The transmitted electromagnetic wave is θ_t, the incident angle of the incident wave θ_i, and the critical angle shown in orange θ_c.

The angular dependence of the reflectivity and the transmittance can be described by solving Maxwells or Fresnel's equations resulting in the Equations 2.1.3.[2, 3] The relation between the refractive indices (n), the incident angle (Θ_i), the angle of the transmitted beam (Θ_t), and the ratio of the reflected light for p- (r_p) and s-polarized (r_s) light is described as well as the ratio of the transmitted light for p- (t_p) and s-polarization (t_s).

$$r_s = \frac{n_2 \cos\Theta_i - n_1 \cos\Theta_t}{n_2 \cos\Theta_i + n_1 \cos\Theta_t} \qquad r_p = \frac{n_2 \cos\Theta_t - n_1 \cos\Theta_i}{n_2 \cos\Theta_t + n_1 \cos\Theta_i}$$

$$t_s = \frac{2n_1 \cos\Theta_i}{n_2 \cos\Theta_i + n_1 \cos\Theta_t} \qquad t_p = \frac{2n_1 \cos\Theta_t}{n_2 \cos\Theta_i + n_1 \cos\Theta_t} \tag{2.1.3}$$

A surface plasmon electromagnetic wave is excited for one specific incident angle higher than the angle of total internal reflection (TIR) and matching the resonant condition. For this angle the light is dissipated into the metal film and a surface plasmon is generated.

In case of resonant conditions and thus surface plasmon generation the incident light wave and the surface plasmon need to have the same wave vector. The wave vector of the surface plasmon ($k_{x,\mathrm{plasmon}}$) is given by Equation 2.1.4 based on Maxwell's equations.[2]

$$k_{x,plasmon} = \frac{\omega}{c}\sqrt{\frac{\varepsilon_m \varepsilon_d}{\varepsilon_m + \varepsilon_d}} \tag{2.1.4}$$

Thereby, ω represents the angular frequency, ε_m is the dielectric constant of the metal, ε_d is the dielectric constant of the dielectric medium and c is the speed of light. Because the momentum of the surface plasmon will always exceed the wave vector of the incident beam in air or water, a special configuration for coupling the incident beam has to be used in order to match the momentum of the incident light with the one of the surface plasmon. Therefore, prism or grating coupling can be applied. In this work the Kretschmann configuration (Figure 2.1.3) was used, coupling the laser beam with an optically denser prism to the gold covered glass surface.[4]

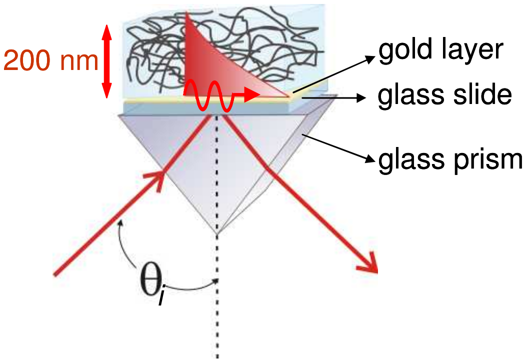

Figure 2.1.3: *Schematic description of the Kretschmann configuration used in this work. The glass slide (LaSFN9) is refractive index matched to the glass prism.*

If the momentum of the incident laser beam matches the momentum of the surface plasmon mode the photons interact with the free electron gas of the metal layer and a surface plasmon is generated. A surface plasmon can only be generated by p-polarized (T_M) light, because it has an electric field component perpendicular to the surface, but not by s-polarized light (T_E).

In the Kretschmann configuration the wave vector of the incident light and thus the surface plasmon generation depends on the incident angle of the laser beam (Θ_i). The relation between the incident angle (Θ_i) and the surface plasmon resonance are given by Equation 2.1.5 with $k_{x,photon}$ as the wavevector of the photon in x-direction, ω being the angular frequency, ε_{prism} the dielectric constant of the prism, c the speed of light and Θ_i the inicident angle of the laser beam.

$$k_{x,photon} = \frac{\omega}{c}\sqrt{\varepsilon_{prism}}\sin\Theta_i \tag{2.1.5}$$

At a certain angle $k_{x,photon}$ matches the resonance conditions and a surface plasmon is generated for a fixed angular frequency (ω) of the laser (Figure 2.1.4 A).

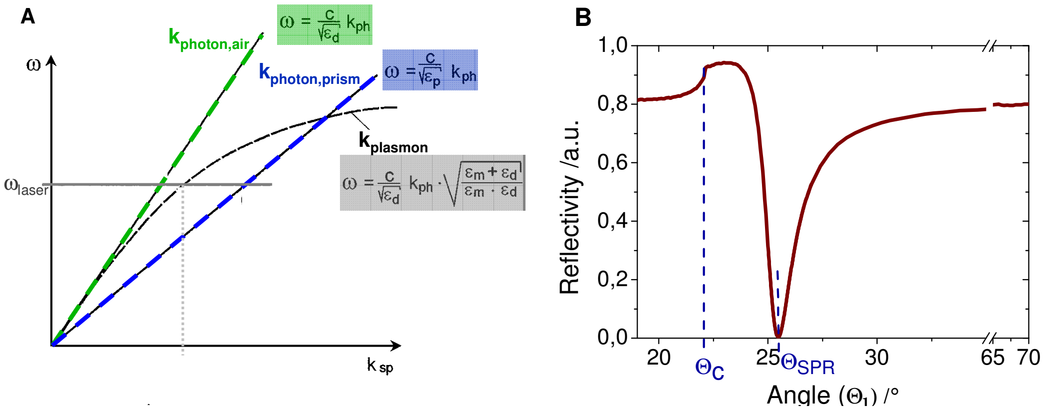

Figure 2.1.4: A) Dispersion relations of a photon coupled in air and with a prism and of the surface plasmon.[2] ***B)*** *Measured angular SPR spectra of a gold covered glass substrate in the Kretschmann configuration against air.*

Resonant conditions result in a decreased intensity of the reflected beam and thus a minimum in the angular spectrum because light is dissipated into the surface plasmon (Figure 2.1.4 B).

Any variation in the optical density on the gold surface in the penetration depth of the surface plasmon leads to changes of the wave vector of the surface plasmon and thus results in a shift of the resonance angle Θ_{SPR} (Figure 2.1.5 A).

Thus, the surface plasmon is very sensitive to any change, such as the adsorption of molecules, in close proximity to the metal surface. Refractive index changes in the field of the evanescent surface plasmon wave result in changes of the reflectivity according to Fresnel's equations (Equation 2.1.3). Such refractive index changes can be caused by adsorption of an additional layer of molecules for example. Consequently, surface plasmon resonance spectroscopy (SPR) can be applied to characterize the optical properties of thin films (d < 200 nm) at the metal surface without destroying them.

An increase of the optical density occurring due to molecule adsorption to the surface corresponds to a shift in the surface plasmon resonance to higher incident angles. The signal change can be observed either by recording angular scans or in real time by recording a kinetic at a fixed angle in the linear part of the surface plasmon (Figure 2.1.5 B and blue line in Figure 2.1.5 A).

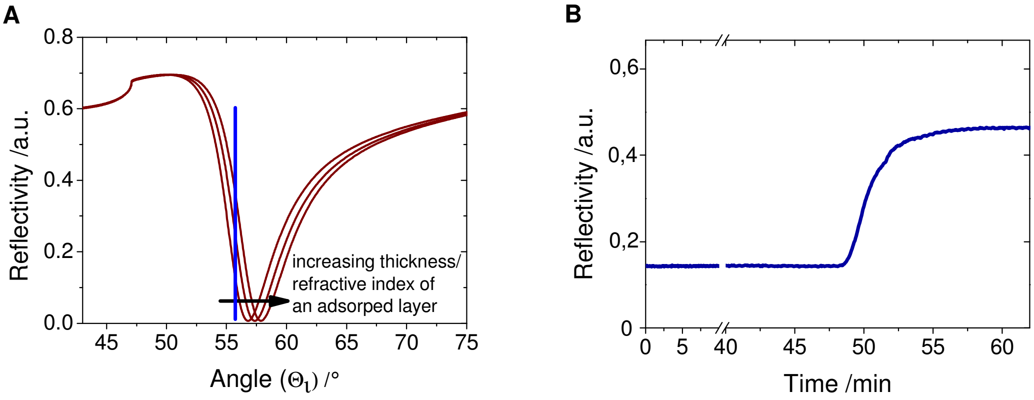

Figure 2.1.5: ***A)*** *Simulated angular scans for adhesion of an additional layer on a gold covered glass substrate. The blue line indicates the angle for a real time kinetic measurement. The black arrow represents the shift of the surface plasmon to higher angles upon adsorption of molecules.* ***B)*** *Example for a real time kinetic measurement corresponding to a surface plasmon shift to higher angles as depicted in (A).*

The shift of the resonance angle is proportional to the thickness and the dielectric constant of the adsorped layer following Equation 2.1.6. Using this relation the thickness or the refractive index can be determined by simulating the angular spectra.[5]

$$\Delta\Theta \propto \left(\sqrt{\varepsilon_d} - \sqrt{\varepsilon_p}\right)d \tag{2.1.6}$$

Thereby, the dielectric constant (ε) is described by Equation 2.1.7:

$$\varepsilon = (n + ik)^2 = n^2 + 2ikn - k^2 = \varepsilon' + i\varepsilon'' \tag{2.1.7}$$

With Θ_i being the angle of incidence, ε_d the complex dielectric constant of the dielectric, ε_p the complex dielectric constant of the buffer, *d* the thickness of the adsorbed layer, *n* the real part of the refractive index, *k* the imaginary part of the refractive index, ε' the real part of the dielectric constant ($\varepsilon'=n^2-k^2$), and ε'' the imaginary part of the dielectric constant ($\varepsilon'' = 2kn$). Consequently, for the simulation of the optical properties of an adsorped layer by simulating one surface plasmon resonance two variables have to be simulated: the thickness and the refractive index.

Although, surface plasmon resonance spectroscopy is a versatile method for the detection of changes close to a metal surface it requires the knowledge of either the refractive index or the thickness of the adsorped layer to determine the respective other parameter. Consequently, many applications do not allow the extraction of quantitative information without calibration. To overcome this disadvantage related optical methods such as the combination of SPR and optical waveguide mode spectroscopy (OWS) or long range surface plasmon spectroscopy can be applied. For all SPR/OWS experiments the incident laser beam energy of the 633 nm HeNe-laser was adjusted to 100 % reflectivity corresponding to a power of 145 µW.

2.1.2 Optical Waveguide Mode Spectroscopy (OWS)

For optical waveguide mode spectroscopy a waveguiding layer is needed. The laser beam is coupled into the waveguide material and the light is guided inside the waveguide. An ideal waveguide (Figure 2.1.6 A) consist of three layers with the three refractive indices n_1, n_2, and n_3. To allow light to be the condition $n_2 > n_1$, n_2 has to be fulfilled. The configuration used in this work is depicted in Figure 2.1.6 B and guides leaky optical waveguide modes.

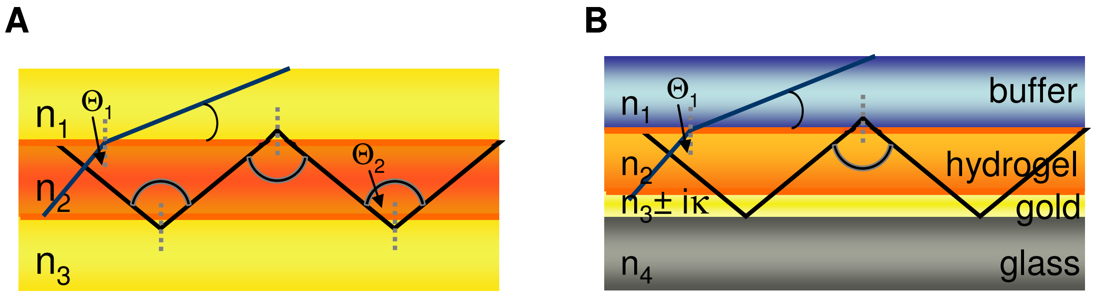

Figure 2.1.6: *Schematic view of the waveguiding principle* ***(A)*** *and schematic view of the layer system for leaky optical waveguiding modes used in this work* ***(B)****.*

For angles larger than the critical angle of total internal reflection (TIR) (Θ_c) (Figure 2.1.6 A), the optical wave is guided inside the layer. Only waveguide modes of discrete angles or discrete wavelength can be guided, as the interference after two reflections has to be constructive (Figure 2.1.6 A, black, Θ_2). However, optical waveguide modes, show an exponentially decaying electromagnetic field outside the waveguide. Description of these phenomena can be found in wave optics theory.[3, 6, 7]

On the basis of Maxwell's equations two groups of solutions and thus two possible types of waveguide modes are obtained: transversal electric (T_E) modes and transversal magnetic (T_M) modes. The T_E-waveguide modes are characterized by an electric field polarized perpendicular to the plane of incidence whereas the T_M-waveguide modes consist of an electric field polarized parallel to the plane of incidence. Because surface plasmon resonance on a metal surface can only be excited by p-polarized light with an electric field parallel to the propagation direction the combination of SPR and OWS only allows the detection of T_M-waveguide modes. If the polarization of the incident beam is modified to s-polarized light no surface plasmon but still T_E-waveguide modes can be excited.

Starting with the wavefunctions in the three media (Figure 2.1.6) the dispersion relation and than the wavefunctions can be derived. Thereby, the dispersion relation is only solvable for discrete propagation constants (β). Thus only discrete wavelength with a wave vector $k_x = \sqrt{k_0^2 n - \beta^2}$ can be guided. For a real k_x, the guided wave propagates in *x* direction, for an imaginary k, the wave is evanescent.[8]

The optical waveguide modes discussed here are called leaky optical waveguide modes and can only be partly described by the conventional optical waveguide modes. The sample configuration used for SPR/OWS measurements is depicted in Figure 2.1.7.

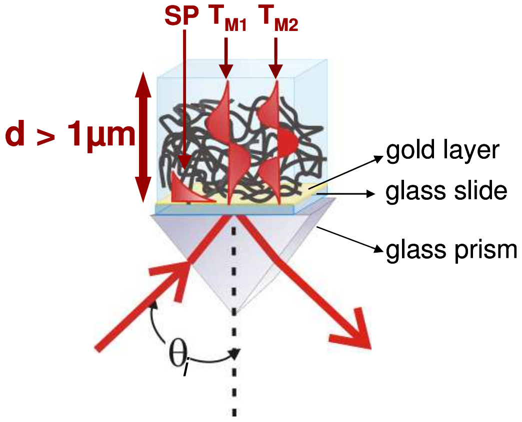

***Figure 2.1.7**: Sample configuration for combined SPR/OWS spectroscopy in the Kretschmann configuration.*

The gold layer with a thickness of 50 nm is too thin to allow the complete evanescent decay of the optical waveguide mode wavefunction. An optical wave, guided between gold and buffer or air is called leaky mode or tunneling mode. This is a mode that decays monotonically for a finite distance in the transverse direction but becomes oscillatory everywhere beyond that finite distance. Mathematically, leaky modes can be described by a quantum mechanical tunneling effect. For a closed expansion waveguide, like in a fiber, the covering media with n_1 and n_3 can be treated as potential walls of finite height and infinite width. Schrödinger's equation leads to the same result as derived by the wave optics theory mentioned above: an evanescent solution in the walls and an oscillating optical wave in between. The gold layer can be treated as potential wall of finite height and width. The two effects of a guided wave as well as the evanescent decay are possible within this theory. Waveguiding occurs due to reflection and the evanescent decaying field outside the waveguiding layer occurs due to tunneling effects.[9, 10] These tunnerling effects lead to loss of light especially at the gold hydrogel interface and thus lead to a limited lifetime of a leaky optical waveguide mode. Thereby, the coupling efficiency, which is an important parameter for fluorescence excitation (Chapter 2.3), depends on the thickness of the gold layer as proofed experimentally by Robert Roskamp.[11]

2.1.3 Long Range Surface Plasmon Spectroscopy (LRSP)

Long range surface plasmons (LRSP) are a particular type of surface plasmon modes that are characterized by electromagnetic fields that are mostly contained in the region outside of the metal. They originate from the coupling of surface plasmons on opposite surfaces of a thin metallic film that is embedded between dielectrics with similar refractive indices. The LRSP setup with the substrate configuration is depicted in Figure 2.1.8.

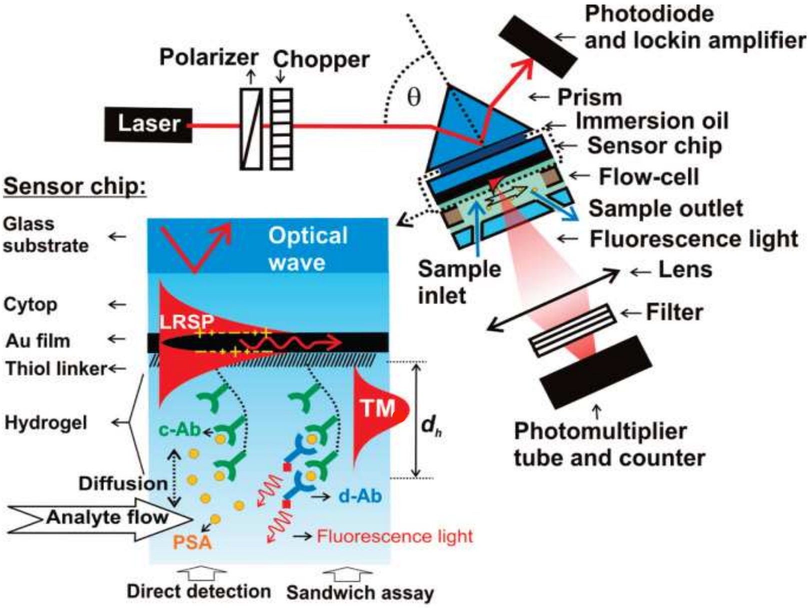

Figure 2.1.8: Schematic description of the LRSP experimental setup and especially of the substrate configuration by Y. Wang and J. Dostálek.[12] *The sample configuration is different to SPR and OWS.*

The setup itself is identical to the one used for SPR and OWS experiments only the sensor configuration changes.LRSPs exhibit orders of magnitude lower damping as compared to conventional surface plasmons on an individual metallic surface and show an increased penetration depth.[13, 14] The increased penetration depth facilitates the detection with 3D binding matrices exhibiting a higher surface density of analyte capturing units and to exploit the whole evanescent field of the LRSP.[15] Like all plasmon modes, LRSPs remain extremely sensitive to their surrounding environment and are thus of interest for detection and sensing purposes. Furthermore, their excitation provides larger enhancement of the electromagnetic field intensity enabling a further increase of the fluorescence signal in SPFS-based detection.[14]

2.2 Surface Plasmon Resonance and Optical Waveguide Mode Enhanced Fluorescence Spectroscopy (SPFS/OWFS)

Fluorescence is the emission of light after a fluorophore has been excited with light of a lower wavelength and thus higher energy. The term “fluorescence” was introduced by Stokes in 1852.[16] The excitation and fluorescence process is described in a Jablonski Diagramm (Figure 2.2.1).[17, 18]

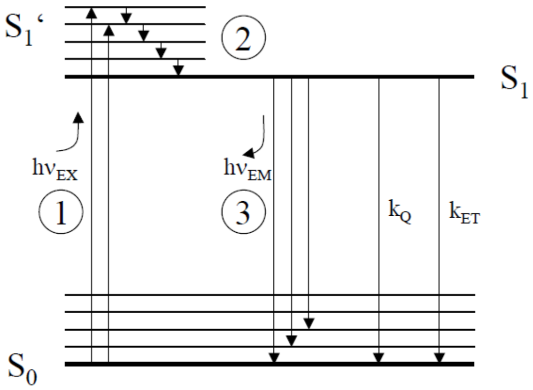

Figure 2.2.1: *Simplified Jablonski Diagramm summarizing the excitation and Fluorescence process.*[17, 18]

Absorption of a photon with the energy $h\nu_{EX}$ (Figure 2.2.1-1) results in the excitation from the electronic ground state (S_0) into an excited vibrational level of the electronic excited state (S_1). According to the Franck Condon principle the electronic excitation is combined with a change of the vibrational level due to a more significant overlap of the wave functions. Subsequently, the excited molecule undergoes changes such as conformational changes and relaxes into its vibrational ground state of the electronically excited state (S_1). Subsequently, the transition into the S_0 state can occur by fluorescence. A photon with the energy $h\nu_{EM}$ can be detected. Thereby, $h\nu_{EM}$ is smaller than $h\nu_{EX}$ due to the energy loss occurring by the relaxation to the vibrational ground state of S_1. This energy shift or visible by the higher wavelength of the fluorescence as compared to the excitation wavelength is called the Stokes shift. The higher the Stokes shift the easier is the experimental discrimination of fluorescence photons from the exciting laser beam.

In general, the transition back to the electronical ground state (S_0) can occur via various mechanisms that can be classified into radiative and non-radiative. Non-radiative transitions are for example internal conversion or intersystem crossing. Internal conversion (IC, k_{IC}) is a vibrational energy transfer from an exited vibritional state in the S_1 state to a molecule in the S_0 state. Intersystem crossing (ISC, k_{ISC}) describes a transition to a state with a different spin multiplicity. Further processes are for example fluorescence resonance energy transfer (FRET, k_{ET}), or collisional quenching (CQ, k_{CQ}). All these mechanisms depopulate the S_1 state and thus minimize the number of molecules that undergo a radiative decay between S_1 and S_0 by fluorescence (F, k_F). Consequently, not the total number of excited molecules returns to the ground state by fluorescence emission. The life time of the S_1-state is around 1-10 ns.

The ratio of the number of fluorescence photons emitted to the number of absorbed photons is called the fluorescence quantum yield (Φ) and is described by Equation 2.2.1.

$$\phi = \frac{k_F}{k_F + k_D} \qquad (2.2.1)$$

with $k_D = k_{ET}+k_{ISC}+k_{IC}+k_{CQ}$. The quantum yield is thereby governed by the relation of the rate constant of the fluorescence decay (k_F) and the rate constants of the depopulation processes (k_D).

Fluorescence Quenching

Quenching of fluorescence is caused by any process that leads to energy transfer from the fluorophore to another molecule and thus results in a reduction of the quantum yield. Thereby, the energy can be transferred to the quencher molecule either by collision or by complex formation. Both mechanisms induce the relaxation of the fluorophore into its electronic ground state (S_0). The collisional energy transfer is described by the Stern-Vollmer equation (Equation 2.2.2):

$$\frac{I_0}{I} = 1 + k_q [Q] \tau \qquad (2.2.2)$$

with I_0 representing the fluorescence intensity in the absence of a quenching molecule, I the intensity in the presence of a quencher, *[Q]* the quencher concentration, k_q the rate of the collisional quenching, and τ the observed lifetime.

Quenching due to a ground state-complex formation between a fluorophore and a quenching molecule is described by Equation 2.2.3:

$$\frac{I_0}{I} = 1 + k_C[Q] \tag{2.2.3}$$

with k_C representing the complex formation constant.

Consequently, the higher the quencher concentration the lower the fluorescence quantum yield. In case the fluorophores quench their own fluorescence (“self-quenching”) an increased fluorophore concentration does not lead to an increased fluorescence signal.[19]

Bleaching by Flurorescence Resonance Energy Transfer

Another very important quenching mechanism, especially for SPFS, is the quenching by fluorescence resonance energy transfer (FRET) also known as Förster energy transfer. The non-radiative Förster energy transfer is a distance dependent dipole-dipole interaciton and occurs over a distance of 1-10 nm.[20] The efficiency of FRET is a key factor, which depends on the inverse sixth power of the intermolecular distance (R) as described by Equation 2.2.3:

$$\phi_{ET(R)} = \frac{R^6}{R^6 + R_0^6} \tag{2.2.3}$$

Thereby, the distance at which the efficiency of the energy transfer reaches 50%, related to the number of deactivated fluorophors, is defined by the Förster radius (R_0).[20]

Photobleaching

Photobleaching is an often irreversible, photon-induced damage of a fluorophore and occurs in case the irradiation time or the irradiation intensity are exceeding a critical value. A fluorophore can undergo a finite number of excitation-relaxation cycles prior to photochemical destruction. Thereby, the number of cycles depends on the fluorophore. A stable fluorophore undergoes approximately 100 cycles of excitation and subsequent relaxation. Photobleaching is largely due to the generation of free oxygen radicals that attack and permanently destroy the light-emitting properties of the fluorophore. Consequently, the rate of photobleaching can be reduced by including free radical scavengers such as ascorbate or by reducing the concentration of oxygen in the medium. A more practical prevention is the reduction of the irradiation intensity and the irradiation time for example by using a shutter.

2.2.1 Surface Plasmon Resonance Enhanced Fluorescence Spectroscopy (SPFS)

In surface plasmon enhanced fluorescence spectroscopy (SPFS) fluorophores are excited by the evanescent electromagnetical field of the surface plasmon. Due to the penetration depth of about 200 nm[2] only fluorophores located within this distance from the surface can be excited (Figure 2.2.2). This can be an advantage because the detection is localized and is not disturbed by molecules being outside the detection range. On the other hand the fluorescence intensity is limited by the amount of fluorophores located within this distance.

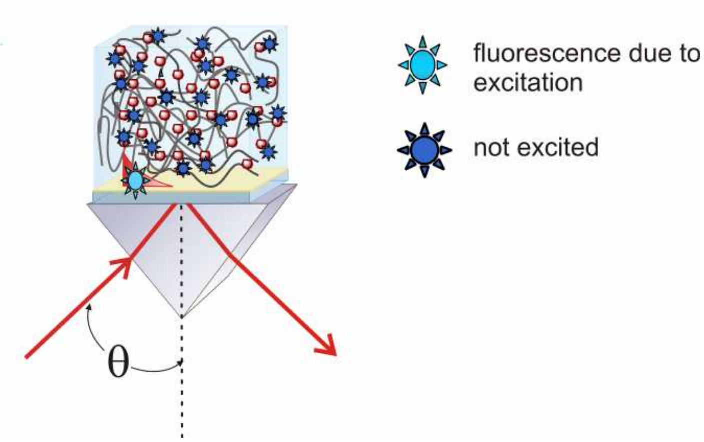

Figure 2.2.2: *Schematic description of the SPFS principle.*

A crucial parameter is the distance of the fluorophore to the gold layer which is used to generate the surface plasmon. The gold layer quenches fluorescence by resonant fluorescence energy transfer. To prevent quenching the distance of the dye to the gold surface has to be increased. On the other hand the field intensity of the surface plasmon decays exponentially with increasing distance from the gold surface and has its maximal intensity close to the gold surface. Within a distance of approximately 10 nm, fluorescence quenching due to Förster transfer between the fluorophore and the gold surface can occur. The energy is thereby transferred to heat. As described above the Förster transfer rate depends on the distance from the quencher with R^{-6}. Due to the enlarged number of effective acceptor sites in a gold layer the distance dependence can be changed to R^{-3}-R^{-4}.[21, 22] At sufficient separation distances free emission of the fluorophores are dominant. Besides, the fluorescence emission gradient due to Förster transfer between the fluorophore and the gold surface, the exponential evanescent field gradient, and finally fluorescence reflection by the gold surface causing light interference has to be considered.

Long Range Surface Plasmon Enhanced Fluorescence (LR-SPFS)

To increase the fluorescence signal the excitation of fluorescence by long range surface plasmons is a versatile technique. First the overall electromagnetic field intensity is higher as compared to conventional surface plasmons and second the penetration depth is increased. Consequently, a higher amount of fluorophores can be excited with a higher field intensity resulting in an enhancement of the fluorescence signal.

2.2.2 Optical Waveguide Mode Enhanced Fluorescence Spectroscopy (OWFS)

Optical leaky waveguide modes can be used for fluorescence excitation (OWFS) like surface plasmons. The combination of SPFS and OWFS is possible as well as depicted in Figure 2.2.3. Thereby, the electromagnetic field of the optical waveguide modes is distributed over the entire distance of the waveguiding matrix.

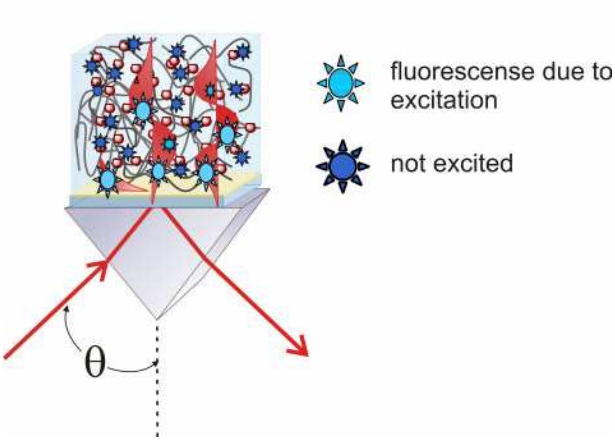

Figure 2.2.3: *Schematic description of the SPFS/OWFS principle.*

If a fluorophore is located inside the waveguiding matrix a significant fluorescence increase as compared to conventional surface plasmons is expected. One reason is the excitation not by the decaying evanescent electromagnetic field of an optical waveguide mode or surface plasmon but an excitation by the maximum of the guided electromagnetic field. Another reason is the increased number of fluorophores located within the electromagnetic field of the optical waveguide mode. A thickness of the waveguide of around one micrometer in the swollen state is required for waveguide mode generation and allows to couple an increased number of fluorophores. Furthermore, the electromagnetic field itself is increased as compared to conventional surface plasmons. Even long range surface plasmons only have a penetration depth of approximately 1 μm with an evanescent decaying electromagnetic field.[12]

Another advantage of optical waveguide mode excited fluorescence detection is the possibility to work without the gold layer. In case only OWFS and no combination of SPFS and OWFS should be performed the gold layer is not needed and thus quenching effects due to FRET close to the gold surface can be avoided. The fluorescence intensity in OWFS depends on the amount of fluorophores localized inside the waveguide and thus indirectly on the thickness of the waveguide. Furthermore, the fluorescence intensity depends on the coupling efficiency of the optical waveguide modes and can be modulated by tuning these factors.

2.3 The Wentzel-Kramers-Brillouin Approximation - Data Analysis

Waveguide modes traveling in a layer with uniform refractive index and the data analysis in this case are described in Chapter 2.1.[8] If the refractive index of the waveguide layer shows a refractive index gradient the situation becomes more complex. For a homogeneous gradient the exact solution can be calculated,[3] for an inhomogeneous one only approximations can be applied. The approximation used in this work is called the reversed Wentzel-Kramers-Brillouin approximation (WKB).[3, 6] In summary the scalar wavefunction (Equation 2.3.1) is solved.

$$\frac{\partial^2 H_y}{\partial x^2} + \left(k_0^2 n^2(x) - \beta^2\right) H_y = 0 \qquad (2.3.1)$$

Thereby, the terms of zero order results in two possible solution: an oscillating and an evanescent for $k_0^2 n^2(x) < \beta^2$. If discontinuity occurs both solutions merge into eachother. The transition point is used as integration limit for the oscillating solution, introducing the effective refractive index sensed by every optical waveguide mode. Practically the effective refractive index (n_{eff}) is determined by the measured incident angle of each optical waveguide mode as described by Equation 2.3.2:

$$n_{eff} = n_p \sin\left(\gamma + \arcsin\left(\frac{\sin\Theta_i}{n_p}\right)\right) \qquad (2.3.2)$$

with n_p as the refractive index of the prism, γ as the prism angle of 45° (Figure 2.1.1), and Θ_i as the angle of incidence. The refractive index or more exact $n^2(x)$ can be approximated according to Equation 2.3.3:[3]

$$n^2(x) = n^2_{eff,k} + \frac{n^2_{eff,k-1} - n^2_{eff,k}}{x_k - x_{k-1}} (x_k - x) \tag{2.3.3}$$

Thereby, the condition $x_{k-1} \leq x \leq x_k$ and k=1,2,3,…,m has to be fulfilled.

With the approximation of $n^2(x)$ the effective refractive index (n_{eff}) can be determined for every optical waveguide mode. For this purpose the effective refractive index (n_{eff}) is deduced from the angular position of each leaky optical waveguide mode. Subsequently, n_{eff} is related to a certain distance from the substrate surface by applying an algorithm[3] Due to the way of performing the WKB-approximation based calculation of a refractive index-distance profile of a waveguiding matrix it is referred to as “reversed WKB-approximation”.

The experimental procedure for the determination of the refractive index-thickness profile of a waveguiding hydrogel film on a gold covered glass substrate swollen in buffer is described in the following part. The angular positions of the four optical waveguide modes (Figure 2.3.1 A, black curve) are used to calculate the hydrogel film profile (Figure 2.3.1 B) using the WKB approximation as described above. The swollen thickness was extracted from these WKB profiles. For the profile shown in Figure 2.3.1 B this would be 7.2 µm. The value calculated for the waveguide-gold interface (z=0) is set to 150 nm assuming a penetration depth of the surface plasmon of 150-200 nm.[2] The refractive index value at the hydrogel gold interface (z = 0 nm) is derived experimentally from the surface plasmon by setting the thickness in a one layer model to 1 µm or higher and simulating the surface plasmon by fitting the refractive index. The angular spectrum cannot be reproduced by simulating a one layer model which is consistent with the results of the WKB approximation and reported hydrogel systems.[23] In this example the WKB profile shows a 3-layer structure: one layer for the 150 nm at the gold hydrogel interface, one layer up to approximately 5 µm and the last layer for the hydrogel buffer interface showing a gradient into the solution. If this 3-layer structure is simulated the experimentally recorded scan can be reproduced (Fig 2.3.1 A, red curve). For an angular scan with four optical waveguide modes 2 layeres for the hydrogel film plus the “surface plasmon layer” leads to one parameter per signal which is the maximum of parameters that can be reasonably fitted. The exact values used for the simulation are summarized in the table of Figure 2.3.1 C.

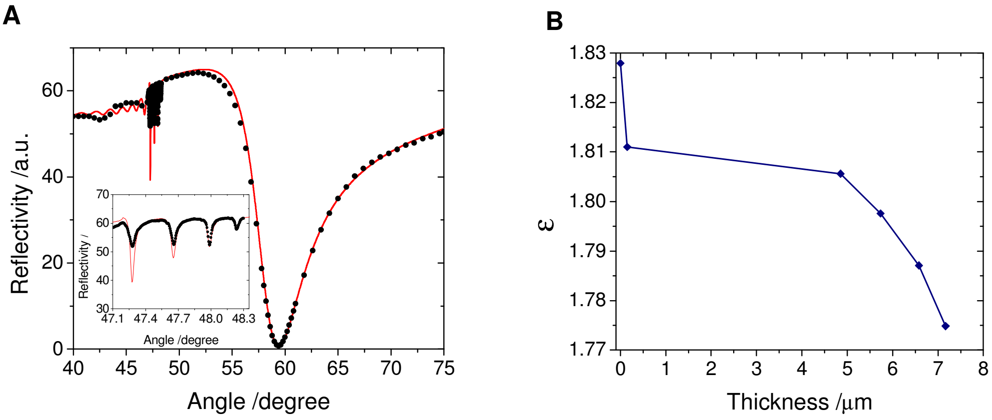

C

Layer	*Thickness /nm*	*ε' (real)*	*ε'' (imaginary)*
LaSFN9	0	3.407	0
Chromium	1.9	-4	16.8
Gold	45	-12.4	1.6
SAM	2	2.06	0
Hydrogel-1	150	1.828	0
Hydrogel-2	4800	1.8105	0.006
Hydrogel-3	1600	1.802	0.001
Buffer	0	1.774	0

Figure 2.3.1: *Implementation of the WKB approximation and the procedure of data simulation exemplified for a dextran-based hydrogel film. The hydrogel film profile **(B)** is derived from the angular position of the optical waveguide modes ((**A**) black) and the refractive index of the surface plasmon. The WKB profile indicates a 3 layer system which reproduces the angular scan ((**A**), red curve). The exact values of the simulated curve are shown in table **(C)**.*

The relation between the refractive index (n) and the dielectric constant (ε) is described by Equation 2.1.7.

2.4 Cyclic Voltammetry

Cyclic voltammetry is a potentiodynamic electrochemical measurement. The first works are going back to Randles[24], Nicholson and Shain,[25, 26] and to Kalthoff and Tomsicek.[27] The setup consists of three electrodes, a reference electrode, a working electrode, and a counter electrode. As reference electrode a Ag/AgCl electrode was used. A platinium wire served as counter electrode and a gold layer on top of a glass substrate was used as working electrode. The potential window of a cyclic voltammetry experiment is determined by the electrode materials, the solvent, and the background electrolyte. Mass transport generally takes place by diffusion, migration and convection. Diffusion is determined by a concentration gradient whereas migration occurs due to a potential gradient. Convection occurs due to the mechanical forces like stirring and can be eliminated on a short time scale. Usually, salt is added to the background electrolyte to increase the conductivity and to suppress charge transport by migration. Thus, the electron current can be balanced by the passage of ions in the solution and only a neglectable number of electroactive species is transported by migration.

For cyclic voltammetry measurements the electrode potential is continuously increased with time until a certain potential (E_2) is reached. Subsequently, the potential is continuously reversed back to the starting potential (E_1). Thereby, the whole process is controlled by a potentiostate. The rate of the potential increase and decrease is known as scan rate (V/s). The scan rate can have a significant influence on the peak current (i_p) because it determines the time available for analyte diffusion towards the electrode. Therefore, cyclic voltammograms are usually recorded at various scan rates to investingat this effect. The potential is measured between the working electrode and the counter electrode resulting in a triangular shape[28] for plotting the potential versus time. The measured data is plotted as current (i) versus the potential (E) giving the cyclic voltammogram.[29] A representative example is depicted in Figure 2.4.1.

In case an electroactive species is present, the measured current increases as the potential reaches the oxidation potential (E_{ox}) or the reduction potential (E_{Red}) and is reduced again as the concentration of the analyte close to the electrode is depleted. For a reversible redox system the reversed potential scanning leads to a similar reduction peak with inversed current as observed for the oxidation.

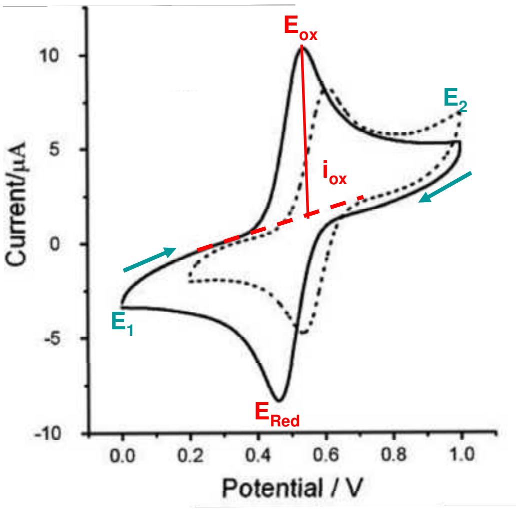

Figure 2.4.1: *Representative cyclic voltammogram*[30] *for a reversible electron transfer reaction.*

The oxidation and reduction potential E_{ox} and E_{red} are characteristic for the redox species and they indicate the ability of an analyte to change its oxidation state. A typical redox system is ferrocene (Figure 2.4.2).

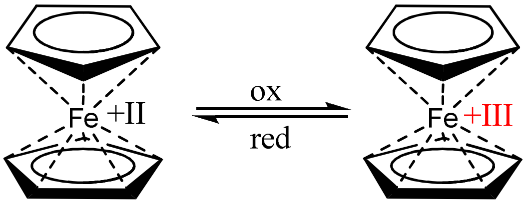

Figure 2.4.2: *Oxidation and reduction reaction in ferrocene.*

The oxidation potential of ferrocene depends for example on its substituents[31]and the solvent.[32] The oxidation potential of pure ferrocene is known to be 0.05 V against a saturated calomel electrode.

For a reversible oxidation/reduction the electrode potential is related to the concentration of oxidized and reduced species by Nernst's equation (Equation 2.4.2):

$$E = E^0 + \frac{RT}{nF}\ln\left(\frac{c[ox]}{c[red]}\right) \tag{2.4.2}$$

with *E* representing the electrode potential, E^0 being the standard electrode potential, *R* the universal gas constant, *T* the temperature in Kelvin, *F* the Faraday constant, *n* the number of electrons transferred, and *c* the concentration of the oxidized (ox) and the reduced (red) species respectively. According to Nernst equation the difference between the reduction and the oxidation potential ($\Delta E = E_{ox} - E_{red}$) is theoretically 59 mV for a reversible reaction.

The electron transfer close to the electrode surface is fast. In case the current is diffusion limited, the current is proportional to the square root of the scan rate as described by the Cottrell equation (Equation 2.4.1):

$$i = \frac{nFAc_j^o\sqrt{D_j}}{\sqrt{\pi t}} \tag{2.4.1}$$

with *i* being the current (A), n for the number of electrons, F for the Farraday constant, A for the area of the planar electrode, c_j^o for the initial concentration of the reducible analyte in mol/cm³, D_j for the diffusion coefficient in cm²/s, and t for the time in seconds. The influence of the scan rate on the current can be extracted by screening various scan rates.

The peak current (i_p) resembles the height of the oxidation and reduction peak and is described by the Randles-Sevcik equation (Equation 2.4.3). It depends on *A* describing the electrode area in cm², c the concentration in mol/cm³, D the diffusion coefficient in cm²/s, and v the scan rate in V/s.

$$i_p = \left(2.69 \times 10^5\right) n^{3/2} A c D^{1/2} \upsilon^{1/2} \tag{2.4.3}$$

The current described by this equation is a Faradaic current caused by the oxidation and reduction of an electroactive species. Consequently, the peak current (i_p) is directly proportional to the concentration of electroactive species that are detectable by the electrode. Furthermore, according to this equation i_p should be directly proportional to the square root of the scan rate. This relationship becomes particularly important in the study of electrode mechanisms. The ratio of $i_{p,ox}$ to $i_{p,red}$ should be close to one. A non-Faradaic current, also called charging current, is caused by the movement of ions in the solution while applying a potential to the working electrode.

Electrochemistry experiments were performed by using a controlling stage (Autolab, Metrohm) and connecting the gold covered glass substrate as working electrode. A silver/silver chloride electrode was used as reference and a platinium wire as counter electrode. The sample cell had a diameter of 0.385 cm and a thickness of 0.7 cm.

2.5 Atomic Force Microscopy

Atomic Force Microscopy (AFM) was used to investigate the surface structure on a small scale of µm². A cantilever with a tip at its end is used to scan a sample surface.[33-35] The tip commonly consists of silicon or silicon nitride. In close proximity to a sample, surface forces described by Hook's law act on the cantilever. These forces can be van der Waals forces, capillary forces, electrostatic forces, magnetic forces, etc. To influence the acting forces the cantilevers can be coated with a self-assembled monolayer of hydrophobic, hydrophilic or charged molecules, for example. In case the surface topography and thus the forces on the cantilever are changing, the position of the cantilever is changed in z-direction, perpendicular to the surface. A laser that is directed to the top surface of the cantilever and reflected onto an array of photodiodes is deflected as soon as the cantilever moves up and down. Thereby, the photodiode array can detect the variation in the position of the laser spot during scanning resulting in the detection of the topography of a sample. In contrast to SEM techniques, with AFM 3D pictures can be recorded. Typically, AFM images are recorded in "contact mode", where the tip is in physical contact with the sample surface. An alternative is the "non-contact mode" also called “tapping mode”, which operates at a given tip-sample separation under oscillation of the cantilever at its resonance frequency.

In this work AFM images were recorded with a commercially available AFM (Dimension 3100 CL) in the tapping mode. Micro cantilevers (Olympus) 160µm long, 50µm wide and 4.6µm thick with an integrated tip and a nominal spring constant of 42 N/m were used. The tip was scanned at rates about 0.7 Hz for a scan area of ~1 μm^2. In a simplified description of the tapping mode the cantilever is oscillated in z-direction perpendicular to the surface near its resonance frequency by a piezoelectric element mounted in the AFM tip holder. AFM tips with a resonance frequency of 300 kHz were used. Forces acting on the cantilever close to the sample surface result into a decrease of the oscillation amplitude. The height of the cantilever above the sample is thereby controlled and kept constant. An AFM image in the tapping mode is thus produced by mapping the force of the oscillating contacts of the tip with the surface of the sample allowing the recording of both the amplitude and the phase image. The height image displays the topography, whereas the phase image provides information about the mechanical properties of the sample. Furthermore, in the tapping mode it is generally possible to measure a surface under liquid medium such as water.

2.6 Cryo-Scanning Electron Microscopy

In Scanning Electron Microscopy (SEM) an electrons are used to visualize sample structures in the range of nanometers. The smaller wavelength of accelerated electrons as compared to photons of visible light allows to achieve better resolution as compared to optical microscopy. The maximum resolution is determined by the Abbé criterion (Equation 2.6.1), with N_A being the numerical aperture and λ being the wavelength.

$$d = \frac{\lambda}{2N_A} \tag{2.6.1}$$

The electron beam focused onto a sample causes various effects such as ejection of secondary electrons and backscattering of electrons, production of Auger electrons and x-rays. Usually, the secondary electrons are detected for SEM. The contrast in SEM is determined by the intensity of electrons at the detector while the focused electron beam is scanned over the sample surface to obtain a 2D microscopic picture. Mostly, voltages below 5 kV are used. Due to the low energy of the secondary electrons they are only able to leave the sample within a thin layer at the surface resulting in a high lateral and depth resolution.

Besides the commonly used focused electron beam a focused ion beam (FIB) can be used to generate secondary electrons that can be analyzed as described for SEM. Ions are larger and heavier than electrons and thus show a lower penetration depth into the sample surface as compared to electrons.

Both classical SEM as well as FIB measurements require solid surfaces. Because hydrogels contain a hughe amount of water while they are swollen they have to be frozen to be able to perform SEM and FIB measurements. The freezing step is critical and artefacts due to sample preparation and the water structure have to be taken into account.[36]

Therefore, no detailed structure analysis were carried out by cryo-SEM. This type of microscopy was rather used to get an idea about the macroporous structure that can occur in hydrogel samples. The hydrogel samples were swollen in buffer, rapidly frozen in liquid nitrogen, and transferred into the pre-cooled (about -160°C) Cryo preparation chamber (PP2000T, Quorum Technologies). The sample was broken and sputtered with a thin platinium layer (~20 nm) after the frozen water was sublimed off and then placed into the precooled chamber of the Focused Ion Beam (Nova, 600 Nanolab (FIB), FEI). The stage was slowly heated up to room temperature while measuring.

2.7 UV-VIS/NIR-Spectroscopy

UV-VIS spectroscopy uses the absorption of light with wavelength from the UV to the near infrared range for analyzing concentrations for example. Thereby, a target molecule is excited by light undergoing an electronic transition. The sample of interest in placed into a light beam with tunable wavelength. The intensity of light passing through the sample (I) is recorded and compared to the intensity of the incident beam (I_0). The ratio of I/I_0 is called the transmittance. Usually, the absorbance (A) of the solution is plotted in dependence of the excitation wavelength. The position of an absorption maximum, and thus the excitation wavelength, is related to the energy necessary to excite an electron from the HOMO to the LUMO whereas the absorbance is related to the concentration of the excited species and the quantum yield of the absorption process. By applying the Lambert-Beer law (Equation 2.6.1) the absorbance of a solution is directly proportional to the concentration (c) of the absorbing species as long the concentration is kept low and the path length (d) is kept constant. If the molar extinction coefficient (ε) is known it can be taken from references. To be more exact a concentration dependent calibration curve should be recorded to perform exact concentration determinations.

$$A = -\log\left(\frac{I}{I_0}\right) = \varepsilon c d \tag{2.6.1}$$

with *A* representing the absorbance, I_0 the intensity of the incident light at a fixed wavelength, *I* the transmitted intensity after passing the sample solution, *ε* the molar extinction coefficient (1/M*cm), *c* the concentration of absorbing species, and *d* the path length or the thickness of the analyte solution.

The molar extinction coefficient is a constant for each species as long as the wavelength, the solvent, the temperature, and the pressure are kept constant. Consequently, the spectral bandwith should be kept as narrow as possible and must be much smaller than the width of the absorbance of the sample to avoid that ε changes within the absorption band.

In this work UV-VIS spectra were recorded with a UV-VIS/NIR (Perkin Elmer, Lambda 900). The width of the slit was set to 4 nm.

2.8 Contact Angle measurements

The contact angle is defined as the angle between the three phases of a solid surface, a liquid, and a vapor phase. As liquid phase usually water and as vapor phase usually air with a constant humidity is used. The contact angle is specific for every system and contains information about surface properties, such as roughness and hydrophobicity. The shape of the water droplet on a solid surface is determined by the thermodynamic equilibrium which is described by the Young-equation:

$$\gamma_s = \gamma_{sl} + \gamma_l \cos\Theta$$

with γ_s being the surface tension of the solid substrate, γ_{sl} the interfacial tension (solid/liquid), γ_l the surface tension of the liquid and Θ the equilibrium contact angle.

The more hydrophobic a solid surface the higher the water contact angle (Figure 2.9.1).

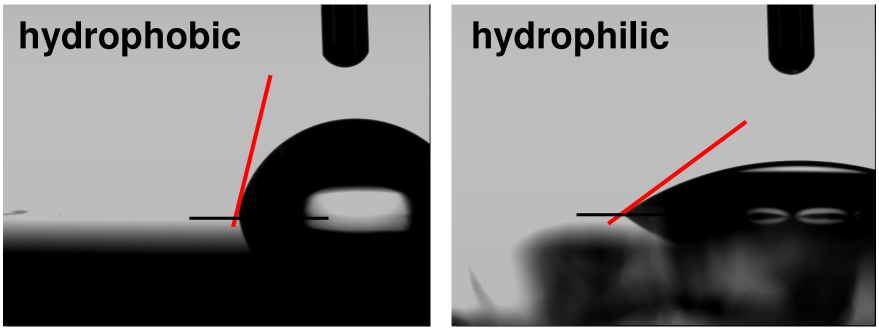

Figure 2.9.1: *Exemplified contact angle measurements for a more hydrophobic covered gold surface and a more hydrophilic covered gold surface.*

Very hydrophilic surfaces have contact angles below 30° and very hydrophobic surfaces show contact angles above 90°. Ultrahydrophobic surfaces such as known from the lotus effect show contact angles up to 180°. In this case the water droplet tries to avoid the contact with the surface and rolls off as soon as the surface is not in an exactly horizontal position. In this work the static contact angles in the “Sessile-Drop”-mode were measured. The system applied is the Drop Shape Analysis System DSA 10 (Kruess, Germany) with a thermo stage and degassed ultrapure water (Milli Q, 18.2 MΩcm, 4 µL droplets). To avoid evaporation effects evaluation was performed on the basis of pictures taken right after placing the droplet. At least five measurements were carried out on different positions of each surface. The contact angle was extracted by the commercially available software (SCA202, V3.4.7., DataPhysics Instruments, Germany).

2.9 Bibliography

[1] A. Sato, B. Menges, W. Knoll, *J. Appl. Phys.* **2009**, *105*, 014701.
[2] W. Knoll, *Annu. Rev. Phys. Chem* **1998**, *49*, 569.
[3] W. Karthe, R. Müller, *Integrierte Optik*, Leipzig, Germany, **1991**.
[4] E. Kretschmann, H. Raether, *Zeitschrift für Naturforschung Part A - Astrophysik Physik und Physikalische Chemie* **1968**, *23*, 2135.
[5] G. Kovacs, *Electromagnetic Surface Modes*, John Wiley & Sons, New York, **1982**.
[6] Y. Pochi, *Optical waves in layered media*, Wiley-VCH, **1988**.
[7] D. L. Andrews, Z. Gaburro, *Frontiers in surface nanophotonics: principles and applications*, Springer, **2007**.
[8] P. K. Tien, *Rev. Mod. Phys.* **1977**, *49*, 361.
[9] R. E. Smith, S. N. Houde-Walter, *Journal of the Optical Society America A - Optics Image Science and Vision* **1995**, *12*, 715.
[10] P. K. Tien, *Reviews of Modern Physics* **1977**, *49*, 361.
[11] R. Roskamp, Johannes Gutenberg - University (Mainz), **2009**.
[12] Y. Wang, A. Brunsen, U. Jonas, J. Dostalek, W. Knoll, *Analytical Chemistry* **2009**, *81*, 9625.
[13] D. Sarid, *Phys. Rev. Lett.* **1981**, *47*, 1927.
[14] J. Dostálek, A. Kasry, W. Knoll, *Plasmonics* **2007**, *2*, 97.
[15] A. Kasry, J. Dostálek, W. Knoll, *Advanced Surface Design for Biomaterial and Life Science Applications*, Wiley VCH, Weinheim, Germany, **2009**.
[16] G. G. Stokes, *Philosophical Transactions of the Royal Society of London* **1852**, *142*, 463.

[17] B. Valeur, *Molecular Fluorescence Principle and Applications*, Wiley-VCH, Weinheim, Germany, **2002**.

[18] J. R. Lakowicz, *Principles of Fluorescence Spectroscopy, 2nd Ed.*, Kluwer Academic/ Plenum Publishers, New York, **1999**.

[19] R. I. Macdonald, *J. Biol. Chem.* **1990**, *256*, 13533.

[20] T. Foerster, *Annalen der Physik* **1947**, *437*, 55.

[21] D. L. Andrews, *Chem. Phys.* **1989**, *135*, 195.

[22] B. B. Postacchini, V. Zucolotto, F. B. Dias, A. Monkman, O. N. Oliveira, *J. Phys. Chem. C* **2009**, *113*, 10303.

[23] P. W. Beines, I. Klosterkamp, B. Menges, U. Jonas, W. Knoll, *Langmuir* **2007**, *23*, 2231.

[24] J. E. B. Randles, *Trans. Faraday Soc.* **1952**, *48*, 828.

[25] R. S. Nicholson, *Anal. Chem.* **1964**, *36*, 706.

[26] R. S. Nicholson, *Anal. Chem.* **1965**, *37*, 1351.

[27] I. M. Kalthoff, W. J. Tomsicek, *J. Phys. Chem.* **1935**, *39*, 945.

[28] C. N. Reilley, *J. Chem. Ed.* **1962**, *39*, A853.

[29] P. T. Kissinger, W. R. Heinemann, *J. Chem. Ed.* **1983**, *60*, 702.

[30] K. A. Mahmoud, H.-B. Kraatz, *J. Inorg. Organomet. Polym.* **2008**, *18*, 69.

[31] S. M. Batterjee, M. I. Marzouk, M. E. Aazab, M. A. El-Hashash, *Appl. Organomet. Chem.* **2003**, *17*, 291.

[32] D. Bao, B. Millare, W. Xia, B. G. Steyer, A. A. Gerasimenko, A. Ferreira, A. Contreras, V. I. Vullev, *J. Phys. Chem. A* **2009**, *113*, 1259.

[33] G. Binning, C. F. Quate, C. Gerber, *Phys. Rev. Lett.* **1986**, *56*, 930.

[34] Y. Martin, C. C. Williams, H. K. Wickramashinghe, *J. Appl. Phys.* **1987**, *61*, 4723.

[35] T. R. Albrecht, P. Grutter, D. Horne, D. J. Rugar, *J. Appl. Phys.* **1991**, *69*, 668.

[36] P. Echlin, *Low Temperature Microscopy and Analysis.*, Plenum Press, New York, **1992**.

3 *Materials*

3.1 Synthesis of a Photo-Crosslinkable, pH-Responsive Dextran Hydrogel

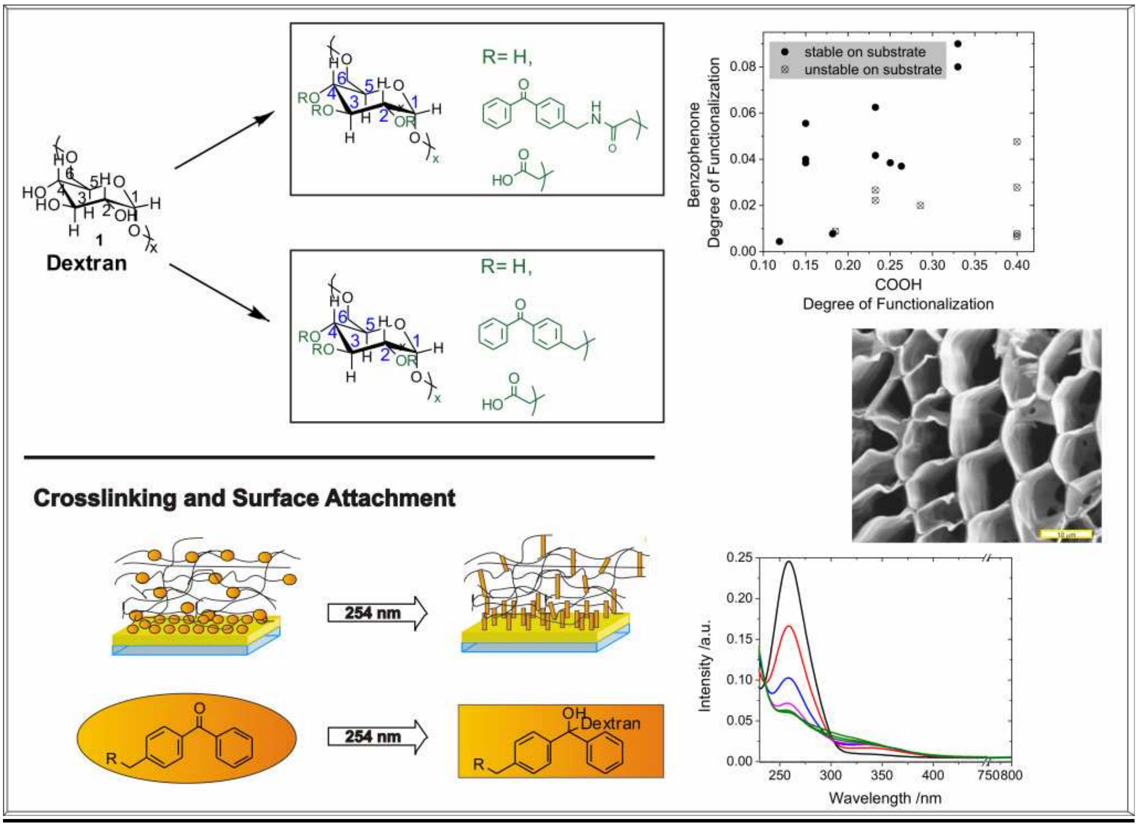

A photo-crosslinkable and pH-responsive dextran based polymer was prepared by two different synthesis routes differing in the photo-crosslinker coupling mechanism. In the first method amino-functionalized crosslinker moieties were coupled to pre-synthezised carboxyl groups, whereas in the second method the crosslinker coupling was separated from the carboxyl functionalities. Active ester chemistry was used as route for further modification of carboxyl groups implementing the possibility of introducing a variety of functionalities into the dextran based polymer. This versatile approach renders those hydrogels an attractive material for many applications from sensors to nanoparticle stabilization. Benzophenone moieties are introduced as photo-crosslinking unit. Hydrogel formation and surface coupling are carried out simultaneously by UV-irradiation.

3.1.1 Introduction

Hydrogels often exhibit specific characteristics like functional or stimuli-responsive behavior. They can for example be functionalized with carboxyl-, amino-, sulfonic acid- or hydroxyl groups and subsequently exhibit responsive behavior towards temperature, pH, or electric stimuli. Furthermore, certain molecules like glucose can be intercalated causing a responsive behavior. Typical systems are based on PNIPAAm having a lower critical solution temperature (LCST), poly(acrylic acid) or methacrylic acid exhibiting pH responsivity due to ionizable groups, polyethylenimine or 2-hydroxyethyl methacrylate used in medical applications.[1-5] For many applications, especially in the field of medicine, pharmaceutics, and sensing dextran is a promising material due to its biocompatibility[6-8] and its degradability by the enzyme dextranase.[9, 10] Pure dextran is reported to be crosslinked with 1,6-hexanediisocyanate[11] or glutaraldehyde[12], acrylated dextran was polymerized[13], acrylated and methacrylated dextrans were crosslinked via UV-irradiation.[14, 15] Carboxymethylated dextran was crosslinked by ester bond formation between active ester-activated carboxyl groups and its hydroxyl groups.[16-18] Sodiumperiodate-oxidized dextran was crosslinked with adipic acid dihydrazide.[19]

Generally, the three hydroxyl groups per glucose unit in the dextran backbone can be used for chemical modification. They are mainly transformed into ethers or esters.[20] Furthermore, the hydroxyl groups can be oxidized resulting in aldehyde formation.[21] These possibilities can be used for further wet-chemical modification of the dextran backbone. Examples are grafting of PNIPAAm onto a carboxymethylated dextran[22-24] to implement a LCST behavior, or introducing hydroxyethyl methacrylate (HEMA)[25, 26] or polyethyleneglycol (PEG),[27] to couple lactic acid oligomers[28, 29], methacrylate[14], maleic anhydride[14] or allyl isocyanate.[30]

Network formation of dextran chains can be performed by photo-crosslinking of chemically modified dextrans, by physical crosslinking, and by chemical crosslinking. Photo-crosslinking of dextran is carried out after chemical modification of the dextran backbone with photo-crosslinkable groups like dextran-azide derivatives[31] glycidyl acrylate[32] or glycidyl methacrylate derivatives.[21, 33, 34] Other possibilities for photo-crosslinking is the dextran modification with acryolyl chloride,[35] allyl isocyanate,[29, 30] dimethylmalemid,[3, 4] or the use of 2-dimethylmaleinimido ethylacrylamide (DMIAAm)[36] reacting in a [2+2]-cycloaddition upon UV-irradiation.[4] Besides bulk hydrogels as well the preparation of nano-gels via photo-crosslinking is reported.[37] Chemical crosslinking can be achieved by using epichlorhydrin[38] or concavalin A[39] as crosslinking unit. Another possibility is the chemical crosslinking by using two functional groups introduced into the dextran like carboxyl and adipic hydrazide,[40] or 4-aminobutyric acid and 1,10-diaminodecane[41] leading to *in situ* chemical crosslinking. Other methods use aldehydes instead of carboxylic acids created via oxidizing dextran followed by crosslinking with adipic acid dihydrazide[19] or the nucleophilic substituton of pre-introduced amino functions at a pre-bound 2,4-dichloro-1,3,5-triazin derivative.[42] Chemical crosslinking can also be performed by radical polymerization. Therefore, polyacryl-dextran[43] or watersoluble vinyl-derivatized dextran is polymerized by initiating the reaction with peroxodisulfate and N,N,N',N'-tetramethylene-diamine (TEMED).[44-47] In case of physical crosslinking, dextran has to be functionalized with ionic groups such as carboxyl functionalities. For this purpose, succinylanhydride[48] or carboxymethyl, sulfopropyl, and sulfate functionalities are applied.[49] Crosslinking subsequently occurs by chelation of multivalent ions like calcium for example. Another option of functionalizing dextran-hydrogels is the preparation of semi-interpenetrating networks (sIPN). An example is the sIPN consisting of PNIPAAm and dextran to induce temperature sensitivity.[50]

Besides the crosslinking of polymer chains to form a hydrogel network the hydrogel has to be coupled covalently to a surface for production of a sensor chip. Usually, thin sensor films in the range of nanometers are prepared by grafting polymer brushes onto a surface. Carboxymethylated dextran brushes are for example grafted onto active ester activated carboxyl terminated self assembled thiol monolayers on gold.[51]

In this thesis, the well investigated carbxoymethylation of dextran by forming ether bridges[52] was applied as outlined in the following chapter. The carboxyl groups serve as binding points for further modification and generate pH-responsivity of the dextran-based polymer. Active ester chemistry opens a wide range of subsequent modification possibilities for the carboxyl groups, enables the chemical modification of dextran as described above, and permits protein or antibody coupling, which is especially interesting for bio-sensor applications.[53] In our group various active esters were developed tailored to different applications. Mainly, their charge and hydrophilicity can be tuned to improve the reaction with certain proteins.[54]

Besides the introduction of binding points for further functionalization crosslinking units have to be introduced to be able to create a dextran network as discussed above.

Therefore, benzophenone as a UV-crosslinking unit was chosen as crosslinking unit. It is already well known for the crosslinking of PNIPAAm polymers.[54-56] Benzophenone can be excited by UV-irradiation at 254 nm or at 365 nm into the singlet state ($\pi\pi^*$) forming a biradical. After transition into its triplet state benzophenone is able to abstract a hydrogen atom of a C-H-bond of the dextran backbone resulting in crosslinking the dextran network.[57, 58] Additionally, benzophenone derivatives can simultaneously be applied as adhesion promoter on glass and gold surfaces.[55, 59] Post-crosslinking via benzophenone units after polymer synthesis allows an easier characterization of the polymer before formation of an insoluble hydrogel. Not only polymers but every C-H-containing molecules can react photochemically with benzophenone as reported for polyelectrolyte layers,[60] or chemically inert perylene C coatings.[61]

3.1.2 Two Strategies for the Synthesis of a Photo-Crosslinkable and Functional Dextran-Based Hydrogel

Synthesis

The pH responsive hydrogel based on photo-crosslinkable dextran was synthesized by two routes differing in the linkage of the benzophenone photo-crosslinker as shown in Figure 1. In the first strategy dextran is carboxymethylated[20, 52] (CMD) followed by the introduction of 4-aminomethylbenzophenone as photo-crosslinking unit via active ester chemistry. The second route starts with the coupling of 4-bromomethylbenzophenone to the hydroxyl groups of the dextran backbone via Williamsson's ether synthesis followed by the carboxymethylation. The advantage of the second strategy can be seen in the chemical separation of the carboxyl- and benzophenone moieties leaving more carboxyl groups for subsequent functionalization.

Carboxymethylation is carried out under basic, aqueous conditions and degrees of carboxymethylation up to 0.67 (every 1.5 repeating unit carries one carboxyl group) in one reaction cycle were achieved with eightfold excess of sodium chloroacetate. In the literature the limit for the degree of substitution under optimized condition and repeated reaction cycles is reported to be around 1.5 (1.5 carboxyl groups per repeating unit).[52] The drawback of carboxymethylated dextran containing such high amounts of carboxyl groups is the low solubility in organic solvents like DMSO or DMF. A degree of carboxymethylation higher than 0.35 for the high-molecular dextrans used in this work results in insolubility, even if the CMD-DMSO dispersion was heated up to the boiling point of DMSO.

Primary amino groups show a higher nucleophilic reactivity compared to hydroxyl groups in a nucleophilic substitution with active ester activated carboxyl groups. Therefore, it is possible to prevent self-crosslinking of the dextran polymer especially while working at room temperature without heating. During the active ester activation trifluoracetic acid is generated as a side product. Because heating up might lead to self-crosslinking the active ester activated carboxymethyl-dextran (CMD) (**2**) was not precipitated but cleaned by dialysis over night against dry DMSO to remove the trifluoroacetic acid. N-hydroxysuccinimide trifluoroacetate (TFA-NHS) (**7**) or pentafluorophenyl trifluoroacetate (TFA-PFP) (**8**) were tested for active ester formation with comparable results in the benzophenone coupling. The dialyzed, active ester activated polymer is directly reacted with the nucleophile 4-aminomethylbenzophenone leading to amide bond formation between the carboxyl group and the photo-crosslinkable benzophenone unit. With TFA-NHS or TFA-PFP and a crosslinker amount of 1-1.8 eq the carboxyl units are not transformed quantitatively. Around 25% of the carboxyl groups are modified with benzophenone under these conditions.

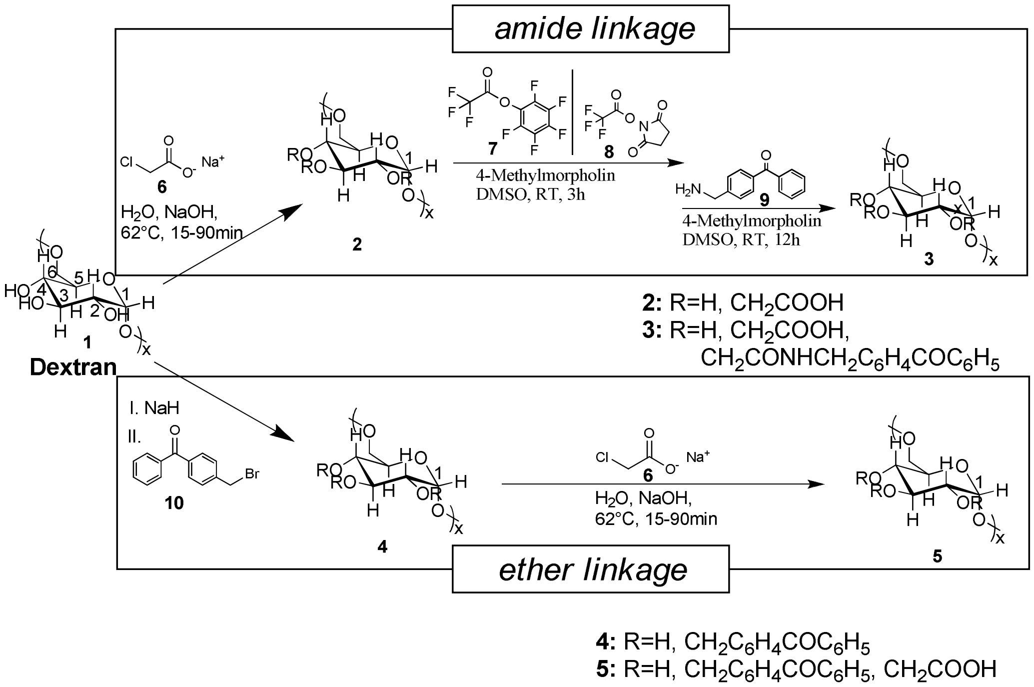

2: R=H, CH_2COOH
3: R=H, CH_2COOH, $CH_2CONHCH_2C_6H_4COC_6H_5$

4: R=H, $CH_2C_6H_4COC_6H_5$
5: R=H, $CH_2C_6H_4COC_6H_5$, CH_2COOH

Figure 3.1.1: *Schematic synthesis overview for the modification of dextran (M_r=200000 or M_r = 2000000) with carboxyl groups and benzophenone as crosslinking unit.*

The independent coupling of the carbxoymethyl groups and the benzophenone units results in a material (**5**) with comparable characteristics than the polymer prepared with the first strategy (**3**). With Williamsson's ether synthesis degrees of benzophenone functionalization up to 0.06 were achieved by using 2 eq of sodium hydride and 1 eq of 4-bromomethylbenzophenone. Consequently, only 6% of the introduced benzophenone molecules were consumed. A possible explanation might be an aggregation of the dextran in DMSO. Solubility can only be achieved by heating of the solution and aggregation effects of high molecular weight dextrans in solution is discussed in the literature as well.[20, 52] The subsequent carboxymethylation in water, which is the best solvent for dextran, shows comparable degrees of carboxymethylation as for the pure dextran. This independent coupling strategy leaves more carboxyl groups for later modification with analyte capturing molecules or other functional groups. To investigate the effect of the molecular weight a dextran with factor 10 lower M_r of 200.000 was used with identical results than obtained for a M_r 2.000.000 dextran.

The content of benzophenone and the carboxymethyl groups was determined by nuclear magnetic resonance (^{1}H-NMR) spectroscopy in D_2O. The determination in DMSO is only possible for very low degrees of substitution due to the decreasing solubility with increasing degree of carboxymethylation and the peak broadening because of inter- and intramolecular proton interaction (Figure 3.1.2). These interactions are usually more pronounced in aprotic solvents like DMSO compared to protic solvents like water.

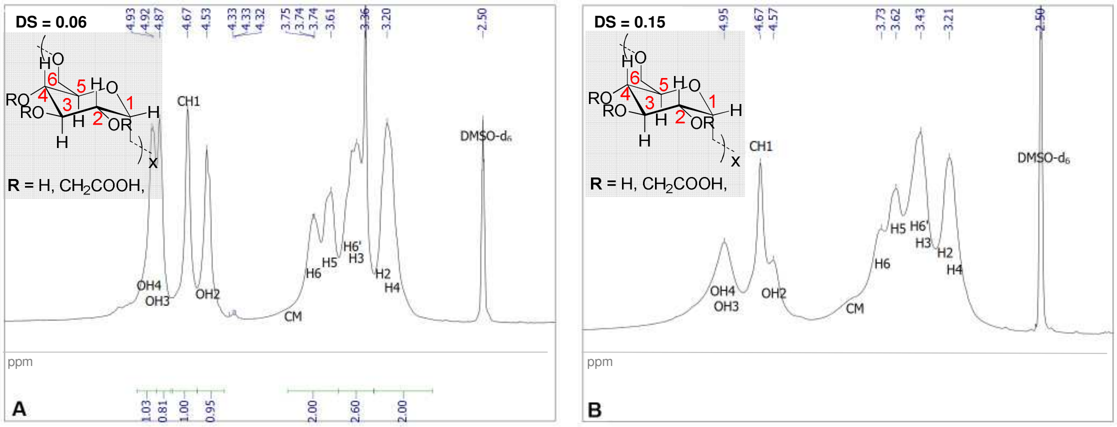

Figure 3.1.2: *NMR spectra of carboxymethylated dextran (CMD) (**2**) with varying degree of functionalization (d_s = 0.06 (**A**) and 0.15 (**B**)) in DMSO. The peak broadening with increasing amount of carboxyl groups is clearly visible (**B**).*

In D_2O the hydroxyl groups are invisible in the NMR spectrum due to the proton-deuterium exchange which results in a free and easily integrable CH(1) proton signal. The overall integral of the CH(1)-protons of the dextran backbone in D_2O (5.24 ppm (CH(1) $_{\alpha\text{-}1,3}$), 5.08 ppm (CH(1') $_{\alpha\text{-}1,6}$), 4,89 ppm (CH(1)$_{\alpha-1,6}$)) was set to one and used as reference. The different CH(1) signals result from different branches present in the backbone.[20] For the determination of the degree of carboxymethylation the proton signal of the two diastereotope methyl protons of the carboxymethyl group

(4.32 ppm) for the determination of the benzophenone content the signal of the nine aromatic benzophenone protons (7.80 ppm) was integrated relatively to CH(1).

Because of the peak broadening in DMSO and the invisibility of the hydroxyl signals in D_2O it was not possible to determine the reactivity of the three different hydroxyl groups of the dextran backbone for the carboxymethylation. For very low degrees of substitution (d_s) (<0,08) the order of signal decrease of the hydroxyl protons indicates the following reactivity OH2/OH3 > OH4 which is consistent with the literature[62].

Besides NMR spectroscopy, the benzophenone introduction can be verified by UV-VIS spectroscopy (Figure 3.2.3). The benzophenone absorption shows a maximum at 260 nm which can be attributed to the $\pi\pi^*$-absorption and an additional shoulder for the $n\pi^*$-transition at 360 nm.[57, 58]

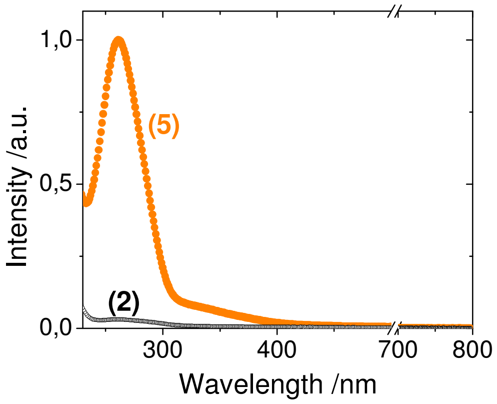

Figure 3.1.3: *UV-VIS spectra of a carboxymethylated dextran* ***(2)*** *(black) (d_s = 0.19) and a benzophenone modified and carboxymethylated dextran type* ***(5)*** *(orange) with a degree of substitution for benzophenone of d_s = 0.02 and for the carboxymethylation of d_s = 0.19.*

In summary, dextran can be chemically functionalized but the degree of functionalization is limited most likely due to aggregation effects in solution.[20] The best solvent for dextran is water. Therefore, organic reactions that can be performed in water[63] are preferable.

3.1.3 Film Preparation, Surface Attachment and Photo-Crosslinking

For sensor chip production the hydrogel has to be grafted onto a substrate and covalently attached to the substrate surface. In the following Chapter a versatile method for hydrogel film preparation inducing simultaneous crosslinking and surface attachment is discussed.

Film Preparation and Surface Attachment

In order to use the modified dextran as biosensor matrix, films were produced by spin-coating the dextran-based polymer onto a substrate. Depending on the subsequent application the dextran-based hydrogel is deposited on glass, chromium/gold covered glass substrates, silizium or oxygen-plasma treated polystyrene. For a covalent immobilization an adhesion promoter is required. Therefore, a self-assembled monolayer of either *S*-3-(4-benzoylphenoxy)propyl ethanthiol for gold covered surfaces or 4-(3-triethoxysilyl)propoxybenzophenone for glass, silizium or plasma-activated polystyrene surfaces is deployed. If more hydrophilic surfaces are required mixed monolayers, using for example hydroxyl terminated thiols, can be prepared. A mixed thiol-monolayer with benzophenone- and hydroxyl groups (10 % in solution) renders contact angles with water at room temperature of 70º (±4)º. For gold a two-step modification by creating a monolayer of 3-mercaptopropyltriethoxysilane followed by crosslinking with hydrochloric acid[64-67] and subsequent deposition of 4-(3-triethoxysilyl)propoxybenzophenone. The surface treated like this is very hydrophilic with contact angles of 15 (±2) for the glass monolayer and can be tuned by adjusting the second benzophenone monolayer composition. The higher hydrophilicity can be an advantage for film adhesion during the spincoating process but simultaneously is disadvantageous for the film stability due to the lower amount of benzophenone crosslinking units. The subsequent irradiation at 254 nm results in a photo-crosslinked and surface-bound hydrogel film in one step (Figure. 3.1.4).

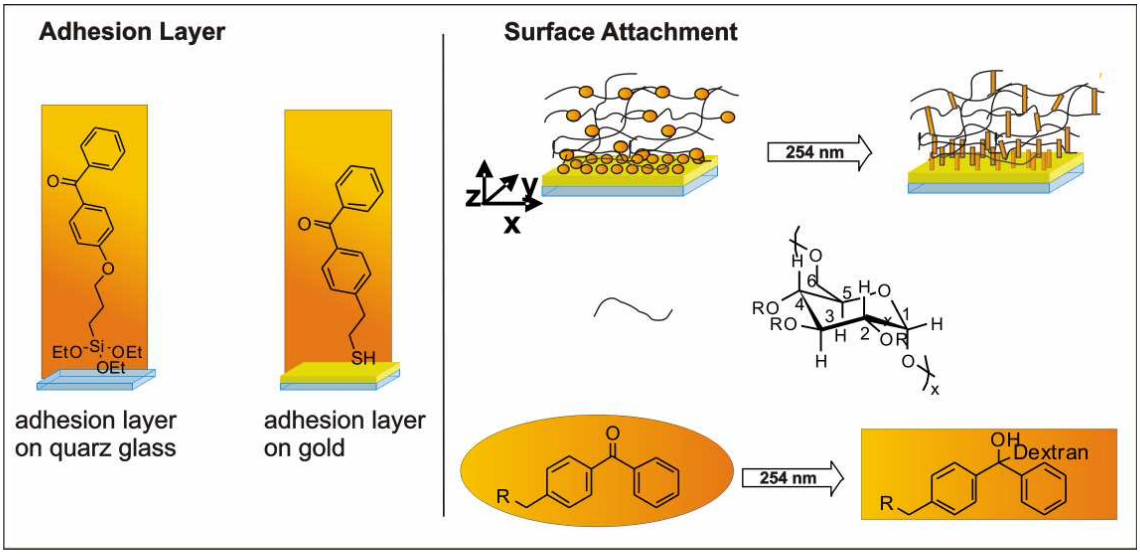

Figure 3.1.4: *Schematic depiction of the simultaneous dextran-film crosslinking and surface attachment to glass, gold or plasma treated polystyrene surfaces by irradiation at 254 nm.*

The dextran film thickness could be varied from tens of nanometers to micrometers in the dry state by changing the spinning speed and the concentration of the polymer solution. In general relatively high polymer concentrations (7-40 wt%) are resulting in homogeneous films, whereas at much lower concentrations de-wetting was observed. The observed de-wetting effects can be attributed to the hydrophilicity difference between the hydrophilic polymer and the hydrophobic adhesion promoter (contact angle with water at room temperature = 70-80º).

Photo-Crosslinking

To determine the effect of the UV-irradiation a hydrogel film was prepared on a quartz glass slide (PGO) covered by a self-assembled monolayer of 4-(3-triethoxysilyl)propoxybenzophenone and the UV-VIS spectra after increasing crosslinking intervals were recorded (Fig 3.1.5). The decrease of the benzophenone $\pi\pi^*$-absorption at 259 nm is clearly visible. Furthermore, an absorption around 345 nm, the wavelength of the $n\pi^*$-transition, occurs during crosslinking. This absorption reaches its maximum value directly after exposing the sample to UV-light for every crosslinking time. It subsequently decreases with time after the irradiation in the dark but does not vanish completely. Simultaneously, the benzophenone absorption at 259 nm increases. Therefore, the second absorption at 345 nm might be attributed to long-living radicals produced by UV-irradiation. This phenomenon was already observed by Horie and co-workers in 1987 for benzophenone moieties in a poly(vinyl alcohol) matrix[57] and attributed to “some reaction product” with an absorption around 340 nm. The different recombination pathways of benzophenone radicals are summarized by Dorman *et al.*[58]. In summary, the small increase of the benzophenone absorption and the simultaneously decreasing absorption at 345 nm with time in the absence of light show a relation between both signals (Figure 3.1.5 B inset).

Regarding the benzophenone absorption after approximately 15-20 minutes of irradiation at 254 nm, the crosslinking seems to be completed. Besides the UV-VIS spectra the influence of varying the crosslinking time on the swelling degree for a 390 nm thick hydrogel film of type **3** (d_s (carboxymethylation) = 0.16 and d_s(benzophenone) = 0.04) at pH 3 and pH 8 (c = 10mM) is shown in Figure 3.1.5A (Chapter 4.1). The data are consistent with the UV-VIS data. For crosslinking times up to 13 minutes the variation of swelling degree with crosslinking time is very high, whereas for crosslinking times of 30 minutes and more no change of the swelling degree was observed.

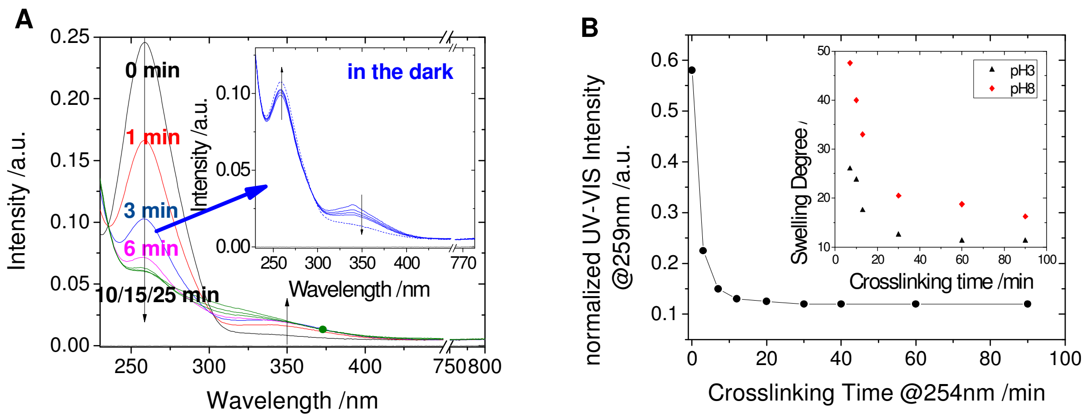

Figure 3.1.5: A) UV-VIS spectra for decreasing crosslinking times (0 (black), 1 (red), 3 (blue), 6 (magenta), 10 (green), 15 (green), 25 (green) minutes) and 10 minutes in the absence of light after crosslinking. The change of the UV-VIS absorption with increasing time (4 (line), 7, 10 min, 12 h (points)) in the dark after crosslinking for 3 minutes is shown in the inset of A. ***B)*** *Decrease of the benzophenone absorption (@259nm) with increasing crosslinking time @254nm.* ***B inset)*** *decrease in swelling degree related to the crosslinking time for pH 3 (10mM) and pH 8 (10mM). The dextran hydrogel film was adhered to a quartz substrate with a SAM of 4-(3-triethoxysilyl)propoxybenzophenone. The degree of benzophenone substitution was 0.04 and the one for the carboxymethylation 0.16 with film thickness of 390nm (after spincoating).*

The exponential relation between the crosslinking and the swelling of the hydrogel film is in agreement with the theory for polyelectrolyte gels with long crosslinked chains.[68]

Cryo SEM

To investigate the hydrogel's porous super-structure Cryo-SEM measurements were carried out. Therefore, a part of dried bulk hydrogel was crosslinked, swollen in buffer, and frozen in liquid nitrogen. The water was sublimed the hydrogel was coated with platinium and observed with the cryo-SEM under high vacuum (Fig 3.1.3). The measurements show a macroporous structure in the micrometer range which is consistent with the literature for various dextran based hydrogel systems[19, 24, 39, 69, 70] and points out that a type of macropores exists. One has to keep in mind that the macropores are not expected to represent rigid pores in the swollen state but rather resemble a flexible network. Furthermore, the freezing step is expected to influences the structure in the frozen state. The heterogeneity of a hydrogel sample becomes obvious by comparing Figure 3.1.3 B, C. The same hydrogel batch shows structure variations that can be dedicated either to heterogeneities inside the sample itself, for example due to inhomogeneous crosslinking, or these heterogeneities are introduced during the cryo-SEM sample preparation process. However, it is clearly visible that the hydrogel can expand to pores in the range of several micrometers which should in general allow for diffusion of big analytes such as antibodies for example. Furthermore, for hydrogel bulk samples and for hydrogel films on a substrate comparable structures were observed.

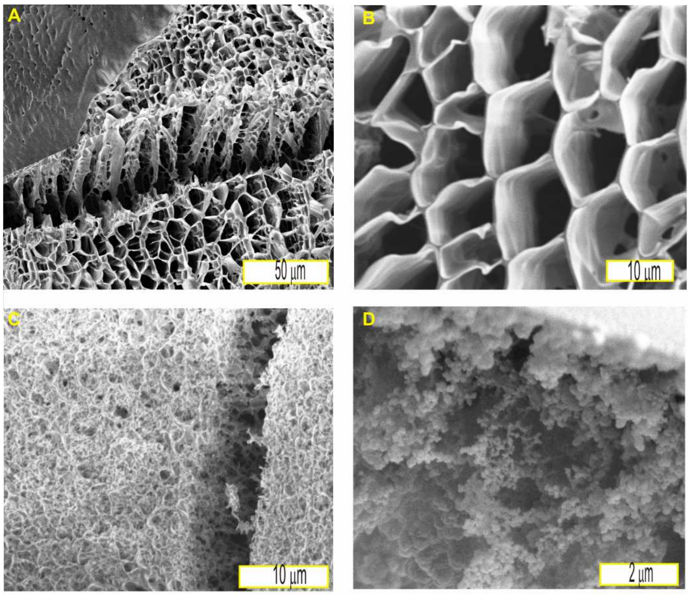

Figure 3.1.3: *Cryo SEM images after freeze drying in liquid nitrogen and water evaporation in high vacuum.* ***(A, B, C)*** *show cross sections of a crosslinked bulk hydrogel (type* ***(3)****) (d_s(benzophenone)=0.04; d_s(carboxymethyl)=0.16) in HEPES (10mM).* ***(C)*** *was recorded at another sample position than* ***(B)****. A hydrogel film on a silizium substrate after freeze drying and coated with gold is shown in* ***(D)****. The images were recorded with an acceleration voltage of 2 kV at a working distance of 5.2 mm.*

A macroporous hydrogel structure was recently observed in the swollen state by Chalal *et al.* by two-photon fluorescence microscopy, too.[71] They reported macropores up to 75 µm for pure PNIPAAm and up to almost 250 µm for pHEMA-LLA-D (poly(hydroxyethyl methacrylate-L-lactide-dextran) hydrogels.

3.1.4 Conclusion and Outlook

Two different synthesis strategies for the preparation of a pH-responsive and photo-crosslinkable dextran-based polymer were discussed. Basically, two functionalities, carboxyl groups inducing the pH-responsivity and serving as binding points for subsequent chemical modification and benzophenone groups as photo-crosslinking units were inserted. Active ester chemistry was introduced as a versatile platform to couple primary amines to the carboxyl groups in the dextran polymer, which will be vital for further functionalization and biosensor application. Furthermore, the hydrogel formation by UV-irradiation was followed by UV-VIS spectroscopy. After about 30 minutes crosslinking a maximum crosslinking density was achieved. This reflected in a concominant minimum degree of one-dimensional swelling with a swelling ratio of ~11 for a hydrogel with a degree of benzophenone substitution $d_s = 0.04$ and a degree of carboxymethylation of $d_s = 0.16$ (Chapter 4.1). The morphology of freeze dried hydrogel samples was analyzed by Cryo SEM measurements revealing a macroporous structure similar to results reported in the literature for comparable systems. Future perspectives can be seen in tailoring the synthetic flexibility towards various applications in medicine or sensor applications for example. Furthermore, the stabilization on a surface of highly functionalized and tens to hundreds of micrometer thick films has to be improved. Such thick and surface coupled films are required for many medical applications for example in cell growth studies (Chapter 4.5). Another important challenge is the detailed investigation of the macroporous hydrogel structure in the swollen state. For this purpose, fluorescence correlation spectroscopy might be one possible method to expand the information about the hydrogel structure in the swollen state. A first approach towards this characterization has been initiated in cooperation with Riccardo Raccis and Prof. G. Fytas at our institute. First experiments on these samples introduced here will be discussed in Chapter 4.1.

3.1.5 Experimental

PCMD Synthesis: The photo-crosslinkable, dextran-based hydrogel was synthezised by carboxymethylation followed by an activation of the carboxyl groups via active ester chemistry and nucleophilic substitution with 4-aminomethylbenzophenone.

The carboxymethylation was carried out according to the literature.[18, 52] Typically 10g of dextran (Sigma Aldrich, M_r~2.000.000 or 200.000) were dissolved in 150 mL distilled water followed by the addition of 20g (0.21 mol) sodium chloroacetate (Acros Organics). To initiate the reaction 50mL of 8M sodiumhydroxide solution were added and the reaction was carried out for 1 hour at 62°C. After cooling down for 10 minutes the reaction was terminated by neutralizing the reaction mixture with 6M hydrochloric acid. The carboxymethylated dextran (CMD) was precipitated in ice cold ethanol and purified by dialysing against distilled water. After drying the CMD is obtained as white powder.

^{1}H-NMR (d_6-DMSO) (300MHz), $\delta\in$[ppm]: 4.93 (1H, OH4), 4.88 (1H, OH3), 4.66 (1H, CH1), 4.53 (1H, OH2), 4.32 (2H, MeCMH), 3.74 (1H, H6), 3.61 (1H, H5), 3.43 (2H, H6',H3), 3.20 (2H, H2, H4).

^{1}H-NMR (D_2O) (300MHz) $\delta\in$[ppm]: 5.24, 5.08, 4.89 (1H, CH1), 4.10 (m, 2H MeCMH), 3.90 (1H ,H6), 3.81 (1H, H5), 3.64 (2H, H6',H3), 3.60 (2H, H2, H4).

^{13}C-NMR (DMSO) (176MHz) $\delta\in$[ppm]: 98.16 (1C, C1), 73.37 (1C, C3), 71.82 (1C, C2), 70.14 (2C, C4, C5), 65.96 (1C, C6)

Prior to the benzophenone binding the carboxy groups were activated either with N-hydroxysuccinimide trifluoroacetate (TFA-NHS) or with pentafluorophenyl trifluoroacetate (TFA-PFP). Therefore 1g CMD was dissolved by gently heating up to 80°C in dried DMSO and kept under argon. The reaction was carried out at room temperature for 3 hours after addition of 0.35g (1.66mmol) TFA-NHS or 0.29mL (0.45g, 1.6mmol) TFA-PFP (Fluka) and ~5 mL of 4-methylmorpholine (Merck). To remove the major amount of trifluoracetic acid the reaction mixture was dialyzed against DMSO over night, directly followed by the reaction with 4-aminomethylbenzophenone (typically 0.4g, 1.9mmol) in DMSO with 5mL of 4-methylmorpholine at room temperature under argon. For purification the reaction mixture was extensively dialyzed against DMSO and distilled water.

^{1}H-NMR (D_2O) (300MHz) $\delta\in$[ppm]: 7.80 (m,9H,arom BP), 5.30, 5.16, 4.97 (1H, CH1), 4.19 (2H, MeCMH), 3.92 (2H, H6, H5), 3.71 (2H, H6',H3), 3.54(2H, H2, H4).

^{13}C-NMR (DMSO) (176MHz) $\delta\in$[ppm]: 98.15 (1C, C1), 73.36 (1C, C3), 71.82 (1C, C2), 70.3-70.1 (2C, C4, C5), 65.94 (1C, C6)

To couple the benzophenone via an ether linkage typically 5g dextran (Sigma Aldrich, M_r~2000000/200000) were dissolved in approximately 350mL DMSO and cooled down with ice/water. To the cold solution 1.35g (0.056 mol) sodiumhydride (Sigma Aldrich) were added slowly. After stirring for 30 min 2g (7 mmol) of 4-bromomethylbenzophenone were added and the mixture was stirred at room temperature over night. The reaction was terminated by the careful addition of 100mL of destilled water and the product was precipitated in approximately 1L of ice cold acetone, centrifuged and dialyzed against DMSO and water.

^{1}H-NMR (DMSO) (300MHz) $\delta\in$[ppm]: 7.68, 7.66, 7.54, 7.43, 7.26 (9H, arom BP), 4.88 (1H, OH4), 4.82 (1H, OH3), 4.63 (1H, CH1), 4.47 (1H, OH2), 3.70 (1H, H6), 3.58 (1H, H5), 3.40 (2H, H6', H3), 3.17 (2H, H2, H4).

^{1}H-NMR (D_2O) (300MHz), $\delta\in$[ppm]: 7.80-7.40 (m, 9H, arom BP), 5.30, 4.95 (1H, CH1), 4.18 (2H, MeCMH), 3.97 (1H, H6), 3.89 (1H, H5), 3.70 (2H, H6',H3), 3.53 (2H, H2, H4).

For the subsequent carboxymethylation typically 5g of the benzophenone-ether modified dextran were dissolved in 150 mL distilled water followed by the addition of 10g (0.1 mol) sodium chloroacetate (Acros Organics). To initiate the reaction 25mL of 8M sodiumhydroxide solution were added and the reaction was carried out for 1 hour at 62°C. After cooling down for 10 minutes the reaction was terminated by neutralizing the reaction mixture with 6M hydrochloric acid. The carboxymethylated dextran (CMD) was precipitated in ice cold ethanol and purified by dialysing against destilled water.

^{1}H-NMR (D_2O) (300MHz $\delta\in$[ppm]): 7.82-7.57 (m, 9H, arom BP), 5.30, 5.15, 4.95 (d, 1H, CH1), 4.18 (m, 2H, MeCMH), 3.97 (d, 1H, H6), 3.89 (d, 1H, H5), 3.70 (dd, 2H, H6',H3), 3.53 (dd, 2H, H2, H4).

Cryo-SEM: To investigate an superstructure of the hydrogel a hydrogel sample was crosslinked in bulk or as a film on a silicon wafer, swollen in buffer, rapidly frozen in liquid nitrogen, and transferred into the precooled (about -160°C) Cryo preparation chamber (PP2000T, Quorum Technologies). The sample was broken and sputtered with a thin platinium layer (~20 nm) after the frozen water was sublimed or measured without being metal-coated. Finally, the sample was transfered into the precooled chamber of the Focused Ion Beam (Nova, 600 Nanolab (FIB), FEI). The stage was slowly heated up to room temperature while measuring.

Film Preparation: Hydrogel films were prepared on SiO_x or *gold* surfaces depending on the application. For the immobilization of 4-(3-triethoxysilyl)propoxybenzophenone on SiO_x surfaces the silane was chemisorbed from ethanol solution (5 mM) at room temperature for ~24h. Afterwards the slides were cleaned by extensively rinsing with ethanol and acetone and blown dry with air.

Especially for the SPR measurements (Chapter 4.1) LaSFN9 glass slides (LaSFN9 glass, Hellma Optik GmbH Jena, refractive index n=1,8449) were coated with a 2nm chromium and a 50 nm gold film, deposited by evaporation with a Edwards Auto 306 evaporator followed by chemisorption of *S*-3-(4-benzoylphenoxy)propyl ethanthiol from 5 mM ethanol solution for ~24h at room temperature. Afterwards the slides are cleaned by extensively rinsing with ethanol and acetone and blown dry with air.

Deposition of Dextran Films and Photo-Crosslinking: Dextran films up to several micrometers in thickness were deposited onto the pre-treated substrates by spin-coating from polymer/water solutions with 3000-6000 rpm. A solution with a polymer content of 20 wt % results in a film thickness of approximately 500 nm with 5500 rpm. The

samples were dried in vacuum at 45°C over night and crosslinking was performed for 7-90 minutes with a Stratagene UV Stratalinker 2400 operating at 75 W with an emission maximum at 254 nm. The crosslinking is performed with an irradiation dose of 0.105 J $cm^{-2}min^{-1}$ at 365 nm and with 0.2 J $cm^{-2}min^{-1}$ at 254 nm.
UV-VIS: To investigate the crosslinking UV-VIS spectra were recorded with a UV-VIS/NIR (Perkin Elmer, Lambda 900) for different crosslinking times and different periods after the crosslinking was finished.

3.1.6 Bibliography

[1] P. Vicennati, A. Giuliano, G. Ortaggi, A. Masotti, *Current Medicinal Chemistry* **2008**, *15*, 2826.
[2] J. P. Montheard, M. Chatzopoulos, D. Chappard, *J. Macromol. Sci. - Rev. Macromol. Chem. Phys.* **1992**, *C32*, 1.
[3] M. E. Harmon, D. Kuckling, C. W. Frank, *Macromolecules* **2003**, *36*, 162.
[4] D. Kuckling, M. E. Harmon, C. W. Frank, *Macromolecules* **2002**, *35*, 6377.
[5] D. Kuckling, *Colloid Polym. Sci* **2009**, *287*, 881.
[6] G. W. Bos, W. E. Hennink, L. A. Brouwen, W. D. Otter, T. F. J. Veldhuis, C. V. V. Nostrum, M. J. A. V. Luyn, *Biomaterials* **2005**, *26*, 3901.
[7] W. E. Hennink, S. J. D. Jong, G. W. Bos, T. F. J. Veldhuis, C. F. V. Nostrum, *Int. J. Pharm.* **2004**, *277*, 99.
[8] T. Coviello, P. Matricardi, C. Marianecci, F. Alhaique, *Jounal of Controlled Release* **2007**, *119*, 5.
[9] S. R. V. Tomme, W. E. Hennink, *Expert Reviews of Medical Devices* **2007**, *4*, 147.
[10] K. Moriyama, N. Yui, *J. Contr. Release* **1996**, *42*, 237.
[11] L. Hovgaard, H. Brondsted, *J. Contr. Release* **1995**, *36*, 156.
[12] H. Brondsted, C. Anderson, L. Hovgaard, *J. Control. Release* **1998**, *53*, 7.
[13] N. Yamamoto, N. Kurisawa, N. Yui, *Macromol. Rapid Commun.* **1996**, *17*, 313.
[14] S. H. Kim, C. C. Chu, *J. Biomed. Mater. Res.* **2000**, *49*, 517.
[15] S. H. Kim, C. Y. Won, C. C. Chu, *Carbohyd. Polym.* **1999**, *40*, 183.
[16] S. Benslimane, R. Guidoin, D. Marceau, Y. Merhi, M. W. King, M. F. Sigo-Luizard, *Eur. Surg. Res.* **1988**, *20*, 18.
[17] K. Tomihata, Y. Ikada, *J. Biomed. Mater. Res.* **1996**, *37*, 243.
[18] R. Zhang, M. Tang, A. Bowyer, R. Eisenthal, J. Hubble, *Biomaterials* **2005**, *26*, 4677.
[19] J. Maia, L. Ferreira, R. Carvalho, M. A. Ramos, M. H. Gil, *Polymer* **2005**, *46*, 9604.
[20] T. Heinze, T. Liebert, B. Heublein, S. Hornig, *Adv. Polym. Sci.* **2006**, *205*, 199.
[21] G. Pitarresi, F. S. Palumbo, G. Giammona, M. A. Casadei, F. M. Moracci, *Biomaterials* **2003**, *24*, 4301.
[22] K. M. Huh, J. Hashi, T. Ooya, N. Yui, *Macromol. Chem. Phys.* **2000**, *201*, 613.
[23] Y. Kumashiro, T. Ooya, N. Yui, *Macromol. Rapid Commun.* **2004**, *25*, 867.
[24] S. Namkung, C.-C. Chu, *J. Biomater. Sci. Polymer Edn* **2007**, *18*, 901.
[25] W. E. Hennink, C. F. v. Nostrum, *Advanced Drug Delivery Reviews* **2002**, *54*, 13.
[26] X. Zhang, D. Wu, C.-C. Chu, *Biomaterials* **2004**, *25*, 4719.
[27] N. A. Peppas, Y. Huang, M. Torres-Lugo, J. H. Ward, J. Zhang, *Annu. Rev. Biomed. Eng* **2000**, *2*, 9.
[28] S. J. d. Jong, S. C. d. Smedt, J. Demeester, C. V. v. Nostrum, J. J. K.-v. d. Bosch, W. E. Hennink, *J. Contr. Release* **2001**, *72*, 47.
[29] Y. Zhang, C. C. Chu, *J. Biomed. Mater. Res. A* **2000**, *54*, 1.
[30] Y. L. Zhang, C. Y. Won, C. C. Chu, *J. Polym. Sci. A* **2000**, *38*, 2392.
[31] V. T. Bhat, N. R. James, A. Jayakrishnan, *Polymer Int.* **2008**, *57*, 124.
[32] R. Kalpana, K. Park, K. Park, *Polymer Gels and Networks* **1995**, *3*, 243.
[33] S. C. D. Smedt, A. Lauwers, J. Demeester, M. J. V. Steenbergen, W. E. Hennink, S. P. F. M. Roefs, *Macromolecules* **1995**, *28*, 5082.
[34] H. Zhang, H. Wu, L. Fan, F. Li, C.-H. Gu, M. Jia, *Polymer Composites* **2009**, *30*, 1243.
[35] M. R. Rodrigues, D. Gasetta, *Journal of Carbohydrate Chemistry* **2007**, *26*, 439.
[36] D. Kuckling, C. D. Vo, H.-J. P. Adler, A. Voelkel, H. Coelfen, *Macromolecules* **2006**, *39*, 1585.
[37] D. Kuckling, C. D. Vo, H.-J. P. Adler, A. Voelkel, H. Coelfen, *Macromolecules* **2006**, *39*, 1585.
[38] D. Imren, M. Gümüsderelioglu, A. Güner, *J. Appl. Polym. Sci.* **2006**, *102*, 4213.

[39] R. Zhang, M. Tang, A. Bowyer, R. Eisenthal, J. Hubble, *Reactive and Functional Polymers* **2006**, *66*, 757.

[40] T. Ito, Y. Yeo, C. B. Highley, E. Bellas, D. S. Kohane, *Biomaterials* **2007**, *28*, 3418.

[41] H.-C. Chiu, G.-H. Hsiue, Y.-P. Lee, L.-W. Huang, *J. Biomater. Sci. Polymer Edn.* **1999**, *10*, 591.

[42] M. Tang, R. Zhang, A. Bowyer, R. Eisenthal, J. Hubble, *Biotechnology Bioengineering* **2003**, *82*, 47.

[43] P. Edman, B. Ekman, I. Sjoholm, *J. Pharm. Sci.* **1980**, *69*, 838.

[44] W. N. E. v. Dijk-Wolthuisen, O. Franssen, H. Talsma, M. J. v. Steenbergen, J. J. K.-v. d. Bosch, W. E. Hennink, *Macromolecules* **1995**, *28*, 6317.

[45] R. J. H. Stenekes, W. E. Hennink, *Polymer* **2000**, *41*, 5563.

[46] H.-C. Chiu, Y.-F. Lin, S.-H. Hung, *Macromolecules* **2002**, *35*, 5235.

[47] F. Plieva, A. Oknianska, E. Degerman, I. Y. Galaev, B. Mattiasson, *J. Biomater. Sci. Polymer Edn.* **2006**, *17*, 1075.

[48] M. M. Stevens, S. Allen, M. C. Davies, C. J. Roberts, E. Schacht, S. J. B. Tendler, S. VanSteenkiste, P. M. Williams, *Langmuir* **2002**, *18*, 6659.

[49] K. Gekko, H. Noguchi, *Macromolecules* **1974**, *7*, 224.

[50] Y. Kumashiro, W. K. Lee, T. Ooya, N. Yui, *Macromol. Rapid Commun.* **2002**, *23*, 407.

[51] J.-F. Masson, T. M. Battaglia, Y.-C. Kim, A. Prakash, S. Beaudoin, K. S. Booksh, *Talanta* **2004**, *64*, 716.

[52] R. Huynh, F. Chaubet, J. Jozefonvicz, *Angew. Makromol. Chem.* **1998**, *254*, 61.

[53] S. Löfas, M. Malmqvist, I. Roennberg, E. Stenberg, B. Liedberg, I. Lundstroem, *Sensors and Actuators B* **1991**, *5*, 79.

[54] A. Aulasevich, R. F. Roskamp, U. Jonas, B. Menges, J. Dostalek, W. Knoll, *Macromolecular Rapid Communications* **2009**, *30*, 872.

[55] P. W. Beines, I. Klosterkamp, B. Menges, U. Jonas, W. Knoll, *Langmuir* **2007**, *23*, 2231.

[56] D. Matsukuma, K. Yamamoto, T. Aoyagi, *Langmuir* **2006**, 5911.

[57] K. Horie, H. Ando, I. Mita, *Macromolecules* **1987**, *20*, 54.

[58] G. Dorman, G. D. Prestwich, *Biochemistry* **1994**, *33*, 5661.

[59] O. Prucker, C. A. Naumann, J. Rühe, W. Knoll, C. W. Frank, *J. Am. Chem. Soc.* **1999**, *121*, 8766.

[60] M.-K. Park, S. Deng, R. C. Advincula, *J. Am. Chem. Soc.* **2004**, *126*, 13723.

[61] K. Länge, S. Grimm, M. Rapp, *Sensors and Actuators B* **2007**, *125*, 441.

[62] T. Heinze, A. Koschella, *Macromol. Symp.* **2005**, *223*, 13.

[63] C.-J. Li, L. Chen, *Chem. Soc. Rev.* **2006**, *35*, 68.

[64] C. A. Gross, D. H. Charych, M. Majada, *Anal. Chem.* **1991**, *63*, 85.

[65] R. Matmour, T. J. Joncheray, Z. Gnanou, R. S. Duran, *J. Colloid Interf. Sci* **2007**, *311*, 315.

[66] D. G. Kurth, T. Bein, *Langmuir* **1995**, *11*, 3061.

[67] I. U. Vakarelski, C. E. McNamee, K. Higashitani, *Colloids and Surfaces A: Physiochem. Eng. Aspects* **2007**, *295*, 16.

[68] J. Wilder, T. A. Vilgis, *Phys. Rev. E* **1998**, *57*, 6865.

[69] R. P. Apkarian, E. R. Wright, V. A. Seredyuk, S. Eustis, L. A. Lyon, V. P. Conticello, F. M. Menger, *Microsc. Microanal.* **2003**, *9*, 286.

[70] Y.-Y. Liang, L.-M. Zhang, W. Jiang, W. Li, *Chem. Phys. Chem* **2007**, *8*, 2367.

[71] M. Chalal, F. Ehrburger-Dolle, I. Morfin, J.-C. Vial, M.-R. A. d. Armas, J. S. Roman, N. Bolgen, E. Piskin, O. Ziane, R. Casalegno, *Macromolecules* **2009**, *10.102/ma802820w 16.03.2009.*

3.2 Modification of a Photo-Crosslinkable Carboxymethylated Dextran with Ferrocene Derivatives

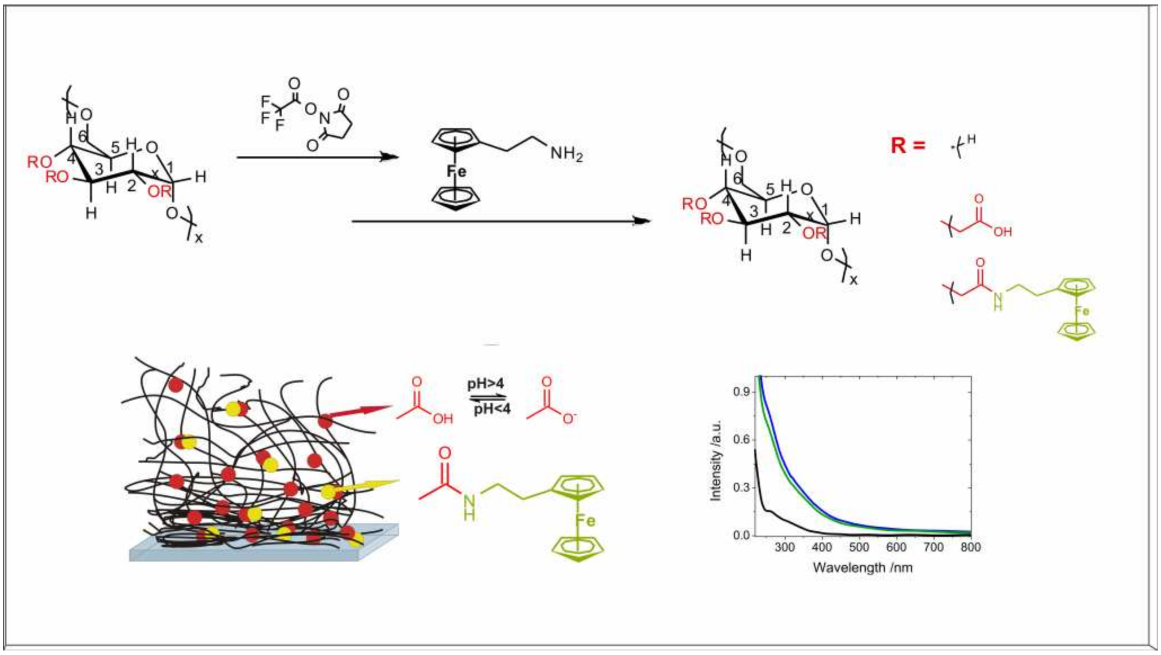

The reversible manipulation or tuning of swelling degree and charge of hydrogels is a decisive characteristic for actuation, sensing or affinity binding applications. Especially biomolecules carry pH-dependent charges that are attractive or repulsive with the charge of the hydrogel matrix at a certain pH. Additionally, the swelling degree of a hydrogel can complicate or circumvent the diffusion of larger molecules. Reversible and external charge generation allows the manipulation of the swelling degree and the forces acting on diffusing molecules without changing the swelling medium. With dextran as biocompatible and degradable backbone the synthesis of a promising material for sensing applications modified with redox centers is discussed in this chapter.

3.2.1 Introduction

Redox sensitive hydrogels constitute an electron- or ion-conducting phase in which chemicals and biochemicals can dissolve and diffuse and thus can serve as electrical connection or molecular wires. This and their response towards electrical stimuli makes them interesting materials for further investigations.[1] Electrically sensitive hydrogels are either prepared as pure polyelectrolytes or as redox functionalized polymers. Dendrimers,[2] self-assembled monolayers,[3] layer-by-layer deposited films,[4] polymers,[5-8] and polymer brushes,[9, 10] or hydrogels[1, 11-13] are the most common systems for the generation of redox-active films.

Redox responsive polymers can be classified into electronic or ionic according to their operational mechanism. Electroactive polymers are either ferroelectric or dielectric. The most common ferroelectric polymer is polyvinylidene fluoride (PVDF), the most common dielectric polymer is silicone. These polymers respond directly to the external field without the presence of added charge carriers. They do not require mass transport and are thus not diffusion limited.[7] Ionic electroactive polymers can be build out of polymer and carbon nanotube composites, conductive polymers with a conjugated backbone like polypyrrole,[14] or ionic polymer metal composites known as soft actuators for bending and sensing applications for example.[7] Ionic metal composites are of special interest due to their multiple responsiveness namely to pH and ionic strength and an externally applied electric field. Furthermore, many naturally occurring polymers like alginates or hyaluronic acid are ionic. They are of strong interest especially for biomedical and sensing applications due to their biocompatibility. Polymers containing inorganic or organometallic units combine potentially useful chemical, electrochemical, and optical characteristics with the processability of polymers[15] like the reversible oxidation and reduction.[1, 3, 16-18] Polymer metal composites can be prepared as polymer backbones with electrostatically bound metal redox centers[9], with covalently coupled redox centers,[1, 17] or as multicomponent systems by grafting, interpenetrated networks or complex formation.[14, 19, 20] Multicomponent systems often show an enhaced performance because of the independent optimization of different parameters.[21] Various polymer backbones and redox centers have been utilized in the development of redox polymers. The most popular backbones utilized are poly(vinylpyridine),[1, 22, 23] poly(vinylimidazole),[24, 25] poly(allylamine)[5, 26, 27] with ferrocene, osmium and ruthenium as the most commonly used redox mediators.[17, 28] The following characteristics were shown to be desired for redox polymers: a high polymer flexibility and segmential mobility,[27, 29] a high degree of functionalizaiton,[30] and a well hydrated polymer.[31] Another attractive feature is the potential of further modificaiton especially for sensor applications as already reported for poly(ethyleneimine).[17, 32] All these characteristics are fulfilled by the photo-crosslinkable carboxymethylated dextran introduced in Chapter 3.1. Due to its high swelling degrees it should possess a high segmential mobility, the degree of functionalization should be tuneable by using the hydroxyl and the carboxyl functionalities. Because of its hydrophilic character it hydrates very well. Additionally, it is biocompatible[33, 34] being advantageous for biomedical and sensing applications. Ferrocene is a well investigated redox mediator with respect to chemistry and electrochemical characteristics.[35, 36] Ferrocene has been used as redox center coupled to dendrimers,[2] polymer brushes[17, 37] or hydrogels[14, 17] as well as it has been utilized as electron donor.[38] For the covalent attachment of ferrocene derivatives condensation reactions are a versatile synthesis route.[37, 39] Ferrocene derivatives like ferrocenoyl chlorides,[37, 40] hydroxyl modified ferrocenes[41] or ferrocenes with an amino group can be used to be coupled with amine or carboxyl end groups in the polymer respectively. Two structural properties have been reported to determine the reversibility and the half-wave potential ($E_{1/2}$) for the oxidation of ferroceneyl conjugates.[42] The stabilization of the ferrocinium ion can be supported by an electron donor like a ring substituent. The lowest $E_{1/2}$ has been found for ferrocene carboxylic acid in which the positive charge is stabilized by the carboxylate directly attached to the cyclopentadienyl ring and for methyleneamine substituted ferrocenes. If the carboxylic acid is derivatized as the corresponding amide or ester the $E_{1/2}$ increases with the amide functionalization showing a higher stabilization potential. The second effect is related to the way how long-chain substituents are able to fold around the ferrocene unit.[42]

A pH responsive biocompatible hydrogel modified with redox centers would allow external switching of the redox center's charge state. This would open an external way to manipulate the hydrogels charge and with this an external manipulation of its swelling degree. The charge and the swelling degree are the most important parameters that determine the applicability of a hydrogel as biosensor matrix. Furthermore, such a hydrogel allows the solvation of an electroactive ferrocene in water which might be an interesting feature for sensing applications.

3.2.2 Synthesis of a Ferrocene-Modified Photo-Crosslinkable Dextran-Based Hydrogel in Solution

The preparation of a pH-responsive dextran based hydrogel containing benzophenone moieties as photo-crosslinkable units and carboxymethyl functionalities as pH-sensitive groups and as binding points for further modification was described in Chapter 3.1. The strategy of active ester activation and subsequent coupling of a primary amine was applied here for redox-center coupling. Coupling the ferrocene moieties via amide bonds generates stable bonds with respect to hydrolysis under moderate pH conditions. Therefore, a ferrocene derivative with an ethyleneamine linker was synthesized by reducing ferroceneacetonitrile as described in the literature.[43, 44]

To modify the pH responsive dextran-based polymer with ferroceneethyleneamine in solution the carboxyl groups were activated with pentafluorophenyl trifluoracetate (TFA-PFP) (**7**) or N-hydroxysuccinimide trifluoroacetate (TFA-NHS) (**8**) and subsequently reacted with ferroceneethyleneamine as depicted in Figure 3.2.1.

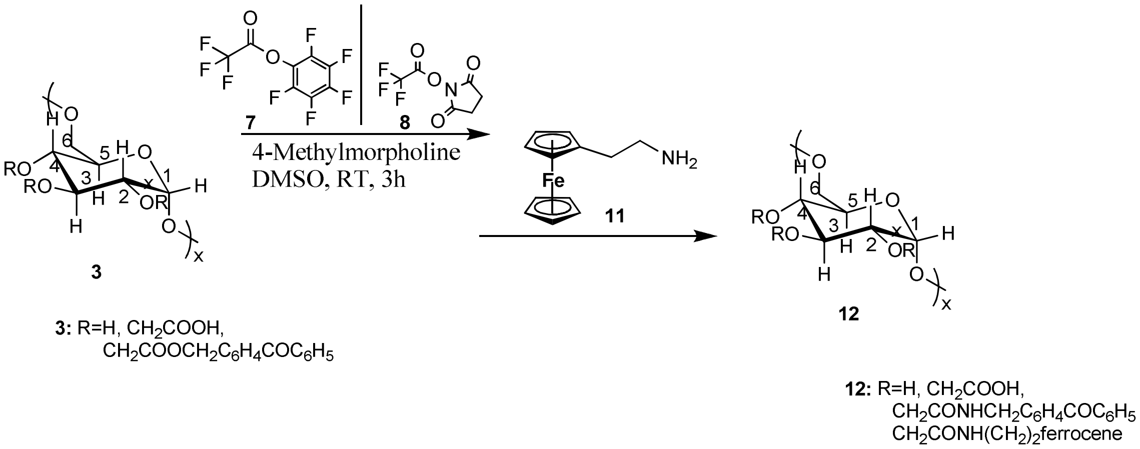

***Figure 3.2.1:** Schematic presentation of the two-step binding of ferroceneethyleneamine to the carboxyl groups of the dextran-based polymer (**3**). Active ester activation with TFA-PFP (**7**) or TFA-NHS (**8**) initiates ferroceneethyleneamine coupling to the carboxyl groups of the dextran-based polymer (**3**).*

Besides the dextran-based polymer (**3**) reacting to (**12**) after ferrocene coupling the dextran-based polymer (**5**) can be used leading to the ferrocene modified polymer (**13**). Because in (**5**) the benzophenone crosslinking units and the carboxymethyl groups are both coupled to the hydroxyl groups of the dextran and are therefore chemically independent more free binding units are available for the ferrocene binding. The degree of substitution is roughly determined by NMR spectroscopy in D_2O integrating the aromatic ferrocene protons (4.22 ppm) with respect to the CH(1) protons of the dextran backbone (*5.24, 5.08, 4.89* ppm). The signals are very small and partly superimposed by the dextran backbone signal. Therefore, integration only gives a very rough estimation about the ferrocene content. The ferrocene detected in the NMR spectra measured in D_2O are expected to be covalently coupled to the dextran backbone due to the insolubility of the pure ferrocene derivative. The calculated degree of substitution was in the range of 0.03-0.05 which means that every 20th-30th repeating unit, and every third to fifth carboxyl functionality carries a ferrocene molecule. Determining the ferrocene content by UV-VIS spectroscopy is not very exact as well because the ferrocene absorption and the benzophenone crosslinker absorption are interfering (Figure 3.2.3).

Film formation and surface attachment is carried out as described in Chapter 3.1 for pure pH-responsive dextran based polymer films on quarz glass substrates for UV-VIS measurements and on gold covered substrates for SPR/OWS and electrochemical characterization. Because the ferrocene molecules are present in the hydrogel film during the crosslinking process they can be involved in the crosslinking reaction which was not further investigated. The ferrocene coupling to the carboxyl functionalities should reduce the swelling degrees of the hydrogel films compared to the hydrogel films without ferrocene redox centers. The swelling degrees of the redox films (**12**) showed swelling degrees of ~7.5 in PBS 150 mM and ~8.5 for PBS 10 mM after crosslinking at 254 nm for 30 minutes. The same hydrogel without ferrocene redox centers had swelling degrees of about 13 for PBS 150 mM and 21 for 10 mM PBS for identical crosslinking conditions. This is true for polymer films with a total thickness of 3-20 μm in the swollen state. The swelling in z-direction is reduced due to the reduced amount of free carboxyl groups upon ferrocene binding. Consequently, the change of the swelling state upon reducing the ion concentration decreases, too. The existence of ferrocene inside the hydrogel film was measured by UV-VIS spectroscopy. Therefore, a hydrogel film was spincoated on a quarz substrate and the UV-VIS spectra were recorded from 200 to 800 nm.

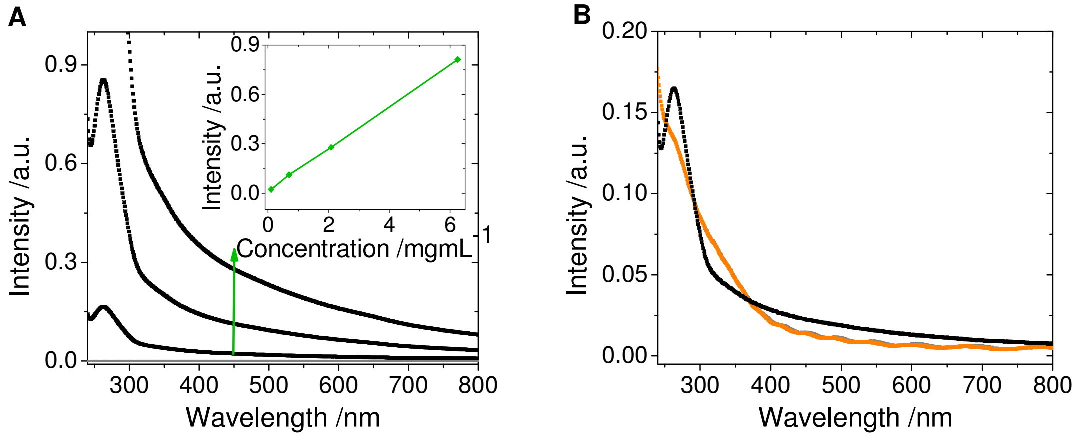

Figure 3.2.3: ***A)****UV-VIS spectra of a un-crosslinked dextran based hydrogel with ferrocene redox centers (d_s(benzophenone = 0.04, d_s(carboxymethyl) = 0.16) for increasing concentrations of 3.4 10^{-4}, 1 10^{-3}, 3 10^{-3}, and 1.5 10^{-2} mol/L.* ***B)*** *UV-VIS spectra for an uncrosslinked dextran-based polymer at a concentration of 0.1 mg/mL measured at a thickness (d = 1cm) (black), and a ferrocene containing dextran-based hydrogel film (orange) crosslinked at 254 nm for 40 min with a thickness of 1.7 μm. According to the calibration (A) the absorption of the hydrogel film (orange) of 0.015 at 450 nm for a thickness of 1.7 μm can be associated with a ferrocene concentration of 680 mg/mL applying a linear correlation between absorption and thickness following Lambert-Beer's law.*

The ferrocene absorption at 450 nm is clearly increased in the ferrocene modified hydrogel compared to the one without ferrocene although not a clear absorption peak but more an absorption shoulder is visible. The absorption value at 450 nm is determined to be 0,015 for this 1.7 µm thick hydrogel film corresponding to a ferrocene concentration of 680 mg/mL according to the calibration shown in Figure 3.2.3 A and Lambert-Beer's law.

3.2.3 Synthesis of a Ferrocene-Modified Photo-Crosslinkable Dextran-Based Hydrogel on a Substrate

A very clean and fast approach is the reaction of the photo-crosslinked and surface attached carboxymethylated dextran-based hydrogel film with ferroceneethyleneamine on a substrate. Besides the clean surface chemistry approach the main advantage is the separation of photo-crosslinking and ferrocene coupling avoiding any influence of the UV-irradiation onto ferrocene.[45] The disadvantages of this method are the even more difficult analysis of the ferrocene amount coupled into the film and the instability of the hydrogel film towards the mechanical stress due to the harsh solvent and rinsing conditions.

The preceding active ester activation can be carried out with EDC/NHS in water or with TFA-NHS or PFP-NHS in DMSO. The water-based system prevail a better film stability whereas the DMSO based reaction prevents the problem of hydrolysis by water. The subsequent reaction with ferroceneethylenamine has to be carried out in DMSO because of the insolubility of ferroceneethyleneamine in water. The rinsing with DMSO between these two steps and the solvent exchange from water to DMSO in case of the EDC/NHS activation in water are critical for the film stability on the substrate and to prevent the precipitation of ferrocene in the hydrogel film. The mechanical stress in DMSO and especially upon solvent exchange seems to be crucial. The amount of solvent on the hydrogel film is therefore reduced as much as possible and the rinsing is performed very slowly to minimize the film instability. This effect increases with increasing film thickness which is in agreement with the film stability investigations discussed in Chapter 4.1 for the dextran-based hydrogel. The swelling degrees of these ferrocene modified hydrogel films (**12**) are reduced compared to the non-modified ones. For hydrogel films crosslinked at 254 nm for 30 minutes the swelling degrees in z-direction were determined to be ~7 for PBS 150mM and ~8 for PBS 10 mM which is comparable to the prepared films of the solution modified dextran. Crosslinking for 90 minutes results in further decrease of the swelling degrees to 4-4.5 for PBS 150 mM and 5 for

PBS 10 mM. The swelling degrees are summarized and compared to the ones for the redox center free hydrogel in Table 3.2.2

Table 3.2.1: *Comparison of swelling degrees for the redox center free and the redox center modified hydrogel films for two different ion concentrations at pH 7,4 (PBS) and two different crosslinking times.*

	pure hydrogel *PBS 150 mM*	*with ferrocene* *PBS 150 mM*	*pure hydrogel* *PBS 10 mM*	*with ferrocene* *PBS 10 mM*
254 nm 30 minutes	~13	~4	~21	~7
254 nm 90 minutes	~12	~5	~17	~8

The reduced swelling degree upon ferrocene introduction can be attributed to a reduced number of free carboxyl groups and thus a reduced number of negative charges. Consequently, the change upon decreasing ion concentration is much smaller for the ferrocene containing hydrogel as well. For a hydrogel with reduced number of free charges the influence of the crosslinking time is more pronounced than for decreased ion concentration. Because the electrostatical force is reduced with reduced number of free charges the critical ion concentration is reduced. This leads to a reduction of the difference in the swelling degree for different crosslinking times, too. This effect is observed for the blocking of charges by counterions as well. The difference in swelling degree for varying degree of crosslinking is more pronounced for low ion concentrations thus for an increased number of free charges. To determine the ferrocene content via UV-VIS spectroscopy (Figure 3.2.3) thicker hydrogel films with a clear absorption maximum at 450 nm would be necessary to allow a precise analysis. At 450 nm the absorption value is determined to be 0.095 before rinsing and 0.08 after additional rinsing for this 870 (± 30) nm thick hydrogel film. Taking into account the thickness this is a factor ten higher absorption than for the pre-functionalized film. With the decreasing absorption upon rinsing, this points out that either unbound ferrocene molecules are still present or the coupling efficiency on a substrate is much higher. Because of this huge difference of one order of magnitude the presence of unbound ferrocene molecules due to incomplete wash out is more likely and is consistent with the results derived from cyclic voltammetry measurements (Chapter 4.3). The main problem here is the insolubility of ferrocenethyleneamine in water, which makes a removal of unbound ferrocene impossible during hydrogel swelling.

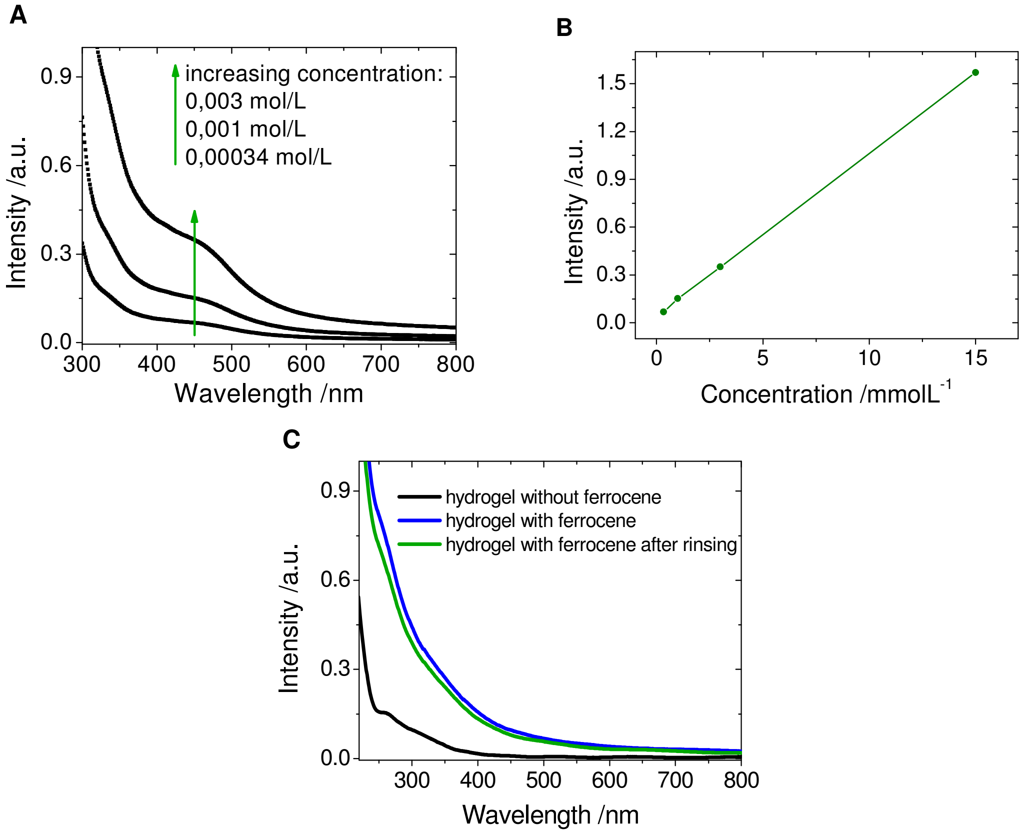

***Figure 3.2.3:** A) Concentration dependent ferroceneethyleneamine spectra for 0.034, 1, 3 mmol/L. **B)** Absorption (0.034, 1, 3 mmol/L) at 450 mm in ethanol for d=1cm. **C)** UV-VIS spectra for the unmodified dextran-based hydrogel before modifying it with ferroceneethyleneamine (black) and the corresponding ferrocene containing dextran-based hydrogel before (blue) and after (green) repeated rinsing with DMSO and water. The film thickness was determined with a profiler to d =* 870 (± 30) nm

3.2.4 Conclusion and Outlook

The modification of a benzophenone and carboxymethyl modified dextran-based polymer with ferroceneethyleneamine redox centers was demonstrated via wet chemical reaction and with surface chemistry. Besides the characterization of the chemical composition, the hydrogel film stability was determined as the most crucial parameter for surface modifications. The redox-center containing dextran-based hydrogel is expected to be a promising candidate for biosensor applications due to its hydrophilicity and high swelling degrees as shown for the redox center free hydrogel matrix. An additional external electrochemical charge switching possibility is expected to open new options especially in the field of sensors and binding studies. The electrochemical and swelling properties of the redox center modified hydrogel films presented here have been investigated by electrochemistry combined with simultaneous analysis by surface plasmon resonance and optical waveguide mode spectroscopy (Chapter 4.3).

3.2.5 Experimental

***Synthesis of Ferroceneethyleneamine*[43, 44]:** A solution of anhydrous aluminum chloride (10.3 mmol, 1.36g) in 12 mL of anhydrous diethyl ether was added dropwise to a stirred suspension of lithium aluminium hydride (10.3 mmol, 0.39 g). Afterwards a suspension of ferrocene-acetonitril (alfa aesar) (4.5 mmol, 1 g) in 50 mL of anhydrous diethyl ether was added. The reaction mixture was refluxed over night. The excess of metal hydride halide was slowly acidified with 34 mL of 6N sulfuric acid. The aqueous phase was extracted two times with diethyl ether and made alkaline with potassium hydroxide pellets until a pH of 9 and again extracted twice with diethyl ether. The combined extracts were dried over potassium carbonate and evaporated to obtain 0.6g (60 mol%) of a dark-brown viscous liquid.

^{1}H-NMR ($CDCl_3$) (250MHz), δ [ppm]: 4.2 (m, 9H, Fc); 2.7 (t, 2H, CH_2-Fc, J = 6,7); 2.4 (t, 2H, CH_2N, J = 6,7); 1.6 (2H, NH_2).

Preparation of a Ferrocene-modified Hydrogel: The photo-crosslinkable, dextran-based hydrogel was synthezised as described in Chapter 3.1. The degree of benzophenone substitution was determined to be 0.04 and the degree of carboxymethylation 0.16. The binding of ferroceneethyleneamine was carried out under argon in dimethylsulfoxide with 0.7 g carboxymethylated and benzophenone-modified dextran-based hydrogel in ~40 mL of DMSO. In the first step the carboxyl groups were activated with pentafluorophenyl trifluoroacetate (TFA-PFP). The reaction was carried out at room temperature by addition of 0.3 mL (0.45 g, 1.6 mmol) TFA-PFP (Fluka) and ~5 mL of 4-methylmorpholine (Merck) for 3 hours. To remove the trifluoracetic acid the reaction mixture was dialyzed against 2L of DMSO over night, directly followed by the reaction with ferroceneethyleneamine (typically 0.1 g, 0.44 mmol) in DMSO with 5mL of 4-methylmorpholine at room temperature under argon for 12h.

For purification the reaction mixture was extensively dialyzed against DMSO and destilled water. In case of excess ferroceneethyleneamine it could be centrifuged from the hydrogel-water solution due to its insolubility in water.

^{1}H-NMR (D_2O) (300MHz), δ [ppm]: 7.8 (9H, arom. H (benzophenone)); 4.7 (1H, CH1); 5.30, 5.16, 4.97 (s,1H,CH1), 4.19 (m,2H,MeCM), 3.92 (m,2H,H6, H5), 3.71 (m,2H, H6',H3), 3.54(m,2H,H2, H4), 2.8 (m, 2H, Me ferrocene); 2.6 (m, 2H, Me ferrocene).

Preparation of Ferroceneethyleneamine-Modified Hydrogel on a Substrate: For the coupling of ferroceneethyleneamine to an already crosslinked hydrogel film the carboxymethylated dextran-based hydrogel containing benzophenone as crosslinking unit was spincoated onto a slide and crosslinked (Chapter 3.1). This hydrogel film was subsequently activated by swelling in a fresh mixture of 500 µL of 0.4 M 1-(3-dimethylaminopropyl)-3-ethyl-carbodiimide hydrochloride (EDC) and 500 µL of 0.1 M *N*-hydroxysuccinimide (NHS) in destilled water for 10 min followed by rinsing with dimethylsulfoxide(DMSO). By carefully dropping a ferroceneethyleneamine-DMSO-solution (c=0.1 g/5mL) containing ~0.1 mL 4-methylmorpholine onto the hydrogel film the active ester activated carboxy groups are converted to amides. In this step it seems to be important to control the volume of DMSO solution on the slide and use as little volume as possible to keep the gel stable. Furthermore the film thickness plays an important role for the film stability and has to be optimized for every gel. The reaction was allowed to proceed for 30-90min followed by rinsing with DMSO and destilled water. The hydrogel films were dried on air.

Film Preparation: For the *UV-VIS measurements* quarz slides (PGO) were coated with a chemisorped layer of 4-(3-triethoxysilyl)propoxybenzophenone from a 5 mM ethanol solution for ~24 h at room temperature. Afterwards the slides were cleaned by extensively rinsing with ethanol and acetone and blown dry with air.

Deposition of dextran films and photo-crosslinking. Dextran-based films up to several micrometers in thickness were deposited onto the pre-treated substrates by spin-coating from polymer/water solutions with 3000-6000 rpm. A solution with a polymer content of 20 wt% resulted in a film thickness of approximately 500 nm at 5500 rpm. The samples were dried in vacuum at 45°C over night and crosslinking was performed for 30 or 90 minutes with a Stratagene UV Stratalinker 2400 operating at 75 W with a emission maximum at 254 nm with an irradiation dose of 0.2 J cm^{-2} per minute.

UV-VIS: To investigate the crosslinking UV-VIS spectra were recorded with a UV-VIS/NIR (Perkin Elmer, Lambda 900) for different crosslinking times and different periods after the crosslinking was finished

Swelling Degree: The swelling degree is obtained by dividing the swollen film thickness as determined with the WKB-approximation (Chapter 4.1) through the dry film thickness after rinsing and drying as determined with the profiler (TLA Tencor).

3.2.6 Bibliography

[1] A. Heller, *Current Opinion in Chemical Biology* **2006**, *10*, 664.
[2] C. Ornelas, J. Ruiz, C. Belin, D. Astruc, *J. Am. Chem. Soc.* **2009**, *131*, 590.
[3] M. Péter, M. A. Hempenius, E. S. Kooij, T. A. Jenkins, S. J. Roser, W. Knoll, G. J. Vancso, *Langmuir* **2004**, *20*, 891.
[4] E. S. Forzani, M. A. Pe´rez, M. L. p. Teijelo, E. J. Calvo, *Langmuir* **2002**, *18*, 9867.
[5] C.-C. Han, H.-Y. Chen, *Macromolecules* **2007**, *ASAP*.
[6] M. Tagliazucchi, D. Grumelli, E. J. Calvo, *Phys. Chem. Chem. Phys.* **2006**, *8*, 5086.
[7] R. Shankar, T. K. Ghosh, R. J. Spontak, *Soft Matter* **2007**, *3*, 1116.
[8] T.-L. Choi, K.-H. Lee, W.-J. Joo, S. Lee, T.-W. Lee, M. Y. Chae, *J. Am. Chem. Soc.* **2007**, *129*, 9842.
[9] E.-Y. Choi, O. Azzaroni, N. Cheng, F. Zhou, T. Kelby, W. T. S. Huck, *Langmuir* **2007**, *23*, 10389.
[10] F. Zhou, H. Hu, B. Yu, V. L. Osborne, W. T. S. Huck, W. Liu, *Ana. Chem.* **2007**, *79*, 176.
[11] R. A. Etchenique, E. J. Calvo, *Anal. Chem.* **1997**, *69*, 4833.
[12] G. Liu, X. Zhao, *Jounal of Macromolecular Science Part A* **2006**, *43*, 345.
[13] T. Tanaka, I. Nishio, S.-T. Sun, S. Ueno-Nishio, *Science* **1982**, *218*, 467.
[14] S. Brahim, A. Guiseppi-Elie, *Electroanalysis* **2004**, *17*, 556.
[15] A. S. Abd-El-Aziz, *Macromol. Rapid. Commun.* **2002**, *23*, 995.
[16] A. Heller, *Phys. Chem. Chem. Phys.* **2004**, *6*, 209.
[17] S. A. Merchant, D. T. Glatzhofer, D. W. Schmidtke, *Langmuir* **2007**, *23*, 11295.
[18] K. Winkler, M. E. Plonska, A. Basa, M. Lach, B. Alan L, *Electroanalysis* **2003**, *15*, 55.
[19] I. C. Kwon, Y. H. Bae, S. W. Kim, *Nature* **1991**, *354*, 291.
[20] S. Murdan, *J. Contr. Release* **2003**, *92*, 1.
[21] S. H. Yuk, S. H. Cho, H. B. Lee, **1992**, *9*, 955.
[22] C. P. Andrieux, O. Haas, J. M. Saveant, *J. Am. Chem. Soc.* **1986**, *108*, 8175.
[23] B. Gregg, A. Heller, *Anal. Chem.* **1990**, *62*, 258.
[24] T. J. Ohara, R. Rajagopalan, A. Heller, *Anal. Chem.* **1993**, *65*, 3512.
[25] E. Mikeladze, A. Schulte, M. Mosbach, A. Blochl, E. Csoregi, R. Solomonia, W. Schumann, *Electroanalysis* **2002**, *14*, 393.
[26] E. J. Calvo, R. Etchenique, C. Danilowicz, L. Diaz, *Anal. Chem.* **1996**, *68*, 4186.
[27] A. Aoki, R. Rajagopalan, A. Heller, *J. Phys. Chem.* **1995**, *99*, 5102.
[28] R. J. Forster, J. G. Vos, *J. Inorg. Organomet. Polym.* **1990**, *1*, 67.
[29] F. Mao, N. Mano, A. Heller, *J. Am. Chem. Soc.* **2003**, *125*, 4951.
[30] K. Rajagopalan, A. J. Chavan, B. E. Haley, D. S. Watt, *The Journal of Biological Chemistry* **1993**, *268*, 14230.
[31] A. Aoki, A. Heller, *J. Phys. Chem.* **1993**, *97*, 11014.
[32] C. L. Chuang, Y. J. Wang, H. L. Lahn, *Anal. Chim. Acta* **1997**, *353*, 37.
[33] T. Coviello, P. Matricardi, C. Marianecci, F. Alhaique, *Jounal of Controlled Release* **2007**, *119*, 5.
[34] Y. Qiu, K. Park, *Advanced Drug Delivery Reviews* **2001**, *53*, 321.

[35] A. Togni, T. Hayashi, *Ferrocene-homogeneous catalysis, organic synthesis and materials science.*, VCH, New York, **1995**.

[36] M. Sato, S. Tanaka, S. Ebine, K. Morinaga, S. Akabori, *J. Organomet. Chem.* **1985**, *282*, 247.

[37] A. Anne, *Tetrahedron Letters* **1998**, *39*, 561.

[38] A. A. O. Sarhan, M. S. Ibrahim, M. M. Kamal, K. Mitobe, T. Izumi, *Monatsh. Chem.* **2009**, *140*, 315.

[39] K. A. Mahmoud, H.-B. Kraatz, *J. Inorg. Organomet. Polym.* **2008**, *18*, 69.

[40] E. J. Kupchick, R. J. Kiesel, *J. Org. Chem.* **19666**, *31*, 456.

[41] Y. Li, N. Wang, X. He, S. Wang, H. Liu, Y. Li, X. Li, J. Zhuang, D. Zhu, *Tetrahedron* **2005**, *61*, 1563.

[42] I. Tranchant, A.-C. Herve, S. Carlisle, P. Lowe, C. J. Slevin, C. Forssten, J. Dilleen, D. E. Williams, A. B. Tabor, H. C. Hailes, *Bioconjugate Chem.* **2006**, *17*, 1256.

[43] P. Godillot, H. Korri-Youssoufi, P. Srivastava, A. E. Kassmi, F. Garnier, *Synthetic Metals* **1996**, *83*, 117.

[44] A. Ratajczak, B. Czech, L. Drobek, *Synthesis and Reactivity in Inorganic, Metal-Organic, and Nano-Metal Chemistry* **1982**, *12*, 557.

[45] A. Jaworska-Augustyniak, *Transition Met. Chem.* **1982**, *7*, 16.

3.3 Synthesis of a Magnetic Dextran Composite Hydrogel

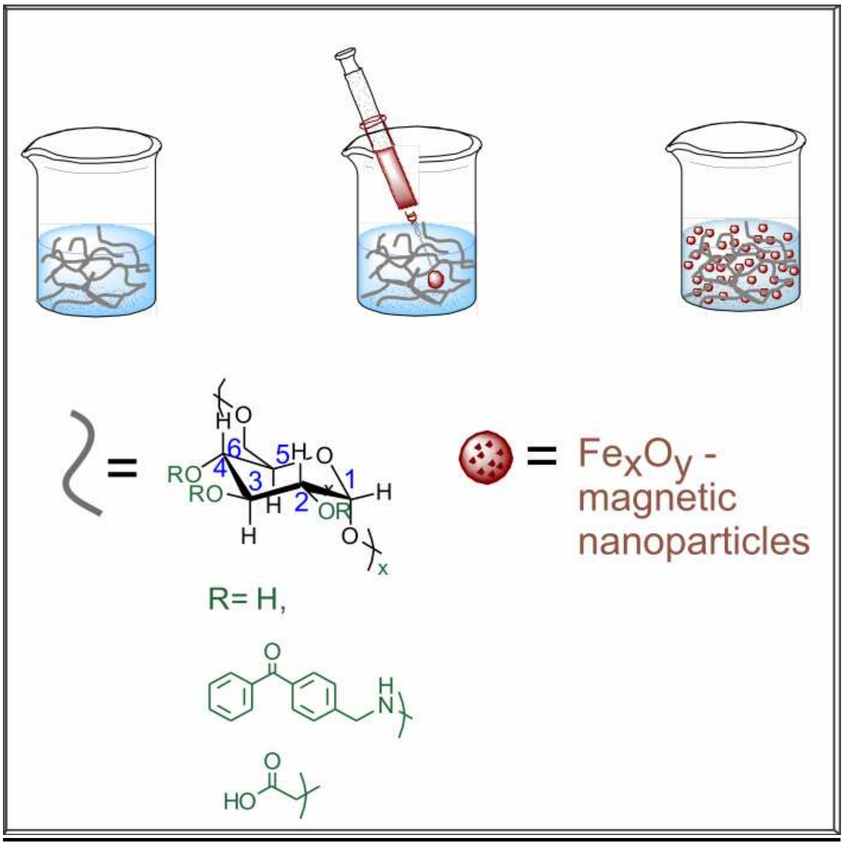

Magnetic composite hydrogels are useful candidates for a broad field of applications from medicine to mechanical engineering. Here, a method for the fabrication of a magnetic composite hydrogel based on dextran and iron oxide nanoparticles is presented. The separation of the nanoparticle- and the polymer synthesis allows a separate tuning of the polymer and nanoparticle properties. Composite hydrogel films on glass or gold surfaces were prepared and photo-chemically crosslinked. The pH-stability of the magnetic hydrogel is shown and optimal fabrication conditions are discussed.

3.3.1 Introduction

Dextran is known as a biocompatible and enzyme-degradable material with low unspecific binding to biomolecules. Thus, it is a good material for medical[1-5], or sensing[6-9] applications, and protein binding studies[7, 10, 11].

Several dextran derivatives are reported as precursor for dextran-based hydrogels (Chapter 1.1). The variety of dextran derivatives enables the synthesis of dextran-based hydrogels with a multitude of characteristics, tunable for specific desired applications. Magnetic nanoparticle modified polymers[12, 13] open new possibilities for applications like inductive heating[14, 15] and potentially triggering a temperature induced collapse, catalysis[16], magnetic separation[15, 17-19], drug release[20, 21], contrast agents[22], magnetic resonance imaging[23] and other biomedical applications.[1, 21, 24-27] This can mainly be attributed to improved aqueous stability, biocompatibility and conjugation properties of nanoparticles. Various materials and methods are used for the synthesis of magnetc particle-modified polymers. Unfortunately, methods yielding monodisperse particles with a nice size distribution and excellent magnetic properties, often do not allow chemical functionalization of the material's surface.[28] Thus, from the plethora of synthetic possibilities, a different optimal method has to be chosen for every single application. For the incorporation of magnetic nanoparticles into polymers and hydrogel structures mainly five different strategies are implemented: The most common one is the encapsulation of magnetic iron oxide nanoparticles during the synthesis by co-precipitation methods.[24, 29, 30] Sometimes, nanoparticles and polymer are synthesized simultaneously.[31] In this case the polymer replaces the stabilizing surfactant and serves as stabilizing and capping agent. Especially the nucleation and growth, and with this the particle size is influenced by the nature, quality and amount of the polymer. Therefore, the reaction conditions required optimization. Delayed addition of dextran, for example, leaves the nucleation process unaffected, and consequently leads to bigger particles.[32] The particles are in most cases mechanically locked inside the polymer. With this fabrication method not only nanoparticle containing hydrogels but also core-corona particles and microgels can be fabricated.[22, 33] The second strategy focuses on generating the nanoparticles inside the pre-designed hydrogel. Here, the gel serves as a template or nanoreactor and the nanoparticle properties, especially their shape and size, are influenced by the gel structure. [19, 34, 35] The most common reaction sequence for this fabrication method is the swelling of the hydrogel in an iron salt solution followed by the particle generation by co-precipitation inside the hydrogel pores. The particles can be mechanically locked inside the gel. Alternatively, they can be coupled electrostatically in case the hydrogel is functionalized with carboxyl groups, for example. The third strategy utilizes the swelling characteristics of hydrogels by swelling a pre-synthesized hydrogel in a nanoparticle solution. The pre-designed particles are soaked up or "breathed" into the hydrogel.[33, 36] The fourth strategy uses pre-synthesized and very often surfactant-stabilized nanoparticles. The polymeric shell is synthesized in the presence of the nanoparticles and coupled in-situ to their surface, either by a "grafting from" approach or by producing a functionalized polymer, that can bind to the particle surface through its functional groups. With this technique, both polymer- and surfactant-coated magnetic materials have been embedded into polymeric networks using suspension, emulsion, or precipitation polymerisation. [37-40] Recently, a fifth strategy, similar to the one used in this work, was applied by J. Wotschadlo and co-workers to manipulate nanoparticle uptake by living human tumor cells.[41] This strategy fully separates the nanoparticle and polymer syntheses. The pre-synthesized suspended nanoparticles are mixed with pre-synthesized carboxymethylated dextran (M_w 20.000 $gmol^{-1}$) and magnetically separated from any unbound polymer in a washing step. The separation of nanoparticle and polymer synthesis facilitates the independent modification of particles and polymer and is advantageous for following steps like hydrogel formation and adjustment of composite material properties like the nanoparticle load and distribution of the polymer. Pursuing this strategy, especially the modification of the polymer functionalization and the nanoparticle properties like shape, monodispersity and magnetization can be improved. In the nanoparticle synthesis the coprecipitation method can be replaced by organic phase synthesis, for example allowing better control over the nanoparticle size, monodispersity and therefore magnetic properties.[24]

Compared to mechanically entrapping magnetic nanoparticles inside a polymer structure, electrostatical binding facilitates higher stability of the composite material. To couple iron oxide nanoparticles electrostatically to a polymer like dextran, binding points are needed. Carboxyl groups are known to bind electrostatically to iron oxide,[16] whereas the interactions between magnetic cores and the hydroxyl groups of dextran itself is reported to be too weak to form a stable bond. Thus, efficient derivatization of pure dextran with magnetic nanoparticles is prevented.[30, 42] . In pure dextran, magnetic nanoparticles can therefore only be mechanically trapped, which is disadvantageous for the stability of highly swelling hydrogels. Additionally, carboxyl functionalities are interesting as coupling points for further modification e.g. with biomolecules or analytes.

In this Chapter the preparation of a composite hydrogel based on dextran, containing magnetite nanoparticles with application potential for magnetic separation and affinity studies is reported. To this end, a decoupled approach of nanoparticle and polymer synthesis was developed and bulk as well as film properties of the magnetic hydrogel were investigated.

3.3.2 Magnetic Nanoparticles – Synthesis and Properties

The magnetic iron oxide nanoparticles used in this work were synthesized and characterized by Stefanie Utech in the group of PD. M. Maskos at the University of Mainz. A co-precipitation reaction of Fe(III) and Fe(II) cations in NaOH or NH_4OH solution was carried out analoguos to the literature.[43, 44] The reaction conditions are summarized in table 3.3.1. The nanoparticles contain Fe_3O_4 as well as γ-Fe_2O_3 as determined by Mößbauer spectroscopy for Fe_xO_y-I. Because Fe_3O_4 is relatively easy oxidized to γ-Fe_2O_3 the Fe_xO_y-I nanoparticles mainly consist of γ-Fe_2O_3.

Table 3.3.1: *Reaction conditions during synthesis of iron oxide nanoparticles by coprecipitation of iron oxide salts in basic media.*

	Fe(II) / Fe(III)	*Coprecipitation Reagent*
Fe_xO_y-I	1/1	NaOH
Fe_xO_y-II	1/2	NaOH
Fe_xO_y-IV	1/2	NH_4OH

The nanoparticles were suspended in solution acidified with hydrochloric acid after cleaning. Nanoparticles with a size of 3.2 to 8.3 nm were prepared. The average hydrodynamic radius was determined with asymmetric flow field-flow fractionation (AF-FFF) and is summarized in Table 3.3.2. The superparamagnetic nature of these particles was confirmed by SQUID measurements as can be seen in Figure 3.3.1. The magnetic nanoparticles contain Fe_3O_4 and γ-Fe_2O_3. The saturation magnetization increases with increasing Fe_3O_4 content due to its higher saturation magnetization compared to γ-Fe_2O_3 and with increasing size of the particles. Magnetic nanoparticles prepared from a Fe(II)/Fe(III) ratio of 1:2 are expected to contain more Fe_3O_4 and the ones prepared in NH_4OH are expected to be larger.

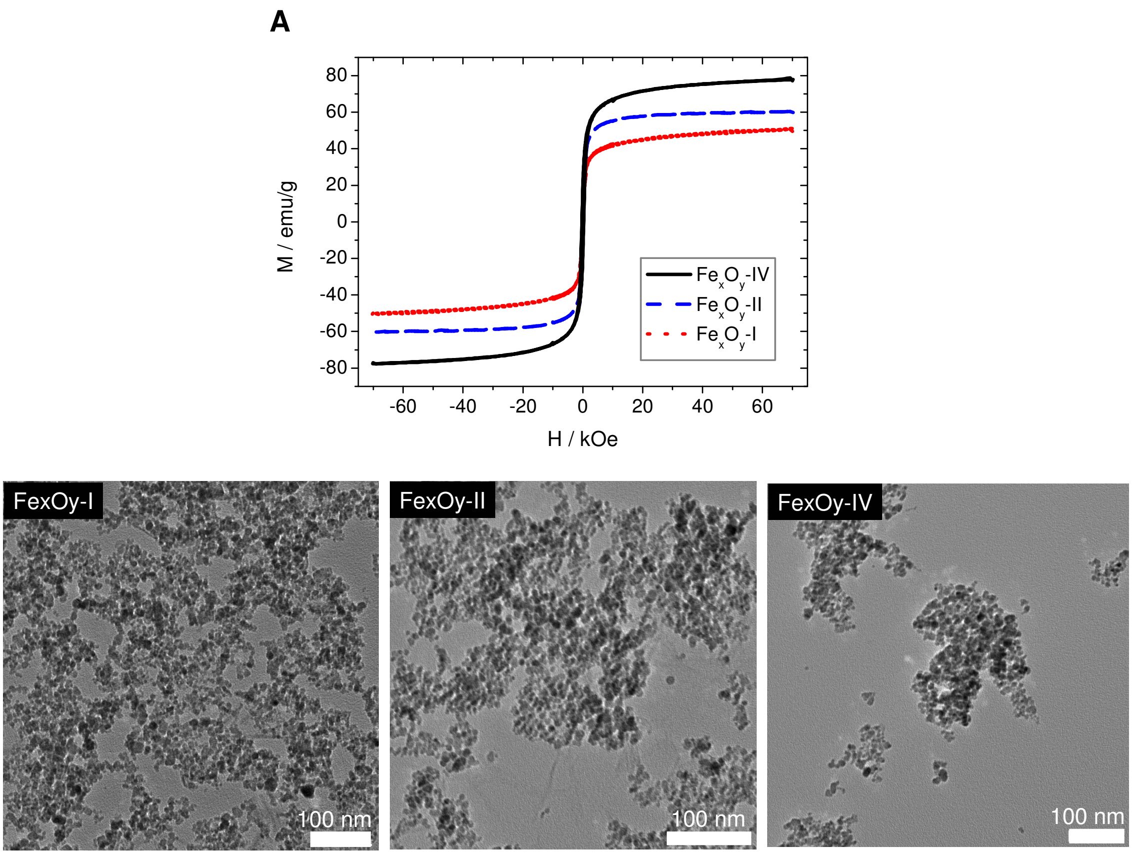

Figure 3.3.1: *SQUID measurements of the iron oxide nanoparticles at 5K* ***(A)*** *and representative TEM images of the magnetic nanoparticles. All types of particles are superparamagnetic but show a decrease in their saturation magnetization in the following order:* Fe$_x$O$_y$-IV > Fe$_x$O$_y$-I I> Fe$_x$O$_y$-I.

Nanoparticles with different characteristics were used as summarized in Table 3.3.2. The influence of different particle characteristics on the synthesis of magnetic composite dextran based hydrogels, are discussed in Chapter 3.3.3. Knowing the size of the particles the determined order for the saturation magnetization of Fe$_x$O$_y$-IV> Fe$_x$O$_y$-II> Fe$_x$O$_y$-I represents the expected sequence.

Table 3.3.2: *Nanoparticles used for the preparation of magnetic photo-crosslinked composite dextran based hydrogels.*

Sample	*Average particle size (hydrodynamic radius) /nm*	*Saturation magnetization /emu g^{-1}*
Fe$_x$O$_y$-I	3.2	50
Fe$_x$O$_y$-II	5.6	78
Fe$_x$O$_y$-IV	8.3	89

Nanoparticle suspensions without any surfactant as stabilizing agent can be synthesized because the iron oxide nanoparticles are stabilized by electrostatic repulsion in acidic water solutions below pH 4. Consequently, the nanoparticle surface can be used to electrostatically bind ligands, independently from the nanoparticle synthesis, which opens new possibilities for the preparation of nanoparticle composite materials and allows for the independent tuning of the nanoparticle characteristics.

3.3.3 Synthesis of a Composite Dextran Hydrogel with Embedded Magnetic Nanoparticles

The photo-crosslinkable carboxymethylated dextran-based hydrogel (PCMD), described in Chapter 3.1, contains benzophenone groups as photo-crosslinking units and carboxymethyl groups, that serve as possible binding points for analytes. Additionally, the carboxyl groups introduce a pH- and ionic strength-responsive behaviour, as discussed in Chapter 4.1. The PCMD was pre-synthesized independently from the nanoparticle preparation in a three step synthesis. At first the dextran is carboxymethylated in water[45], followed by the conversion of a part of the carboxymethyl functionalities to active esters with TFA-NHS or PFP-NHS. Subsequently, 4-aminomethylbenzophenone was coupled *in-situ* via nucleophilic substitution. Like this the benzophenone photo-crosslinking units were bound via an amide bond.

For the preparation of the magnetic composite iron oxide nanoparticle-PCMD blend, the pre-synthesized polymer and the nanoparticle suspension ($pH = 4$) need to be mixed under acidic conditions. Therefore, the PCMD was dissolved in water at concentrations between 0.05 g/mL and 0.2 g/mL and the pH was lowered to $pH = 1\text{-}2$ with hydrochloric acid. Slow dropwise adding of the nanoparticle suspension directly into the polymer solution while shaking, leads to the formation of the blend, due to electrostatically binding of the iron oxide nanoparticels to the carboxyl groups of the PCMD. The preparation procedure is schematically shown in Figure 3.3.1. In order to prevent precipitation in this process of electrostatical coupling of the iron oxide particles, lower polymer concentrations are advantageous as well as very slow addition of the nanoparticle solution, intense mixing and low viscosity and acidic pH of the polymer solution. In general, the local concentration of the nanoparticles and the viscosity of the PCMD solution should be low to prevent aggregation. A possible reason for the observed aggregation might be a “depletion effect” resulting in a local aggregation of particles. This interaction originates from a loss of conformational entropy of the polymer between the surfaces of neighboring particles due to a lower effective polymer concentration. This lower effective concentration causes osmosis and thus the depletion of the solvent, resulting in a phase separation at high enough polymer and nanoparticle concentrations.

A second effect responsible for aggregation can be a “bridging effect”, which mainly occurs if the polymer concentration is low. In case two or more particles are bridged by one polymer chain, the repulsion due to a polymer brush layer covering a nanoparticle is inhibited and aggregation occurs.

The influence of the reaction conditions on the stability of nanoparticles without surfactants, was reported for other water based iron oxide nanoparticle systems as well.[28, 46, 47] Usually, the mixing of polymer and nanoparticles is used to prepare polymer microspheres with encapsulated nanoparticles or nanoparticle aggregates with a size below 100 nm.[41, 48] The coupling of the magnetic nanoparticles to the PCMD is indicated by the stability of the composite material at neutral pH.

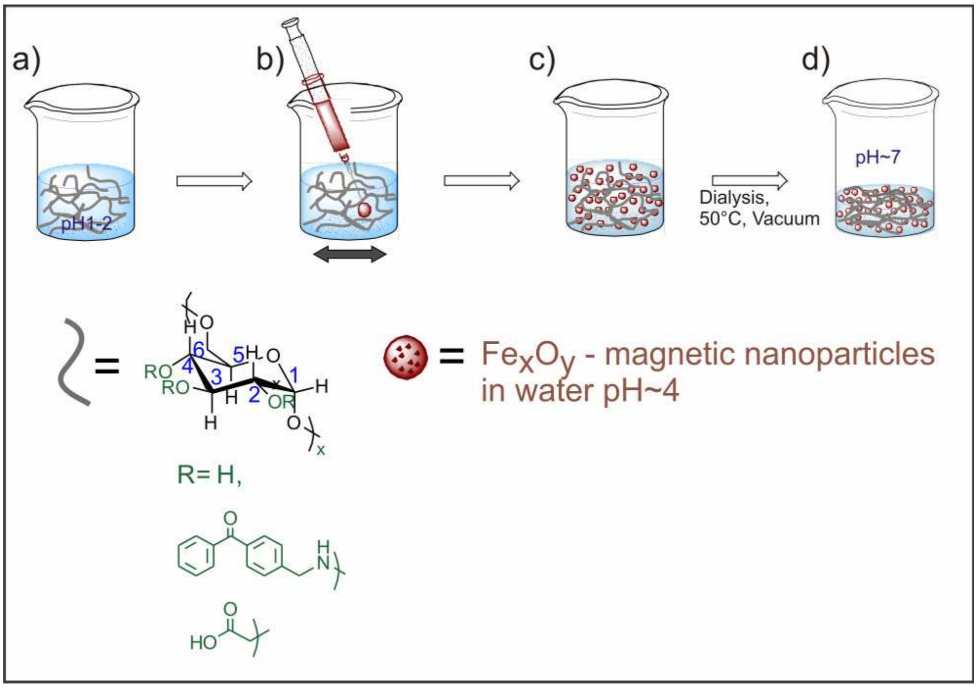

Figure 3.3.1: *Synthetic concept of the preparation of the magnetic polymer composite, including the acidic polymer solution (a), mixing of polymer and nanoparticle solution (b), dialysis to neutral pH (c) and volume reduction at increased temperature under vacuum (d).*

To investigate the pH-stability, the composite material was dialyzed against water and against a sodiumhydroxide solution at pH 8. No precipitation of iron oxide nanoparticles or of the composite material due to pH-change was observed. Unbound and aggregated nanoparticles, which sometimes occur after mixing, can be removed by sedimentation. Under optimized conditions, minimized precipitation and single distributed non-aggregated particles in the polymer blend were achieved. Based on the pH-stability of the composite material it is assumed that these particles inside the polymer solution are effectively stabilized by the dextran polymer. The particle distribution inside the composite was studied by transmission electron microscopy (TEM). Exemplarily results are shown in Figure 3.3.2.

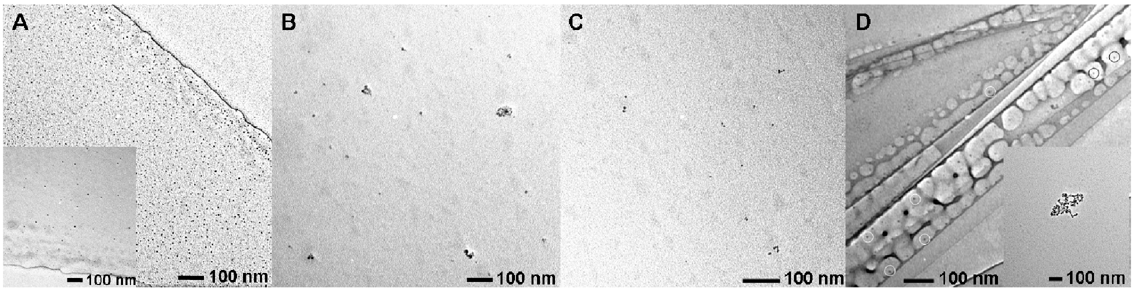

Figure 3.3.2: *TEM images (recorded by S. Utech, University of Mainz) of composite iron oxide nanoparticle dextran-based polymers at neutral pH with increasing nanoparticle content:* ***A)*** Fe_xO_y-II *2,5%,* ***B)*** Fe_xO_y-IV *5%,* ***C)*** Fe_xO_y-I *5%,* **D)** Fe_xO_y-II *15%. The nanoparticle content refers to the weight of iron oxide nanoparticles added to a dextran-based polymer (d_s(carboxymethyl) = 0.16; d_s(benzophenone) = 0.04) solution of 0.1 g/mL during the preparation process. For all concentrations up to 15% single distributed particles were present but the amount of aggregated particles increased especially for the composite gel with a particle content of 15%.*

The TEM measurements clearly show well distributed individual magnetic nanoparticles for all concentrations, although, for a particle content of 15 wt% some aggregates are present as well. The nanoparticle content of 2.5 – 15 wt% is comparable to values reported in the literature for composite gels synthesized with other methods. The amount of particles that can be stabilized via electrostatical binding to the carboxyl groups in the dextran-based polymer is probably limited by its carboxyl group content. For a particle content of 15 wt% the amount of particles that can be stabilized due to electrostatic forces might be already exceeded resulting in an aggregation of nanoparticles which is in agreement with the results we found. This saturation effect was not further investigated in this work. Liang *et al.* for example reported polysaccharide composite gels with nanoparticle contents around 9% after particle formation inside the polysaccharide hydrogel.[19]

For film formation by spin-coating the composite solution was concentrated by evaporating water up to concentrations of 0.1-0.2 mg/mL or even up to dryness followed by dissolving the composite polymer. Composite films from approximately 100 nm up to several micrometers in thickness could be prepared by adjusting the spin-coating conditions. The hydrogel films were prepared on 4(3-triethoxysilyl)propoxybenzophenone-coated quartz (Fig. 3.3.3) or S-3-(4-benzoylphenoxy)propyl ethanethiol-coated gold-covered glass substrates depending on the application (Chapter 3.1).

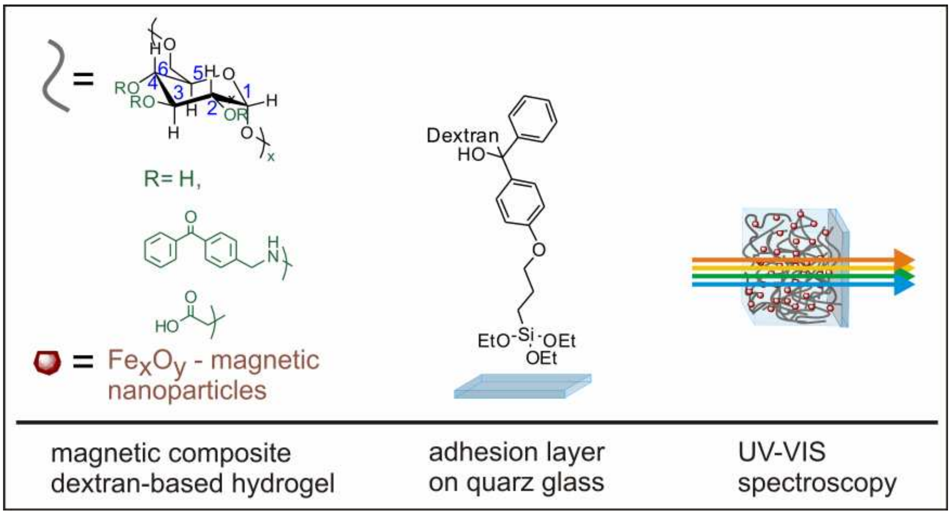

Figure 3.3.3: *Schematic view of the sample preparation for UV-VIS measurements. The magnetic composite hydrogel is crosslinked and coupled to a quarz glass slide covered with a monolayer of 4(3-triethoxysilyl)propoxybenzophenone via UV-light irradiation.*

Crosslinking and coupling to the surface-bound monolayer was achieved by irradiation with UV-light as described in Chapter 3.1. With this technique, the crosslinking density can easily be tuned by varying the crosslinking irradiation energy dose, giving rise to an easy manner of manipulating the swelling degree of the composite gel. To verify the stability of the nanoparticle bonding to the PCMD, composite hydrogel films on quarz were investigated by UV-VIS spectroscopy while rinsing with water or buffer.

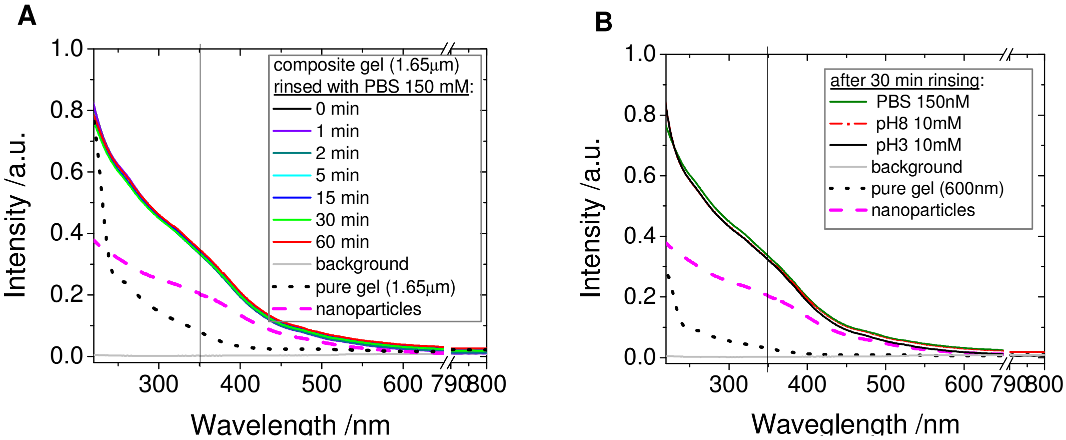

Figure 3.3.4: ***A)*** *Representative UV-VIS measurements of a composite magnetic dextran-based hydrogel (d_s(carboxymethyl) = 0.16; d_s(benzophenone) = 0.04, Fe$_x$O$_y$-I nanoparticle content ~15 wt%, d = 1.65 μm) for different periods of rinsing (0.8 mL/min) with PBS (150 mM).* ***B)*** *UV-VIS spectra after 30 min of rinsing with different buffers (PBS, pH 3, pH 8). For comparison, the pure nanoparticle suspension (- -), the pristine hydrogel spectrum for the same film thickness (...) and the background measurement (-) are shown as well. The nanoparticle absorption at ~350 nm is indicated by the black vertical line. The composite hydrogel spectra are stable for more than 60 minutes of rinsing indicating no loss of nanoparticles due to rinsing with different buffers.*

As can be seen in Figure 3.3.4 the particles seem to be permanently fixed into the hydrogel network, no decrease in the iron oxide nanoparticle absorption at ~350 nm and thus no loss of material, even after 60 minutes of rinsing, could be observed.

The particles are permanently fixed into the hydrogel for different ion concentrations (10-150 mM) and various pH-values (pH = 3-8). Consequently, the coupling of the particles inside the hydrogel does not seem to be influenced by the swelling state and the pH.

3.3.4 Conclusion and Outlook

In summary, the fabrication of a magnetic iron oxide nanoparticle photo-crosslinkable dextran based blend and subsequent composite hydrogel formation was shown. The dextran blend was prepared by simply mixing of pre-synthesized magnetic nanoparticles with the also pre-synthesized photo-crosslinkable dextran-based polymer in aqueous solution. This method allows separately optimizing of the nanoparticle and the hydrogel characteristics and avoids the interferences of polymer and nanoparticles in case both are present during the synthesis. The fabrication conditions could be optimized and hydrogels containing evenly distributed, non-aggregated particles were achieved. Besides the bulk synthesis composite hydrogel films were prepared and their stability in general as well as the pH-stability of the nanoparticles coupled to the hydrogel was shown by UV-VIS spectroscopy.

Further developments of this project aim towards optimizing the nanoparticle content for different applications, the polymer functionalization towards analyte binding or stimuli responsiveness and to expand this simple fabrication method to a broad field of different polymer types.

3.3.5 Experimental

***Dextran-Based Hydrogel*:** For the hydrogel synthesis the commercially available dextran (Sigma Aldrich, $M_r = 2.000.000$) was first carboxymethylated followed by the introduction of 4-aminomethylbenzophenone via active ester chemistry as described in Chapter 3.1 resulting in a photocrosslincable, pH-responsive dextran with tuneable swelling and binding properties. The carboxyl groups can serve as electrostatical binding points for magnetic nanoparticles.

***Magnetic Nanoparticles:*_** The superparamagnetic iron oxide nanoparticles were synthesized by coprecipitation of Fe(II) and Fe(III) in NaOH or NH_4OH solution. An aqueous solution of various ratios of $FeCl_2{\cdot}4\ H_2O$ (0.1 M) and $FeCl_3{\cdot}6\ H_2O$ (0.1 M and 0.2

M respectively) was added dropwise into 50 mL of alkali solution (1 M NaOH, alternative 1 M NH_4OH) under vigorous stirring for 30 min at room temperature. The black precipitate was washed three times with water and collected by centrifugation. After addition of HCl solution a stable aqueous dispersion was obtained.

Magnetic Composite Dextran-Based Hydrogel: The magnetic dextran-based photo-crosslinkable hydrogel was produced by mixing the magnetic nanoparticles with the modified dextran-based hydrogel under diluted acidic conditions. Therefore, the carboxymethylated and 4-aminobenzophenone-modified dextran was dissolved in ultrapure water (MilliQ, Millipore) at a concentration of 0.05-0.25 g/mL. The pH was adjusted with HCl to a pH of 1-2 followed by the dropwise addition of the nanoparticle solution (pH~4, c=52.43 mg/mL (Fe_xO_y-I), 49.83 mg/mL (Fe_xO_y-II), 33.70 mg/mL (Fe_xO_y-IV)) directly into the polymer solution while shaking. The mixture was dialyzed against water to a neutral pH. In case of addition of too many nanoparticles to the solution the excess amount of particles precipitates and can be removed by centrifugation (8000 rpm, 30 min). If the added amount of nanoparticles was carefully adjusted to the amount of polymer in the solution no precipitation was seen at a neutral pH.

TEM Measurements: Transmission electron microscopy (TEM) was performed with a Philips CM-12 microscope at 120 kV. Samples were prepared evaporation of aqueous solutions of the preparations on carbon films supported by copper grids.

AF-FFF Measurements: The asymmetrical flow-field flow fractionation device (AF-FFF) from Consenxus consisted of an AF-FFF channel system 2.0. Poly(ethersulfone) membranes were utilized as semipermeable walls (MWCO: 4 kDa). Degassed ultrapure water (MilliQ) with NaCl (5 mmol/L) and TWEEN 20 (100 mg/L) was used as eluent. A Waters 486-UV detector operating at 254 nm monitored the eluting particles.

SQUID Measurements: The superconducting quantum inference device (SQUID) measurements were performed with a Quantum Design Squid-Magnetometer MPMS XL at *5 K* with dried particle suspensions.

Film Preparation and Photo-Crosslinking: Films of the magnetic hydrogel were prepared on SiO_x or *gold* surfaces depending on the application. For the *UV-VIS measurements* 4-(3-triethoxysilyl)propoxybenzophenone was chemisorbed onto SiO_x surfaces (quartz glass (PGO)) from ethanol solution (5 mM) at room temperature for ~24 h. Afterwards the slides were cleaned by extensively rinsing with ethanol and acetone and blown dry with air.

To produce *hydrogel films* the nanoparticle-polymer blend solution was concentrated by evaporating the water (60°C, 20 mbar) until a desired concentration of 0.1-0.2 g/mL followed by spincoating. Magnetic dextran films up to several micrometers in thickness were deposited onto the pre-treated substrates by spin-coating from polymer/water solutions with 3000-6000 rpm. A solution with a polymer content of 20 wt% resulted in a film thickness of approximately 500 nm at 5500 rpm. The samples were dried in vacuum at 45 °C overnight and crosslinking was performed for 7-90 minutes with a Stratagene UV Stratalinker 2400 operating at 75 W with an emission maximum at 254 nm corresponding to 0.2 $Jcm^{-2}min^{-1}$.

UV-VIS Measurements: The UV-VIS measurements were performed with a UV-VIS (Perlin Elmer, L900) spectrometer. A teflon flow cell (d = 5 mm, V= 1 mL) with two quartz (PGO) windows, one of them coated with the composite hydrogel sample, was used. The flow during rinsing was controlled to 0.8 mL/min by a peristaltic pump (Ismatec, Reglo Digital).

The composite hydrogel samples were rinsed with PBS 150 mM (Sigma Aldrich) and pH 3 and pH 8 buffers with a concentration of 10 mM. The buffers were composed of

1.25 mM citric acid, 1.25 mM KH_2PO_4, 1.25 mM Na_2HPO_4, 1.25 mM tris-(hydroxymethyl)-aminomethane and 1.25 mM KCl were dissolved in ultrapure water and the pH was controlled by adding HCl or NaOH.

3.3.6 Bibliography

[1] S. Mornet, S. Vasseur, F. Grasset, E. Duguet, *J. Mater. Chem.* **2004**, *14*, 2161.

[2] U. Schillinger, T. Brill, C. Rudolph, S. Huth, S. Gersting, F. Krötz, J. Hirschberger, C. Bergmann, C. Plank, *J. Magn. Magn. Mater.* **2005**, *293*, 501.

[3] L. Frank, C. Lebreton-Decoster, G. Godeau, B. Coulomb, J. Jozefonvicz, *J. Biomater. Sci. Polymer Edn.* **2006**, *17*, 499.

[4] N. A. Peppas, P. Bures, W. Leobandung, H. Ichikawa, *European Journal of Pharmaceuticals and Biopharmaceuticals* **2000**, *50*, 27.

[5] N. A. Peppas, Y. Huang, M. Torres-Lugo, J. H. Ward, J. Zhang, *Annu. Rev. Biomed. Eng* **2000**, *2*, 9.

[6] B. Johnsson, S. Loefas, G. Lindquist, *Anal. Biochem.* **1991**, *198*, 268.

[7] R. L. Rich, D. G. Myszka, *J. Mol. Recognit.* **2007**, *20*, 300.

[8] D. J. Winzor, *Anal. Biochem.* **2003**, *318*, 1.

[9] S. Löfas, M. Malmqvist, I. Roennberg, E. Stenberg, B. Liedberg, I. Lundstroem, *Sensors and Actuators B* **1991**, *5*, 79.

[10] R. Karlsson, A. Faelt, *J. Immunol. Methods* **1997**, *200*, 121.

[11] S. Löfas, *Pure & Appl. Chem.* **1995**, *67*, 829.

[12] G. Filipcsei, I. Csetneki, A. Szilagyi, M. Zrinyi, *Adv. Polym. Sci.* **2007**, *206*, 137.

[13] A. N. Shipway, I. Willner, *Chem. Commun.* **2001**, *20*, 2035.

[14] N. S. Satarkar, J. Z. Hilt, *Acta Biomaterialia* **2008**, *4*, 11.

[15] D. Hora'k, M. Babic', H. Makova', M. J. Benes', *J. Sep. Sci.* **2007**, *30*, 1751.

[16] T. Gelbrich, M. Feyen, A. M. Schmidt, *Macromolecules* **2006**, *39*, 3469.

[17] D. W. Inglis, R. Riehn, R. H. Austin, J. C. Sturm, *Appl. Phys. Lett.* **2004**, *85*, 5093.

[18] A. H. Latham, M. E. Williams, *Accounts of Chemical Research* **2008**, *41*, 411.

[19] Y.-Y. Liang, L.-M. Zhang, W. Jiang, W. Li, *Chem. Phys. Chem* **2007**, *8*, 2367.

[20] S. Bhattacharya, F. Eckert, V. Boyko, A. Pich, *Small* **2007**, *3*, 650.

[21] J. K. Oh, R. Drumright, D. J. Siegwart, K. Matyjaszewski, *Prog. Polym. Sci.* **2008**, *33*, 448.

[22] V. Thomas, M. Namedo, Y. M. Mohan, S. K. Bajbai, M. Bajpai, *J. Macromol. Sci. A* **2008**, *45*, 107.

[23] M. Baghi, M. G. Mack, M. Hambeck, J. Rieger, T. Vogl, W. Gstoettner, R. Knecht, *Anticancer Res.* **2005**, *25*, 3665.

[24] J. Xie, J. Huang, X. Li, S. Sun, X. Chen, *Current Medicinal Chemistry* **2009**, *16*, 1278.

[25] L. F. Gamarra, W. M. Pontuschka, J. B. Mamani, D. R. Cornejo, T. R. Oliveira, E. D. Vieira, A. J. Costa-Filho, E. A. Jr, *J. Phys.: Condens. Matter* **2009**, *21*, 115104(6pp).

[26] A. K. Gupta, M. Gupta, *Biomaterials* **2005**, *26*, 3995.

[27] A. Ito, Y. Kuga, H. Honda, H. Kikkawa, A. Horiuchi, Y. Watanabe, T. Kobayashi, *Cancer Lett.* **2004**, *212*, 167.

[28] D. Horák, M. Babic, H. Maková, M. J. Benes, *J. Sep. Sci.* **2007**, *30*, 1751.

[29] H. Pardoe, W. Chua-anusorn, T. G. S. Pierre, J. Dobson, *Journal of Magnetism and Magnetic Materials* **2001**, *225* 41.

[30] X. Q. Xu, H. Shen, J. R. Xu, J. Xu, X. J. Li, X. M. Xiong, *Applied Surface Science* **2005**, *252*, 494.

[31] L. L. Beecroft, C. K. Ober, *Chem. Mater.* **1997**, *9*, 1302.

[32] S. Nath, C. Kaittanis, V. Ramachandran, N. S. Dalal, J. M. Perez, *Chem. Mater.* **2009**, *21*, 1761.

[33] A. Z. Pich, H.-J. P. Adler, *Polym. Int.* **2007**, *56*, 291.

[34] Y. M. Mohan, K. Lee, T. Premkumar, K. E. Geckeler, *Polymer* **2006**, *48*, 158.

[35] L. Raymond, J. F. Revol, D. H. Ryan, R. H. Marchessault, *Chem. Mater.* **1994**, *6*, 249.

[36] V. Thomas, M. M. Yallapu, B. Sreedhar, S. K. Bajpai, *J. Appl. Polym Sci.* **2009**, *111*, 934.

[37] R. Fuhrer, E. K. Athanassiou, N. A. Luechinger, W. J. Stark, *Small* **2009**, *5*, 383.

[38] N. A. D. Burke, H. D. H. Stöver, F. P. Dawson, *Chem. Mater.* **2002**, *14*, 4752.

[39] W. C. Jiang, J. J. Yao, X. L. Gong, L. Chen, *Chin. J. Chem. Phys.* **2008**, *21*, 87.

[40] K. C. Souza, G. Salazar-Alvarez, J. D. Ardisson, W. A. Macedo, E. M. B. Sousa, *Nanotechnology* **2008**, *19*, 185603.

[41] J. Wotschadlo, T. Liebert, T. Heinze, K. Wagner, M. Schnabelrauch, S. Dutz, R. Mueller, F. Steiniger, M. Schwalbe, T. C. Kroll, K. Hoeffken, N. Buske, J. H. Clement, *Journal of Magnetism and Magnetic Materials* **2009**, *321*, 1469.

[42] S. Mornet, J. Portier, E. Duguet, *Journal of Magnetism and Magnetic Materials* **2005**, *293*, 127.

[43] Y. S. Kang, S. Risbud, J. F. Rabolt, P. Stroeve, *Chem. Mater.* **1996**, *8*.

[44] M. Mikhaylova, D. K. Kim, N. Bobrysheva, M. Osmolowsky, V. Semenov, T. Tsakalakos, M. Muhammed, *Langmuir* **2004**, *20*, 2472.

[45] R. Huynh, F. Chaubet, J. Jozefonvicz, *Angew. Makromol. Chem.* **1998**, *254*, 61.

[46] J. P. Jolivet, R. Massart, J. M. Fruchart, *Nouv. J. Chim.* **1983**, *7*, 325.

[47] R. Massart, *IEEE Trans. Magn.* **1981**, *17*, 1247.

[48] J. Fresnais, C. Lavelle, J.-F. Berret, *J. Phys. Chem. C* **2009**, *113*, 16371.

3.4 Modification of a Dextran-Based Hydrogel for Cell Adhesion

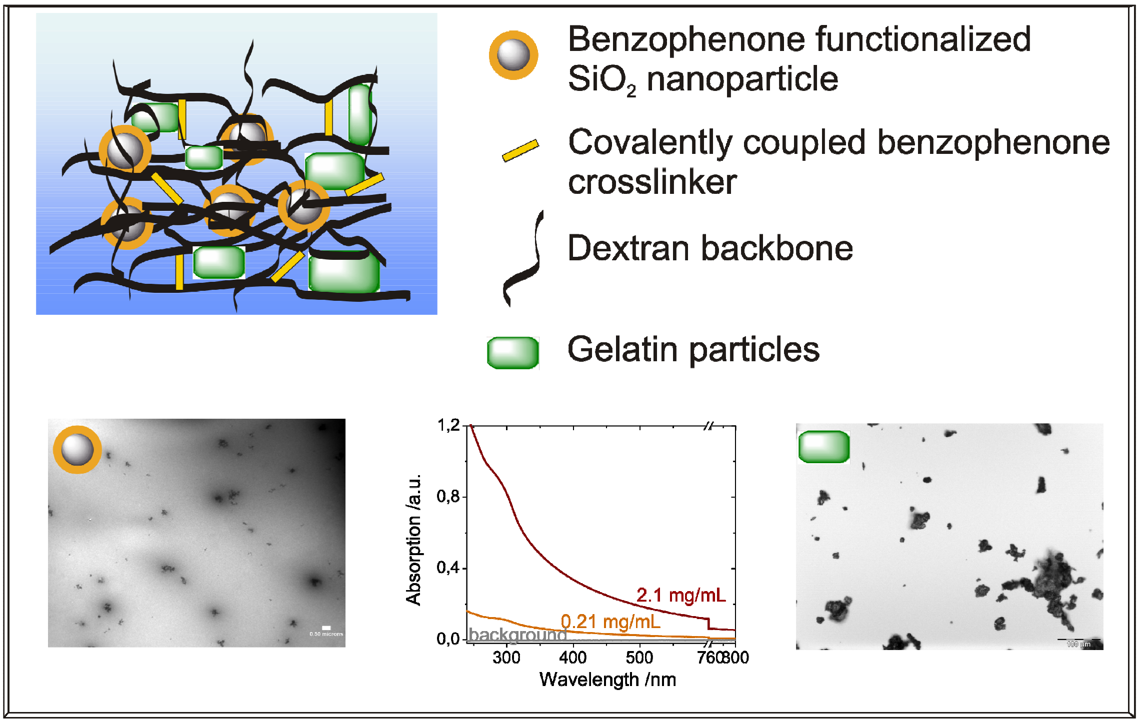

Hydrogel scaffolds are promising candidates for cell growth with potential applications in bone regeneration or wound healing. To permit cell attachment and cell growth the mechanical strength as well as the pore size of the hydrogel matrix has to be optimized. Furthermore, the possibility of introducing growth factors or other biomolecules is a desirable feature. Here, the preparation of a hydrogel matrix for potential applications in tissue engineering is presented.

3.4.1 Introduction

Hydrogels are widely used for cell attachment and cell growth[1-4] as well as to prevent cell growth on surfaces.[5, 6] Various types of hydrogels are reported to be used for cell attachment and cell growth. Synthetical polymers are for example acrylate-based or poly(ethyleneglycol)-based polymers.[1, 6-8] For these materials the crosslinking method can be varied from chemical crosslinking to photo-crosslinking.[9] An advanced method for the generation of pores adequate for cell migration is the sphere template technique applied for poly(HEMA)-based hydrogels for example.[6]

Nanocomposite hydrogels are unique materials combining the benefits of a hydrogel matrix with special properties of certain nanoparticles. These materials are especially investigated in terms of structural reinforcement.[10, 11] Various hydrogel nanocomposites have been reported in the literature. Depending on the gel and on the nanoparticle properties the characteristics can be tuned and responsive behavior can be introduced. Nanocomposites of hydrogels with gold nanoparticles allow solvent-switchable electronic properties[12] and optical pH-sensing.[13] Furthermore, responsive hydrogels have been combined with polystyrene colloidal crystals,[14] for application in metal-ion sensors,[15] for example.

For applications in vivo, biodegradable hydrogels are desirable.[16] Gel degradation within these polymers can be tailored by varying length and chemistry of the hydrolytic labile groups such as poly(lactic acid) (PLA) for example or by incorporating enzyme cleavable groups like peptide sequences within the crosslinker.[17-19] Besides synthetic polymers, natural polymers like peptides or polysaccharides can be used.[20] Within this class of materials agarose,[21] chitosan,[22, 23] collagen.[24] alginate,[25] gelatin,[26] or dextran[1, 27] are versatile materials. Dextran-based systems are for example reported to be crosslinked with peptides to create an enzymatically degradable matrix for cell growth.[28] Furthermore, the combination of different polymers is applied to tune their properties.

The spreading of cells requires pores with a size in the range of several micrometers to allow cells to penetrate into the hydrogel. On the other hand, a certain density of the hydrogel matrix is necessary to allow cell adhesion to the hydrogel. Consequently, the swelling degree has to be optimized with respect to maximum pore size and required mechanical strength.[29]

The interaction of cells with polymers are governed by a variety of factors, including biophysical (degree of hydrophilicity and hydration), chemical (functional groups), mechanical properties, and topography.[30]

The following criteria have to be fulfilled to create a scaffold for cell growth:[31, 32]

- a surface that promotes cell growth
- biocompatibility of the matrix and the degradation products
- biodegradability
- a porosity that is high enough for cell penetration and allows homogeneous tissue formation
- mechanical strength

Approaches to control cell growth by surface modification included silane-based chemistry,[33, 34] electrostatic interations,[35] and plasma treatment.[36]

As further developments the hydrogels can be modified with bioactive molecules. For example, growth factors like RGD sequences or sacrificial substances like gelatin or collagen can be used for hydrogel modification. Adhesive peptide sequences interact with receptors on the cell surface in order to mediate cell adhesion and spreading. Whereas gelatin can be digested by cells and thus facilitates cell growth and simultaneously enables a degradation of the matrix.[6, 37-41] The incorporation of gelatin provided cell adhesive and enzymatically degradable properties and simultaneously led to a significantly increased compressive modulus and strength.[42]

Dextran is hydrophilic, biocompatible, and can be degraded through dextranase in various organs in the human body.[8] The methacrylation of dextran for example leads to biodegradable and biocompatible hydrogels.[43, 44] Recently, the preparation of interpenetrating networks of dextran-based polymers and gelatin, as another promising approach to create 3-dimensional matrices for cell growth, was reported.[42] Thereby, the dextran component was characterized to induce elastic properties superior to those reported for PEG-based hydrogels.

In the following chapter, the modification of the dextran-based and photo-crosslinkable hydrogel matrix for the growth of osteoblasts and endothelial cells is reported.

3.4.2 Dextran-Based Hydrogels with Enhanced Mechanical Stability

For the preparation of mechanically denser but still porous networks a two-component crosslinking approach was developed. The benzophenone photo-crosslinkable dextran-based hydrogels described in Chapter 3.1 are used as highly swelling porous basic material. To achieve structural reinforcement super-crosslinkers were introduced that consist of nanoparticles, functionalized with benzophenone as multiple photo-crosslinking unit. With this strategy the porous hydrogel structure is maintained between the crosslinking benzophenone-functionalized nanoparticles (Figure 3.4.1) Simultaneously, the mechanical strength of the matrix is enhanced leading to improved cell adhesion (Chapter 4.6). The use of super-crosslinkers in a highly swelling hydrogel matrix seems to be superior to alternatives. The alternative of using a bi-functionalized crosslinker molecule is expected to be less effective due to the expected lower solubility of a bi-functionalized benzophenone derivative in water and the limitation to only two directly linked benzophenone units. In addition, the crosslinking is expected to be more continuous resulting in smaller pore sizes as compared to the crosslinking by a lower amount of super-crosslinkers. With an identical overall amount of benzophenone units the crosslinking molecules are expected to be more localized allowing bigger pores to be created in the interstitials. Another option might be a dendrimer-like structure carrying benzophenone moieties. The synthesis is complex compared to the nanoparticle approach. However, the introduction of super-crosslinking benzophenone functionalized nanoparticles revealed strong mechanical reinforcement of the PCMD hydrogels.

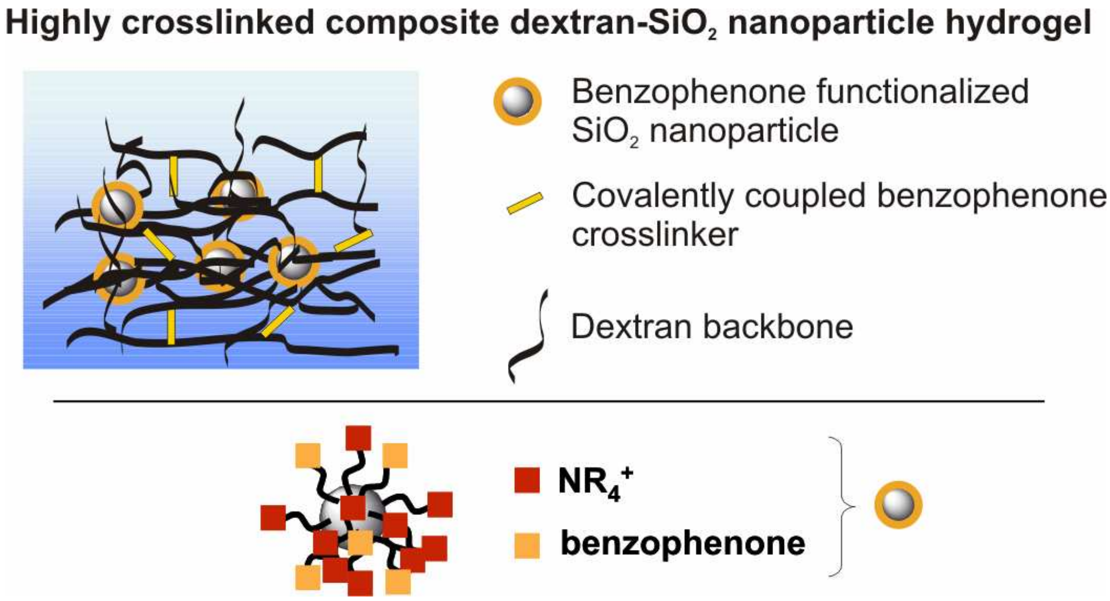

Figure 3.4.1: *Scheme of the two component photo-crosslinked hydrogel matrix for cell adhesion.*

The introduction of more benzophenone molecules into the dextran backbone would result into a less hydrophilic hydrogel and into smaller pores upon crosslinking which is disadvantageous for subsequent cell growth applications. Thus, the application of crosslinker-functionalized nanoparticles as crosslinking centers seems to be a versatile approach for the fabrication of mechanically more stable but still highly porous scaffolds.

Nanoparticles as Second Component Super-Crosslinker

The benzophenone-functionalized nanoparticles (NP's) were prepared by Coenraad van den Brom at the Max Planck Institute for Polymer Research.[11] The method for the silicon oxide nanoparticle synthesis was adopted from Giesche *et al.*,[45] applying conditions that lead to 40 nm diameter SiO_2-particles. These particles were subsequently functionalized with benzophenonetriethoxysilane (BPTES) and *N*-(trimethoxysilylpropyl)-*N*,*N*,*N*-trimethylammonium chloride (NR_4^+) and passivated with hexamethyldisilazane (HMDS). The degree of benzophenone functionalization was kept low at a ratio of approximately NR_4^+ : BPTES = 10:1 by adjusting the ratio in the reaction mixture to NR_4^+ : BPTES = 1:0.65 taking into account the different reactivities. With this ratio the water solubility of the particles is maintained. The nanoparticles were subsequently transferred into an aqueous dispersion by centrifugation and redispersion. In the following the nanoparticles were characterized in terms of size, separation and degree of functionalization. Comparing SEM samples of the latest decantate and the latest precipitated NPs after cleaning both have a very similar appearance (Figure 3.4.2 A, B).

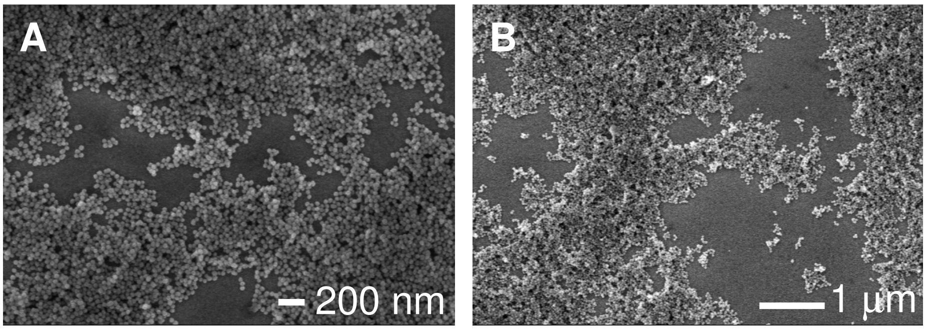

Figure 3.4.2: *SEM images of NR_4^+/BPTES-coated SiO_2 NPs.* ***A)*** *NPs from the most concentrated fraction used for subsequent experiments and* ***B)*** *NPs obtained from the latest supernatant after cleaning by centrifugation and re-dispersion in fresh solvent.*

The particle diameter was determined to be R = 45 nm (± 4 nm). To evaluate the hydrodynamic radius of the particles dynamic light scattering (DLS) was performed with a filtered 6.5 wt% solution. The average hydrodynamic radius (R_h) obtained by DLS was dependent on the angle at which it was measured as can be seen in Figure 3.4.3. The angular dependence is an effect of the particle size distribution: For larger objects the scattered intensity decreases stronger as a function of angle than for smaller objects.[46] The obtained radii are clearly larger than those obtained by SEM (45 nm). The average number of particles in an aggregate (*n)* can be qualitatively estimated from the hydrodynamic volume (V_h) (equation 3.4.1)

$$n \approx V_h / V_{\mathrm{NP}} \mathrel{\hat{=}} R_h^3 / R_{NP}^3 \qquad (3.4.1)$$

assuming that the aggregates are sufficiently spherical for the Stokes-Einstein relation to be still valid. Furthermore, assuming that the hydration shell of the particles is small compared to their diameter (i.e. R_{NP} = 45 nm) leads to an aggregate size of about 13-28 NPs. As large particles are generally much stronger scatterers than small particles ($I \propto r^6$), the relatively strong angular dependence implies that there must be smaller particles as well. Because small aggregates are not expected to be a problem in for their subsequent application as super-crosslinkers they were used without further purification.

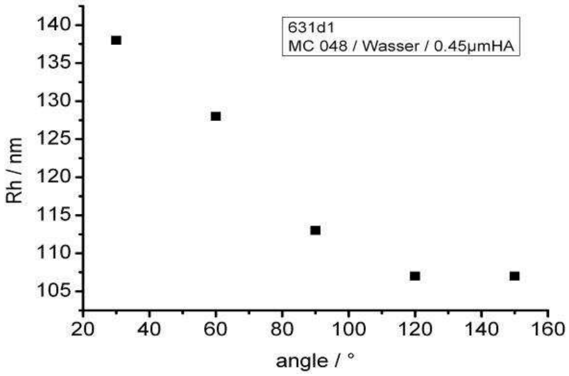

Angle / °	Z_{ave} / *nm*
30	138
60	128
90	113
120	107
150	107

Figure 3.4.3: *Hydrodynamic radius R_h measured for an aqueous dispersion of benzophenone-modified SiO_2 NP's.*

To estimate the amount of benzophenone attached to the nanoparticles, UV-VIS spectra of the nanoparticles in water were recorded at different concentrations. The spectra for 2.1 and for 0.21 mg/mL are depicted in Figure 3.4.4.

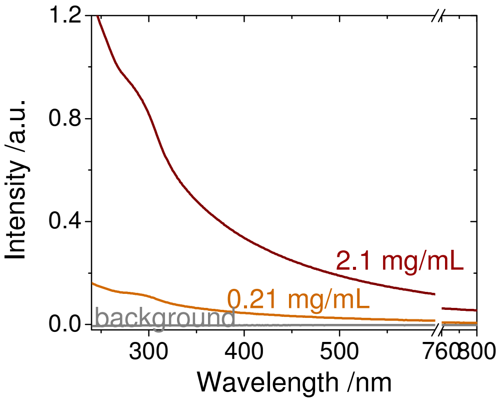

Figure 3.4.4: *UV-VIS spectra of the benzophenone modified SiO_2 nanoparticles in water at a concentration of 2.1 mg/mL and at 0.21 mg/mL.*

By comparing the benzophenone absorption at 300 nm with the concentration dependent absorption of the pure benzophenone derivative (BPTES) in chloroform[11] the degree of benzophenone attachment can be estimated to approximately $5*10^{-14}$ mol BPTES per mg functionalized particles.

Dextran Hydrogel Silica Nanoparticle Composite Formation

The preparation of a composite SiO_2 nanoparticle dextran hydrogel material was carried out by mixing the pre-synthesized PCMD polymer and the pre-synthesized benzophenone modified silica-nanoparticles. A comparable strategy was already applied to synthesize a magnetic composite hydrogel (Chapter 3.3). The PCMD hydrogel was dissolved in destilled water at concentrations of 0.1 g/mL or 0.2 g/mL and the aqueous suspension of nanoparticles was added under extensive shaking. Suspensions with 5, 10 and 20 wt% nanoparticles were prepared. The composite suspension was concentrated to 0.1-0.2 g/mL polymer and samples for cell adhesion experiments were prepared. TEM images of the hybrid material revealed that small nanoparticle aggregates were formed. The amount and size of aggregates is relatively low with clusters of < 20 particles for a particle content of 5 wt% and increases slightly with increasing nanoparticle content from 5-20 wt%. The aggregate formation can be explained by "bridging" and "depletion" effects as discussed more detailed in Chapter 3.3. In addition, the partly hydrophobic particle surface due to the benzophenone functionalization has to be taken in to account. Although, the degree of functionalization is low in order to conserve their dispersion in water. It is expected to achieve a reduced aggregation upon optimization of the mixing conditions. For example, a reduced concentration of the polymer solution and a slower addition should result into less aggregation.

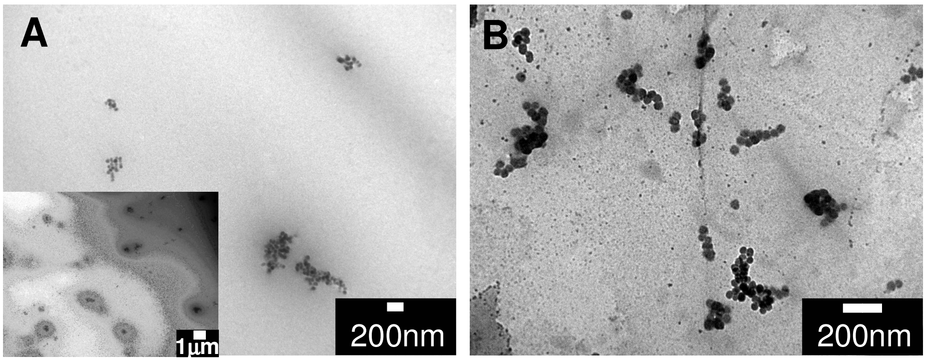

Figure 3.4.5: *TEM images of the benzophenone modified SiO_2 NP's in the polymer composite environment for a 5 wt% **(A)** and a 10 wt% **(B)** solution. The increasing aggregate formation is clearly visible.*

These aggregates are not expected to form a problem in the further processing of the sample and should serve as multiple crosslinking points as well. During the photo-crosslinking process the benzophenone should covalently bind the nanoparticles inside a cluster and simultaneously, the cluster is covalently coupled to the surrounding dextran polymer.

For the cell growth expermiments a petri dish (diameter = 3 cm) was treated with oxygen plasma (60 W, 0.2 mbar, 5 min) to create a more hydrophilic surface and thus enhance the wettability of these surfaces for the highly hydrophilic dextran-based polymer. The concentrated composite hydrogel suspension was dropcasted onto the surface and the solvent was evaporated over night at room temperature and atmospheric pressure. Subsequently, the matrices were crosslinked by irradiation with UV-light at

254 nm for one hour achieving sterilization simultaneously. The irradiation thereby induces three processes:

I) the crosslinking with the benzophenone units chemically bound to the dextran backbone

II) the multiple crosslinking with the benzophenone-functionalized silica nanoparticles

III) the surface attachment in case of a polymer composite film on a benzophenone monolayer-modified substrate (SPR/OWS characterization).

Because structuring of the matrix creates three dimensional textures that might be beneficial for cell adhesion, the crosslinking process was performed with three different approaches. 1/3 of the Petri dish area was crosslinked through a µm-grating-mask (Figure 3.4.10), 1/3 of the petri dish area was structured with a macroscopic grating produced by scratching with a sterile needle, and 1/3 of the area was left as prepared. Examples of the hydrogel matrices as seen in the microscope are shown in Figure 3.4.6.

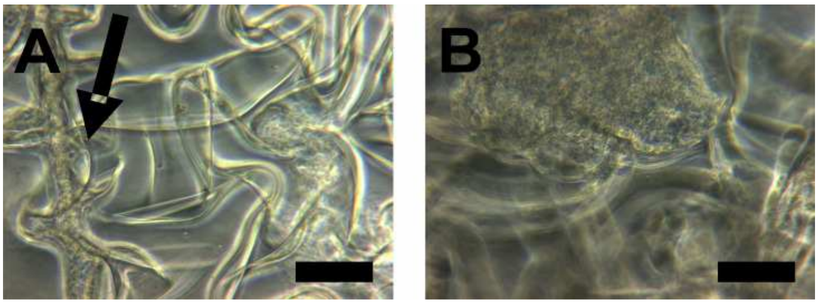

Figure 3.4.6: *Microscope images of swollen hydrogel matrices (10 wt% SiO_2 NP's). The unmodified hydrogel surface (**B**) as well as the structuring with a sterile needle (**A**, black arrow) is shown. Structures induced by photo-crosslinking through a µm-grating-mask can not be resolved (scalebar = 100 µm).*

3.4.3 Gelatin-Dextran Composite Hydrogels

An alternative strategy to facilitate cell growth inside the hydrogel matrix is the introduction of gelatin, which can be digested by cells and thus can serve as spacer for cell growth and as cell attracting agent simultaneously. Gelatin was introduced either as macroscopic pestled powder with a polydisperse particle size in the range between several up to hundred micrometers or as polydisperse nanoparticles (Figure 3.4.7/ 3.4.8).

Gelatin Preparation

Gelatin powder was purchased from Sigma Aldrich and pestled to create particles with a size in the micrometer range (Figure 3.4.7). The particles are stable in cold water based solutions up to temperatures of approximately 50 °C. At higher temperatures they dissolve. Therefore, it is important to keep the temperature during the entire preparation process at room temperature. Single chains dissolving even at low temperatures are not expected to resemble a problem in subsequent cell growth applications.

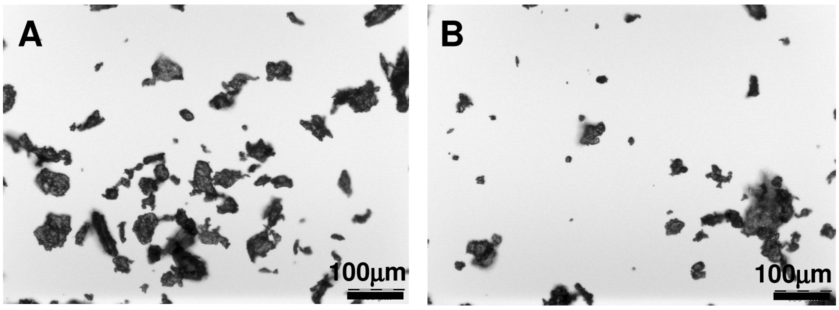

Figure 3.4.7: *Optical micrographs of pestled gelatin. The polydisperse particle size between several micrometers to approximately hundred micrometers is clearly visible.*

To investigate the influence of the size of gelatin inside the hydrogel smaller gelatin particles in the nanometer range were prepared. To this end, gelatin was dissolved in water at 70°C and precipitated into ice-cold acetone.[47] The suspension was subsequently dialyzed against water at room temperature and the gelatin nanoparticles were characterized by DLS measurements (Figure 3.4.8 A). A bimodal size distribution was determined by DLS at 90º: one with a maximum at 85 nm and a second one around 540 nm. The particles with a size around 540 nm can be attributed to bigger particles or more likely to aggregate formation. Because monodisperse particles are not necessary for cell adhesion experiments and polydisperse gelatin particles might be beneficial the particles were used without further purification. The gelatin is invisible in the TEM (Figure 3.4.8 B).

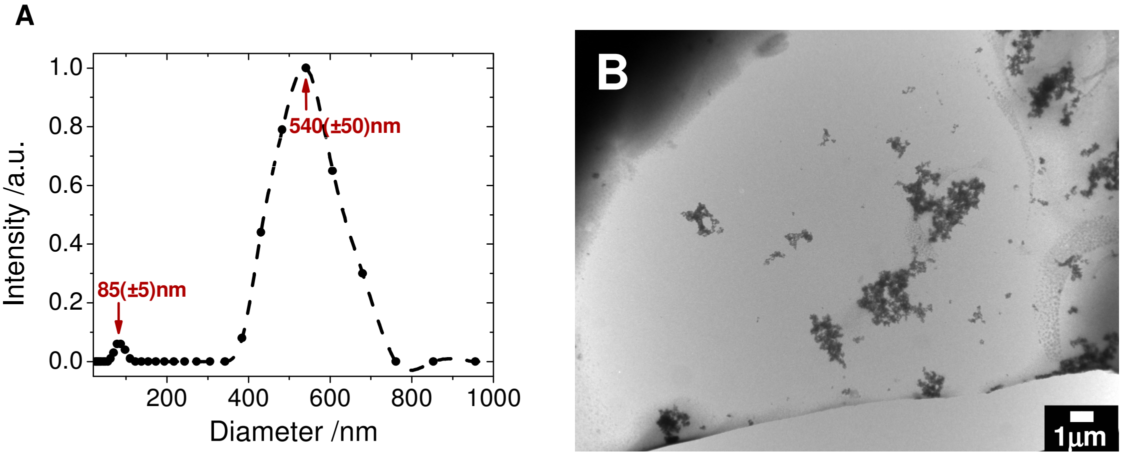

Figure 3.4.8: *A) DLS results* (90 °) *for the gelatin nanoparticles and* ***B)*** *TEM image of a dextran-silica super-crosslinker (10%)-gelatin nanoparticle (10%) composite. The polymer components are not visible.*

The silica particles seem to form even bigger aggregates (compare Figure 3.4.5 B) after gelatin addition and repeated concentration of the composite suspension.

Gelatin Dextran Composite Preparation

Because gelatin is only water-soluble at temperatures higher than 50°C it can be mixed with the water based dextran polymer solution without dissolving. In this way, gelatin centers of various sizes can be generated inside the hydrogel matrix. To create gelatin-dextran hydrogel composite materials either the pestled gelatin was added to the pure dextran polymer solution or to the dextran polymer-silica nanoparticle suspension. The gelatin nanoparticles were added as suspension in water (c ~ 4mg/mL) either to the pure PCMD polymer water solution or to the PCMD-silica nanoparticle suspension. The solution was concentrated to 0.1-0.2 g/mL at reduced pressure. Heating was avoided to prevent the gelatin from dissolving. Afterwards the suspensions were dropcasted onto a oxygen plasma pre-treated petri dish as already described for gelatin-free matrices followed by structuring and crosslinking as described above as well. Representative hydrogel surfaces are summarized in Figure 3.4.9.

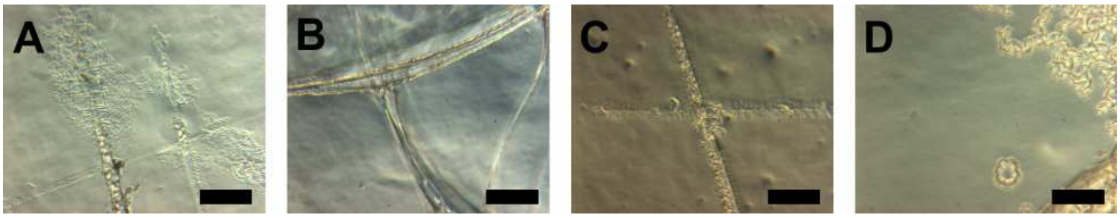

Figure 3.4.9: *Microscope images of the gelatin containing composite PCMD matrix. The linear structures visible in A, B, C are introduced with a sterile needle. The composition varies:* ***A)*** *10 wt% SiO_2 NP's and 10 wt% gelatin NP's* ***B)*** *10 wt% SiO_2 NP's and 10 wt% gelatin pestled,* ***C)*** *20 wt% SiO_2 NP's and 10 wt% geltin pestled,* ***D)*** *10 wt% SiO_2 NP's and 20 wt% gelatin pestled. The surfaces are comparable for all different composite materials. The scalebar represents 100 μm.*

These hydrogel matrices where tested for cell growth experiments as discussed in Chapter 4.6. All matrices were prepared with a thickness resulting in a swollen thickness in the range of hundrets of micrometers. For these thick matrices, stable surface attachment could not be achieved by a benzophenone terminated self-assembled monolayer as adhesion layer. This is in agreement to the stability experiments discussed for the PCMD hydrogel matrix in Chapter 3.1. Thus, the prepared matrices where used without being covalently attached to the petri dish.

3.4.4 Conclusion and Outlook

The dextran-based PCMD hydrogel introduced in Chapter 3.1 and 4.1 was optimized to serve as scaffold material for cell growth. For this purpose, benzophenone-modified

SiO_2 nanoparticles were successfully introduced as multiple crosslinking units. Although these particles tend to form small aggregates, this should not limit their potential as crosslinking component. Higher crosslinking leads to structural reinforcement which is necessary to allow cell attachment due to the high swelling degrees of the PCMD hydrogel. To create pores and simultaneously attract cells gelatin was used as sacrificial material. The preparation procedure of the composite material is fast and easy and the matrix only consists of natural polymers. Furthermore, structuring of the matrix can be achieved relatively easy by using appropriate masks due to the light-induced crosslinking reaction. Possible improvements can be achieved in the surface attachment for this type of millimeter thick films. This might be optimized by plasma modification of the surface with allylamine[48] and further covalent attachment of benzophenone-derivatives. These matrices were applied for cell growth experiments (Chapter 4.6) and further optimization of the composition as well as further optimization of the size and crosslinking are desirable.

3.4.5 Experimental

Dextran-Based Hydrogel (PCMD): For the hydrogel synthesis, the commercially available dextran (Sigma Aldrich, M_r = 2.000.000) was carboxymethylated, followed by the introduction of 4-aminomethylbenzophenone via active ester chemistry as described in Chapter 3.1. The degree of benzophenone substitution was determined by ^{1}H-NMR in D_2O to be d_s =0.09 and the degree of carboxymethylation to be d_s = 0.30 for the PCMD hydrogel used here.

Benzophenone-Modified Silica Nanoparticles: SiO_2 nanoparticles were prepared by Coenraad van den Brom[11] following a method adapted from Giesche *et al.* [49], using the Stoeber process.[50] A stock solution of tetraethylorthosilicate (TEOS, 98%, Acros, destilled before use) (0.14 M) in ethanol (5 ml) was diluted with ethanol (20 ml), warmed to 60 °C and added to a stirred mixture of aqueous ammonia (0.86 M, 10 ml) and ethanol (125 ml) in a reactor flask kept at 60 °C. The mixture was stirred overnight at 60 °C and became slightly turbid. The crude reaction mixture was used in the following experiments without intermediate workup (in order to prevent coalescence/aggregation of the NPs).

***Surface Functionalization*:** To 50 ml of the crude SiO_2 mixture – transferred into a round-bottom flask with stirrer – was added 33 ml of DMSO. A premixed solution of 470 mg of a 50% solution of *N*-(trimethoxysilylpropyl)-*N*,*N*,*N*-trimethylammonium chloride (NR_4^+) in methanol (0.9 mmol) with 3.2 g of a BPTES stock solution in EtOH (0.6 mmol), (yielding a ratio of NR_4^+ / BPTES = 1:0.65) was than added. A functionalization ratio of NR_4^+ / BPTES = 10:1 should be achieved taking into account the diffrence in reactivity between trimethoxy- and triethoxysilanes. After stirring for 22 hours at RT 0.5 ml HMDS was added and the mixture was stirred for another 12 hours. The material was divided into three fractions and centrifuged for 45 minutes at 6000 rpm (RCF = 3904g) at 20°C. The supernatant was decanted and the precipitate was easily redispersed in water/EtOH (1:1) (3×20 ml) with some shaking. Centrifugation at 6000 rpm for 45 minutes at 20°C led to a good separation. The supernatant was decanted and the material was redispersed in 3×20 ml water/EtOH by vigorous shaking for 5 minutes and some sonication. The turbid suspension was centrifuged at 2000 rpm for 30 minutes. After decanting, the material was redispersed in 3×23 ml water by shaking for 5 minutes, 1 minute of sonication and an additional minute of shaking. A more concentrated batch was prepared by transferring one batch of material into a clean centrifuge tube and centrifugation at 2000 rpm for 30 minutes. Most of the still somewhat turbid supernatant was decanted. The deposit was easily redispersed in the remaining liquid by combined sonication and shaking for about 1 minute. This concentrated dispersion had a dry matter content of ca 6.5%.

SEM samples of both the concentrated dispersion and the latest decantate were prepared by placing a droplet of liquid on a siliciumi wafer and blotting it off with filtration paper. A Gemini field emission electron microscope (Zeiss), equipped with an InLense detector was used.

Gelatin Nanoparticles_were prepared by precipitation of gelatin in acetone. 0.5 g of gelatin were dissolved in 10 mL of water by heating up to 70 °C. After complete dissolution the gelatin was precipitated in ice-cold acetone (80 mL). A turbid nanoparticle suspension is prepared which is dialyzed against water at room temperature afterwards.

Dextran-Silica Composites were prepared by dropping the benzophenone modified SiO_2 nanoparticles water suspension (c ~ 0.6 mg/mL) into a water based solution of the PCMD polymer (c = 0.2 g/mL) to get a SiO_2 fraction of 5, 10, 15, or 20 wt%. The mixture was concentrated up to 0.1 – 0.2 g/mL (referred to the PCMD fraction) under reduced pressure and a temperature of 45 °C.

Dextran-Gelatin Composites: Gelatin was either used as pestilled particles with a pore size in the range of micrometers or as nanoparticles. The composite was prepared by simple mixing of both components. Pestilled gelatin was added with a fraction of 5 (5 mg), 10 (10 mg), and 20 (20 mg) wt % to a 0.1 g PCMD containing water-based solution of V€= 1 mL. Gelatin nanoparticles were added as aqueous suspension (c ~ 4 mg/mL) to obtain a gelatin content of 5 – 20 wt%. In case a three component system with the PCMD polymer, SiO_2 particles and gelatin was prepared, gelatin was added as the last component to the concentrated PCMD-SiO_2 composite material. The PCMD-gelatin nanoparticle mixture was concentrated under reduced pressure at room temperature to prevent the dissolution of the gelatin.

Hydrogel Formation: To create three dimensional textures that the UV-crosslinking process was performed using three different approaches. 1/3 of the petri dish area was crosslinked through the two µm-grating-mask (Figure 3.4.10), 1/3 of the petri dish area was structured with a macroscopic grating produced by scratching with a sterile needle, and 1/3 of the area was left as prepared.

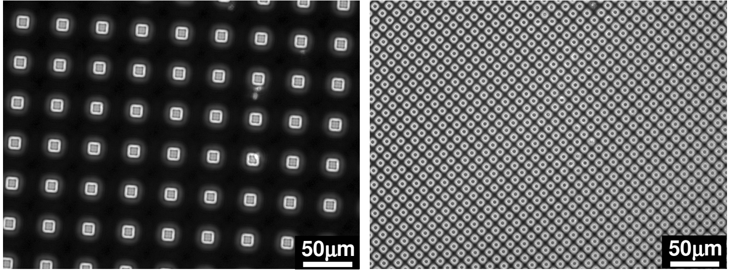

Figure 3.4.10: *Two areas of the mask used for structuring the hydrogel matrix during the photo-crosslinking process.*

Microscope: The microscope pictures of the pestled gelatin and the mm-grating mask were recorded with a 20x lens in an Olympus IX70.

DLS: The particle size measurements of gelatin nanoparticles were performed by DLS using a Submicron Particle Sizer Nicomp 380 (Nicomp, USA). Dynamic light scattering measurements were performed using a ALV/CGS3 Compact Goniometer System, with He/Ne Laser (632.8 nm), ALV/LSE-5004 Correlator and ALV5000 software at various angles (30°, 60°, 90,°120°,150°). R_h was calculated from the correlation data using a regularised fitting method. A 1 mg/ml dispersion of SiO_2 NPs in CHCl3 was prepared by combining appropriate amounts followed by sonication and simultaneous shaking for 5 minutes. The resulting dispersion was diluted down further and filtered 3 times using a 0.45µm PTFE filter.

***UV-VIS Measurements*:** The UV-VIS spectra were recorded with a UV-VIS/NIR (Perkin Elmer, Lambda 900) The measurement was carried out with an aqueous nanoparticle suspension in a quarz cuvette with d = 0.5 cm, a slit of 4 nm.

3.4.6 Bibliography

[1] M. R. Hynd, J. N. Turner, W. Shain, *J. Biomater. Sci. Polymer Edn.* **2007**, *18*, 1223.

[2] G. D. Nicodemus, S. J. Bryant, *Tissue Engineering: B* **2008**, *14*, 149.

[3] N. E. Fedorovich, J. Alblas, J. R. D. Wijn, W. E. Hennink, J. Verbout, W. J. A. Dhert, *Tissue Engineering* **2007**, *13*, 1905.

[4] J. L. Drury, D. J. Mooney, *Biomaterials* **2003**, *24*, 4337.

[5] Y. Yeo, C. B. Highley, E. Bellas, T. Ito, R. Marini, R. Langer, D. S. Kohane, *Biomaterials* **2006**, *27*, 4698.

[6] B. D. Ratner, S. J. Bryant, *Annu. Rev. Biomed. Eng.* **2004**, *6*, 41.

[7] W. H. Wong, D. J. Mooney, in *Synthetic biodegradable polymer scaffolds.* (Eds.: A. Atala, D. J. Mooney), Birkhäuser, Boston, **1997**, pp. 49.

[8] L. Ferreira, M. H. Gil, A. M. S. Cabrita, J. S. Dordick, *Biomaterials* **2005**, *26*, 4707.

[9] J. L. Ifkovits, J. A. Burdick, *Tissue Engineering* **2007**, *13*, 2369.

[10] D. R. Paul, L. M. Robeson, *Polymer* **2008**, *49*, 3187.

[11] C. v. d. Brom, I. Anak, R. F. Roskamp, M. Retsch, U. Jonas, B. Menges, J. A. Preece, *J. Mater. Chem.* **2010**, *submitted.*

[12] V. Pardo-Yissar, R. Gabai, A. N. Shipway, T. Bourenko, I. Willner, *Adv. Mater.* **2001**, *13*, 1320.

[13] I. Tokarev, I. Tokareva, S. Minko, *Adv. Mater.* **2008**, *20*, 2730.

[14] J. M. Weissmann, H. B. Sunkara, A. S. Tse, S. A. Asher, *Science* **1996**, *274*, 959.

[15] J. H. Holtz, S. A. Asher, *Nature* **1997**, *389*, 829.

[16] K. Y. Lee, D. J. Mooney, *Chem. Rev.* **2001**, *101*, 1869.

[17] A. S. Sawhney, C. P. Pathak, J. A. Hubbell, *Macromolecules* **1993**, *26*, 581.

[18] Y. D. Park, N. Tirelli, J. A. Hubbell, *Biomaterials* **2003** *24*, 893.

[19] J. L. West, J. A. Hubbell, *Macromolecules* **1999**, *32*, 241.

[20] N.-B. Thébaud, D. Pierron, R. Bareille, C. L. Visage, D. Letourneur, L. Bordenave, *J. Mater. Sci: Mater. Med.* **2007**, *18*, 339.

[21] P. D. Sawant, H. N. Achuth, S. M. Moochhala, *Biotechnol. J.* **2006**, *1*, 462.

[22] K. E. Crompton, J. D. Goud, R. V. Bellamkonda, T. R. Gengenbach, D. I. Finkelstein, M. K. Horne, J. S. Forsythe, *Biomaterials* **2007**, *28*, 441.

[23] J.-K. F. Suh, H. W. T. Matthew, *Biomaterials* **2000**, *21*, 2589.

[24] T. C. Flanagan, B. Wilkins, A. Black, S. Jockenhoevel, T. J. Smith, A. S. Pandit, *Biomaterials* **2006**, *27*, 2233.

[25] B. J. Willenberg, T. Hamazaki, F. W. Meng, N. Terada, C. Batich, *J. Biomed. Mater. Res. A* **2006**, *79*, 440.

[26] A. Hoshikawa, Y. Nakayama, T. Matsuda, H. Oda, K. Nakamura, K. Mabuchi, *Tissue Eng.* **2006**, *12*, 2333.

[27] L. S. Ferreira, S. Gerecht, J. Fuller, H. F. Shieh, G. Vuniak-Novakovic, R. Langer, *Biomaterials* **2007**, *28*, 2706.

[28] S. G. Lévesque, M. S. Shoichet, *Bioconjugate Chem.* **2007**, *18*, 874.

[29] T. V. Chirila, I. J. Constable, G. J. Crawford, S. Vijayasekaran, D. E. Thompson, Y.-C. Chen, W. A. Fletcher, B. J. Griffin, *Biomaterials* **1993**, *14*, 26.

[30] A. I. Teixeira, J. K. Duckworth, O. Hermanson, *Cell Res.* **2007**, *17*, 56.

[31] H. C. H. Ko, B. K. Milthorpe, C. D. McFarland, *European Cells and Materials* **2007**, *14*, 1.

[32] G. Chen, T. Ushida, T. Tateishi, *Macromol. Biosci.* **2002**, *2*, 67.
[33] J. M. Curran, R. Chen, J. A. Hunt, *Biomaterials* **2005**, *26*, 7057.
[34] G. A. Truskey, T. L. Proulx, *Biomaterials* **1993**, *14*, 243.
[35] J. Fukuda, A. Khademhosseini, J. Yeh, G. Eng, J. Cheng, O. C. Farokhzad, R. Langer, *Biomaterials* **2006**, *27*, 1479.
[36] G. Assero, C. Satriano, G. Lupo, C. D. Anfuso, G. Marletta, M. Alberghina, *Microvasc. Res.* **2004**, *68*, 209.
[37] E. H. Anderson, M. A. Ruegsegger, G. Murugesan, K. Kottke-Marchant, R. E. Marchant, *Macromol. Biosci.* **2004**, *4*, 766.
[38] K. H. Park, K. Na, H. M. Chung, *Biotechnol. Lett.* **2005**, *27*, 227.
[39] C. Wallace, J. T. Jacob, A. Stoltz, J. Bi, K. Bundy, *J. Biomed. Mater. Res. A* **2005**, *72*, 19.
[40] J. L. Drury, T. Boontheekul, D. J. Mooney, *J. Biomech. Eng.* **2005**, *127*, 220.
[41] D. L. Elbert, J. A. Hubbell, *Annu. Rev. Mater. Sci.* **1996**, *26*, 365.
[42] Y. Liu, M. B. Chan-Park, *Biomaterials* **2009**, *30*, 196.
[43] M. H. Lee, D. Boettiger, R. J. Composto, *Biomacromolecules* **2008**, *9*, 2315.
[44] C. J. D. Groot, M. J. A. V. Luyn, W. N. E. V. Dijk-Wolthuis, J. A. Cadée, J. A. Plantinga, W. D. Otter, W. E. Hennink, *Biomaterials* **2001**, *22*, 1197.
[45] H. Giesche, e. al., *J. Eur. Ceram. Soc.* **1994**, *14*, 189.
[46] W. Schärtl, *Light Scattering from Polymer Solutions and Nanoparticle Dispersions*, Springer, Berlin, **2007**.
[47] M. Jahanshahi, M. H. Sanati, Z. Minuchehr, S. Hajizadeh, Z. Babaei, *Nanotechnology and its applications, AIP Conference Proceedings* **2007**, *929*, 228.
[48] B. Yameen, *Dissertation* **2009**, *Johannes Gutenberg-Universität Mainz.*
[49] H. Giesche, *Journal of the European Ceramic Society* **1994**, *14*, 189.
[50] W. Stöber, A. Fink, E. Bohn, *Journal of Colloid and Interface Science* **1968**, *26*, 62.

4 *Results and Discussion*

4.1 Hydrogel Film Characteristic

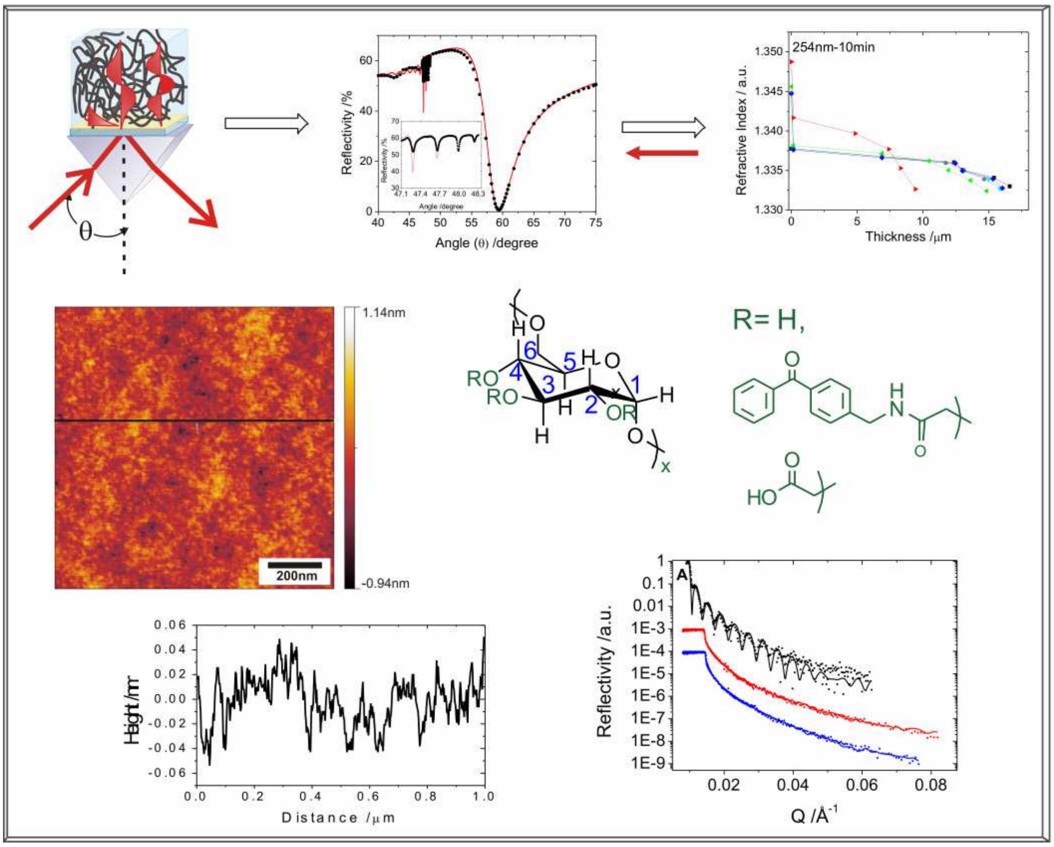

Hydrogel films are versatile structures for coatings in medicine or for sensor matrices. These applications require stable but highly swelling gels to allow the diffusion of species inside the hydrogel matrix. Furthermore, thick hydrogel films in the range of micrometers facilitate the guiding of leaky optical waveguide modes. Leaky optical waveguide modes enable a more detailed film characterization with respect to the refractive index and thickness perpendicular to the surface. So far poly(N-isopropylacryl amide) films were reported to be characterized according to their refractive index using optical waveguide mode spectroscopy. Apart from that, mainly thinner films in the range of tens to hundreds of nanometers, or macroscopic gels are discussed in the literature. Here, the film stability and its tuning by modification of "external" and "internal" parameters are reported. Furthermore, the swelling behavior for stable films in the range of up to 20 µm is discussed. Special emphasis is put on the manipulation of the swelling degree by variation of "external" parameters such as pH and its investigation with surface plasmon resonance (SPR) and optical waveguide mode (OWS) spectroscopy.

4.1.1 Introduction

Functionalized dextrans as described in Chapter 3.1 are expected to be versatile materials for biosensor applications.[1-4] In order to apply them as biosensor matrices their material and film characteristics have to be understood. For many interesting applications from sensing to medicine highly swelling hydrogels are desirable to allow the diffusion of molecules or antibodies or to permit cell growth. In the literature swelling degrees are mainly related to a weight increase upon water uptake and are calculated by dividing the weight of the swollen hydrogel by the weight of the dry hydrogel.[5, 6] Swelling degrees of 1.5 for a mixed hydrazide-modified carboxymethyldextran/ aldehyde-modied dextran[5] and swelling degrees up to 13 for a γ-irradiation crosslinked glycidylacrylated dextran[6] are reported. Other swelling ratios are calculated by relating the water uptake to the weight of the hydrogel. For this purpose, the water-uptake (weight of the swollen hydrogel substracted by the weight of the dry hydrogel) is divided by the weight of the dry hydrogel. Swelling ratios of 0.5 to 30 are reported for dextran based systems.[7-12]

The swelling degree generally depends on the balance between various forces such as solvation, elastic, electrostatic, and osmotic pressure.[13-16] Swelling forces are determined by internal parameters like the hydrogel composition, density and hydrophilicity as well as by external parameters like type of solvent or ion concentration and pH. A variety of stimuli sensitive polymers was developed.[17] Depending on the polymer and the environmental conditions the influence of certain forces varies. The interplay of the present forces with varying environmental parameters on the swelling behavior of polyelectrolyte hydrogels was intensively investigated by simulation studies. Especially the influence of external parameters like salt concentration,[18-21] crosslinking density,[22, 23] or solvent quality[19] are discussed. For uncharged surface attached polymers the equilibrium swelling is an interplay between elasticity of the polymer and the osmotic pressure of the polymer. For charged polymers the situation changes: the swelling equilibrium is mainly determined by electrostatic interactions and the osmotic pressure of the counterions rather than by the osmotic pressure of the polymer. Generally, the electrostatic interaction increases with decreasing salt concentration, the elastic force increases with decreasing crosslinking density and the better the solvent quality the higher the solvent pressure resulting in higher swelling.

Surface Plasmon Resonance (SPR) and Optical Waveguide Mode Spectroscopy (OWS)[24-26] are useful techniques to investigate the swelling behavior of hydrogel films. The change of the swelling state is thereby followed by a change in the angular position of the surface plasmon and the optical waveguide modes due to the change of the thickness and the refractive index of the hydrogel film (Chapter 2.1). The most common method to extract the thickness and the refractive index from the SPR/ OWS data is to assume a homogeneous one-layer like hydrogel film and to adjust the thickness and refractive index to the measured data (Chapter 2.3).[27] For more complex systems especially for films with a refractive index gradient this “one-box” model does not represent the hydrogel film structure. In these cases the hydrogel film parameters can be determined with the reversed Wentzel-Kramer-Brillouin (WKB) approximation. The WKB approximation determines the variation of the refractive index perpendicular to the surface[28] by allocating a thickness and a refractive index value to every optical waveguide mode (Chapter 2.3).[29] The performance of this theory for hydrogel films was validated for PNIPAAm hydrogel films by Beines *et al.*[27] Usually, a hydrogel film refractive index-thickness profile can be modeled by two or three homogeneous layers meaning with two or three layers of constant but different refractive index. The number and thickness of these layers can be extracted from the WKB calculations. Supplementary information on the hydrogel film structure, especially on its surface properties in the swollen state such as topography and roughness, can be obtained by neutron reflectivity measurements.[30-33] A very smooth surface comparable to water was reported for comparable systems.[34, 35]

4.1.2 Hydrogel Film Stability

In order to investigate the hydrogel-film stability films were produced by spin-coating the dextran-based polymer on a chromium/gold covered glass slide coated with a self assembled monolayer of *S*-3-(4-benzoylphenoxy)propyl ethanthiol as adhesion promoter. The subsequent irradiation at 254 nm resulted in a photo-crosslinked and surface-bound hydrogel film in one step as schematically described in Chapter 3.3.2. The film thickness could be varied from tens of nanometers to micrometers in the dry state by changing the spinning speed and the concentration of the polymer solution. In general relatively high polymer concentrations (7-40 wt%) are resulting in homogeneous films.

The film stability of these immobilized hydrogel films depends on one hand on external parameters like film thickness, irradiation time, solvent quality, salt concentration, and pH. On the other hand the film stability is influenced by internal parameters like the benzophenone and the carboxyl groups. Thereby, film instability is defined as a delamination of the hydrogel film, which results in the loss of the otherwise existing optical waveguide modes. The hydrogel film stability increases with

- *decreasing film thickness*: the thinner the film the lower the mechanical forces at the surface while swelling and the higher the layer modulus
- *increasing irradiation time*: the longer the films are exposed to UV-light, the higher the degree of crosslinking and the lower the degree of swelling
- *decreasing solvent quality*: the lower the solvent quality, the less pronounced the swelling and consequently the lower the mechanical forces upon swelling
- *increasing salt concentration*: the higher the salt concentration the more charges can be neutralized leading to decreased swelling and reduced mechanical forces at the surface
- *decreasing pH*: at pH 3 or lower the carboxyl groups are protonated and the swelling is reduced due to reduced electrostatic repulsion. For pH values above 5 all carboxyl groups are deprotonated and the gel is completely swollen as long as no ions are neutralizing the negative charge of the carboxyl groups. The pKa value of the carboxyl groups in vicinity of an ether oxygen is between 3 and 4.

Mainly, two parameters are determining the impact of the external effects, namely the density of the network itself and the ability of manipulation due to charge generation. In general, increasing number of charges leads to enhanced swelling due to electrostatic repulsion. Deprotonation of carboxyl groups or decrease of the salt concentration at high pH generates negative charges. The effect of a decreasing ion concentration is based on charge screening by counterions and a salting out effect. These effects are of course more pronounced for intrinsically less dense - meaning low crosslinked - networks. For optimized external parameters the hydrogel film stability seems to be defined by the proportion of the benzophenone crosslinker and the charge generating carboxyl functionalities as can be seen by plotting the degree of carboxyl functionalization versus the degree of benzophenone functionalization (Figure 4.1.1). The values are obtained by dividing the CH(1) integral of the ^{1}H-NMR in D_2O by the integral for one proton of the functional group as described in Chapter 3.1.2. The black circles represent the hydrogels that are stable on the substrate even under non-optimal conditions while the white circles present the ones that are delaminating even under optimal external conditions meaning they are even deliminating if they are completely crosslinked

(254 nm, 90 minutes), prepared as thin films (<1 µm in the swollen state), swollen in low pH (pH = 3) and high ionic concentration (150 mM or higher).

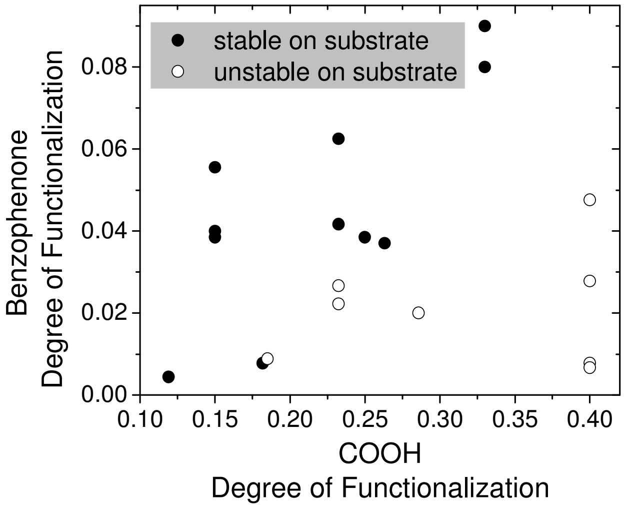

*Fig. 4.1.1: Degree of benzophenone functionalization versus degree of carboxymethylation for completely photo-crosslinked (90 min) hydrogels (type(**3**)). The hydrogel films (100 nm-1 µm in the dry state) that are stable on a gold surface coated with a self-assembled monolayer of S-3-(4-benzoylphenoxy)propyl ethanthiol after photo-crosslinking are shown by the filled black circles, the ones that are not stable even if their thickness is decreased are represented by the white circles.*

As can be concluded from the results shown in Figure 4.1.1, a diagonal boundary divides the stable films from the instable ones implying the increasing amount of benzophenone crosslinker that is necessary to stabilize the hydrogel films with increasing amount of carboxyl functionalities. In the vicinity to this boundary one finds a critical crosslinking density, at which a stable gel in low pH or high ionic strength solvents can be obtained. Lowering the ionic strength, however, below 10 mM induces pronounced swelling, which ultimately leads to a failure of the surface attachment and consequently delamination. The delamination is detected by SPR/OWS upon the disappearance of optical waveguide modes and a shift of the surface plasmon to lower angles. As already mentioned decreasing the ionic strength leads to reduced electrostatic shielding and an increased swelling of the hydrogel matrix.[18, 22] Delamination occurs increasingly likely when swelling a dry gel with a critical benzophenone to carboxyl group ratio directly in a low ionic strength solvent, compared to solvent exchange to low ionic strength buffer after swelling in a high ionic strength medium first. This implies that the intermittent forces upon swelling play a major role in the film stability and need to be counteracted by the crosslinking points of the hydrogel. For biological, medical or sensing applications molecules or cells are intended to diffuse through the gel. A highly swelling but stable network is required making it necessary to optimize the swelling properties according to the above discussed effects.

4.1.3 Hydrogel Film Characteristics – Surface and Swelling Properties

In order to characterize the swelling properties of the hydrogel films, they were crosslinked with varying energy and swollen at pH 3-8 (10mM buffer), in HEPES (10mM) and in PBS with varying ionic strength followed by surface plasmon resonance and optical waveguide-mode spectroscopy (SPR/OWS). The SPR/OWS angular scans were translated into refractive index-thickness profiles of the hydrogel films by applying the Wentzel-Kramer-Brillouin (WKB) approximation (Chapter 2.3).

For every crosslinking time three cycles of swelling over night, pH- and salt-screening, and drying were performed with AFM measurements in between to investigate the surface roughness. Additionally, the dry film thickness was measured with a profiler before and after every swelling cycle. A loss of material mainly occurs during the first swelling cycle before starting the pH and salt-screening and can be up to 50 % of the initial dry thickness. The results for the thickness and refractive index profile were comparable for all three cycles.

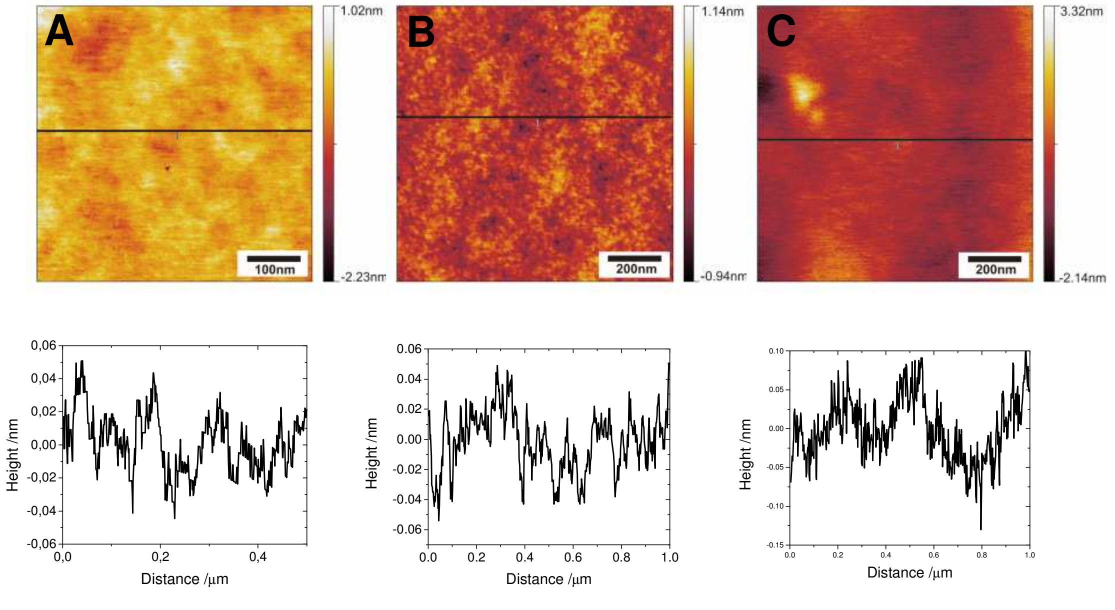

Figure 4.1.2: *AFM measurements in the dry state for a completely (90 minutes) crosslinked hydrogel film (d_s(benzophenone) = 0.04; d_s(carboxymethylation) = 0.16) before swelling **(A)**, after one cycle of swelling and drying **(B)**, and after 3 cycles of swelling and drying **(C)**. The surface roughness along the black line indicated in every AFM picture is shown below.*

Furthermore, the AFM measurements (Figure 4.1.2) show very smooth and defect-free surfaces with a surface roughness of 0.2-0.5 nm (rms) at a scale of 1x1µm even after 3 cycles of swelling, pH-screening, and drying.

Depending on the spin-coating conditions, mainly on the concentration of the polymer solution, the overall surface roughness on a scale of centimeters is in a range of tens to hundreds of nanometers, as determined with a profilometer. For the samples shown here the large-scale roughness was determined to be 10% of the thickness over an area of 9 cm^2 .

To study the gel thickness-refractive index profile change due to pH- or ionic strength induced shrinking the reversed Wentzel-Kramer-Brillouin (WKB) approximation (Chapter 2.3) was used to model the hydrogel profile[27] (Figure 4.1.3). This method calculates a thickness-refractive index profile from the angular positions of the optical waveguide modes in an SPR/OWS-spectrum by allocating a thickness and a refractive index value to every optical waveguide mode.[29] For this purpose, the accuracy of the calculated profile is mainly determined by the number of optical waveguide modes available which depends on the thickness and refractive index of the hydrogel film.

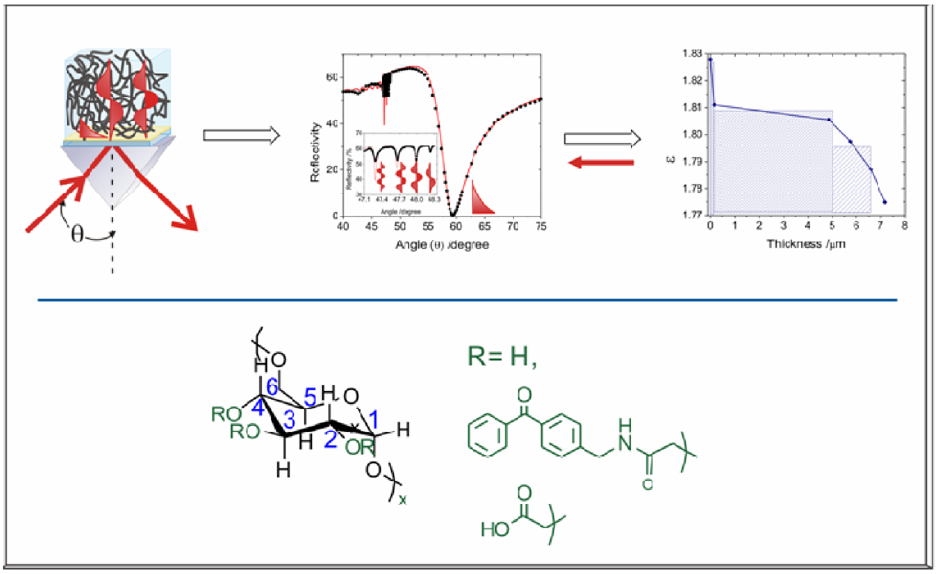

Figure 4.1.3: *Chemical structure of the hydrogel matrix and the procedure to extract the model of the photo-crosslinked dextran-based hydrogel film profile from the SPR/OWS measurements and simulating the measured data according to the hydrogel film refractive index - thickness profile. The WKB thickness refractive index profile is deduced from the angular position of the optical waveguide modes and the refractive index calculated for the surface plasmon.*

The gold-hydrogel interface is set as z-position z = 0 defining the origin of height. The refractive index closest to the interface was deduced from the surface plasmon, which is sensitive on the first hundreds of nanometers and was therefore assigned to a layer height level perpendicular to the gold—hydrogel interface of z = 0 nm. The value closest to the gold-hydrogel interface calculated from the optical waveguide modes by the WKB approximation is set to z = 150 nm, assuming a detection length for the surface plasmon of 150 nm.[36] Further details are described in Chapter 2.3. Usually, the hydrogel refractive index-thickness profile does not resemble a single-layer-like structure but is denser at the gold interface and shows a gradient transition at the hydrogel-solution interface. This gradient at the film-solution interface can be sharpened by creating a denser network either by increasing the crosslinking time or by compaction of the gel. The photo-crosslinked dextran based hydrogel films can be simulated with a two-box layer model for high crosslinking times and a three-box layer model for incomplete crosslinking: namely, a denser layer up to ~150 nm, a subsequent box-like layer and for low crosslinked films a further box layer with even lower refractive index than the previous one was used, which is in agreement with the WKB-based profiles. Contradictory reports on the refractive index profile of such hydrogel films exist. Even for one system like PNIPAAm different film structures are reported. Beines *et al.* reported a denser film at the substrate interface.[27] Harmon and Kuckling characterized photo-crosslinked PNIPAAm-based hydrogel films with a denser network at the solution interface but in the deswollen state.[37] They differenciated thin homogeneous films and thicker films consisting of two refractive index regimes, with a less dense conformation at the substrate interface and defined a critical film thickness between 280 and 500 nm.[37, 38] Thereby, the chemical differences for example the different crosslinker, and the different crosslinking reaction has to be taken into account and might be one reason for the different behaviour. Harmon and Kuckling are using a [2+2]-cycloaddition for crosslinking involving a sensitizer, whereas Beines *et al.* use the same benzophenone crosslinking concept as applied for the dextran-based systems reported in this work. Besides chemical influences, two effects seem to be responsible for the refractive index gradient: one effect is the decreasing light intensity due to absorption from the surface to the substrate interface initiating the photo-crosslinking reaction. The second influence is the wettability during the hydrogel film preparation by spin coating. For long crosslinking times the absorption should become negligible because all absorbing, crosslinking molecules are reacted. The volume-phase transition should be affected by the non-equilibrium chain conformation resulting from the sample preparation as well as the stress distribution in the hydrogel layer. This varies as a function of the gel modulus and the gel equilibrium state as a consequence of the film preparation. As representative examples the hydrogel profiles for crosslinking times of 10, 30, 60 and 90 minutes are shown in Figure 4.1.4 A and 4.1.4 B and the variation of the swelling degree $\left(\frac{d_{swollen}}{d_{dry-afterswelling}}\right)$ with crosslinking time and pH in Figure 4.1.5. The thickness in the swollen state was extracted from the WKB thickness-refractive index profiles, as indicated in Figure 4.1.3 and described in detail in Chapter 2.3, whereas the thickness of the dry state was measured with a profiler after swelling and drying.

The thickness-refractive index profile derived from one SPR/OWS scan represents one specific state of the hydrogel film for a specific crosslinking time, pH and ionic strength. The influence of the pH on the swelling of the hydrogel film can be attributed to the charging of the carboxyl groups in the hydrogel network as discussed above. By reducing the pH below the pKa value of the carboxyl groups, these are protonated and the electrostatic repulsion and with this the degree of swelling of the hydrogel network is reduced (Figure 4.1.4 A). Additionally, hydrogen bond formation for example with the backbone-hydroxyl groups becomes possible.[39] This deswelling of the hydrogel film occurs relatively abrupt upon passing the pKa value.

For pH values between five and eight no significant change in the hydrogel film profile takes place. Even if the buffer type, and thus the type of counterion, is changed to HEPES or PBS, which are frequently used in sensing experiments, the swelling state stays constant while maintaining the pH and ionic concentration. Whereas the change from pH 4 to pH 3 induces a shrinking of the hydrogel film up to 50%. According to Hofmeister series one would expect an influence of the ion-type on the swelling as well. For PBS, HEPES and the pH 8 buffer such an effect was not observed. Thereby, PBS and the pH-screening buffers contain similar types of counterions, mainly Cl^- and HPO_4^- whereas HEPES is a zwitterionic organic chemical buffering agent namely (4-(2-hydroxyethyl)-1-piperazineethanesulfonic acid). Furthermore, specific binding effects are known for certain combinations of ions and functional groups. For example a special binding effect overlaying simple charge screening is reported for potassium to dextran sulphate.[40]

The charge screening effect of counterions is more pronounced for low crosslinked hydrogel films due to their less dense network and thus higher degree of swelling as visible in Figure 4.1.4 A by comparing the pH-dependent hydrogel profiles for 10, 30, 60, and 90 minutes of crosslinking. The extracted pH-dependent swelling degrees for one distinct crosslinking time in Figure 4.1.4 A show the abrupt swelling upon passing the pKa value of the network carboxyl groups and the increasing swelling with decreasing crosslinking density. Adjacent to the pH influence on the hydrogel film profile the change upon ionic strength variation was investigated by diluting a 150 mM PBS solution. The corresponding WKB refractive index-thickness profiles are presented in Figure 4.1.4 B for decreasing ionic strength in one plot and for increasing crosslinking time in one row.

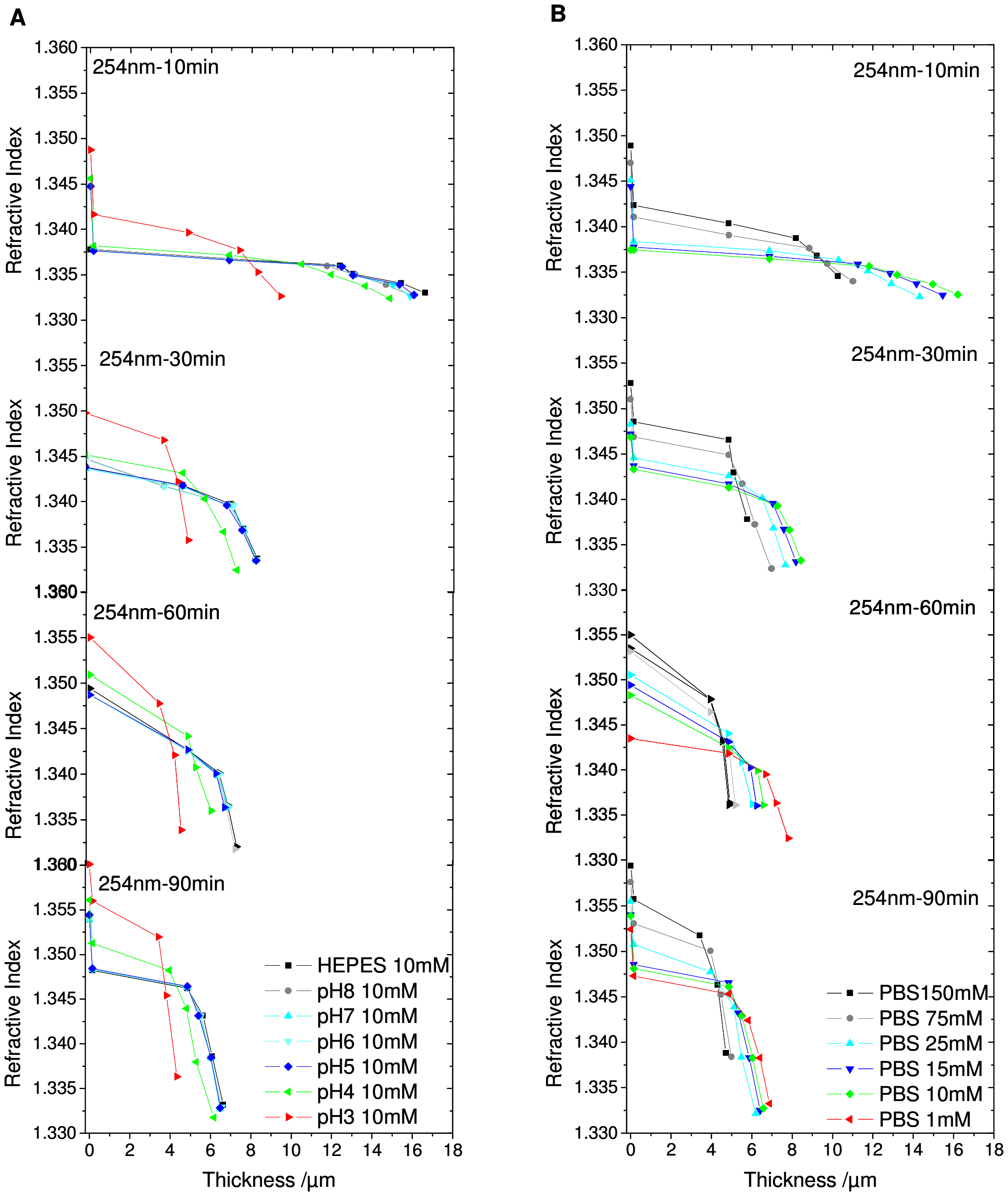

Figure 4.1.4: *The hydrogel film profile calculated with the WKB approximation upon variation of the pH* ***(A)*** *and ionic strength (PBS, pH = 7.4)* ***(B)*** *for different crosslinking times. The degree of substitution of benzophenone as photo-crosslinking unit was determined to be 0.04 and the one of the carboxyl functionalities to be 0.16. The film thickness in the dry state after swelling and drying was 400nm (±10%).*

For one distinct crosslinking density the decrease in ionic strength leads to reduced neutralization of the deprotonated carboxyl functionalities in the hydrogel network resulting in increased swelling of the hydrogel film. For an ionic concentration of 150mM the hydrogel profile is comparable to the one for pH 3 (10mM) indicating that all charges are electrostatically screened. In contrast to the pH effect on the swelling degree the ionic strength effect is a continuous screening effect. For very low ionic strength an increase in swelling upon increasing ion concentration for weak polyelectrolyte, surface attached polymers, passing a maximum swelling at a certain ion concentration, followed by the described shrinking due to charge screening is known.[41-47]

This effect could not be observed for these hydrogel systems. Either the refractive index of the hydrogel film at ion concentrations below 10 mM decreased that much, that no optical waveguide modes were guided inside the film or delamination of the hydrogel film occured. For a crosslinking time of 90 minutes PBS concentrations of down to 1 mM were measured. For PMMA brushes a concentration of 2 mM $NaNO_3$ is reported to cause maximum swelling.[46] The theoretical swelling for low ion concentrations (osmotic brush) should scale with $L \infty c_s^{1/3}$, whereas for higher ion concentrations (salted brush regime) the swelling state should scale with $L \infty c_s^{-1/3}$. For crosslinked hydrogel systems one has to take into account the balancing force of the crosslinking points that might prevent higher swelling or in case the crosslinking density is too low to stabilize the swelling force, delamination occurs.

Besides the pH and ionic strength, the influence of the crosslinking time on the swelling behaviour was investigated (Figure 4.1.5 B).

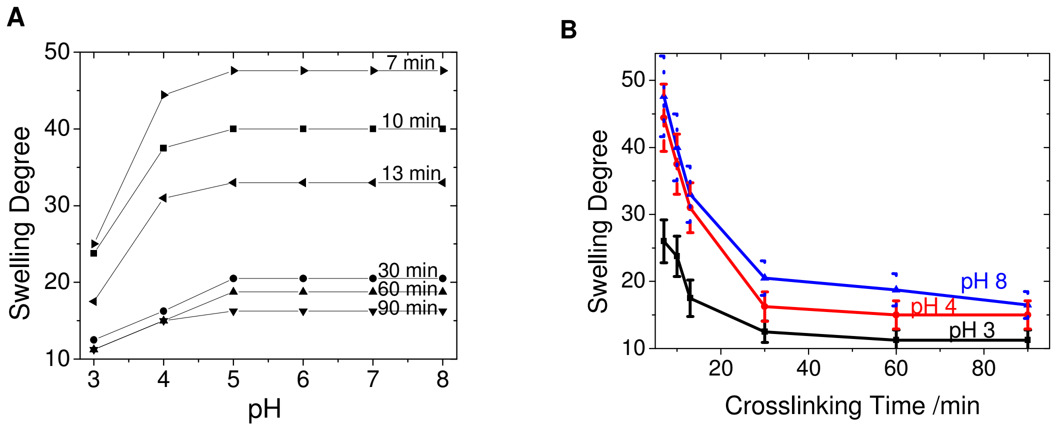

Figure 4.1.5: *The changes of the swelling degree extracted from the WKB profiles in dependence of the pH **(A)** and the crosslinking time **(B)** at an ionic concentration of 10 mM for a 400 nm (±10%) thick hydrogel film in the dry state after swelling (d_s(benzophenone) = 0.04; d_s(carboxymethylation) = 0.16). The error results from the thickness variation of the dry film which is around 10% over an area of 9 cm².*

The effect of the crosslinking time on the swelling degree correlates with the decrease of the benzophenone absorption at 260 nm (Chapter 3.1) and is more distinctive for pH values above the pKa and thus for higher swollen gels. This can be attributed to the balancing of the electrostatic force by the elastic force of the more rigid hydrogel network as discussed above. With the particular gel shown here swelling degrees up to almost 50 in z-direction could be achieved.

The swelling degrees for the extreme external conditions are summarized in table 1. Besides the influence of the pH, ionic strength, and crosslinking time the correlation between the similar swelling behavior at pH 3 (10 mM) and in PBS 150 mM and for pH 8 (10 mM) and PBS 10mM is noteworthy. This indicates a complete neutralization of charges for pH 3 (10 mM) and PBS 150 mM and a full swelling for pH 8 (10mM) and PBS 10mM.

Table 4.1.1: *Swelling degree for stable gels with increasing crosslinking times at pH 3 and pH 8 and for 150 mM and 10mM PBS (pH 7.4) derived from the WKB for a hydrogel film with a dry-state thickness of ~400nm (d_s(benzophenone) = 0.04; d_s(carboxymethylation) = 0.16).*

crosslinking @ 254 nm	pH 3, 10 mM (WKB)	pH 8, 10 mM (WKB)	PBS 150 mM (WKB)	PBS 10 mM (WKB)
7min	26(± 3.2)	48(± 6.0)	26(± 3.2)	42(± 5.3)
10min	24(± 3.0)	40(± 5.0)	25(± 3.1)	40(± 5.0)
13min	17(± 2.3)	33(± 4.2)	17(± 2.3)	33(± 4.2)
30min	11(± 1.5)	20(± 2.6)	13(± 1.7)	21(± 2.7)
60min	11(± 1.5)	19(± 2.4)	13(± 1.7)	19(± 2.4)
90min	11(± 1.5)	16(± 2.0)	12(± 1.6)	17(± 2.2)

Overall, the swelling degrees show a consistent behaviour with pH, ion concentration and crosslinking time and are higher than swelling degrees reported in the literature for dextran-based systems.[10, 11, 48] This makes them a promising material for biosensor applications due to less hindered protein diffusion which is consistent with a macroporous structure observed in cryo-SEM measurements for freeze dried expanded hydrogel samples. Especially with the opportunity not only to use the surface plasmon but also the optical waveguide modes for precise signal detection, these thick hydrogel films have great potential in the field of sensors.

Considering the swelling degrees and the refractive indices of the presented hydrogel films the thickness necessary to get a required number of optical waveguide modes can be deduced. An estimation of the expected number of optical waveguide modes is important for the preparation of biosensor matrices. Consequently, a “single-box” model is applied and a highly swollen hydrogel matrix (low crosslinking, pH > 5) with a refractive index of n = 1.335 (ε = 1.787) and a compacted film (highly crosslinked, pH<4) with n = 1.355 (ε = 1.836) were simulated. The simulated angular spectra for a hydrogel film guiding 3 optical waveguide modes, is depicted in Figure 4.1.6. For the highly swollen hydrogel film (n = 1.335) a thickness of 3 µm is necessary to guide one optical waveguide mode. With a film-thickness of 6 µm two and with 9.2 µm three optical waveguide modes are guided.

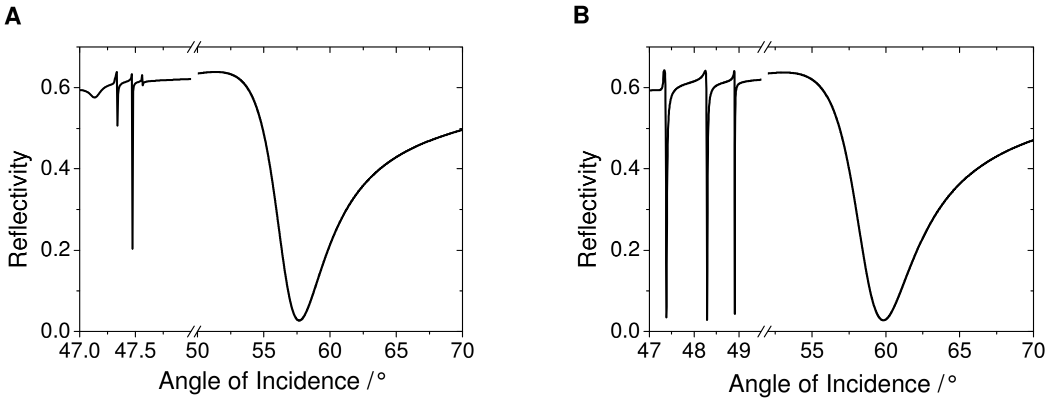

Layer-Parameters:

No	Thick	EpsX-real	EpsX-im
1	0	3,407	0
2	2	-4	16,8
3	48	-12,4	1,6
4	2	2,06	0
5	9200	1,787	0
6	0	1,778	0

Layer-Parameters:

No	Thick	EpsX-real	EpsX-im
1	0	3,407	0
2	2	-4	16,8
3	48	-12,4	1,6
4	2	2,06	0
5	3600	1,836	0
6	0	1,778	0

Figure 4.1.6: *Simulated SPR/OWS spectra for a "one-box" hydrogel film (layer 5) model on a chromium (layer2) gold (layer 3) covered glass substrate (layer 1) with a self assembled monolayer (layer 4) as adhesion promoter.* ***A)*** *shows the simulated spectra for a highly swollen hydrogel matrix,* ***B)*** *the one for a denser hydrogel matrix. The spectra were simulated with 6000 points corresponding to the maximum experimental resolution of 0.005°.*

For the less swelling and thus optically denser hydrogel film (n = 1.355) a thickness of 1 µm is required to guide one optical waveguide mode. With a thickness of 2.3 µm and 3.6 µm two and three optical waveguide modes are guided inside the film. Besides, the required thickness to allow the generation of optical waveguide modes, the width of the optical waveguide modes is influenced by the optical density of the hydrogel matrx. This influences the detected coupling efficiency because of the limited experimental resolution of maximal 0.005°. A reduced coupling efficiency due to the hydrogel film characteristics is mathematically reflected by the imaginary part (ε') of the refractive index. A reduced coupling efficiency can be caused by mechanisms leading to a reduction of the guided amount of light due to scattering or absorption for example. For the simulation discussed here this effect is neglected (ε' ≡ 0).

4.1.4 Film Characterization with Neutron Reflectivity

In a comparative study a hydrogel film was investigated by neutron reflectivity measurements to analyze the surface structure of the swollen hydrogel films. These measurements were performed by Ann Falk on the reflectometer AndR at the Center for Neutron Research at the National Institute for Standards and Technology in Gaithersburg, USA. Therefore a silicon wafer was covered with an adhesion monolayer of 4-(3-triethoxysilyl)propoxybenzophenone and a hydrogel layer (type (**5**), d_s(carboxymethyl) = 0.1 and d_s(benzophenone) = 0.025) (compare Chapter 3.1). The specular reflectivity was first measured in the dry state before swelling the hydrogel film in a D_2O based PBS buffer (pH = 7.4, c = 150mM). After measuring the neutron reflectivity for the dry and the swollen hydrogel film the hydrogel was reacted with deuterated ethanolamine after active ester activation of the carboxyl groups and again analyzed with neutron reflectivity.

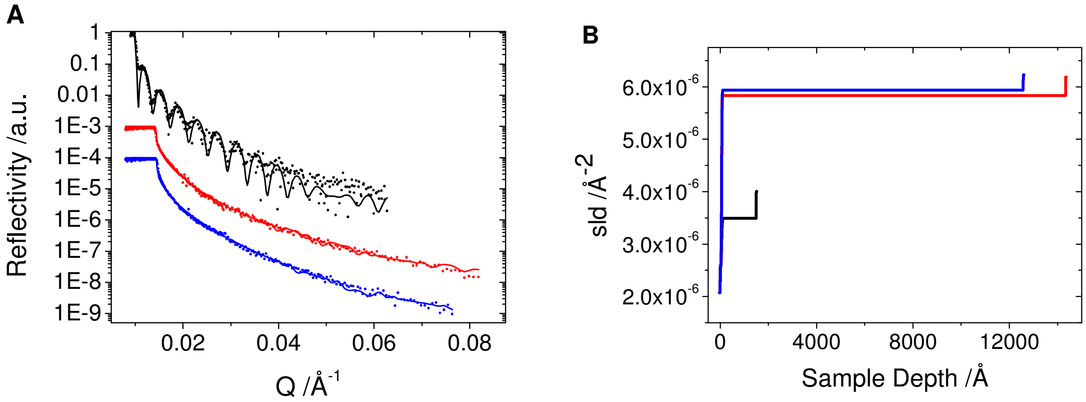

(C)	***d /Å***	***sld /Å^{-2}***	***Roughness /Å***
Si	0	2.07e-06	7
SiO$_x$	61.2	2.5566e-06	10
Hydrogel (dry)	1434.69 (1435±10-25)	3.4901e-06	52.6035
Hydrogel (D2O)	14278 (14300±100)	5.8339e-06	23.8355
Hydrogel + Ethanolamine (D2O)	12514 (12500±100)	5.93896e-06	36.3635

Figure 4.1.7: *Fitted neutron reflectivity profiles* ***(A)*** *and corresponding scattering length density profiles* ***(B)*** *of a dextran based hydrogel film (type (**5**) (compare Chapter 3.1),* d_s*(carboxymethyl) = 0.1 and* d_s*(benzophenone) = 0.025, crosslinked at 254 nm for 90 min). The neutron reflectivity results in the dry state (black), swollen in D2O (red) and after ethanolamine coupling in D2O (blue) are shown. The determined values are summarized in Table(**C**).*

The background intensity offset to both sides of the specular ridge was determined separately and the neutron reflectivity was calculated from the recorded specular raw data, the background data and the incident beam. The background neutron radiation mainly originates from incoherent scattering from the bulk solvent reservoir. The fitted neutron reflectivity profiles and the corresponding scattering length density profiles are shown in Figure 4.1.7 A and B. In the dry state the neutron reflectivity profile of the hydrogel film exhibits pronounced fringes that can be simulated to a layer thickness of about 143.5 nm (sld = 3.5 10^{-6} Å^{-2}) and a surface roughness of 5.3 nm. After swelling in buffer, the hydrogel thickness increased by a factor of ten to 1430 nm, with an sld of 5.8 10^{-6} Å^{-2}. The later value was only slightly lower than for pure D2O which suggests a very hydrated polymer network. After the reaction with ethanolamine, the layer thickness decreased to 1250 nm with a sld of 5.9 10^{-}6 Å^{-2}, which implies an even more aqueous structure and a swelling degree of approximately 8.7. These swelling degrees are consistent with the swelling degrees reported in Chapter 4.1.3 for swelling in PBS buffer at a concentration of 150mM PBS buffer. Furthermore, the deswelling upon ethanolamine coupling was expected. Ethanolamine was coupled to the carboxyl groups resulting in a reduction of the number of negative charges in the hydrogel film and consequently to a reduced swelling. This effect was expected to be less pronounced in PBS 150 mM compared to lower concentrated buffers at neutral pH due to the blocking of the negative charges by counterions. The influence of molecules bound to the carboxyl groups into the hydrogel film upon its degree of swelling is discussed in Chapter 4.2, too. Additionally, the effect of ethanolamine coupling to the hydrogel film (type (**3**), crosslinked at 254nm for 90min, with a d_s(carboxymethyl) = 0.16 and a d_s(benzophenone) = 0.04 is exemplarily shown in Figure 4.1.8 by displaying the refractive index – thickness profile before and after ethanolamine coupling in PBS 150 mM. The deswelling is relatively small from 6150 nm to 6080 nm.

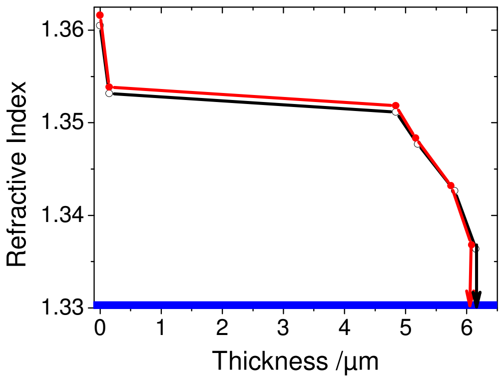

Figure 4.1.8: *Refractive index-thickness profiles of a hydrogel film (type (**3**) compare Chapter 3.1), d_s(carboxymethyl) = 0.16 and d_s(benzophenone) = 0.04, crosslinked at 254 nm for 90 min) before (black, empty circles) and after (red, full circles) ethanolamine coupling in PBS 150 mM. The coupling of ethanolamine results in a slight deswelling of the hydrogel film and an increased refractive index.*

A hydrogel film prepared under identical conditions compared to the sample measured with neutron reflectivity was investigated by SPR/OWS spectroscopy. Due to the film thickness in the range of 120 nm in the dry state after swelling the angular scan in the dry state didn't show any optical waveguide mode but only a surface plasmon. After swelling in buffer the hydrogel film was guiding one optical waveguide mode allowing the determination of the thickness and the refractive index with a one-box model. The refractive index was fitted to the position of the surface plasmon, the thickness to the position of the optical waveguide mode (TM$_1$). With this approach the normally occurring gradient of the refractive index in z-direction is neglected resulting in an error of the thickness and refractive index values. The thickness is expected to be higher than simulated and the refractive index to be lower. To minimize the error due to the gradient angular scans with p-and with s-polarized light respectively were recorded.

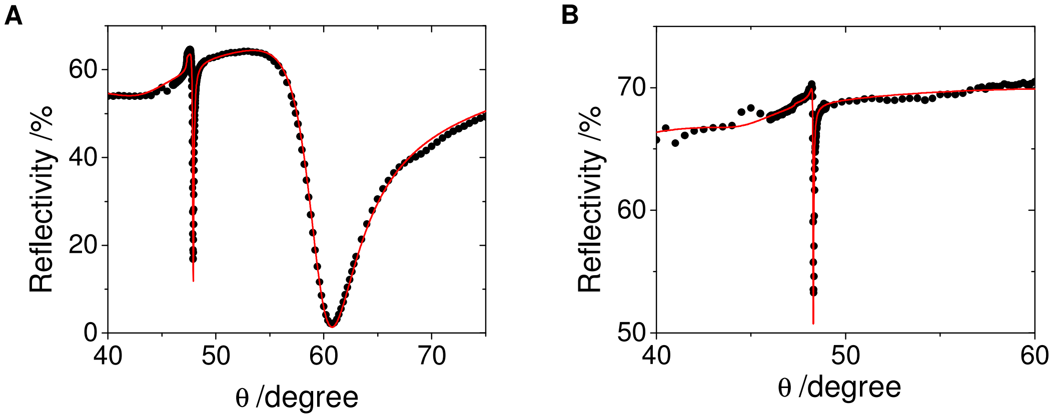

Layer	*Thickness /nm*	*ε' (real)*	*ε'' (imaginary)*
LaSFN9	0	3.407	0
Chromium	1.9	-4	16.8
Gold	46	-12.4	1.6
SAM	3	2.06	0
Hydrogel	1050	1.854	0.0011(A)/0.0007(B)
PBS	0	1.778	0

Figure 4.1.9: *SPR/OWS spectra (black) of a comparable hydrogel film as used for the neutron reflectivity measurements. The spectra were recorded for the hydrogel film swollen in PBS 150 mM after ethanolamine coupling with p-polarized* ***(A)*** *and s-polarized* ***(B)*** *light (633 nm) an simulated with a one box model (table).*

Because the angular scans recorded with p- and with s-polarized light after ethanolamine coupling can be simulated with the same thickness and refractive-index values the gradient is assumed to be small in this case. In conclusion the swelling results should be in a comparable range than the ones determined with the neutron reflectivity measurements. The angular scan and the corresponding simulation in PBS 150 mM after ethanolamine coupling for p- and s-polarized light are depicted in Figure 4.1.9 A and B. The values used to simulate the measured data are displayed in the table in Figure 4.1.9.

The magnitude of the simulated thickness is 200 nm smaller than the one determined by neutron reflectivity after ethanolamine coupling which might be attributed to thickness variation in the dry state depending on the position on the sample.

In conclusion the neutron reflectivity results are consistent with the results of the SPR/OWS measurements and constitute the high water content and swelling degrees and the very smooth surface of the dextran-based hydrogel presented in this work. Due to the enormous water content of this hydrogel it was not possible to determine the surface structure in the swollen state, neither by neutron reflectivity nor by AFM measurements in the swollen state.

4.1.5 Film Characterization with Fluorescence Correlation Spectroscopy

To obtain more information on the diffusion inside the hydrogel matrix, which is related to the pores size of the swollen hydrogel, fluorescence correlation spectroscopy experiments were performed in cooperation with Riccardo Raccis and Prof. G. Fytas at the Max Planck Institute for Polymer Research. In first experiments the diffusion of Alexa Fluor 647 and the diffusion of bigger quantum dots (d ~ 20 nm) were investigated in dependence of the hydrogel's swelling state. The PCMD films (d_s(carboxymethyl) = 0.16; d_s(benzophenone) = 0.04) were crosslinked at 365 nm. The lower irradiation energy per time as compared to 254 nm allows a more exact tuning of the crosslinking density and the generation of very low crosslinked hydrogel matrices. After crosslinking the hydrogel films were extensively rinsed to remove unbound polymer chains, dried in order to determine the dry film thickness and swollen in buffer to perform the desired FCS experiment.

FCS experiments revealed the reduced diffusion coefficient (*D'*) which is calculated by dividing the diffusion coefficient inside the hydrogel matrix (*D*) by the diffusion coefficient of the target analyte in solution (D_0) (equation 4.1.1).

$$D' = \frac{D}{D_0} \qquad (4.1.1)$$

Subsequently, the dependence of D' on two different crosslinking times (15 and 120 min) and on the one dimensional swelling ratio was investigated so far (Figure 4.1.10) A clear dependence of D' on the crosslinking time and with this on the swelling ratio was observed.

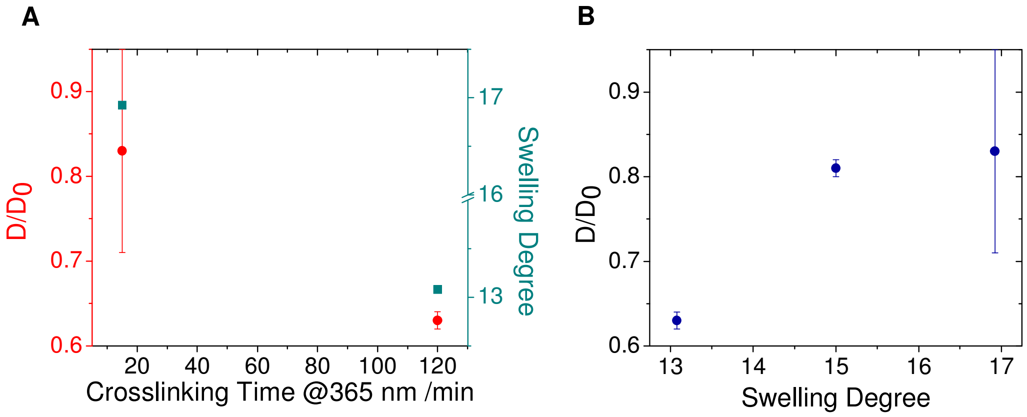

Figure 4.1.10: ***A)*** *The reduced diffusion coefficient (D') for Alexa Fluor 647 and the swelling degree for a low (15 min) and a highly crosslinked (120 min) hydrogel matrix in 10 mM acetate buffer at pH = 5.* ***B)*** *The reduced diffusion coefficient (D') for Alexa Fluor 647 in dependence of the hydrogel's swelling ratio.*

Figure 4.1.10 A shows the dependence of the swelling ratio (blue squares) and the dependence of the diffusion coefficient (D') (red circles) of Alexa Fluor 647 on the crosslinking time. The swelling ratio (blue squares) after 120 min of irradiation of 13-14 in 10 mM acetate buffer at pH = 5 indicates a fully crosslinked hydrogel network whereas the network after 15 min of irradiation shows a decreased swelling ratio. This behaviour is expected and results from the incomplete crosslinking after 15 minutes. The values for D' (red circles) show a correspondence with the swelling ratio and thus with the crosslinking density. For increased crosslinking a decreased D' is observed indicating larger pores for the lower crosslinked network. The error for the diffusion in the low crosslinked hydrogel network is much higher as compared to the error of D' inside the highly crosslinked network. This might be attributed to the enhanced inhomogeneities in the low crosslinked hydrogel. For lower crosslinking time chain entanglements for example have a pronounced influence on the hydrogel network structure especially in high molecular weight polymers as used here. In higher crosslinked networks the photo-crosslinking due to the benzophenone moieties becomes the decisive crosslink. The structure becomes more rigid and maybe more homogeneous resulting in a lower error of D'.

Figure 4.1.10 B depicts the relation between D' and the swelling ratio. Thereby, the factor which induces the different swelling degree such as pH or crosslinking time is neglected. Although a more detailed investigation of the diffusion on the crosslinking process is required it becomes clear that the diffusion of Alexa Fluor 647 can be tuned by modulating the crosslinking density and with this the swelling degree and the pore size of the hydrogel. With this network formation can be followed indirectly.

To obtain first information about the pore size of the completely crosslinked hydrogel matrix crosslinked for 120 min in the swollen state the diffusion of quantum dots (d~20 nm, Q-dot 545, Invitrogen) with a diameter of ~ 20 nm was investigated. The results are depicted in Figure 4.1.11. The diffusion of these quantum dots inside the hydrogel matrix was possible but the diffusion coefficient shows a remarkable slow down (D/D_0) compared to the 2.6 nm diameter Alexa Fluor 647 (Figure 4.1.11).

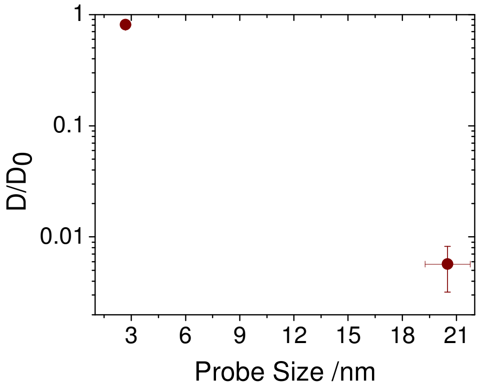

Figure 4.1.11: *The reduced diffusion coefficient (D') for two different probe sizes with a diameter of 3 nm(Alexa Fluor or quantum dot?) and 20 nm (quantum dot). The hydrogel matrix was crosslinked for 120 min at 365 nm and swollen in HEPES (pH = 7.4, c = 10 mM).*

This observation indicates a hydrogel structure with pores allowing quantum dots with a diameter of 20 nm to diffuse even in their fully crosslinked state. These results are consistent with the high swelling degrees and and the expanded superstructure observed by cryo-SEM measurements.

4.1.6 Conclusion and Outlook

The film characteristics of a photo-crosslinkable and carboxymethylated dextrans were investigated. For the film stability the benzophenone versus carboxyl group ratio was found to be crucial resembling the interplay between electrostatic and mechanical force during the swelling process. For stable film formation the influence of the external parameters crosslinking time, pH, and ionic strength were determined using SPR/OWS spectroscopy and analyzing the data with the WKB approximation. Swelling degrees between 10 and almost 50 in z-direction were measured for a 400 nm thick film in the dry state. In agreement with the literature for a comparable system based on PNIPAAm the hydrogel refractive index-profile shows a gradient towards lower refractive index at the solution interface and a higher refractive index at the gold interface. The local surface roughness over an area of μm^2 was found to be very small as determined by AFM and neutron scattering. These highly swelling hydrogel films are promising candidates for biosensing applications (compare Chapter 4.2) especially because they allow the diffusion of relatively big molecules as proofed by FCS measurements. For a long-term perspecitive it would be very interesting to study the swelling and film stability characteristics theoretically by simulations as well as investigate the diffusion of big and non-fluorescing analytes in thick hydrogel films by SPR/OWS spectroscopy and WKB assisted data analysis.

4.1.7 Experimental

Film Preparation: Hydrogel films were prepared as described in Chapter 3.1. LaSFN9 glass slides (LaSFN9 glass, Hellma Optik GmbH Jena, refractive index n=1,8449) were coated with a 2nm chromium and a 50 nm gold film, deposited by evaporation with a Edwards Auto 306 evaporator followed by chemisorption of *S*-3-(4-benzoylphenoxy)propyl ethanthiol from 5 mM ethanol solution for ~24 h at room temperature. Afterwards the slides were cleaned by extensively rinsing with ethanol and acetone and blown dry with air.

Deposition of dextran films and photo-crosslinking. Dextran films were deposited onto the pre-treated substrates by spin-coating from polymer/water solution with a polymer weight content of 10 % with 4000 rpm for 60 s. The samples were dried in vacuum at 45°C over night and crosslinking was performed for 7-90 minutes with a Stratagene UV Stratalinker 2400 operating at 75 W with an emission maximum at 254 nm.

SPR/OWS Measurements: Surface plasmon resonance- and optical waveguide mode spectroscopy were performed in the Kretschmann configuration.[24]

The sample glass slide (LaSFN9 glass, Hellma Optik GmbH Jena, refractive index n = 1.8449, corresponding to $\varepsilon = 1.3583$) was positioned onto a custom-made glass flow cell (V~40 µl) and was optically matched to the base of the glass prism (refractive index n = 1.8449, corresponding to $\varepsilon = 1.3583$) at the backside. Monochromatic and linear, transverse-magnetic polarized (Glan-Thompson polarizer, Owis) laser light (He/Ne laser, Uniphase, $\lambda = 632.8$ nm) was directed through the prism onto the sample slide. By variation of the angle of incidence (θ) (two cycle goniometer, resolution 0,005°, Huber) and detecting the intensity of the reflected laser light $I(\theta)$ with a photodiode (BPW 34B silicon photodiode, Siemens) an angular dependent spectrum was recorded. The laser intensity was adjusted to 100 % reflectivity for all SPR/OWS experiments corresponding to 145 µW.

SPR/ OWS Data Treatment: To model the measured spectra Fresnel equations were solved by a transfer algorithm[49] for a planar multilayer system consisting of the LaSFN9 glass, chromium, gold, a self assembled monolayer as adhesion promoter, the hydrogel and the swelling solvent. For every layer a value for the thickness (d) and the dielectric constant (ε) consisting of a real part (ε') and the imaginary part (ε'') had to be defined.

To determine the parameters for the sample without hydrogel first a slide only coated with chromium and gold was measured. To define the adhesion promoter values a slide with chromium, gold and *S*-3-(4-benzoylphenoxy)propyl ethanthiol as the adhesion promoter was measured and the recorded spectra were simulated with the above mentioned model assuming all other values as fixed.

If the hydrogel reaches a certain thickness (d~1.5 µm for ε~1.78) it acts as an optical waveguide and optical waveguide mode spectroscopy (OWS) can be performed without changing the setup. Because these waveguide modes directly depend on the thickness and the refractive index of the hydrogel film a further characterization of the hydrogel film refractive index profile, perpendicular to the surface of the slide, was possible. The more waveguide modes exist, the more detailed the characterization of refractive index profile. To simulate the SPR/OWS spectra in the above mentioned model an average refractive index for every layer was assumed (box model). As the hydrogel films were thicker and acted as waveguide the reversed Wentzel-Kramers-Brillouin (WKB) approximation was used to model the refractive index profile perpendicular to the substrate surface of these films[28]. Thereby the hydrogel film was assumed to be laterally (parallel to the substrate surface) homogeneous.

Refractive Index-Thickness Profiles: In the reversed WKB approximation it is assumed that at the position of the electromagnetic field distribution, where the oscillating and evanescent solution of the wave equation are identical, the physical refractive index is equal to the measured effective refractive index for each waveguide mode. The refractive index at the gold-hydrogel interface (x = 0 µm) was experimentally determined by the refractive index of the surface plasmon. This value can be extracted from the box-model simulation of the measured spectrum by simulating the refractive index of the surface plasmon after modeling the waveguide modes and keeping the thickness that was concluded from the simulation of the waveguide modes constant.

The hydrogel samples were swollen in buffer, usually PBS 150mM, over night to reach an equilibrium state followed by the screening of the different buffers.

pH-Buffers: To screen the pH-response of the hydrogel films a 10mM buffer with varying pH between 3 and 8 was prepared. Therefore 1.25mM citric acid, 1.25mM KH_2PO_4, 1.25mM Na_2HPO_4, 1.25mM tris-(hydroxymethyl)-aminomethane and 1.25mM KCl were prepared in ultrapure water and the pH was controlled by adding HCl or NaOH. To investigate the ionic strength effect in a charged hydrogel at pH 7.4 the commercially available PBS solution (150mM) was diluted with ultrapure water. The HEPES buffer was prepared from commercially available HEPES (Sigma Aldrich) by dissolving 2.4g in one liter of ultrapure water to get a 10mM HEPES solution.

Profiler: The hydrogel film surface topography and the film thickness in the dry state were characterized with a profiler (KLA Tencor, P-15 Profiler) with a vertical measuring range of up to 1 mm and a resolution of ~7.5 Å.

Atomic Force Microscopy (AFM): The topography of the hydrogel films before and after swelling and drying cycles was investigated by atomic force microscopy (AFM) in air at room temperature with a commercial AFM (Dimension 3100 CL) in tapping mode. Micro cantilevers (Olympus) 160 µm long, 50 µm wide and 4,6µm thick with an integrated tip of a nominal spring constant of 42 N/m and a resonance frequency of 300 kHz were used. The tip was scanned at rates about 0.7 Hz for scan sized ~1 µm.

Neutron Reflectivity Measurements: The neutron reflectivity measurements were performed on the reflectometer AndR at the Center for Neutron Research, National Institute for Standards and Technology (NIST) in Gaithersburg, MD/USA by Ann Falk.

The samples were placed in a silicon wet cell, mounted on the instrument and aligned. Prior to the neutron reflectivity measurement an incident beam scan through the thick fronting wafer is performed in order to measure the direct beam intensity. The later-on measured specular reflectivity was normalised to the direct beam incident intensity. The specular reflectivity of the sample was first measured in the dry state and afterwards the cell was filled with a D_2O-based PBS buffer (150 mM). The background intensity offset to both sides of the specular ridge was measured separately. The background neutron radiation mainly originates from incoherent scattering from the bulk solvent reservoir.

The neutron reflectivity was calculated from the measured specular raw data, the background data and the incident beam data. The reflectivity profile, hence the plotted intensity of reflected radiation as a function of angle, provides information about the structure of the surface, including thickness, density, and roughness.

Data Reduction with the NCNR 'Reflpak' Reflectometry Package: The NCNR 'reflpak' reflectometry package[50] is one of many different methods to fit neutron reflectivity data. It uses Parratt's recursion relation to calculate reflectivities from a model profile and parameters are varied in a systematic way. In order to calculate the neutron reflectivity, the background intensity is first subtracted from the specular reflectivity and the difference is divided by the incident beam intensity, so called data reduction. The data is fitted by `Reflfit' to a model of neutron scattering length density (sld) profile along the axis perpendicular to the substrate surface. The fitted sld profile is structurally interpreted in terms of chemically distinct layers. In case of a solid supported hydrogel layer, the following order of layers was used: the silicon substrate, the silicon oxide layer, the chromium layer, the gold layer, the spacer region, the hydrogel layer, and the bulk solvent phase. As `Reflfit' only simulates single data sets, it was only used for a rough calculation of the parameters. These parameters were then fed into `Garefl'. This software is also part of the `refpak' package, and allows to simultaneously fit data sets with isotopically different bulk solvents. ``Ga_refl'' is a C++-based system for modelling reflectivity data using Paratt-formalism and model refinement using a genetic algorithm. It has been designed to enable the simultaneous fitting of multiple data sets. The initial model, data sets, constraints and beam details are adjusted in setup c-file. After compiling the setup file, the fitting procedure is started, which involves solution of a coupled linear equation system by GNU octave. Sets of possible values of fitting parameters are created randomly, the reflectivity is calculated for each data set and then evaluated against a test function χ^2.

Fluoresecence Correlation Spectroscopy (FCS): Sample Preparation: The glass substrate was coated with a self-assembled monolayer of 4-(3-triethoxysilyl)propoxybenzophenone followed by spincoating of the aqueous PCMD solution (0.25 g/mL, V = 0.1 mL, 4000 rpm, 60 s). The films were dried in vacuum at 45°C over night and subsequently crosslinked by irradiation of 365 nm (Stratagene UV Stratalinker 2400). The crosslinking is performed with an irradiation dose of 0.105 J $\text{cm}^{-2}\text{min}^{-1}$ at 365 nm.

FCS Experiments: The sample substrates were placed in an attofluor steel chamber (V = 1mL) and kept at a temperature of 16.3 °C with a Peltier element based heating stage. For removing unbound polymer the sample was gently rinsed with with MilliQ water for 5 times. The hydrogel is left for drying at room temperature and the dry thickness is measured. Subsequently, the PCMD film is swollen in buffer and the FCS experiment is performed (Zeiss, Axiovert 200M microscope, ConfoCor 2 FCS unit). For swelling either a pH = 5.0 10 mM acetate buffer (Biacore), a pH = 7.4 10 mM HEPES buffer (Sigma Aldrich) or a pH = 7.4 PBS buffer (Sigma Aldrich) were used.

4.1.8 Bibliography

[1] R. L. Rich, D. G. Myszka, *J. Mol. Recognit.* **2007**, *20*, 300.
[2] S. Löfas, B. Johnsson, *J. Chem. Soc., Chem. Commun.* **1990**, *21*, 1526.
[3] R. Zhang, M. Tang, A. Bowyer, R. Eisenthal, J. Hubble, *Reactive and Functional Polymers* **2006**, *66*, 757.
[4] D. J. Winzor, *Anal. Biochem.* **2003**, *318*, 1.
[5] T. Ito, Y. Yeo, C. B. Highley, E. Bellas, D. S. Kohane, *Biomaterials* **2007**, *28*, 3418.
[6] R. Kalpana, K. Park, K. Park, *Polymer Gels and Networks* **1995**, *3*, 243.

[7] Y. L. Zhang, C. Y. Won, C. C. Chu, *J. Polym. Sci. A* **2000**, *38*, 2392.

[8] F. Plieva, A. Oknianska, E. Degerman, I. Y. Galaev, B. Mattiasson, *J. Biomater. Sci. Polymer Edn.* **2006**, *17*, 1075.

[9] D. Imren, M. Gümüsderelioglu, A. Güner, *J. Appl. Polym. Sci.* **2006**, *102*, 4213.

[10] H.-C. Chiu, G.-H. Hsiue, Y.-P. Lee, L.-W. Huang, *J. Biomater. Sci. Polymer Edn.* **1999**, *10*, 591.

[11] S. Namkung, C.-C. Chu, *J. Biomater. Sci. Polymer Edn* **2007**, *18*, 901.

[12] J. Maia, L. Ferreira, R. Carvalho, M. A. Ramos, M. H. Gil, *Polymer* **2005**, *46*, 9604.

[13] A. Katchalsky, S. Lifson, H. Eisenberg, *Polym. Sci.* **1951**, *7*, 571.

[14] P. Flory, *Principles of Polymer Chemistry, Vol. Chapter XIII*, Cornell University Press, Ithaca, **1953**.

[15] A. Katchalsky, I. Michaeli, *J. Polym. Sci.* **1955**, *9*, 69.

[16] M. Biesalski, D. Johannsmann, J. Rühe, *J. Chem. Phys.* **2004**, *120*, 8807.

[17] Y. Qiu, K. Park, *Advanced Drug Delivery Reviews* **2001**, *53*, 321.

[18] A. E. English, T. Tanaka, E. R. Edelman, *J. Chem. Phys.* **1997**, *107*, 1645.

[19] T. A. Vilgis, A. Johner, J. F. Joanny, *Eur. Phys. J. E* **2000**, *3*, 237.

[20] Y. V. Lyatskaya, F. A. M. Leermakers, G. J. Fleer, E. B. Zhulina, T. M. Birshtein, *Macromolecules* **1995**, *28*, 3562.

[21] O. Azzaroni, S. Moya, T. Farhan, A. A. Brown, W. T. S. Huck, *Macromolecules* **2005**, *38*, 10192.

[22] J. Wilder, T. A. Vilgis, *Phys. Rev. E* **1998**, *57*, 6865.

[23] T. A. Vilgis, J. Wilder, *Computational and Theoretical Polymer Science* **1998**, *8*, 61.

[24] W. Knoll, *Annu. Rev. Phys. Chem* **1998**, *49*, 569.

[25] P. Englebienne, A. V. Hoonacker, M. Verhas, *Spectroscopy* **2003**, *17*, 255.

[26] D. K. Kambhampati, W. Knoll, *Current opinion in Colloid & Interface Science* **1999**, *4*, 273.

[27] P. W. Beines, I. Klosterkamp, B. Menges, U. Jonas, W. Knoll, *Langmuir* **2007**, *23*, 2231.

[28] M. Weisser, F. Thoma, B. Menges, U. Langbein, S. Mittler-Neher, *Opt. Commun.* **1998**, *153*, 27.

[29] P. K. Tien, *Rev. Mod. Phys.* **1977**, *49*, 361.

[30] T. P. Russell, *Physica B* **1996**, *221*, 267.

[31] J. Penfold, *Current Opinion in Colloid & Interface Science* **2002**, *7*, 139.

[32] G. Fragneto-Cusani, *J. Phys.: Condens. Matter* **2001**, *13*, 4973.

[33] J. A. Dura, D. J. Pierce, C. F. Majkrzak, N. C. Maliszewskyi, D. J. McGillivray, M. Lösche, K. V. O'Donovan, M. Mihaisescu, U. Perez-Salas, D. L. Worcester, S. H. White, *Rev. Sci. Instrum.* **2006**, *77*, 074301/1.

[34] B. Struth, A. Vorobiev, T. Seydel, L. Wiegart, J. Major, *Physica B* **2004**, *350*, e917.

[35] B. Struth, F. Rieutord, O. Konovalov, G. Brezesinski, G. Grübel, P. Terech, *Phys. Rev. Lett.* **2002**, *88*, 025502.

[36] E. Stenberg, B. Persson, H. Roos, C. Urbaniczky, *Journal of Colloid and Interface Science* **1991**, *143*, 513.

[37] M. E. Harmon, D. Kuckling, C. W. Frank, *Macromolecules* **2003**, *36*, 162.

[38] M. Harmon, D. Kuckling, P. Pareek, C. W. Frank, *Langmuir* **2003**, *19*, 10947.

[39] L. Brannon-Peppas, N. A. Peppas, *Chem. Eng. Sci.* **1991**, *46*, 715.

[40] H. Noguchi, K. Gekko, S. Makino, *Maromolecules* **1973**, *6*, 438.

[41] G. J. Fleer, *Ber. Bunsenges. Phys. Chem.* **1996**, *100*, 936.

[42] Y. V. Lyatzkaya, F. A. M. Leermarkers, G. J. Fleer, B. Zhulina, T. M. Birshtein, *Macromolecules* **1995**, *28*, 3562.

[43] E. B. Zhulina, T. M. Birshtein, O. V. Borisov, *Macromolecules* **1995**, *28*, 1491.

[44] E. B. Zhulina, O. V. Borisov, *J. Chem. Phys.* **1997**, *107*, 5952.

[45] R. Israels, M. L. F. A, G. J. Fleer, *Macromolecules* **1994**, *27*, 3087.

[46] M. Biesalski, D. Johannsmann, J. Rühe, *J. Chem. Phys.* **2002**, *117*, 4988.

[47] K. Gekko, H. Noguchi, *Biopolymers* **1975**, *14*, 2555.

[48] M. R. Rodrigues, D. Gasetta, *Journal of Carbohydrate Chemistry* **2007**, *26*, 439.

[49] M. Born, E. Wolf, in *Principles of Optics, 7th ed.*, Cambridge University Press, Cambridge, U.K., **1999**.

[50] P. A. Kienzle, M. Doucet, D. J. McGillivray, D. V. O. D. N. F. Berk, C. F. Majkrzak, in *GaRefl. NIST NCNR*, **2000-2006**.

4.2 Dextran-Based Hydrogel Films as Biosensor Matrices

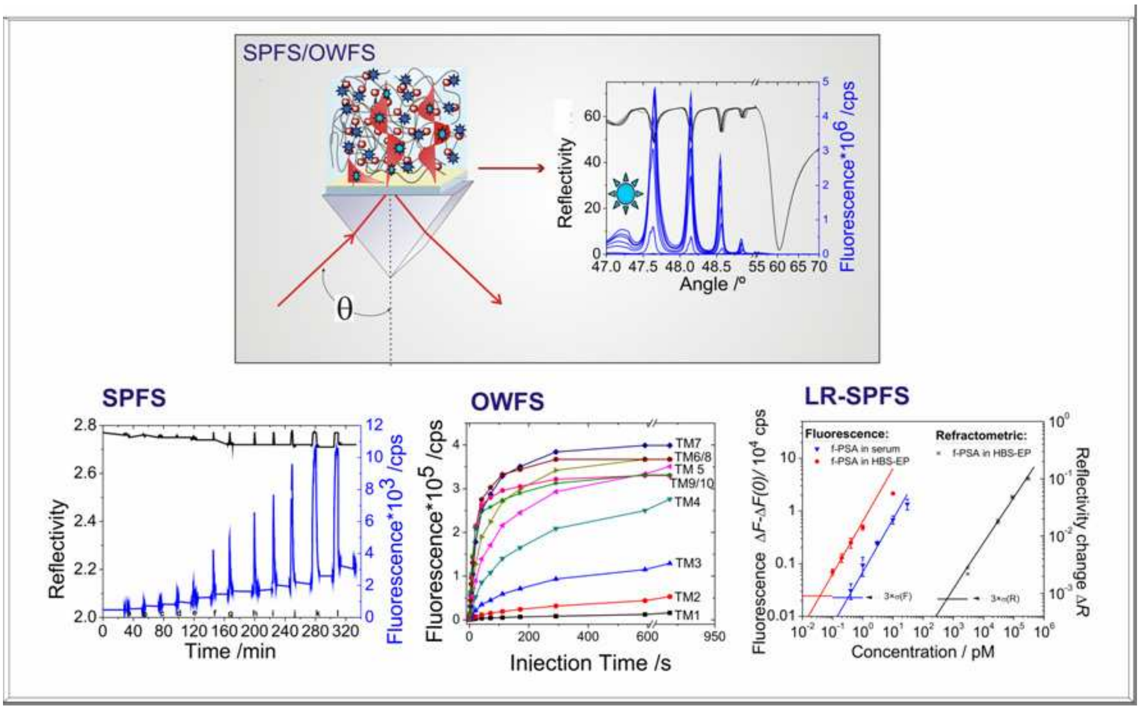

The photo-crosslinked, carboxymethylated dextran-based hydrogel (PCMD) matrices presented in Chapter 3.1 and 4.1 were characterized in terms of their applicability as biosensor matrices. Two different methods requiring thick sensor matrices from one to several micrometers were developed. The analyte detection with optical waveguide mode enhanced fluorescence spectroscopy (OWFS) using the PCMD hydrogel as waveguiding and analyte binding medium shows high potential for sensitive detection. Furthermore, the implementation of the PCMD matrix for analyte detection with long range surface plasmon (LRSP) spectroscopy and LRSP enhanced fluorescence spectroscopy (LR-SPFS) has been demonstrated for model probe solutions as well as with clinically relevant samples.

4.2.1 Introduction

Functionalized dextrans are a well known platform for label free and rapid determination of a wide range of biological compounds.[1-4] As an example, ~100 nm thick carboxymethylated dextran (CMD)[5-7] brushes which show a very low unspecific binding of biomolecules[2, 8, 9] are used as biosensor matrices for analyte detection with surface plasmon resonance (SPR) and surface plasmon resonance fluorescence spectroscopy (SPFS).[10, 11] Comparable systems include functional self-assembled monolayers (SAM), for example carboxyl functionalized thiols and brushes based on aldehyde dextran[12-16] or aminodextran.[17, 18] The chemical characteristics and the thickness of the analyte-capturing matrix are crucial for biosensing. Both determine biomolecule functionality and analyte diffusion and binding. A three dimensional structure of the analyte-capturing matrix results in a high receptor density and thus a high binding capacity of the sensor. The sensitivity of sensor experiments can be increased by two orders of magnitude with three-dimensional receptor matrices compared to a two-dimensional receptor layer.[19] The high binding capacity of a three-dimensional sensor matrix results in diffusion or mass-transport limited analyte binding. This leads to a constant binding rate and a linear concentration dependent signal provided that constant flow conditions are used.[20] To enable a specific analyte detection, biorecognition elements such as antibodies,[21-26] enzymes,[27, 28] peptides,[29, 30] nucleic acids,[30-32] receptors,[33, 34] or cells[35-37] have to be introduced to the biosensor matrix. Preferably, carboxyl groups are used for covalent coupling of analyte capturing units because of the manifold recognition chemistry they enable after active ester activation, which is commonly carried out with EDC/NHS.[10, 38] This active ester activation with EDC/NHS can be achieved under mild conditions in water which is necessary to maintain the functionality of sensitive analyte-capturing biomolecules such as antibodies. This strategy facilitates the coupling of functionalized primary or secondary amines and allows the immobilization of antibodies preserving a good accessability of the recognition site for analytes.[13, 39] Besides these sensor matrices that allow the coupling of analytes, matrices that enable the tuning of analyte detection are fascinating. Sensor matrices can be tuned by utilizing a stimuli responsive behaviour[40, 41] and thereby manipulate the analyte binding or analyte density. Another method is to influence the analyte binding by an extending PNIPAAm brush layer that prevents analyte coupling to an underlying layer in the swollen (T = 18 °C) but allows it in the collapsed state (T = 30 °C)[42] SPR and optical waveguide mode spectroscopy (OWS) allow the real time *in situ* and label free detection of analyte binding events.[43, 44] For medium size proteins with a molecular weigth around 55 kDA such as prostate specific antigen (PSA)[45, 46], hormones like estrogen [47], neurotransmitter like dopamin[48] as well as for drug discovery[49] for example they were shown to allow the direct detection down to nM concentrations. Theoretically, the limit of detectable surface concentration was determined to be around 50 pg/mm².[50]

Not only purified model systems can be analyzed, the system is as well applied to practical samples such as milk, blood or serum.[51-56] Because SPR/OWS is based on monitoring the change of the optical mass density,[25, 49, 57] the limit is given by the detection of small molecules at low concentrations.[58] To overcome this limit either the binding-induced refractive index changes have to be enhanced or another detection technique has to be used. Approaches to enhance the SPR sensitivity include assays with metallic nanoparticle and localized surface plasmons,[59-68] enzyme[69, 70] labels, or higher molecular weight analytes[71] which were demonstrated to improve the limit of detection (LOD) by several orders of magnitude. Furthermore, signal enhancement by immunoreactions,[28, 72] receptor conformational changes[58] and recently by the application of gold atoms[73] was achieved. In addition, an approach for improving the sensitivity through the combining of SPR biosensors with fluorescence spectroscopy was developed.[74-77] In this method, referred to as surface plasmon-enhanced fluorescence spectroscopy (SPFS), the capture of molecules labeled with fluorophores is observed through the detection of the intensity of the fluorescence light emitted from the sensor surface. In this technique the evanescent optical field of the surface plasmon (SP) is used to excite fluorescence in the analytes. A drawback of SPFS is quenching of the fluorescence mainly due to Förster transfer in case the chromophores are too close (30-40nm)[78] to the metal surface of the substrate. However, the interaction of fluorophores with surface plasmons allows to enhance the excitation rate[79, 80] of molecules adhered to the metallic surface as well as the efficient collection of the fluorescence light [81, 82] and thus increases the measured fluorescence signal. SPFS biosensors that rely on immunoassays were reported to enable the detection of protein molecules below fM concentrations.[83, 84] A lot of sensor assays in the field of SPR sensors are reported[85-87] and are already commercially available.[1, 88, 89]

As a further development for improved sensor concepts hydrogel films of a certain thickness might be beneficial as they can not only be used as matrix for SPR and SPFS but also for OWS and optical waveguide mode excited fluorescence spectroscopy (OWFS). To achieve a waveguiding effect, the hydrogel layer has to be uniform, well adhesive and non-conductive to trap the acoustic energy near the surface.[57, 90, 91] Leaky optical waveguide mode spectroscopy allows a preciser thickness and refractive index determination[92] and the detection of thickness and refractive index changes due to the increased number of modes in the angular scan that can be simulated. The common architecture for sensing with leaky optical waveguide modes consists of a uniform waveguiding layer with good adhesion to the surface and an analyte capturing layer on top.[17, 93-95] With this sensor concept the evanescent electromagnetic field of the optical waveguide mode is applied for analyte or molecular changes detection[96] and sensitivities in the range of nanomolar[97] to femtomolar[98, 99] concentrations are reported.

With a highly swelling hydrogel film, allowing analytes to diffuse inside, and a thickness appropriate to generate optical waveguide modes, OWFS is expected to be an efficient technique for *in situ* real time detection and affinity binding studies. This architecture in particular permits the detection in the center of the electromagnetic field of the optical waveguide modes. The increased light intensity in the optical waveguide modes was measured by Dürr and co-workers[100] and verified by Mathias *et al.* as well.[101] Particularly advantageous is the high optical field intensity and the high loading capacity inside the thick hydrogel film.[101] This should be valid especially for small analytes not inducing sufficient increase in the optical mass density to be detected in adequate low concentrations with SPR.

Recently, long-range surface plasmons (LRSPs) were exploited for SPFS biosensing.[102-104] These optical waves originate from the coupling of surface plasmons on opposite surfaces of a thin metallic film that is embedded between dielectrics with similar refractive indices. LRSPs exhibit orders of magnitude lower damping compared to regular surface plasmons on an individual metallic surface.[105] Therefore, their excitation provides a larger enhancement of the electromagnetic field intensity and thus allows for a stronger increase of the fluorescence signal in SPFS sensors. In addition, LRSPs probe the medium adjacent to the metallic surface with a more extended evanescent field than regular surface plasmons.[103] Thus, three-dimensional binding matrices with up to micrometer thicknesses have been proposed for the immobilization of biomolecular recognition elements with large surface density that allows to exploit the whole evanescent field of LRSP.[106] Currently, new hydrogel materials based on NIPAAm [N-(isopropylacrylamide)] and dextran polymers were developed in our laboratory and they were demonstrated to be suitable for the construction of such surface architectures.[25, 40, 107]

A plethora of possible analytes exist. Not only proteins, antibodies, or bacteria[108] but also small molecules like pesticides[97] or protein isomerization[4] can be observed.

A frequently used model system for biorecognition is the binding of streptavidin to biotin.[109] Streptavidin is a medium sized protein with a molecular weight of 60 kDa and a size of 4,4 x 4,5 x 5,8 nm.[110] The high affinity binding constant of $K_A = 10^{13}$M[111] to the low molecular weight biotin[39] is due to the hydrogen bond cooperativity and low desolvation energetics.[112]

Another interesting and clinically relevant analyte is the tumor-suppressor-protein p53 and its primary antibody p53Ab6. The p53 structure and its functional domains are well investigated.[113] p53 functions as transcription factor and blocks the cell cycle in the G1 phase to enable DNA repair or cell apoptosis and thus prevents the proliferation of damaged cells. Mutations of p53 often occur in the so called “core-region” that serves as DNA binding unit leading to a deformed tertiary structure interfering with the DNA binding.[114-117] Subsequently, uncontrolled cell growth is induced resulting in tumor formation which is supported by the prolonged half-life of mutated p53 and its complex formation with wild type p53.[118, 119] Almost 50% of all tumors, especially in bladder, breast, colon and testicular carcinomas and melanomas are reported to carry p53 mutations.[118, 120] The detection of p53 by immunohistochemistry is still under discussion.[118, 120] For bladder cancer a correlation of p53 mutations with tumor stage and grade was shown.[121] Nevertheless, the reports are still contradictory.[122, 123] The identification of protein interaction in a cell extract by screening assays could be helpful for studies of p53-DNA interaction or the search for drugs acting on p53.[119] These kind of interactions are commonly detected by Enzyme-linked Immunosorbend Assay (ELISA)[124-126] but as well by fluorescence assays in the range of ng/ml.[119] Mutants of p53 were sensitively analyzed by mutant enriched PCR-SSCP.[127] To evaluate the binding constant and thus characterize the molecular interactions quantitative information can be obtained by SPR based biomolecular interaction analysis.[128-131] The DNA binding activity of p53 was studied by SPR, too.[132] Recent developments deal with sensitivity enhancement: TP53 mutations were detected[133] with an increased sensitivity and the sensitivity of p53 c-DNA detection was improved to sub-attomolar concentrations by enhancement with gold nanoparticles.[68, 133] Signal enhancement was equivalently achieved by PCR amplification of the practical samples before detection with SPR.[134]

Furthermore, a production of p53-antibodies in an autoimmune response has been reported[125, 135, 136] and circulating anti-p53 antibodies (p53Abs) were found in sera of patients with various human malignancies.[137-142] For p53, antibody prevalence was associated with p53 overexpression or accumulation upon p53 mutation. [125, 135, 136] Antibodies were rarely found (0-3%) in healthy control patients[136] but have been shown recently to function as tumor marker in colorectal cancer for example.[143] The relation between serum p53Abs as a prognostic marker, the prognosis for cancer patients with serum p53Abs and the functional relevance of p53Abs are discussed contradictory.[125, 144-148] [142, 149-151] Nevertheless, the immune response might be used for early detection of cancer, prognosis and post-treatment. Especially for early detection a high sensitivity is necessary to improve the clinical specificity and to allow a diagnosis in an early stage.

An ideal sensor should be sensitive, specific and fast. In the following chapter first developments for an OWFS-detection assay are presented. Therefore, the detection of streptavidin-Cy5 as a model analyte and p53Ab6 as a clinically relevant analyte are discussed. The matrix is characterized for both analytes in terms of covalent modification of analyte capturing units, unspecific binding, and fluorescence enhancement by OWFS compared to SPFS are discussed. Additionally, the application of the developed sensor matrix for the detection of PSA with LRSP is described.

4.2.2 Matrix Modification – Covalent Attachment of Analyte Capturing Units

It is desirable to couple a broad variety of analyte capturing molecules into a sensor matrix to permit a specific detection of certain analytes with one type of sensor matrix. Basically, every molecule containing primary amino groups can be covalently coupled to active ester activated carboxyl groups. The general sensor concept is schematically depicted in Figure 4.2.1. The photo-crosslinked carboxymethylated dextran-based (PCMD) hydrogel matrix (Chapter 3.1, 4.1) was modified with analyte capturing units followed by the detection of (labelled) analytes. Especially, the analyte detection by leaky optical waveguide mode enhanced fluorescence spectroscopy (OWFS) (Figure 4.2.1) is a versatile approach as discussed in this chapter. The active ester activation permits the covalent coupling of proteins or antibodies as selective analyte capturing units by forming an amide bond between amino-functionalized amino acids such as lysine and active ester activated carboxyl group in the hydrogel matrix. The most common active ester activation is a combination of 1-(3-dimethylaminopropyl)-3-ethylcarbodiimide hydrochloride (EDC) and *N*-hydroxysuccinimide (NHS) in water (Figure 4.2.1). [2, 10, 50] The advantage of EDC/NHS-coupling are the mild reaction conditions in water which allows to maintain biomolecule functionality. Simultaneously, water hydrolyses the active ester and limits its stability. Nevertheless, the activation rate was higher than the degradation and under direct coupling after EDC/NHS activation in water a sufficient number of carboxyl groups was transformed. The coupling efficiency to the active ester-modified carboxyl groups is influenced by many parameters related to the matrix, the coupled molecule, and the coupling conditions. These parameters are not independent and open a broad variety of optimization possibilities and necessities.

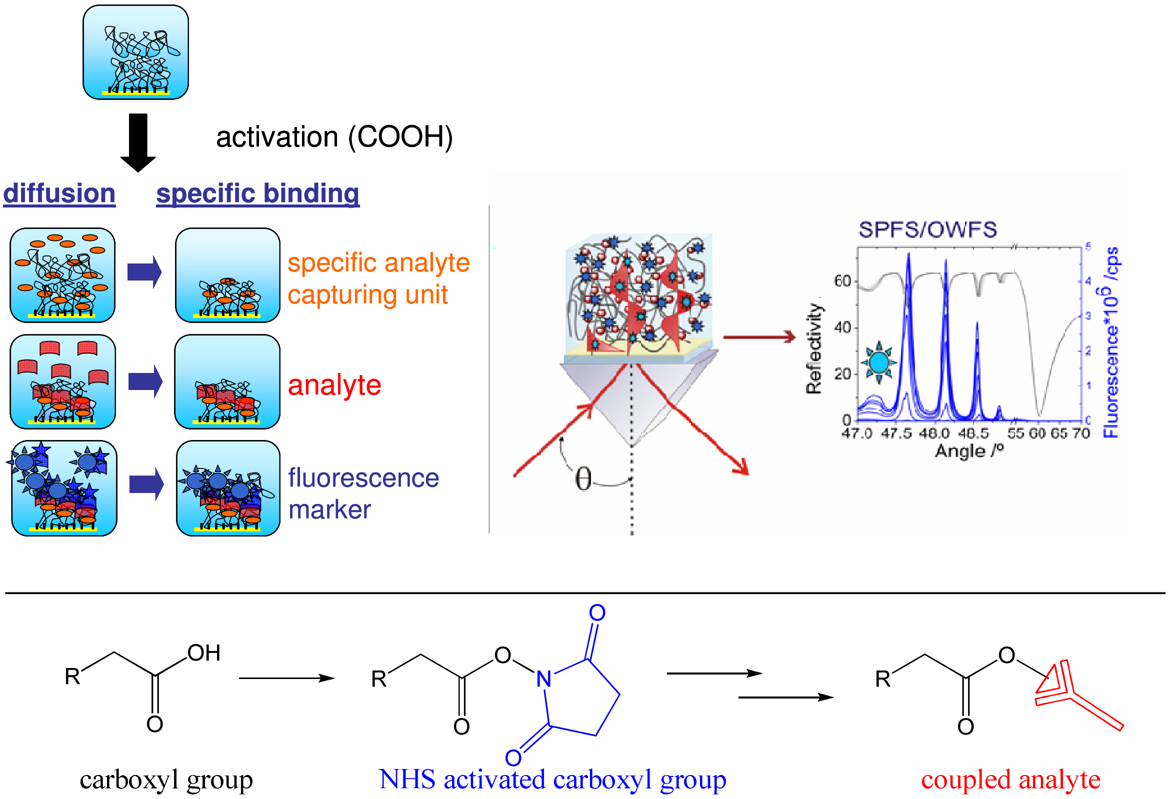

Figure 4.2.1: Schematic presentation of the sensor concept applied in this work. Every coupling step contains diffusion and rinsing procedure. Carboxyl group activation with active ester chemistry facilitates covalent coupling of a specific, amino-functionalized analyte-capturing unit via amide bond formation. Subsequently, analytes (red) are coupled to the capturing unit (orange) and detected directly by OWFS or indirectly with a secondary coupling of a labelled recognition unit (blue).

Different types of active esters from hydrophilic to more hydrophobic and charged active esters were prepared in our group by Robert Roskamp and tested with a poly(NIPAAm) based hydrogel.[40] The individual active esters show varying coupling efficiency with different proteins and antibodies.[25] For the dextran based hydrogel presented here, the anionic active ester sodium para-tetrafluorophenol sulfonate (TFPS) (Figure 4.2.2) was used in combination with EDC to couple bovine serum albumine (BSA).

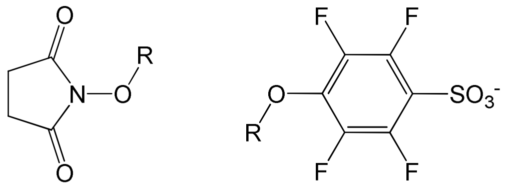

NHS TFPS

Figure 4.2.2: Molecular structure of the active esters para-tetrafluorophenol sulfonate (TFPS) and N-hydroxysuccinimide (NHS).

The refractive index change upon BSA binding with EDC/TFPS in aqueous solution was comparable to the active ester activation with EDC/NHS in the range of 0.007-0.0141 depending on the pH of the swelling medium. The corresponding surface mass density (Γ) can be calculated from the refractive index contrast (n(hydrogel) (n_h) - n(buffer) (n_b)) and the thickness (d_h) of the binding matrix with the following relation:

$$\Gamma = \left(n_h - n_b\right) d_h \frac{\partial c}{\partial n_h} . \tag{4.2.1}$$

The surface mass density of the pure dextran hydrogel for this film was ~90 ng/mm². The surface mass density of the coupled BSA is calculated from the difference in surface mass density before and after coupling, and was determined to be in the range of 20 ng/mm^2 for a 4 µm thick swollen hydrogel film. The calculated surface mass density is about one order of magnitude higher than the reported surface mass densities for a dextran brush system with a thickness of 100-200 nm.[7, 152] The carboxyl groups are partly deprotonated at this pH and the negatively charged carboxyl groups cause an ionic attraction between the positively charged BSA and the hydrogel film. The anionic active ester maintains this charge and the ionic attraction. Since no remarkable difference between the activation with EDC/NHS and EDC/TFPS was observed all biosensor experiments were therefore performed with the commercially available EDC/NHS.

In this work biotinethylenediamine was coupled into the hydrogel matrix as a model system for the detection of fluorescence labeled streptavidin. As a clinically relevant analyte p53 as tumorsuppressor protein and its primary antibody p53Ab6 were used.

Biotin

In order to demonstrate the potential of the developed hydrogel film as a binding matrix, the affinity binding of streptavidin-Cy5 to a biotin-modified PCMD hydrogel matrix was observed by SPFS and OWFS. In further experiments, hydrogel films with a degree of benzophenone substitution of 0.04 and a degree of carboxymethylation of 0.16 were applied. These films were attached to a gold surface by irradiation at 254 nm for 30 minutes and swollen in PBS. They exhibited a swollen thickness of approximately 6 μm with a swelling degree of ~13 and an average refractive index of ~1.358, which corresponds to a surface coverage of ~295 ng/mm² in 150 mM PBS as determined from the angular position of four optical waveguide modes by WKB.[40]

At first, a hydrogel film was functionalized with biotin moieties. In the biosensor experiments 150 mM PBS as buffer was used mimicking physiological conditions.[10] A reference hydrogel film was prepared in which the carboxyl groups were activated by EDC/NHS and subsequently reacted with ethanolamine to investigate a possible unspecific binding of streptavidin (Chapter 4.2.3). Furthermore, the coupling reaction was performed on a self-assembled monolayer of 11-mercaptoundecanoic acid as a 2D system for comparison.

The matrix modification was followed in real time at a fixed angle in the linear part of the surface plasmon (Figure 4.2.3 A). Additionally, after rinsing and reaching the equilibrium surface plasmon signal for every modification step an angular scan is recorded (Figure 4.2.3 B). If the injected molecule causes a signal change in the surface plasmon, this results from a change of the refractive index at the gold interface. The electromagnetic field of the surface plasmon decays exponentially for ~200 nm[57] perpendicular to the gold surface. Therefore, the surface plasmon indicates the diffusion through the entire hydrogel film down to the gold hydrogel interface (Chapter 2.1).

The refractive index-thickness film profiles are extracted from the angular scans using the WKB approximation as described in Chapter 2.3. The alteration in the hydrogel film profile upon matrix modification depicts the binding of molecules and changes of the hydrogel matrix itself. These two contributions are difficult to differentiate. Furthermore, the magnitude of the refractive index change depends on the initial refractive index value of the hydrogel film and is proportional to the amount of molecules coupled into the matrix. EDC/NHS activation and biotinethylenediamine binding lead to a deswelling of the hydrogel film (Figure 4.2.3, 4.2.4) due to a reduced number of charges in the hydrogel network, making it difficult to extract the amount of immobilized biotin from the change in refractive index. With an overall refractive index of $n_h = 1{,}358$ and a refractive index increase of delta $n = 0{,}005$ the biotin surface mass density was determined to be between 20 and 60 ng/mm². The deswelling effect upon biotinethyleneamine binding is more pronounced in low ionic strength buffers and at pH values above the isoelectric point of the carboxyl groups. The swelling of the pure hydrogel matrix is enhanced at low ion concentrations and at pH values above pH = 4 because of electrostatic repulsion between the negative charged carboxyl groups and increased solvent quality (salting out effect). Coupling of uncharged molecules such as biotinethyleneamine causes a charge reduction and thereby a shrinking (Figure 4.2.3). The same effect is observed for the active ester activation. The difference to the unmodified hydrogel matrix is increased in case the pure hydrogel is swollen by electrostatic repulsion of the later blocked charges (Figure 4.2.4). If the hydrogel matrix is rinsed for several hours after biotin coupling a partial re-swelling is detected (Figure 4.2.3 B).

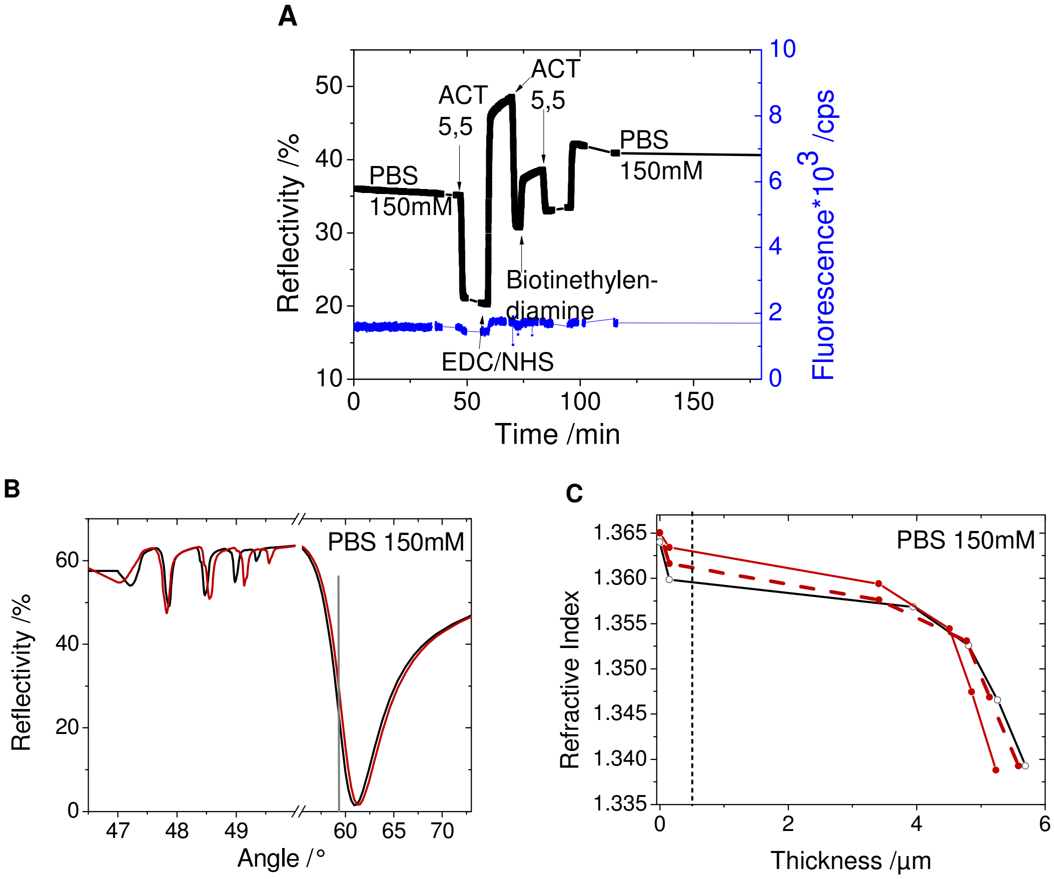

__Figure 4.2.3:__ Matrix modification with biotinethylenediamine. __A)__ Real time observation at a fixed angle in the linear part of the surface plasmon (grey line in B). __B)__ The angular scans in PBS 150 mM before (black, min 40) and after (red, min 150) biotinethyleneamine coupling. __C)__ The corresponding WKB profile of the PCMD binding matrix, extracted from the angular scans, before (black) and after (red) biotinethyleneamine binding and after rinsing over night (red, dotted). The dry layer thickness is indicated by the black dashed line. The coupling was performed with 0.4 M EDC and 0.1 M NHS in 1mL followed by the incubation of 2 mg biotinethyleneamine in 1 mL acetate buffer (10 mM, pH = 5.5).

The re-swelling can be attributed to the hydrolysis of unreacted active esters, an aging effect due to chain disentanglement as observed for pure gels, or the removal of unbound biotinethylenediamine molecules. Most likely, a hydrolysis of unreacted active esters is responsible for the re-swelling because the irreversible swelling usually is not observed anymore after diffusing big molecules such as antibodies or after environmental changes like in the coupling reaction of biotinethyleneamine. Furthermore, the hydrolysis and re-swelling after active ester activation was observed by kinetic measurements (data not shown) to take place on a timescale of several hours. The measured refractive index changes are in the range of 0.001-0.003 in the center of the hydrogel matrix. This is related to a deswelling of the binding matrix. The coupling of biotinethyleneamine results in a surface coverage[25] of Γ=20-60 ng×mm^{-2}. For this calculation a refractive index change with the concentration of biotin and the dextran polymer is assumed to be $\partial n/\partial c$ = 0.2 µL×mg^{-1}[153] and a buffer refractive index of n_b = 1.333. The measured surface mass density is one order of magnitude higher than reported for CM5 chips with a thinner binding matrix of ~100 nm[154] but in agreement with PSA binding experiments performed with comparable dextran matrices in the range of 1µm in the swollen state (Chapter 4.2.7).[155]

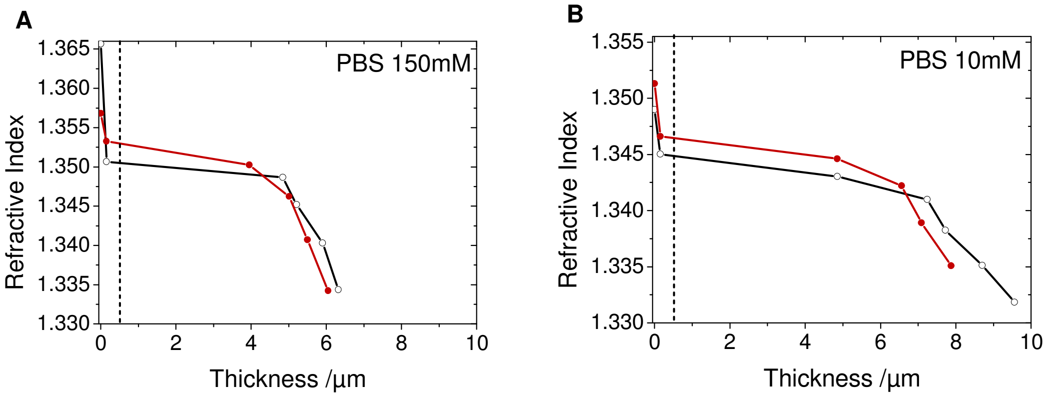

Figure 4.2.4: *WKB refractive index-thickness profiles of the PCMD binding matrix, extracted from the angular scans, before (black) and after (red) biotinethyleneamine binding.* ***A)*** *SPR/OWS measurement was performed in PBS buffer with a concentration of 150 mM and* ***B)*** *a concentration of 10 mM. The compaction effect is more pronounced for PBS 10 mM. The coupling was performed with the same hydrogel as compared to Figure 4.2.3 but different coupling conditions: The EDC concentration was adjusted to 0.8 M and the NHS concentration to 0.025 M with a total volume of 1 mL followed by the incubation of 250 µg biotinethyleneamine in 500 µL PBS 10 mM. The surface mass density was determined to be ~40 ng/mm².* *The dry film thickness is indicated by the black dashed line.*

The reference hydrogel film in which the carboxyl groups were activated by EDC/NHS as described above and subsequently reacted with ethanolamine is shown in Figure 4.2.5 A. After ethanolamine coupling this reference film was used to investigate a possible unspecific binding of streptavidin-Cy5 (Chapter 4.2.3). In PBS 150 mM hardly any difference in the hydrogel film profile upon ethanolamine coupling can be observed. This indicates most probably an almost complete counterion charge screening in PBS (Chapter 4.1). Nevertheless, the refractive index increase indicates ethanolamine coupling as well.

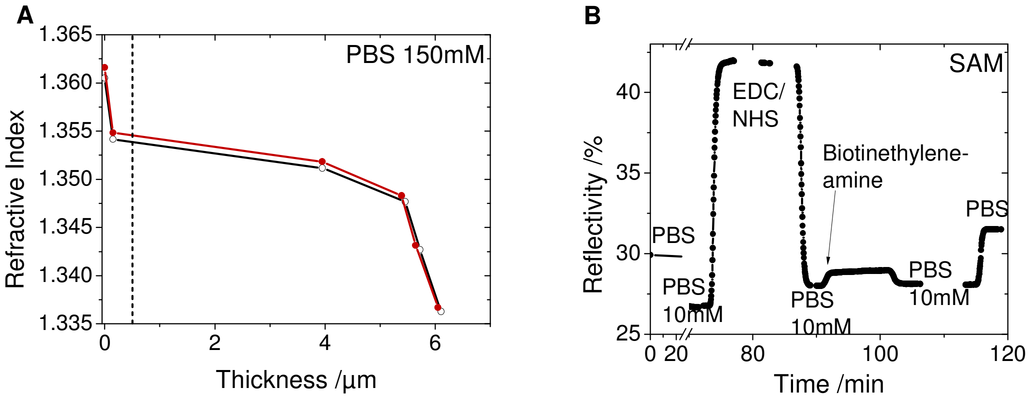

***Figure 4.2.5:** **A)** WKB profile of the PCMD binding matrix, extracted from the angular scans before (black) and after (red) ethanolamine binding for the later investigation of the unspecific binding of streptavidin-Cy5. The dry film thickness is indicated by the black dashed line. **B)** The modification of a self-assembled monolayer of 11-mercaptoundecanoic acid, as a reference system for streptavidin-Cy5 detection, with biotinethyleneamine. The concentrations for coupling were identical to the corresponding reaction in the PCMD matrix shown in Figure 4.2.3.*

As second reference experiment, the coupling of biotinethyleneamine on a self-assembled monolayer (SAM) of 11-mercaptoundecanoic acid as a 2D system with SPR was performed (Figure 4.2.5 B). The reflectivity increases from 30 to 31.5 % in PBS 150 mM which is lower than the reflectivity change observed for biotinethyleneamine coupling into the hydrogel matrix at identical reaction conditions. The reflectivity increase for the hydrogel matrix was determined to be 5.6 % from 35.2 % in PBS 150 mM before biotinethyleneamine coupling to 40.8 % afterwards (Figure 4.2.3 A).

p53/p53Ab6

In order to detect a clinically relevant analyte an assay for the tumor suppressor protein p53 and its primary antibody p53ab6 were developed. The hydrogel can be modified with both, p53 and p53Ab6 after EDC/NHS activation. The following experiments were performed by covalent coupling of p53 as a specific analyte capturing unit and subsequent primary antibody detection. Since the production of antibodies to p53 is an autoimmune response qualifies them as potential tumor markers and there is an expected signal increase of p53Ab6 due to its higher molecular weight compared to p53. Furthermore, the antibodies usually possess a longer lifetime than p53.

The covalent coupling of p53 is carried out after EDC/NHS activation as described for the biotinethyleneamine coupling. For the coupling a 10mM acetate buffer with a pH of 5.5 is used which is below the isoelectric point of p53. The solution with a concentration of 24µg/100µL is injected for 85 minutes after EDC/NHS activation. The binding of p53 induces a deswelling of the hydrogel matrix comparable to the binding of biotinethyleneamine. This shrinking is more pronounced for pH 8 and pH 5.5 than for pH 3 and PBS 150 mM because at pH 8 and 5.5 the swelling of the pure hydrogel matrix is enhanced by the deprotonated carboxyl functionalities (Figure 4.2.6). For the p53-modified hydrogel matrix two effects have to be taken into account: the increase in refractive index due to p53 as an additional component and the charge interaction. The isoelectric point of p53 is located between pH = 6-7, the one of the carboxyl group between pH = 4-5. Consequently, for a complete conversion of carboxyl groups the pH-sensitive swelling is determined by p53.

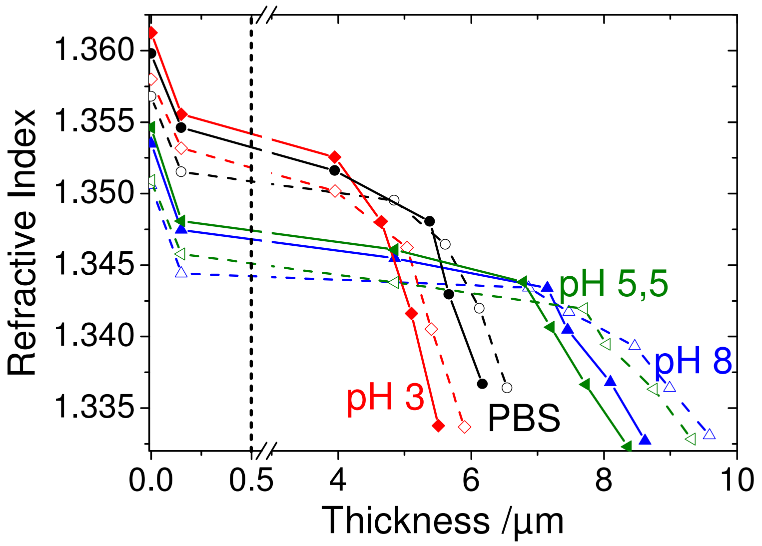

Figure 4.2.6: *WKB profiles of the PCMD matrix at different pH values before (solid line) and after (dotted line) p53 coupling. The dry film thickness is indicated by the black dotted line.*

This observed swelling behavior indicates a smaller number of charges present in the hydrogel after modification than expected.

4.2.3 Diffusion of Analytes and Unspecific Binding

Sensor applications based on the detection of a refractive index or fluorescence signal change are also sensitive to non-specific adsorption. The signal change due to non-specific absorption limits the sensitivity and the limit of detection. The problem increases if complex samples like serum or blood for example are measured instead of pure analyte solutions. Non-specific binding has been studied for many systems.[9, 10, 156-160] To determine the unspecific binding and the background signal of the photo-crosslinked carboxymethylated dextran (PCMD) matrix presented in this work the diffusion of analytes into a capture molecule-free PCMD matrix was investigated.

In aqueous solutions, the protein adsorption onto a surface is driven by the electrical double layer potential, the ionization tendencies and the hydrophilicity of the surface, interface entropic effects and the (hydro-)dynamics of the interface.[161] Proteins have hydrophobic, ionic as well as polar domains. Therefore, protein adsorption is a very complex process and almost unavoidable in complex systems. Controlling and minimizing the amount of unspecific protein adsorption is a key step for sensor preparation. It has been shown that self-assembled monolayers like 16-mercaptohexadecanoic acid or 11-mercaptoundecanoic acid show a higher resistance to non-specific adsorption than carboxymethylated dextran brushes.[9]

Biotinethyleneamine

As discussed in Chapter 4.2.1 biotin is coupled into the PCMD matrix as a capturing unit for streptavidin. Biotin/streptavidin is an extensively studied and well characterized model system for affinity binding due to its high affinity binding constant.[39, 109-112] One streptavidin can bind four biotin units. To investigate the unspecific binding of biotin to the PCMD, the matrix was incubated with a biotinethyleneamine solution in 10 mM PBS buffer (pH = 7,4) of 2 mg/mL for 10 min followed by rinsing with the pure buffer. The incubation was observed in real time at a fixed angle in the linear regime of the surface plasmon (Figure 4.2.7 A) as well as by angular scans giving the refractive index-thickness profile changes (Figure 4.2.7 B).

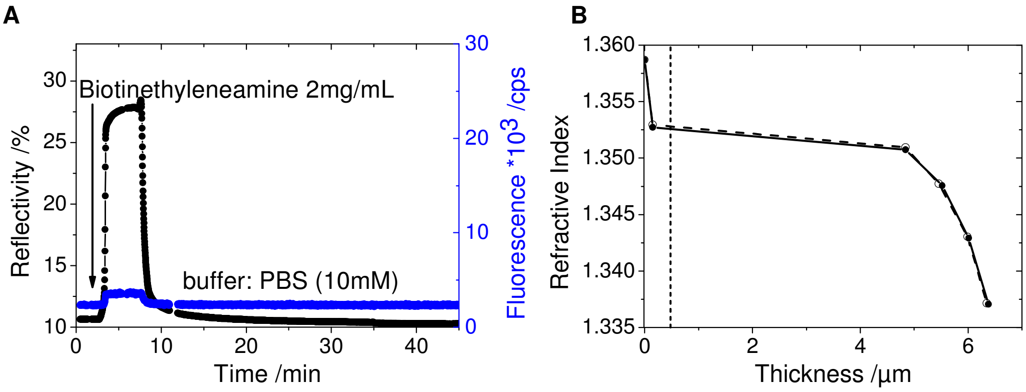

Figure 4.2.7: *Diffusion and unspecific binding of biotinethyleneamine into PCMD matrix.* ***A)*** *Real time SPR (black) and SPFS (blue) kinetic.* ***B)*** *Corresponding WKB profile in PBS 10 mM before and after incubationof biotinethyleneamine. The dry film thickness is indicated by the black dashed line in (B).*

The shift of the surface plasmon to higher angles (increasing reflectivity) indicates a diffusion of biotinethyleneamine through the whole PCMD film until the hydrogel-gold-interface. The hydrogel film profile shows a very slight decrease of the refractive index indicating a negligible irreversible change of the matrix. A non-specific adsorption of biotinethyleneamine could not be detected by SPR/OWS spectroscopy.

Streptavidin-Cy5

In order to demonstrate the potential of the developed hydrogel film as a binding matrix, the diffusion and affinity binding (Chapter 4.2.4) of streptavidin-Cy5 in the PCMD hydrogel film was observed by SPFS and OWFS. In this Chapter the unspecific binding of streptavidin-Cy5 was investigated after ethanolamine coupling. Ethanolamine is used instead of biotin to simulate the real experimental environment. Identical conditions for the diffusion and the detection (Chapter 4.2.4) were used. Streptavidin-Cy5 was dissolved in PBS (150 mM) mimicking physiological conditions at a concentration of 200 µg/mL. The injection time was increased with every incubation step. The real time surface plasmon signal change does not show an unspecific binding neither in the refractive index change nor in the fluorescence (Figure 4.2.8 A). This is consistent with the PCMD matrix refractive index-thickness profile (Figure 4.2.8 B) that shows a negligible swelling after the maximum injection time (blue triangles) compared to the status before streptavidin injection (black circles). The angular position of the surface plasmon and the optical waveguide modes do not change remarkably upon streptavidin incubation (Figure 4.2.8 C).

The fluorescence excited by the surface plasmon as well as the angular shift of the surface plasmon to higher angles during the incubation affirms a diffusion of the solution from the hydrogel solution interface through the entire PCMD matrix to the hydrogel-gold interface (Figure 4.2.8 A). The surface plasmon and the fluorescence excited by the electromagnetic field of the surface plasmon indicate a complete removal of streptavidin-Cy5 upon rinsing with PBS (Figure 4.2.8 A, D). The SPFS value remains constant at a value of $1.5\ x10^3$ cps after every incubation step. Only the fluorescence excited by the optical waveguide modes indicates a low unspecific binding. The fluorescence increases with increasing injection time especially for $TM_{2\text{-}4}$ from $1,9\ x10^4$ to $2.9\ x10^4$ cps (Figure 4.2.8 C, D). The higher fluorescence for $TM_{2\text{-}4}$ compared to TM_1 might be attributed to the higher coupling efficiency and thus a higher excitation energy.

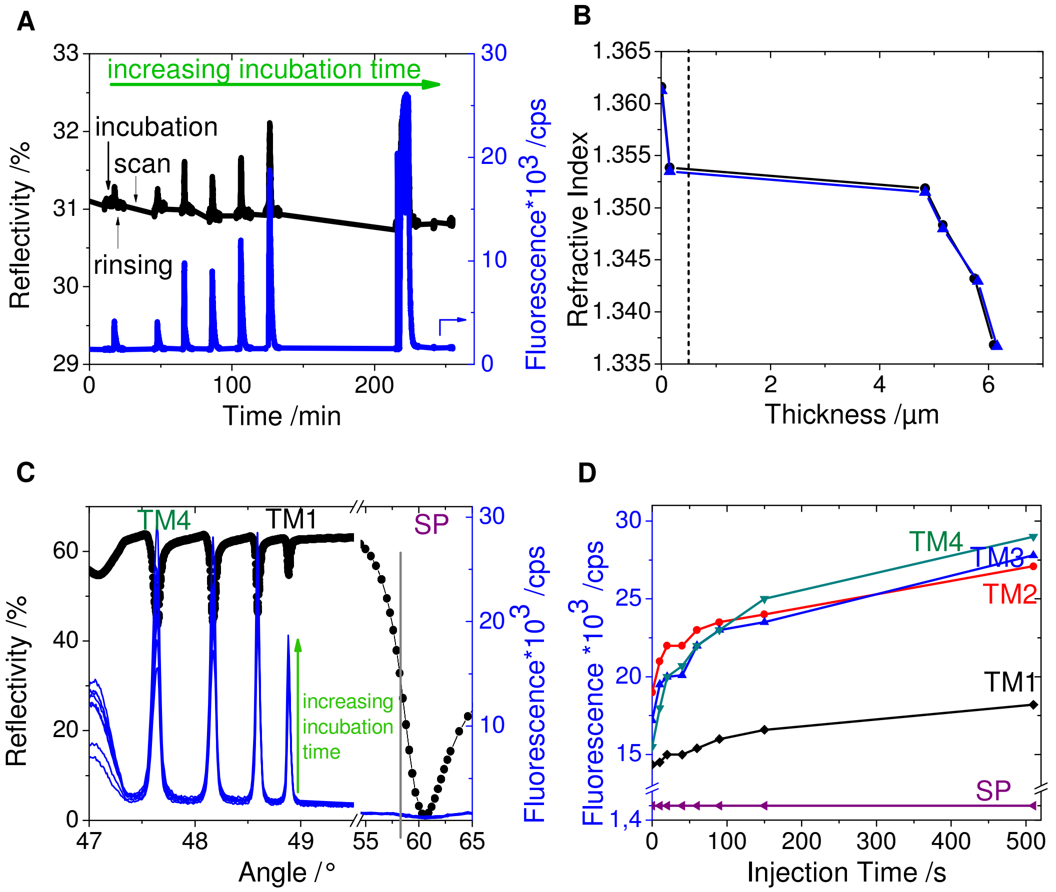

Figure 4.2.8: Diffusion and unspecific binding of streptavidin-Cy5 in an ethanolamine modified PCMD matrix in the absence of biotin. The concentration of the streptavidin-Cy5 solution in PBS 150 mM is kept constant at 200 µg/mL and the incubation time is increased. ***A)*** *Real time kinetic at a fixed angle in the surface plasmon (grey line in (C)), B) WKB refractive index-thickness profile before (black) and after (blue) the diffusion in PBS 150 mM.* ***C)*** *Corresponding SPFS/OWFS angular scans and* ***D)*** *the OWFS/SPFS signal for increasing incubation times are plotted excited by the different leaky optical waveguide modes (TM$_1$-TM$_4$ and by the surface plasmon (SP).*

The fluorescence detected after diffusion of streptavidin-Cy5 is more than two orders of magnitude lower than detected for the specific binding (Chapter 4.2.4). In consistence with these observations the refractive index-thickness hydrogel film profile merely shows a negligible swelling. This can most likely be attributed to irreversible chain disentanglement effects upon the diffusion of big molecules such as streptavidin.

p53/p53ab6

The diffusion of p53 and its primary antibody p53Ab6 was observed in real time with the kinetic mode at a fixed angle in the surface plasmon. Therefore, 1 µg p53 was dissolved in 500 µL acetate buffer (10 mM) with pH 4 or 5.5 or in 10 mM HEPES buffer (pH 7.4). The PCMD matrix was swollen with the corresponding pure buffer until equilibrium signal was reached. The p53 solution was injected for 5 minutes followed by rinsing with the corresponding pure buffer (Figure 4.2.9 A). The diffusion of p53Ab6 was performed under similar conditions with 1µg p53Ab6 in 500µL HEPES (Figure 4.2.9 B).

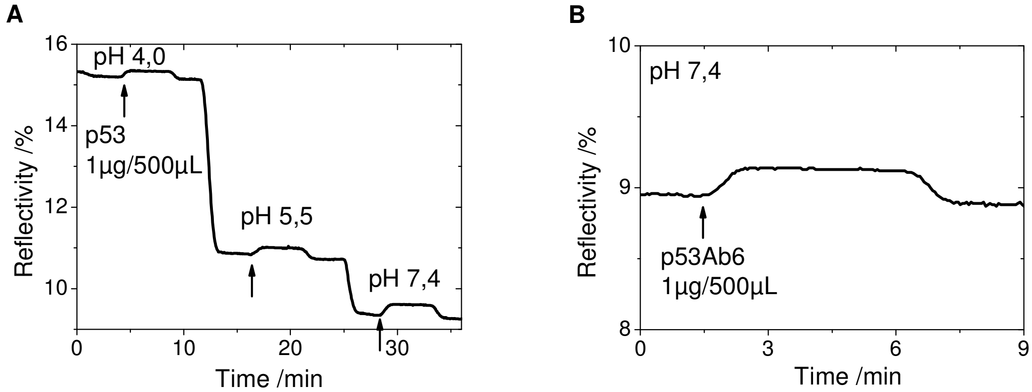

Figure 4.2.9: *A) Diffusion of p53 at different pH and a concentratin of 1µg/500µL.* ***B)*** *Diffusion of p53Ab6 at pH 7.4 with a concentration of 1µg/500µL. From the SPR/OWS response a diffusion but no unspecific binding can be stated.*

For both, p53 and p53Ab6, an increased signal corresponding to a surface plasmon shift to higher angels resulting from an increased refractive index was measured. Upon rinsing the signal decreased to the former level. Consequently, no unspecific binding, neither for p53 at different pH nor for p53Ab6 at neutral pH could be detected by refractive index changes.

Alexa Fluor 647-Labeled Secondary Antibody

The diffusion of the Alexa Fluor 647-labeled secondary antibody for p53Ab6 was measured in a p53 modified PCMD hydrogel and a PBS 150 mM environment. The reaction conditions were chosen to be identical to the detection experiment of Chapter 4.2.5. The concentration of the secondary antibody in PBS (150 mM) was adjusted to 100 µg/500µL. The diffusion time was regulated to be at maximum (6 minutes). The SPFS real time measurement (Figure 4.2.10 A) indicates the diffusion of the secondary antibody through the hydrogel matrix until the PCMD gold interface due to the SPR and SPFS signal increase. Rinsing after the diffusion results in a signal-decay until the base level is reached again. The SPR and the SPFS signal do not show any unspecific binding in agreement with the diffusion of streptavidin-Cy5.

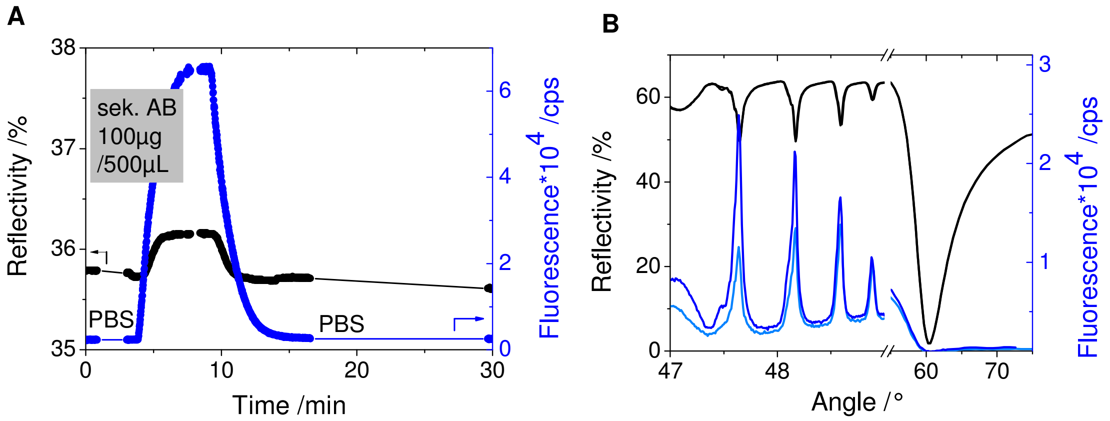

Figure 4.2.10: *Diffusion and unspecific binding of the secondary antibody used as recognition unit for p53Ab6 in a p53-modified PCMD matrix with a thickness of ~6 µm in PBS 150 mM. The concentration was adjusted to 100 µg in 500µL PBS 150 mM. One incubation step with an incubation time of 5 minutes was recorded. The real time surface plasmon kinetic indicates a diffusion of the secondary antibody through the entire matrix **(A)** and a complete removal upon rinsing with buffer. The angular scan recorded in **(B)** show a slight unspecific binding in the OWFS signal (blue) and a continued removal upon rinsing over night (light blue).*

The angular scans (Figure 4.2.10 B) at equilibrium surface plasmon signal in PBS 150 mM before and after diffusion of the secondary antibody do not show any shift of the optical waveguide modes but a slight increase in the OWFS signal. The fluorescence upon unspecific binding is more than two orders of magnitude lower than the detected fluorescence upon specific binding (Chapter 4.2.6).

4.2.4 Streptavidin-Cy5 Detection by Surface Plasmon Resonance and Optical Waveguide Mode Enhanced Fluorescence Spectroscopy

Affinity Binding Study

After the functionalization with biotinethyleneamine (Chapter 4.2.1), the hydrogel film was swollen in 150 mM PBS and the diffusion and affinity binding of streptavidin-Cy5 was observed *in situ* by SPFS and OWFS. In these experiments, the changes in the fluorescence signal, induced by a series of incubations in a solution of streptavidin-Cy5, were measured. Each incubation cycle comprised a specific incubation time range with a Cy5-labeled streptavidin, dissolved at a concentration of 200 µg/mL in PBS 150 mM. Subsequently, unbound streptavidin molecules were removed for 20 minutes rinsing with PBS buffer. The fluorescence signal stabilized after approximately 5 min as can be seen in the real time kinetic which monitores the surface plasmon changes at a fixed angle (Figure 4.2.11 A). After reaching equilibrium surface plasmon signal a SPR/OWS angular scan was measured for 15 minutes, during continuous washing with PBS (Figure 4.2.11 B). The binding of streptavidin to biotin moieties in the gel is manifested as stable fluorescence peaks after rinsing associated to the enhanced excitation of the Cy-5 labels (Fig.4.2.8 A). The magnitude of the peaks increases with the total incubation time until the saturation is reached after 6 minutes. This means that the diffusion of analytes inside the hydrogel matrix reaches equilibrium distribution. (Figure 4.2.11 C).

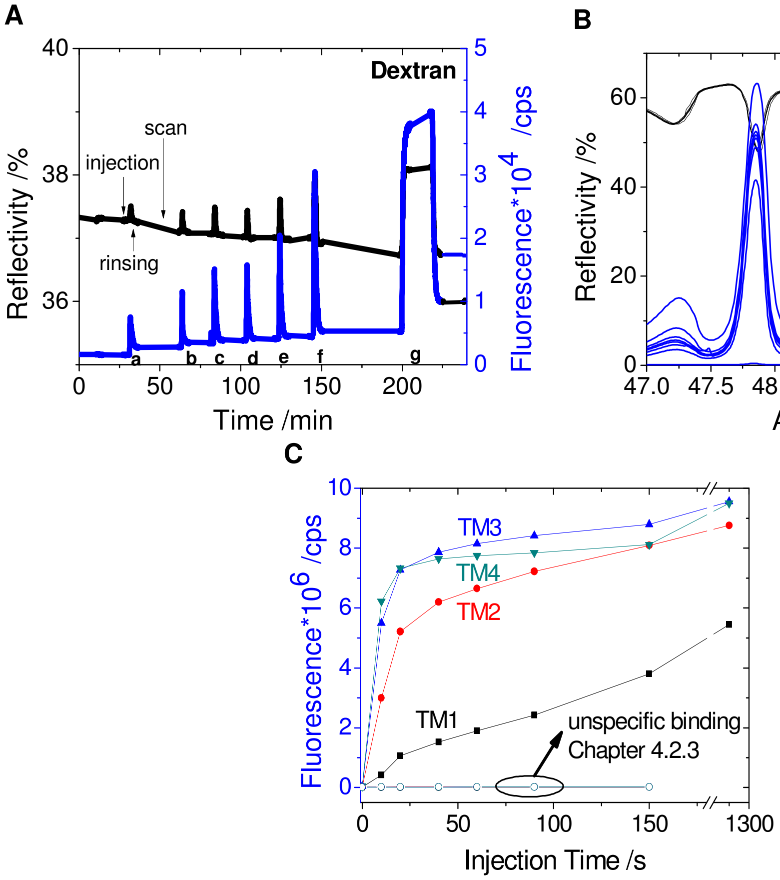

Figure 4.2.11: *Detection of streptavidin-Cy5 by OWFS in a dextran hydrogel film of ~6 μm.* ***A)*** *Real time surface plasmon signal change,* ***B)*** *angular scans recorded after removing the non-bound streptavidin,* ***C)*** *equilibrium fluorescence vs. injection time. The injection time of streptavidin-Cy5 (c = 200 μg/mL) was varied: a = 10s; b = 20s; c = 40s; d = 60s; e = 90s; f = 150s; g = 21.5min and the laser intensity was adjusted to 100% reflectivity corresponding to 145 μW and c(strept-Cy5) = 200 μg/mL.*

The saturation fluorescence intensity measured for the excitation by optical waveguide modes is significantly higher than for the excitation by surface plasmon modes. An enhancement of the fluorescence signal by the factor between 130 (coupling efficiency of the TM ~2% reflectivity) and 2000 fold (coupling efficiency ~15% reflectivity and double concentration of streptavidin-Cy5) was observed. Besides the overall fluorescence enhancement, the signal to noise ratio is improved with OWFS as compared to SPFS in this experimental conformation, too. The background fluorescence for OWFS is one order of magnitude higher than the SPFS background fluorescence but this is overcompensated by the specific fluorescence enhancement of 2-3 orders of magnitude.

In general, the magnitude of the fluorescence signal depends on the concentration of the fluorophore in the hydrogel film, the intensity of the excitation beam, the coupling efficiency,[96] and the field distribution[57] of the exciting guided wave. The enhancement observed here is mainly due to the more intense field of the optical waveguide modes compared to an evanescent field and the location of the fluorophores in the center of the electromagnetic field being the main difference to reported systems.[10, 50, 84, 98, 162] The maximum fluorescence intensity signal of $F = 9\times10^6$ cps was observed for the fluorescence excitation through TM_3 mode in case of four optical waveguide modes in total.

The enhancement of the fluorescence signal results in a fluorescence intensity in the detection limit of the detector whereas the fluorescence excited by the evanescent electromagnetic field of the surface plasmon is in the range of the detector. To circumvent the saturation of the detector the laser intensity was reduced to 10% corresponding to 14.5 µW in a subsequent experiment (Chapter 4.2.5).

The SPFS signal still increases significantly for the longest incubation time of 21.5 minutes, while the OWFS signal of the $TM_{2,3,4}$ only show a slight increase. The limiting factor for the detection of analytes seems to be the diffusion through the matrix. It takes approximately 4-5 minutes until an equilibrium fluorescence signal is reached with a streptavidin-Cy5 solution of 200 µg/mL. The relatively slow diffusion suggests a binding that starts at the hydrogel solution interface and continues towards the hydrogel gold interface.

The specificity of the response was verified with an experiment in which the changes in fluorescence signal were measured for the hydrogel without biotin moieties (Figure 4.2.8). By using this reference hydrogel film with identical thickness and swelling ratio, a fluorescence signal with three orders of magnitude lower intensity was measured compared to the hydrogel with biotin moieties as streptavidinCy5 capturing unit.

For comparison, we detected the streptavidin biotin binding by conventional SPFS. In this experiment, a self-assembled monolayer (SAM) of 11-Mercaptoundecanoic acid was used to couple biotinethylenediamine following the same protocol as described for the hydrogel matrices (Figure 4.2.5 B). After functionalizing the SAM with biotin the evanescent field of the surface plasmon was used to detect the affinity binding of streptavidin-Cy5 (Figure 4.2.12)

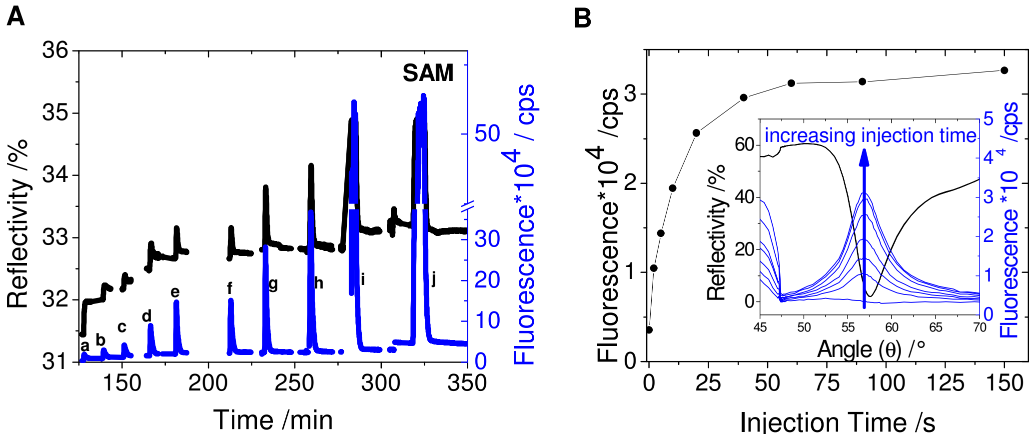

Figure 4.2.12: ***A)*** *Real time detection of streptavidin-Cy5 by SPFS on a self-assembled monolayer (SAM) of biotinethyleneamine-modified 11-mercaptoundecanoic acid.* ***B)*** *Corresponding equilibrium SPFS signal. The angular scans were recorded after removing the non-bound streptavidin. The injection time of streptavidin-Cy5 (c = 200 µg/mL) was varied: a = 2s; b = 5s; c = 10s; d = 20s; e = 40s; f = 60s; g = 90s; h = 150s; I = 8min; j = 14.5min. The excitation intensity of the laser was adjusted to 100 % reflectivity corresponding to 145 µW and c(strept-Cy5) = 200 µg/mL.*

The detected fluorescence with SPFS on the SAM is in the same order of magnitude or up to one order of magnitude lower (data not shown) than the SPFS signal for the hydrogel matrix. In contrast to the hydrogel matrix (Figure 4.2.11) the affinity binding of streptavidin is not only visible in the increasing fluorescence but as well in the increasing reflectivity in the kinetic scan, due to an increasing refractive index caused by the adsorption of an additional streptavidin-Cy5 layer.

Because of the higher thickness and the resulting higher functional density of the hydrogel film one would expect a higher fluorescence signal for the surface plasmon fluorescence in the hydrogel matrix than for the self-assembled monolayer. Possible reasons might be an incomplete conversion of biotin to biotin-streptavidin in the hydrogel matrix or an inhomogeneous biotin distribution in z-direction. As the fluorescence, measured in the surface plasmon of the hydrogel film, still increases after 15 min of incubation indicates an incomplete affinity binding as well. This could be attributed to a diffusion limited reaction. Thus, a preferential binding at the hydrogel solution interface with a gradually increasing coupling towards the hydrogel gold interface can be assumed. In contrast the self-assembled monolayer shows a surface saturation already after approximately one minute of incubation with a streptavidin-Cy5 solution of 200 µg/mL and a flow of 0.1 mL/min (Figure 4.2.9 B).

In summary the coupling and detection of analytes inside a waveguiding hydrogel film shows high potential for a sensitive detection. The enhanced field intensity results in a significantly increased fluorescence signal. This technique should be a remarkable inovation compared to reported sensor models with fluorescence excitation by the evanescent field of the surface plasmon[10, 50, 84, 162] or by the evanescent field of an optical waveguide mode.[98]

4.2.5 Detection of p53Ab6 with a Labeled Secondary Antibody as a Clinically Relevant Analyte in a Sandwich Assay

In order to demonstrate the capability of detecting clinically relevant analytes p53Ab6, which is a primary antibody to the tumor suppressor protein p53, was detected by screening with a fluorescence labeled secondary antibody in a sandwich assay. In principle the assay can be performed in a reversed order for the detection of p53 as well. The short half-life of p53 and the permanently present ground level of p53 in healthy humans is a disadvantage for the analysis of p53. The detection of mutated p53 would be more reasonable.[118] The detection of p53-antibodies, produced in an autoimmune response associated with a p53 overexpression or accumulation upon p53 mutation,[125, 135, 136] is a more useful sensor approach. Especially because p53-antibodies were rarely found (0-3%) in healthy control patients[136] but were shown to function as tumor marker for example recently in colorectal cancer.[143]

Analog to the covalent immobilization of biotinethylenediamine and as depicted in the sensor concept (Figure 4.2.1) p53 was covalently bound to the dextran hydrogel network incubating the hydrogel matrix with a 24 µg/100µL solution of p53 in 10mM acetate buffer at pH 5.5 after activation of the carboxyl groups with EDC/NHS. Alternatively, the primary antibody p53Ab6 can be bound to the hydrogel network with the same strategy followed by p53 coupling to the antibody in the second step (data not shown). The p53 functionalization of the hydrogel matrix is followed by coupling at increasing concentrations of the primary antibody p53Ab6 (0,1-50 µg/mL PBS 150 mM) which is subsequently screened by an Alexa Fluor647-labeled secondary antibody solution (200 µg/mL in 150mM PBS) (Figure 4.2.13). To proof the specificity of the p53Ab6 detection a blind experiment without p53Ab6 but with p53 present in the hydrogel network was performed. Similar to the case of biotin/streptavidin-Cy5 almost no unspecific binding could be observed and the fluorescence signal for the highest analyte concentration was in the range of $1\text{-}2{,}5 \times 10^4$, which is more than two orders of magnitude lower than the one for the specific detection of p53Ab6 (Figure 4.2.10). To proof the specific binding of p53Ab6 and of the secondary antibody a western blot (Figure 4.2.14) was performed by Sandra Ritz at the Max Planck Institute for Polymer

Research. Thereby, the proteins are separated by gel electrophoresis according to their size. The protein size can be deduced by comparison with a standard mixture containing various size markers. The specific antibody-protein interaction was proofed. The difference in sensitivity between the fluorescence detected with the optical waveguide modes and the surface plasmon for the highest concentration is a factor of ~2000 which is in agreement to the biotin experiment of comparable experimental parameters (Chapter 4.2.4). Comparing the fluorescence intensity the order of fluorescence signal (Figure 4.2.13) is in agreement with the coupling efficiencies of the different optical waveguide modes although the difference in the measured fluorescence does not exactly match the one for the coupling efficiency. The aberration increases from TM$_4$ to TM$_1$. Basically, this follows the same trend than for the streptavidin-Cy5 detection indicating a non-homogeneous analyte distribution in z-direction as discussed for streptavidin in Chapter 4.2.5. Because of the lower amounts of p53 used for covalent matrix modification an even more pronounced inhomogeneity is expected. The molecules are expected to start the binding at the hydrogel solution interface where they enter the sensor matrix.

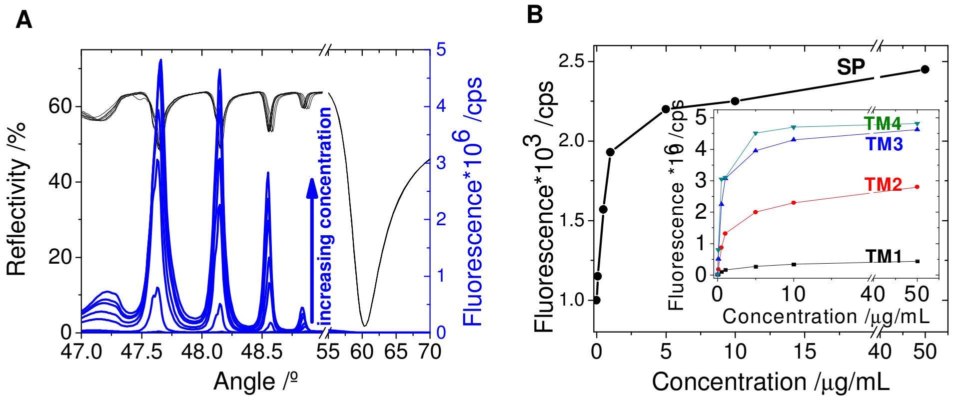

Figure 4.2.13: *Fluorescence detection of p53Ab6 as a clinically relevant analyte*[125] *with a labeled secondary antibody in a sandwich assay. The angular scans are shown in* ***(A)*** *and the fluorescence as a function of the p53Ab6 concentration in* ***(B)****. The laser intensity was adjusted to 100% corresponding to 145 µW and the concentration of the secondary antibody solution to 200µg/mL.*

The lowest concentration of p53Ab6 used was 100 ng/mL. An injection volume of 1 mL and an injection time of 10 min were used. Under these conditions an increase in the fluorescence signal after rinsing of 1,6x10^4 to 9,4x10^5 for TM$_4$, with a TM-coupling efficiency of 15% reflectivity was achieved. This is an increase in the fluorescence signal of almost two orders of magnitude for a ng/mL concentration showing the potential of this technique. This holds true, if the non-optimal parameters like analyte distribution inside the matrix, the number of optical waveguide modes with the corresponding film thickness and the coupling efficiency as well as the amount of analyte capturing units will be optimized. For evanescent OWFS, limits of detection in the range of 100 fM with a coupling efficiency of 50% are reported for DNA hybridization. The corresponding SPFS detection revealed a limit of detection (LOD) of 2 pM.[98] Tumor marker are usually analyzed by ELISA or Western Blot in the range of ng/mL.[125, 136, 142] For SPFS sensitivities down to attomolar concentrations are reported[84]

Western Blot

The performance of the p53-p53Ab6 (monoclonal antibody, Dianova) was tested in a Western Blot by Sandra Ritz at the Max Planck Institute for Polymer Research. The results indicate an effective coupling of the antibody to the protein (Figure 4.2.14). This supplementary information for the biosensor detection of p53-p53Ab6 proofs the specific interaction between p53Ab6 and the protein p53 and thus supports the results of the SPFS/OWFS experiments.

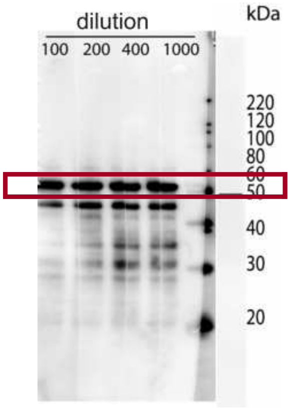

p53 (53kDa) detected by primary antibody

Figure 4.2.14: *Western Blot analysis of the p53-p53Ab6 antibody binding specify to recombinant human p53 (53 kDa). Serial dilutions of the monoclonal p53 antibody from 1:100 – 1:1000 indicated the high antibody reactivity even at lower antibody concentrations.*

4.2.6 Streptavidin-Cy5 Analyte Distribution in a Hydrogel Matrix

To evaluate the potential of analyte detection using the OWFS signal, information about the analyte distribution and the dependence of the OWFS signal on parameters like coupling efficiency and field distribution are necessary. The sensing layer is probed with a varying local sensitivity depending on the waveguide mode-number (TM). Consequently, knowing the field distribution of the different leaky optical waveguide modes (TM), the analyte distribution inside the film can be estimated. On the other hand, the obtained information can be applied to tune the waveguiding matrix towards optimal waveguiding conditions concerning the coupling efficiency and the number of optical waveguide modes. The aim is to characterize critical parameters and to identify optimal conditions for analyte detection with OWFS. The gained knowledge should result in an improved sensitivity by using the maximum of the electromagnetic field instead of using for example the evanescent tail on top of a waveguiding layer for fluorescence excitation.[95, 98]

Fluorescence and Leaky Optical Waveguide Modes

In order to develop a more differentiated picture of the fluorophore distribution and the fluorescence detection with the optical waveguide modes, a hydrogel film of approximately 1µm thickness in the dry state was prepared. The binding hydrogel matrix was swollen to 12 µm in PBS 150 mM with an average refractive index of 1.355 resulting in a surface coverage of 570 ng/mm² (Figure 4.2.15 A) guiding 10 optical waveguide modes.

A high number of optical waveguide modes allows for a more precise film characterization using the reversed Wentzel-Kramer-Brillouin approximation[92] and the theory of the relative photon density.[96] The excitation laser beam intensity was decreased to 10% reflectivity, corresponding to 14.5 µW, reducing the fluorescence intensity by a factor of 10. Besides, the streptavidin-Cy5 concentration was reduced to 100 µg/mL. The real time kinetic SPR/SPFS signal is shown in Figure 4.2.15 A. The inset shows the injection time dependent fluorescence signal excited by the evanescent field of the surface plasmon after removing the non-bound analyte. Obviously, short injection times of 1 or 3 seconds don't allow the labeled streptavidin to diffuse completely through the 12µm thick hydrogel matrix as almost no fluorescence increase is detected with the evanescent field of the surface plasmon located at the gold-hydrogel interface (Figure. 4.2.15 A). Equilibrium SPFS signal and consequently equilibrium diffusion was reached within approximately 5 minutes in agreement with the measurements shown in Chapter 4.2.4. The fluorescence excited by the surface plasmon after matrix saturation is about a factor of 130 lower than the one excited by the electromagnetic field of the optical waveguide modes (Figure. 4.2.15) with a coupling efficiency of the optical waveguide modes being a factor of 7 lower compared to the data shown in Figure 4.2.7 (Chapter 4.2.4). The decreased coupling efficiency can most likely be attributed to an increased film inhomogeneity especially at the gold-hydrogel interface, which was usually observed for very thick hydrogel films. Film inhomogenety results into "loss of light" which becomes noticeable in an increased imaginary part of the refractive index and thus a lower coupling efficiency.

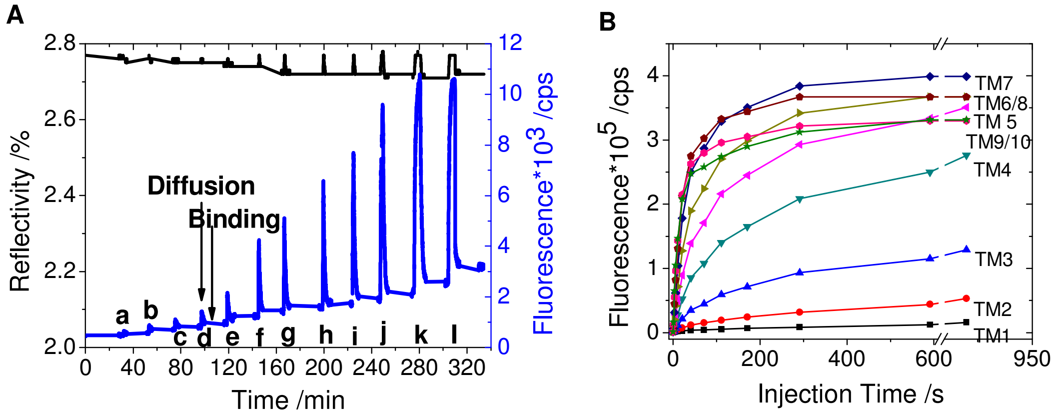

Figure 4.2.15: *Comparison of the fluorophore detection in a thick hydrogel film guiding 10 leaky waveguide modes at a thickness of ~11 µm.* ***A)*** *SPR and SPFS signal for the detection of streptavidin-Cy5 (100 µg/mL) monitored in real time at a fixed angle in the surface plasmon absorption. The reflectivity is shown in black, the simultaneously measured surface plasmon excited fluorescence in blue.* ***B)*** *Fluorescence excited by the electromagnetic field of the optical waveguide modes (OWFS) (laser intensity = 10% reflectivity = 14.5 µW). The injection time of the streptavidin-Cy5 solution was a = 1s; b = 3s; c = 6s; d = 11s; e = 21s; f = 41s; g = 71s; h = 1.8min; I = 2.8min; j = 4.8min; k = 9.8min; l = 15.3min.*

Taking into account the reduced coupling efficiency, the reduced streptavidin-Cy5 concentration (factor 2) and the reduced laser intensity (10% reflectivity) the results are in agreement to the ones discussed in Chapter 4.2.4.

Theory of the Relative Photon Density

The different optical waveguide modes show a significantly different sensitivity and saturation fluorescence intensity (Figure 4.2.15 B). To simulate the theoretically expected relative fluorescence intensity for every optical waveguide mode after analyte saturation the theory of the relative photon density (Chapter 2.3) was applied. This theory was introduced by Zong et. al.[96] and assumes a homogeneous dye-distribution inside the matrix. In case the simulated data reflects the measured fluorescence well, one can state that the fluorophores are homogeneously distributed through the film. The theoretically expected saturation fluorescence (Γ) depends on the electromagnetic field of the optical waveguide mode guided inside the hydrogel film, the coupling efficiency (η), and the effective refractive index (N_{eff}).

$$\Gamma \equiv \frac{N_{eff,real}}{N_{eff,im}} \cdot \eta \cdot a \tag{4.2.1}$$

The lower the number of the optical waveguide mode, the higher the percentage of the electromagnetic field guided inside the matrix (α). The refractive index values introduced into the theory of the relative photon density are calculated on the basis of this WKB profile (Chapter 2.3). The hydrogel film refractive index-thickness profile represents a two-layer model indicated by the two hatched areas in Figure 4.2.16 A. The relative coupling efficiency is extracted from the SPR/OWS angular scans and is depicted in Figure 4.2.16 B. The measured fluorescence in dependence of the injection time for every TM-mode is shown in Figure 4.2.15 B. Normalizing the measured fluorescence on the coupling efficiency, results in a fluorescence intensity sequence from TM_1 with the lowest OWFS signal to $TM_{9/10}$ with the maximum fluorescence signal (Figure 4.2.16 D). Knowing the electromagnetic field distribution of the TM-mode (Figure 4.2.16 C) the reversed order would be expected due to the increasing electromagnetic field-intensity at the hydrogel-solution interface with increasing TM-number. This is a first indication for a non-homogeneous analyte distribution in z-direction through the hydrogel film.

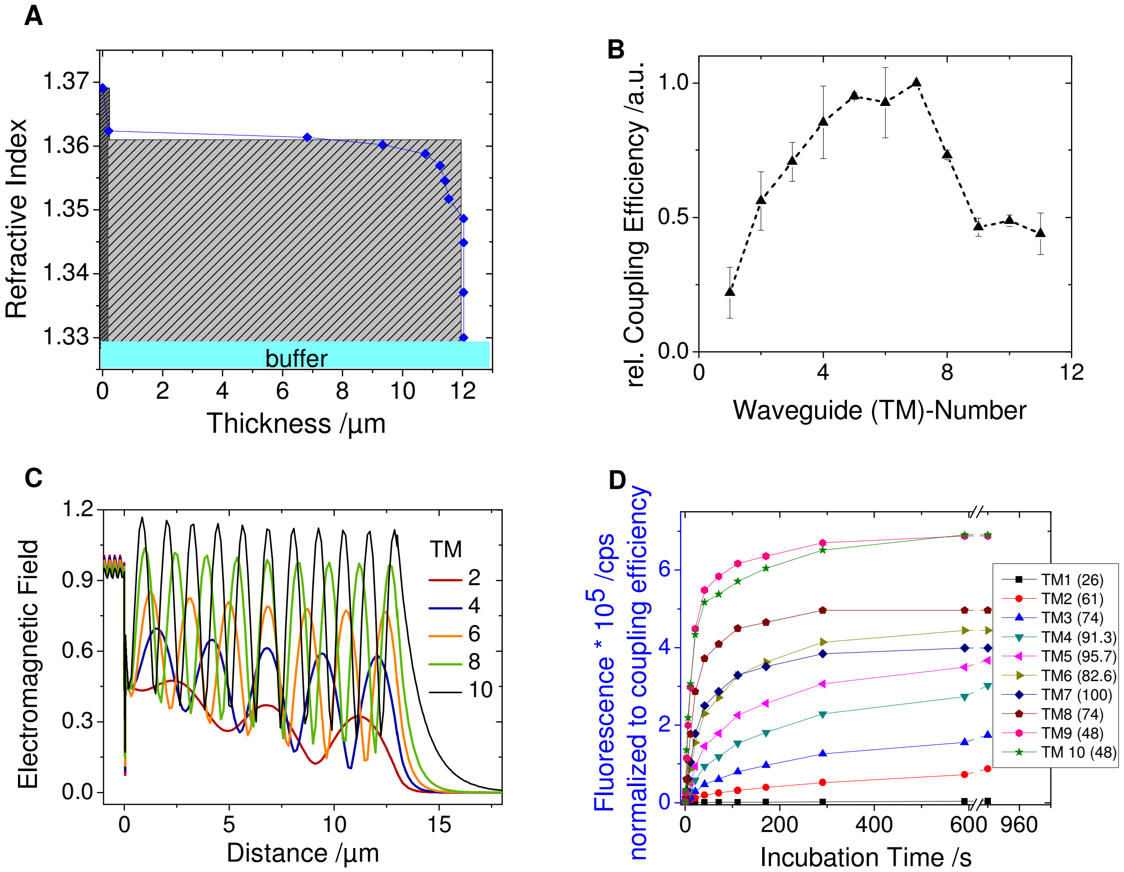

Figure 4.2.16: *A) Refractive index profile of the fully crosslinked hydrogel matrix calculated with the reversed Wentzel-Kramer-Brillouin approximation after the detection of streptavidin-Cy5. A two box-model, indicated by the hatched boxes in **(A)** was used for the simulation of the angular scan. **B)** Relative coupling efficiency extracted from the angular reflectivity scan. **C)** Calculated electromagnetic field distribution of the optical waveguide modes based on the 2 layer-model indicated in (A). **D)** The measured fluorescence excited by the evanescent field of the optical waveguide modes normalized to the coupling efficiency (B) of every optical waveguide mode (laser Intensity = 10% reflectivity = 14.5 µW, c(streptavidin-Cy5) = 100 µg/mL).*

The measured fluorescence in dependence of the optical waveguide mode number is reviewed in Figure 4.2.17 A. The higher the waveguide mode-number the lower is the injection time necessary to detect fluorescence. This could be explained by the increaseing part of the electromagnetic field that is located on the hydrogel-solution-interface where the analytes enter the sensor matrix. The calculated theoretical saturation fluorescence is compared with the measured fluorescence after maximum injection time in Figure 4.2.17 B. The simulated data do not exactly represent the relative values for the measured fluorescence but depicts the overall tendency with the maximum fluorescence detected for the TM_7. Comparing the relative values for the different optical waveguide modes, the simulated data show higher fluorescence to be expected than measured for the lower numbered optical waveguide modes. Furthermore, the coupling efficiency seems to play a decisive role as can be seen by comparing the TM-number dependent coupling efficiency to the measured and calculated TM-number dependent fluorescence. The comparison of the measured OWFS signal for the experiment discussed here with the results discussed in Chapter 4.2.4 show the direct influence of the coupling efficiency on the magnitude of the OWFS signal. The results in Chapter 4.2.4 are recorded with a higher coupling efficiency, with a higher laser intensity, and a higher analyte concentration.

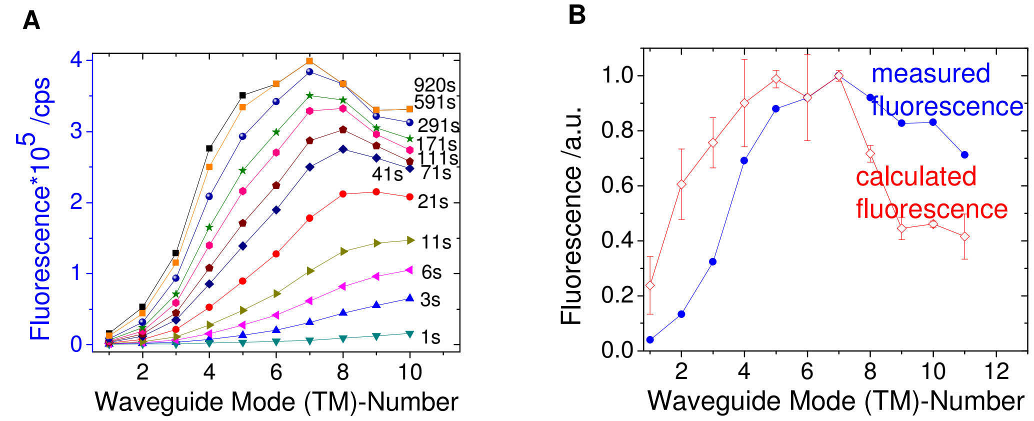

Figure 4.2.17: A) Fluorophore detection in dependence of the number of the optical waveguide mode and the injection time. ***B)*** *The fluorescence after maximum injection time is compared to the expected fluorescence calculated with the relative photon density theory showing the same tendency but no exact reproduction of the measured data.*

Knowing that the portion of the electromagnetic field detecting outside of the matrix increases with increasing number of the optical waveguide mode[100], it can be concluded that a higher amount of fluorophore is bound at the matrix-medium interface than close to the metal-matrix interface. This is consistent with the surface plasmon fluorescence that is on the same order of magnitude for a hydrogel matrix and for a self-assembled monolayer, although the functional density in the surface plasmon detection range is higher for the hydrogel film than for a self-assembled monolayer.

4.2.7 Sensor Concept for the Detection of Prostate Specific Antigen with Long Range Surface Plasmon Enhanced Fluorescence Spectroscopy

An alternative method for the development of sensors that require a thicker binding matrix is the detection by long range surface plasmon enhanced fluorescence spectroscopy (LR-SPFS). A biosensor for the detection of prostate specific antigen (PSA) in human serum was developed in collaboration with Yi Wang and Jakub Dostálek. The concept is based on a photo-crosslinked carboxymethylated dextran (PCMD) (Chapter3.1) as binding matrix and long range surface plasmon-enhanced fluorescence spectroscopy (LR-SPFS).

Recently, long-range surface plasmons (LRSPs) were exploited for SPFS biosensing.[163-165] These optical waves originate from the coupling of surface plasmons on opposite surfaces of a thin metallic film embedded between dielectrics with similar refractive indices. LRSPs probe the medium adjacent to the metallic surface with a more extended evanescent field than regular surface plasmons.[164] Therefore, three-dimensional binding matrices with up to micrometer thickness have been proposed for the immobilization of biomolecular recognition elements with large surface density that allows to exploit the whole evanescent field of LRSP.[166] Currently, new hydrogel-materials based on NIPAAm [N-(isopropylacrylamide)] and dextran polymers were demonstrated to be suitable for the construction of such surface architectures.[167-169] Additionally, LRSPs exhibit orders of magnitude lower damping compared to regular surface plasmons on an individual metallic surface.[170] Therefore, their excitation provides larger enhancement of the electromagnetic field intensity and thus allows for stronger increasing the fluorescence signal in SPFS sensors. The experimental setup is identical to the one used for SPFS and OWFS measurements, only the sample preparation is different as described in Chapter 2.1.

PSA is a 33-34kDa single-chain glycoprotein which has been used for the diagnosis of prostate cancer.[171] In blood serum it is present in its free form (f-PSA) and as a PSA bound to antichymotrypsin (PSA-ACT). Currently, clinically relevant levels of this analyte in blood serum are below 0.3 nM (corresponding to 10 ng mL^{-1}) and they are routinely analyzed in specialized laboratories by *e.g.* enzyme-linked immunosorbent assays (ELISA).[172] Biosensors for rapid detection of PSA at orders of magnitude lower concentrations are expected to provide a valuable tool for diagnosis of female breast cancer,[173] early identification of prostate cancer relapse[174] and in forensic applications.[175] Research for ultra-sensitive and simplified analysis of PSA was carried out including immuno-PCR (LOD of 6 fM and analysis time >150 min),[176] bio barcode-based detection (LOD of 30 aM and analysis time of 80 min),[177] gold nanoparticle sandwich immunoassay combined with surface-enhanced Raman scattering (SERS) (LOD of 30 fM and analysis time of ~ 550 min)[178] and SPR (LOD of 30 pM)[46] and SPFS with sandwich immunoassay (LOD of 80 fM and analysis time of 40 min).[179]

Matrix Properties

The matrix used for the PSA detection was first characterized according to its swelling properties. Figure 4.2.18 shows the reflectivity spectra measured for the bare gold surface, for the swollen hydrogel film attached to the gold surface and for the swollen hydrogel modified by the capture antibody c-Ab. These data reveal that after the attachment of the hydrogel film and its swelling in HBS-EP buffer, the resonance dip associated with the excitation of LRSP shifts to higher angles with respect to that on bare gold surface. In addition, the reflectivity curve is changed in the vicinity of the critical angle $\theta = 47.5°$ due to the appearance of an optical waveguide mode TM_2 supported by the thin hydrogel layer. In Figure 4.2.18 A, reflectivity curves measured for the hydrogel film with the ratio of benzophenone to C-H group of 1:34 and thickness of $d_h = 210$ nm (in contact with air) are shown. By fitting the spectrum measured after the swelling of the gel in HBS-EP buffer, its thickness and refractive index was determined as $d_h = 0.98$ µm and $n_h = 1.346$. Based on the effective medium theory,[180] we determined the polymer volume fraction as $f = 7\%$ by using the equation:

$$f = \frac{\left(n_h^2 - n_b^2\right)}{\left(n_h^2 + 2n_b^2\right)} \frac{\left(n_{h-dry}^2 + 2n_b^2\right)}{\left(n_{h-dry}^2 - n_b^2\right)}, \tag{4.2.2}$$

where $n_{h\text{-}dry} = 1.51$[181] is the refractive index of dry dextran polymer. Figure 4.2.18B shows the reflectivity curves for the hydrogel with the higher ratio of benzophenone to C-H groups of 1:23 that was deposited with a higher thickness $d_h = 280$ nm (in contact with air). The fitting of the respective angular reflectivity spectra measured after the swelling in HBS-EP revealed that it exhibited larger thickness of $d_h = 1.3$ µm and a higher refractive index $n_h = 1.352$ corresponding to higher polymer volume fraction around 10 %.

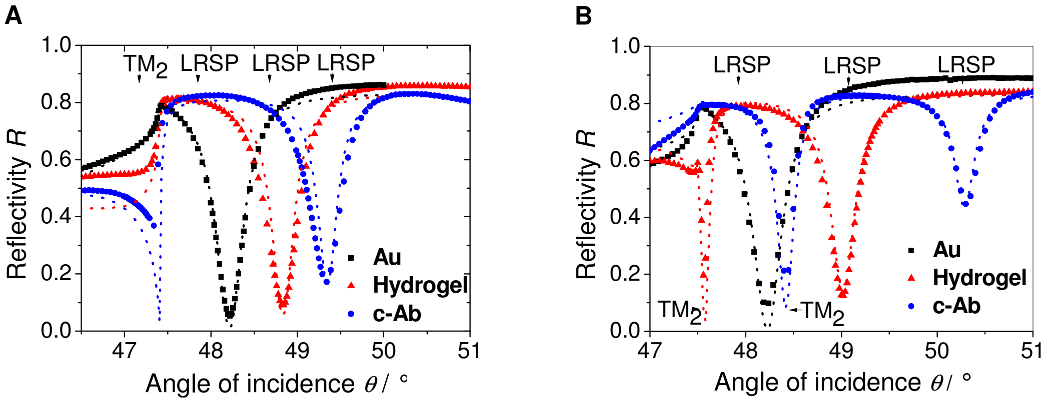

Figure 4.2.18: *Angular reflectivity spectra for a hydrogel film* ***(A)*** *with the ratio of benzophenone to C-H groups of 1:34 and the thickness of 210 nm (measured in the contact with air) and* ***(B)*** *with the ratio of benzophenone to C-H groups of 1:23 and the thickness of 280 nm (measured in the contact with air). The squares show the spectra for bare gold surface, triangles show the spectra measured after the attaching and swelling of the gel and circles show the spectra measured after the immobilization of c-Ab (HBS-EP buffer was flowed along the sensor surface). The dotted lines show the corresponding fits of measured reflectivity curves.*

Let us note that the optical thickness of this gel was high enough to support a TM_2 mode as can be seen from the additional resonance dip located at the angle of incidence $\theta = 47.6$. Surface mass densities of $\Gamma = 59$ and 117 ng mm^{-2} were determined for two hydrogel films with a thickness in the swollen state of $d_h = 0.98$ and 1.3 µm, respectively (measured in HBS-EP buffer). These data indicate a higher gel density in the swollen state for hydrogels with a higher concentration of crosslinking benzophenone groups.

Antibody Immobilization

The immobilization of a capture antibody c-Ab into the hydrogel layer caused an increase in the refractive index of the gel as seen from the shifts of the resonant dips due to the excitation of LRSPs and TM_2 hydrogel waveguide modes. The simulation of the corresponding reflectivity spectra indicate that the refractive index increased to $n_h = 1.355$ and 1.372 for the hydrogels with a thickness of $d_h = 0.98$ and 1.3 µm, respectively, and that the thickness of the hydrogel films swollen in HBS-EP buffer did not change significantly. The surface mass density of the thicker hydrogel film ($d_h = 1.3$ µm) and of the thinner film ($d_h = 0.98$ µm) increased to $\Gamma = 247$ ng mm^{-2} and $\Gamma = 103$ ng mm^{-2}, respectively. The amount of anchored c-Ab molecules was estimated as the difference between the surface mass density before and after the c-Ab coupling as $\Gamma = 130$ and 44 ng mm^{-2} for the thicker and thinner film, respectively, that is up to one order of magnitude higher than that reported for regularly used dextran brushes, which feature a thickness of about 100 nm (CM5 chip from Biacore, Sweden).[182] The prepared dextran hydrogel surfaces allowed for the immobilization of a large amount of c-Ab of which the surface mass density was close to that of the PCMD gel itself. In further experiments, the hydrogel with lower volume fraction around 7% was used.

Kinetic Analysis of the Affinity Binding of f-PSA in Buffer

The affinity binding of f-PSA to the c-Ab receptors immobilized in a PCMD hydrogel was observed by LRSP spectroscopy and by LRSP-enhanced fluorescence spectroscopy. In the following experiment, we used a hydrogel with the thickness and surface mass density of d_h = 0.95 and Γ = 66.5 ng mm^{-2}, respectively, measured prior to the modification by c-Ab. The gel was modified by c-Ab with the surface mass density of Γ = 48 ng mm^{-2}. The HBS-EP buffer was flowed over the sensor surface in order to establish a baseline of the reflectivity signal ΔR. Afterwards, a solution with f-PSA dissolved at a concentration of 300 nM was injected for 30 minutes and a gradual increase in the reflectivity was observed due to the refractive index changes induced by f-PSA binding, see Figure 4.2.19 A. After this association phase, HBS-EP buffer was flowed through the sensor cell and an exponential decrease in the reflectivity R was observed due to the dissociation of the f-PSA from c-Ab.

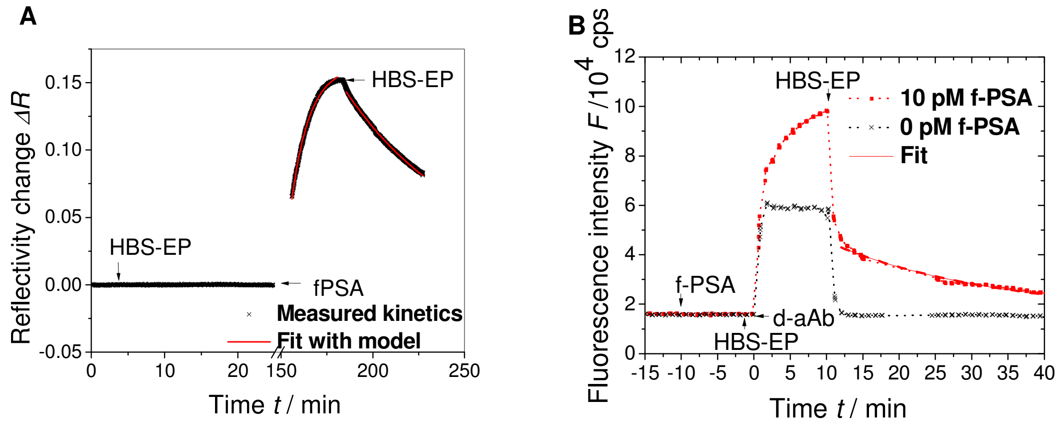

Figure 4.2.19 ***(A)*** *Time evolution of the reflectivity changes ΔR upon the dissociation and association of f-PSA to c-Ab. The concentration of f-PSA in HBS-EP was 300 nM and the c-Ab was immobilized with surface mass density of Γ = 48 ng mm^{-2} in the gel with the thickness of d_h = 950 nm (measured in HBS-EP).* ***(B)*** *Fluorescence signal measured upon the successive flow of a solution with f-PSA (concentration of 10 pM in HBS-EP) and Alexa Fluor 647 chromophore-labeled d-Ab (dissolved in a concentration of 1 nM in HBS-EP).*

By fitting the measured kinetics with a Langmuir adsorption model,[183] the association and dissociation constants were determined as $k_a = 4.8\times10^{3}$ M^{-1} s^{-1} and $k_d = 2.4\times10^{-4}$ s^{-1}, respectively. These values are comparable to those reported by Yu et al. ($k_a = 2.2\times10^{4}$ M^{-1} s^{-1} and k_d = 3.2×10^{-4} s^{-1})[179] who analyzed the identical antigen-antibody pair by a SPR biosensor with c-Ab immobilized with a surface mass density of $\Gamma = 1.8$ ng mm^{-2} on the CM5 chip coated by a dextran brush (from Biacore, Sweden).

The approximately 4-fold lower association constant k_a indicates that the diffusion of f-PSA through the PCMD hydrogel highly loaded with c-Ab did not hinder the binding kinetics dramatically. Moreover, we observed the affinity binding of the detection antibody d-Ab labeled with Alexa-Fluor 647 chromophore to the captured f-PSA molecules by LRSP-enhanced fluorescence spectroscopy. Figure 4.2.19 B shows the time kinetics of the fluorescence signal upon a 15-minute flow of a solution with f-PSA dissolved at a concentration of 10 pM followed by a 2 minute rinsing by HBS-EP buffer, 10-minute flow of d-Ab at a concentration of 1 nM and final rinsing by the HBS-EP buffer for 30 minutes. After the time $t = 0$ when the d-Ab solution was injected, an increase in the fluorescence signal is observed due to the diffusion of d-Ab molecules into the gel and the affinity binding to the captured f-PSA molecules. During the flow of the HBS-EP buffer for time $t > 10$ min, a fast drop of the fluorescence signal F is observed owing to the removal of unbound d-Ab molecules. Afterwards, the fluorescence signal exponentially decreased due to the dissociation of the complex c-Ab/f-PSA/d-Ab. By fitting the exponential decay of the signal with the Langmuir model, we determined the dissociation constant as $k_d = 5.5\times10^{-4}$ s^{-1}. This value is comparable to that measured for the dissociation of the f-PSA bound to c-Ab which indicates good stability of c-Ab, fPSA and the d-Ab complex.

Direct Detection of f-PSA

By using LRSP-spectroscopy and a hydrogel matrix modified with PSA capturing antibodies with thickness $d_h = 950$ nm and surface mass density of $\Gamma = 66.5$ ng mm^{-2}, direct detection of f-PSA in HBS-EP buffer was performed. As shown in Figure 4.2.20 A, the sequential injection of samples with f-PSA at concentrations between 3 nM and 300 nM induced a gradual increase in the reflectivity ΔR. After the injection of the sample with the maximum f-PSA concentration of 300 nM, the increase in the reflectivity shift ΔR started to saturate and reached approximately the value $\Delta R = 0.16$. The specificity of the f-PSA binding was verified in an experiment in which 30 nM f-PSA was flowed over the PCMD without c-Ab which showed no significant change in the reflectivity (Figure 4.2.20 A, green curve). In addition to the specific binding of f-PSA, we investigated the interaction of PCMD hydrogel with human serum that was not spiked with f-PSA. As seen in Figure 4.2.20 B, upon injection of a serum sample a large increase in the reflectivity change ΔR occurs which indicates that the blood serum efficiently diffuses inside the gel.

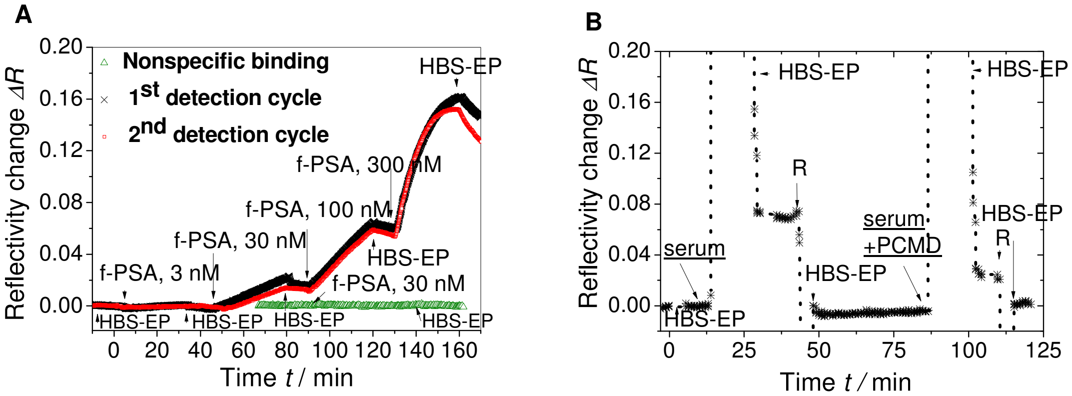

Figure 4.2.20: ***(A)*** *Changes in the reflectivity* ΔR *measured upon the specific (black and red) and non-specific (green) binding of f-PSA dissolved at concentrations between 3 and 300 nM in PCMD binding matrix.* ***(B)*** *Time evolution of reflectivity changes* ΔR *for two detection cycles with the 15 minute incubation in human serum with and without spiking with PCMD at the concentration of 0.5 mg mL*$^{-1}$ *followed by the regeneration (R) and rinsing with HBS-EP buffer.*

After the rinsing with HBS-EP for 5 min, the reflectivity stabilized at $\Delta R = 0.07$ above the original value prior the incubation with serum. This change is due to non-specifically bound serum components adhering within the hydrogel matrix possibly due to electrostatic and physical adsorption. The non-specifically bound serum can be fully washed out by applying the regeneration. In addition, the spiking of serum with free PCMD at a concentration of 0.5 mg mL^{-1} responded in an approximately 2.7 fold decrease of sensor response due to the adhered serum components. This behavior is similar to that in the dextran brush (CM5 chip from Biacore Inc., Sweden) reported by Yu et al.[179] and can be explained by the competitive binding of the substances contained in serum to free PCMD molecules which reduces their adsorption within the gel. The calibration curve for the direct detection of f-PSA in HBS-EP buffer is presented in Figure 4.2.21.

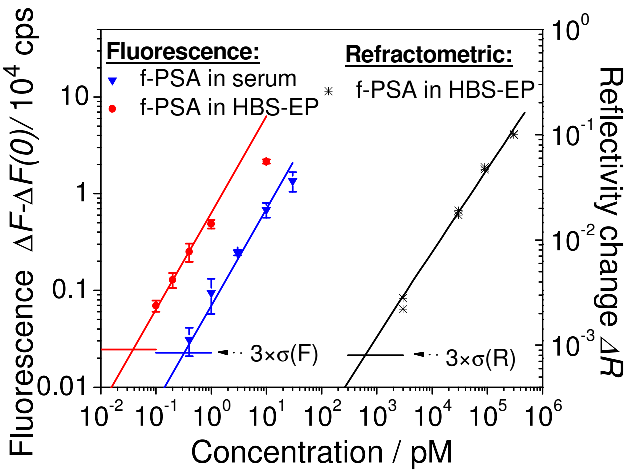

Figure 4.2.21: *Calibration curves for the direct detection of f-PSA (refractometric - black) compared to the sandwich immunoassay-based detection with fluorescence readout for f-PSA dissolved in HBS-EP (red) and in human serum (blue). Lines show the linear fit and the error bars show the standard deviation.*

From these data, we determined a LOD of 0.68 nM as the concentration for which linear fit of the calibration curve reaches three times the standard deviation of the baseline $3\sigma(\Delta R) = 8\times10^{-4}$.

Detection of f-PSA with LR-SPFS

For the SPFS detection of f-PSA in HBS-EP buffer and human serum, a hydrogel with a thickness of d_h = 1.32 µm and a surface mass density of Γ = 56 ng mm^{-2} was used. The antibody c-Ab was immobilized with a surface mass density of Γ = 41 ng mm^{-2} in the gel. In these experiments, buffer and human serum samples spiked with f-PSA were analyzed. As described before, the analysis was performed in cycles comprising the flow of the analyzed sample for 15 min followed by the 10 min incubation of the d-Ab, 5 min rinsing with HBS-EP buffer and regeneration. Figure 4.2.22 shows the time evolution of the fluorescence signal F measured during the five detection cycles for the HBS-EP samples spiked with f-PSA at concentrations of 0 - 10 pM. These data reveal that fluorescence sensor response ΔF increases with the concentration of f-PSA. For the concentration of f-PSA equal to zero, a rapid step-like increase and decrease in the fluorescence signal F was observed at time t = 0 and 10 min, respectively, due to the diffusion of d-Ab in and out of the gel. No measureable change in the fluorescence signal ΔF was observed for the blank HBS-EP buffer sample, and the sample with the f-PSA at a concentration of 10 pM induced a sensor response of $\Delta F = 2.3\times10^4$ cps.After the flow of the detection antibody d-Ab, the angular fluorescence intensity spectra were measured for the concentrations of f-PSA 0, 0.4 and 10 pM, see Figure 4.2.22B. Strong fluorescence peaks were observed at the angle of incidence for which LRSPs were resonantly excited and their maximum intensity increases with the concentration of f-PSA. Moreover, an enhanced fluorescence signal was measured at angles close to the critical angle $\theta = 47.4°$. This increase is due to the coupling of the incident light to the hydrogel waveguide mode TM_2 that provides an additional enhancement of the electromagnetic field intensity similar to LRSPs. Similarly, the sensor response *ΔF* for a series of human serum samples spiked with f-PSA was measured. For the analysis of blank human serum sample not spiked with f-PSA, a significant increase in the senor response of *ΔF(0)* ~ 625 cps was observed which was probably due to the non-specific adsorption of d-Ab to the blood plasma components adhering to the sensor surface.

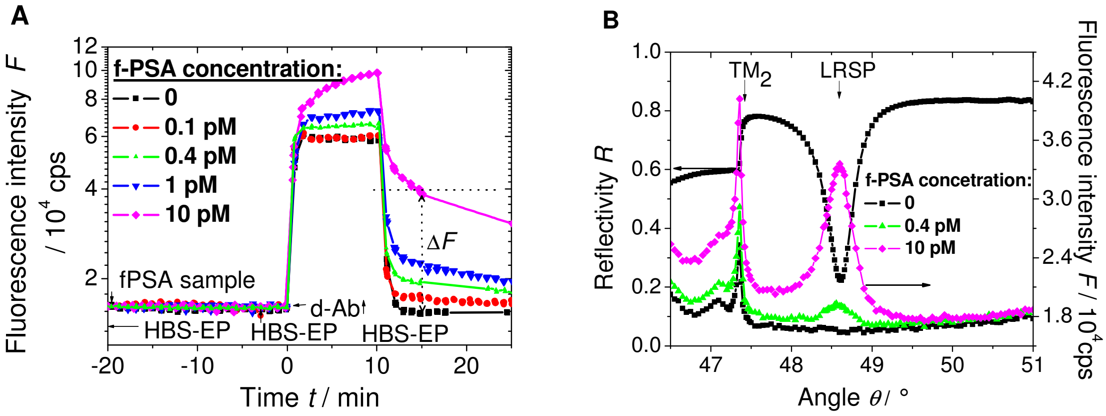

***Figure 4.2.22** (A) Time evolution of the fluorescence signal F upon the analysis of HBS-EP samples spiked with f-PSA at concentrations 0 - 10 pM. **(B)** Angular fluorescence spectra measured after the flow of HBS-EP samples spiked with f-PSA at concentrations of 0, 0.4 and 10 pM.*

The comparison of the calibration curve for the direct detection f-PSA in HBS-EP buffer (SPR) and for the fluorescence readout of sandwich immunoassay detection of f-PSA in HBS-EP and human serum (SPFS) is presented in Figure 4.6.21. The LOD for the SPFS readout was defined as the concentration for which the linear fit of the calibration curve reaches that for a blank sample *ΔF(0)* plus three times the standard deviation of the fluorescence signal $3\sigma(F)$ = ~230 cps. For the detection in HBS-EP buffer and human serum, the LOD of 34 and 330 fM was determined, respectively. The LOD of f-PSA in human serum is about one order of magnitude higher than that of PSA in buffer probably due to slower diffusion of f-PSA into the gel in the serum which exhibit higher viscosity and owing to the blocking the c-Ab antibody immobilized in the hydrogel matrix by means of non-specific adsorption. The sensor surface showed good reproducibility with the relative standard deviation of the sensor response *ΔF* of 4% after 30 detection cycles and four days of operation. SPFS-based analysis of an individual sample was performed in 30 min including the 15 min incubation of the sensor surface with a sample, 10 min flow of the d-Ab and 5 min washout of the sensor surface. In comparison to the regular SPFS and dextran brush surface architecture reported by Yu et al.[179], a moderate improvement of LOD (approximately two-fold) and sample incubation time (two-fold) was achieved. In human serum, the LOD was significantly deteriorated. This effect was probably due to the non-specific interaction of the serum with the PCMD hydrogel matrix that was not observed for the dextran brush on the top of the CM5 chip (from Biacore, Sweden).

We expect that the LOD can be further improved by the optimization of the hydrogel density and thickness in order to provide faster diffusion of target analyte and its binding closer to the surface where the LRSP field enhancement is stronger. In addition, compacting the captured analyte on the sensor surface by externally triggered collapse observed for “smart” gels can be used for more sensitive detection of molecular binding.[184] For the thickness of the hydrogel matrix d_h larger than 1 µm, the excitation of an additional hydrogel waveguide mode was observed to provide enhancement of the fluorescence signal which may provide new, potentially more sensitive, means for the detection of biomolecular binding events.

In summary the PCMD matrix exhibits a highly open structure in which protein catcher molecules can be immobilized with orders of magnitude larger surface mass density compared to *e.g.* the monolayer surface architectures relying on thiol-SAM. The measurement of the kinetics of the binding of f-PSA to the immobilized catcher antibody showed that the target analyte can diffuse fast through the gel and the determined affinity binding constants were comparable to those obtained for other surface architectures. The direct detection of f-PSA by using the spectroscopy of LRSPs and sandwich immunoassay-based detection combined with SPFS were carried out. The LOD for the fluorescence-based detection of 34 fM was achieved in buffer, which was more than 4 orders of magnitude lower than that for the direct detection. In addition, the fluorescence readout combined with the sandwich immunoassay was less affected by the non-specific interaction of human serum with the PCMD hydrogel matrix and allowed for the analysis of f-PSA at concentrations down to 330 fM.

4.2.8 Conclusion and Outlook

Two new biosensor platforms exploiting the excitation of optical waveguide modes and long range surface plasmons in a thick PCMD hydrogel matrix were developed, characterized and applied to clinically relevant analytes. The analyte detection by OWFS inside a several µm thick hydrogel layer showed a fluorescence enhancement of 2-3 orders of magnitude compared to the corresponding SPFS signal and an iimproved signal to noise ratio. Although, many factors such as the analyte distribution inside the matrix, the coupling efficiency of the optical waveguide modes or the thickness of the PCMD matrix can still be optimized, the fluorescence enhancement with OWFS compared to SPFS is very promising. The results for the detection of the clinically relevant p53-antibodies are in agreement with the detection of streptavidin as a model system which proofs the applicability of the concept. Furthermore, the sensor concept can be simplified if no surface plasmon is needed. The gold layer can be reduced resulting in highly enhanced coupling efficiencies of the leaky optical waveguide modes. Increased coupling efficiencies are expected to result in an increased fluorescence signal and thus in an increased sensitivity. Further optimization of the hydrogel matrix could aim for the optimization of the carboxyl group content and thickness for example.

The application of the PCMD binding matrix to clinically relevant samples was performed by exploiting the excitation of long range surface plasmons for the detection of f-PSA in human serum. The LOD for the fluorescence-based detection of 34 fM was achieved in buffer, which is more than 4 orders of magnitude lower than the one for the direct detection. In addition, the fluorescence readout combined with the sandwich immunoassay was less affected by the non-specific interaction of human serum with the PCMD hydrogel matrix and allowed for the analysis of f-PSA at concentrations down to 330 fM.

Further optimization of the hydrogel matrix and modifying the optical sensor concept for the readout of arrays of sensing spots is expected to provide a generic biosensor platform for rapid and ultra-sensitive analysis with potential applications in a range of important areas including medical diagnostics.

4.2.9 Experimental

Hydrogel Matrix: The synthesis of the PCMD hydrogel matrix and its film formation and surface attachment is described in Chapter 3.1. The hydrogel matrix used for these experiments was type (**3**). A schematic synthesis overview is shown in Figure 3.1.1. The hydrogel samples were swollen in buffer, usually PBS 150mM, over night to reach an equilibrium state followed by the screening of the different buffers and the biosensor experiment.

SPR/OWS Measurements: Surface plasmon resonance-, optical waveguide mode and fluorescence spectroscopy were performed in the Kretschmann configuration[57]. The experimental setup and the simulation of the experimental data on the basis of the Fresnel equation for a so called box-model system is described in Chapter 4.1.7 and Chapter 2.1. The simulation of the OWS/SPR spectra applying the reversed Wentzel-Kramers-Brillouin approximation to extract the refractive index-thickness film profiles is described and applied in Chapter 4.1.6 and Chapter 2.3.

The incident laser intensity (HeNe laser, 633 nm) was adjusted to an identical value of 100 % reflectivity for all experiments. Thereby, 100 % reflectivity corresponds to 145 µW. For this purpose the detector was placed at an angular position of 90º. In this position the laser beam directly reflected into the detector. The detected intensity is than adjusted to 100 %.

SPFS/OWFS Measurements: A photomultiplier which is located at the backside of the flow cell at the opposite site of the incoming laser beam detects the fluorescence intensity. To filter the laser light a 633 nm Notch Filter (Semrock, NF01-633U-25) and to select the fluorescence light a 670 nm BrightLine (Semrock) were used. Hence a simultaneous recording of the SPR/OWS- and the fluorescence spectrum is possible. The laser intensity was adjusted to 100 % or 10 % reflectivity corresponding to 145 µW or 14.5 µW respectively. The energy used for fluorescence excitation is further reduced to the light intensity dissipated into the hydrogel matrix.

The exponentially decaying electromagnetic field of the surface plasmon has a detection range of approximately 150-200 nm.[57] Consequently a shift of the surface plasmon indicates a change of the refractive index within the 200 nm from the hydrogel-gold interface whereas the optical waveguide modes are screening refractive index variations of the entire hydrogel matrix. After reaching equilibrium surface plasmon signal an angular scan was measured and the refractive index-thickness PCMD profile was extracted (Chapter 2.3) and compared to the one before incubation

The WKB Profiles were calculated as described in Chapter 2.3 and 4.1.7. The angular position of the optical waveguide modes are used for the calculation of a refractive index-thickness profile on the basis of Fresnel's equations (program: Bernhard Menges, Max Planck Institute for Polymer Research, Mainz, Germany). The value calculated for x = 0 nm is set to x = 150 nm and the refractive index derived from the surface plasmon in the angular spectra is set to x = 0 nm.

The electromagnetic field distribution of the optical waveguide modes and the optical waveguide mode dependent refractive index were calculated by Markus Plum. Therefore, the commercially available program ATSOS (A. Unger, U. Trutschel, and U. Langbein, "Design software for stratified optical systems with planar and cylindrical symmetry," in DGaO-Proceedings 2007, http://www.dgao-proceedings.de/download/108/108_p12.pdf.) was applied. The parameters of the "box-model" simulating the reflectivity-angular scans of the corresponding matrix are used to calculate the electromagnetic field distribution of the optical waveguide modes. The values for the 2 boxmodel system are summarized in table 4.2.1.

Table 4.2.1 *Parameters used for the simulation with "ATSOS".*

Layer	*Thickness /nm*	*ε' (real)*	*ε'' (imaginary)*
LaSFN9	0	3,407	0
Chromium	1.9	-4	16,8
Gold	46	-12,4	1,6
SAM	3	2,06	0
Hydrogel-I	150	1,879	0
Hydrogel-II	11500	1,8567	0,0013
PBS	0	1,778	0

Coupling with Para-Tetrafluorophenol Sulfonate (TFPS): For the coupling of bovine serum albumin (BSA) to the carboxyl groups of the dextran-based hydrogel matrix a BSA concentration of 5 mg in 500µL 10 mM acetate buffer at pH 4 which is below its isoelectric point was injected for 5 minutes. The hydrogel matrix used for this experiment had a degree of benzophenone substitution of ~0.018 and a degree of carboxymethylation of ~0.27.

Biosensor Experiments: The sample cell used for all biosensor experiments consists of a custom-made glass flow cell with an inlet and an outlet needle at a distance of 0.7 cm and a PDMS spacer enclosing the in- and outlet. The volume was ~ 40 µL. This cell is placed onto the hydrogel covered substrate and placed into the SPR/OWS setup.

For the covalent immobilization of biotinethylenediamine hydrobromide and p53 the swollen PCMD-hydrogel matrix was activated with a fresh mixture of usually 500 µL of 0,4 M 1-(3-dimethylaminopropyl)-3-ethyl-carbodiimide hydrochloride (EDC) and 500 µL of 0,1 M *N*-hydroxysuccinimide (NHS) in distilled water for 10 min followed by rinsing with buffer for 3 minutes and the injection of 1 mL of biotinethylenediamine hydrobromide (Sigma Aldrich) in 10 mM sodium acetate buffer (pH 5,5) at a concentration of 2 mg/mL for 10 min. For the p53 immobilization the sensor matrix was typically incubated with 100 µL p53 (Wild-type, Dianova) (20 µg) solution prepared in sodium acetate buffer (10mM, pH 5,5) for 50 min.

For the detection of streptaviding-Cy5 in a biotinethyleneamine modified PCMD-hydrogel matrix streptavidin-cy5 (BioLegend) dissolved in PBS 150 mM was injected with increasing injection times at a fixed concentration of 200 or 100 µg/mL. The binding was followed by the SPR kinetic mode at a fixed angle in the linear part of the surface plasmon and by recording a SPR/OWS/SPFS/OWFS scan before and after every incubation step after reaching equilibrium of the fluorescence and SPR signal.

The p53-modified hydrogel served as matrix for the detection of p53Ab6. Therefore, increasing concentrations of p53Ab6 (monoclonal, Dianova) (0,1-50 µg/mL) in PBS were injected at a flow rate of 0,1 mL/min and the unbound antibody was subsequently removed by rinsing with PBS for 5 minutes until equilibrium signal was reached. Subsequent injection of 100 µg of the secondary antibody Alexa Fluor 647 goat anti-mouse IgG (H+L) (MoBiTec) in 500µL PBS for 5 minutes resulted in screening of the p53Ab6. The unbound antibody was again washed out until the equilibrium fluorescence signal was reached. Every detection step was documented by an SPR/OWS/SPFS/OWFS spectrum.

In case different coupling conditions were used for any of the biosensing steps these are indicated in the corresponding Figure captions.

Western Blot Analysis: The Western Blot was performed by Sandra Ritz at the Max Planck Institute for Polymer Research.. In order to analyse the binding specify and the appropriate working dilution for the p53-antibody, 0.2 µg of p53 (Dianova) were mixed with reducing SDS loading buffer and denaturised at 70°C for 10 min. The protein was separated by electrophoresis on a NuPAGE™ 10% Bis-Tris gel (Invitrogen) and transferred to a 0.45 µm nitrocellulose membrane by semi-dry blotting. The immunodetection performed with a chemiluminescent detection system for mouse primary antibodies (Western Breeze, Invitrogen) according the standard protocol with indicated dilutions of the p53-p53Ab6 monoclonal antibody (Dianova). The protein size was determined with the Magic Mark XP protein ladder (Invitrogen).

Long Range Surface Plasmon Enhanced Fluorescence Detection:

Chemicals and Biochemicals: All reagents were used as received without further purification. f-PSA (>95% pure from human seminal fluid, A32874H), a monoclonal mouse IgG_1 antibody recognizing the PSA epitope 4 used as a capture antibody (c-Ab, M86599M) and a monoclonal mouse IgG_{2a} antibody specific for the PSA epitope 6 used as a detection antibody (d-Ab, M86506M) were obtained from Biodesign (Biosite, Sweden). HBS-EP buffer (degassed 10 mM HEPES buffer saline, pH 7.4, 150 mM NaCl, 3 mM EDTA, 0.005% (v/v) surfactant P-20), acetate buffer (10 mM, pH 5.0), glycine buffer (10 mM, pH 1.7) were obtained from Biacore (Sweden). The d-Ab was labeled using Alexa Fluor 647 labeling kit from Molecular Probes Inc. (USA). The dye-to-protein molar ratio was determined by an UV-visible spectrometer as 5. Single donor female serum was obtained from Innovative Research (USA). The novel photo-crosslinkable carboxymethyl dextran (PCMD) was synthesized as described in Chapter 3.1. The PCMD carried carboxyl groups for the anchoring of protein molecules via their amino groups and benzophenone groups for the crosslinking and attaching of the gel to a metallic surface that was modified with benzophenone moieties by UV light. In the following experiments, we used two PCMDs with the ratio of benzophenone and carboxyl groups to C-H groups of 1 : 6.5 : 34 and 1 : 4.4 : 23, respectively. The benzophenone-terminated thiol was synthesized as described in the literature.[168]

Sensor Instrument As described in Chapter 2.1, an attenuated total reflection (ATR) method was used for the excitation of LRSPs on the sensor surface. A transverse magnetically (TM) polarized beam from a HeNe laser (λ = 632.8 nm) was coupled to a LASFN9 glass prism. Onto the prism base, a sensor chip with a layer structure supporting LRSPs was optically matched. This layer structure consisted of a low refractive index film (Cytop CTL-809M obtained from ASAHI, Japan) and a gold film with the thicknesses of ~770 nm and ~ 20 nm, respectively, prepared as described previously.[164] A flow-cell with a volume of approximately 12 µL was mounted against the sensor surface. Aqueous samples (with a refractive index close to n_b = 1.333) were pumped at the flow rate of 0.5 mL min^{-1} through the flow-cell using a peristaltic pump. The analyzed samples circulated in the fluidic system with a total volume of 800 µL. The fluorescence light emitted from the sensor surface was collected through the flow-cell by a lens (numerical aperture NA = 0.3), passed through a band-pass filter (transmission wavelength of λ = 670 nm) and its intensity was detected by a photomultiplier tube (PMT) from Hamamatsu (H6240-01, Japan). The LASFN9 glass prism was mounted on a motorized rotation stage and angular reflectivity spectra $R(\theta)$ were measured by using a photodiode detector and lock-in amplifier. The monitoring of reflectivity changes ΔR at an angle of incidence θ set to the maximum slope of the dip associated with the resonant excitation of LRSPs allowed the measurement of refractive index changes with the resolution around 10^{-6} refractive index units (RIU). The electronics supporting the sensor system was controlled by using the software Wasplas developed at the Max Planck Institute for Polymer Research in Mainz (Germany). The measured reflectivity curves were fitted by the transfer matrix-based model implemented in the software Winspall developed at the Max Planck Institute for Polymer Research in Mainz (Germany). By using this model, the thickness d_h and the refractive index n_h of the hydrogel binding matrix was determined by fitting the resonant angles for the excitation of LRSP and hydrogel waveguide modes similar as described before.[167] In the further analysis, we assumed that the refractive index of the hydrogel n_h changes with the concentration of proteins and the hydrogel polymer as $\partial n/\partial c \approx 0.2$ µL mg^{-1}. From the refractive index contrast n_h - n_b and the thickness d_h the surface mass density Γ of the hydrogel film was calculated as:

$$\Gamma = \left(n_h - n_b\right) d_h \frac{\partial c}{\partial n_h} . \tag{4.2.1}$$

Functionalization of the Sensor Surface: The gold-coated substrates were immersed in ethanol containing 5 mM benzophenone-terminated thiol to allow the formation of a self-assembled monolayer (SAM). After the overnight incubation, the gold surface was rinsed with ethanol and dried with a nitrogen stream. On the surface modified by the thiol-SAM, a PCMD layer was deposited by spin-coating with the thickness in the range of 210 - 280 nm (measured in contact with air) from an aqueous solution with the concentration of PCMD between 60 and 80 mg mL^{-1}. Afterwards, the PCMD film was dried at a temperature of $T = 45$ °C for 4 hours and exposed to UV-light (wavelength of $\lambda = 254$ nm, irradiation energy dose of 2 J cm^{-2}) for 90 min in order to establish its photo-chemical attachment to the surface and cross-linking. Then, the substrates were mounted to the sensor, the PCMD hydrogel was swollen in ACT buffer at pH = 5 and *in situ* c-Ab were immobilized according to the following recipe. Firstly, a mixture of 1-(3-dimethylaminopropyl)-3-ethylcarbodiimide hydrochloride (EDC, 37.5 mg mL^{-1}) and *N*-hydroxysuccinimide (NHS, 10.5 mg mL^{-1}) was flowed for 8 min in order to form terminal NHS ester moieties. Afterwards, the c-Ab dissolved in sodium acetate buffer (10 mM, pH 5.0) at a concentration of 50 µg mL^{-1} was injected for 30 min followed by rinsing with ACT buffer for 10 min. The unreacted NHS ester moieties were deactivated by the incubation in a 1 M ethanolamine hydrochloride solution for 7 min.

Detection Assay: Series of samples were prepared by spiking HBS-EP buffer and human serum (volume of 800 µL) with f-PSA. Samples with f-PSA dissolved in HBS-EP at concentrations between 3 and 300 nM were used for the evaluation of the direct detection of f-PSA. For the SPFS-based detection, f-PSA was dissolved in human serum (with free PCMD at a concentration of 0.5 mg mL^{-1}) and HBS-EP buffer at concentrations ranging from 100 fM to 10 pM. In the direct detection experiment, HBS-EP buffer was flowed for 10 min in order to establish a baseline followed by an the incubation of the sensor surface with of a sample for 30 min and rinsing by HBS-EP buffer for 10 min. Upon the binding of f-PSA to the PCMD hydrogel with c-Ab, the changes in reflectivity R were measured in time at a fixed angle θ set to the value providing the highest slope of the reflectivity LRSP dip. The direct sensor response was determined as the difference of the reflectivity signal ΔR before and after the f-PSA binding. In the SPFS-based detection, a sandwich immunoassay was employed. Firstly, a sample spiked with f-PSA was flowed through the sensor cell for 15 min. Afterwards, the hydrogel matrix was rinsed for one minute with HBS-EP buffer and d-Ab dissolved at a concentration of 1 nM was flushed through the sensor cell for 10 min followed by rinsing with HBS-EP buffer for 5 min. The fluorescence signal F was measured as a function of time at the resonant angle of incidence θ providing strong enhancement of the electromagnetic field due to the coupling to LRSPs. The fluorescence sensor response ΔF was evaluated as the difference between the fluorescence signal F before the injection of d-Ab and after the 4.5 min rinsing with HBS-EP (data points measured during 1 minute were averaged). The detection was performed in cycles. After each detection cycle, the sensor surface was regenerated by a 5-10 min pulse of glycine (pH = 1.5) and a 5-15 min pulse of 10 mM NaOH in order to release the captured f-PSA leaving free c-Ab binding sites.

4.2.10 Bibliography

[1] R. L. Rich, D. G. Myszka, *J. Mol. Recognit.* **2007**, *20*, 300.

[2] S. Löfas, B. Johnsson, *J. Chem. Soc., Chem. Commun.* **1990**, *21*, 1526.

[3] R. Zhang, M. Tang, A. Bowyer, R. Eisenthal, J. Hubble, *Reactive and Functional Polymers* **2006**, *66*, 757.

[4] D. J. Winzor, *Anal. Biochem.* **2003**, *318*, 1.

[5] T. Heinze, T. Liebert, B. Heublein, S. Hornig, *Adv. Polym. Sci.* **2006**, *205*, 199.

[6] T. Heinze, A. Koschella, *Macromol. Symp.* **2005**, *223*, 13.

[7] S. Löfas, M. Malmqvist, I. Roennberg, E. Stenberg, B. Liedberg, I. Lundstroem, *Sensors and Actuators B* **1991**, *5*, 79.
[8] C. Situ, A. R. G. Wylie, A. Douglas, C. T. Elliott, *Talanta* **2008**, *76*, 832.
[9] J.-F. Masson, T. M. Battaglia, J. Cramer, S. Beaudoin, M. Sierks, K. S. Booksh, *Anal Bioanal Chem* **2006**, *386*, 1951.
[10] B. Johnsson, S. Löfas, G. Lindquist, *Anal. Biochem.* **1991**, *198*, 268.
[11] F. Yu, B. Persson, S. Loefas, W. Knoll, *Anal. Chem.* **2004**, *76*, 6765.
[12] S. Flink, C. J. M. v. V. Frank, D. N. Reinhoudt, *Adv. Mater.* **2000**, *12*, 1315.
[13] M. A. Cooper, *Anal. Bioanal. Chem.* **2003**, *377*, 834.
[14] V. Chegel, Y. Shirshov, S. Avilov, M. Demchenko, M. Mustafaev, *J. Biochem. Biophys. Methods* **2002**, *50*, 201.
[15] W. Knoll, H. Park, E.-K. Sinner, D. Yao, F. Yu, *Surface Sci.* **2004**, *570*, 30.
[16] G. B. Sigal, C. Bamdad, A. Barberis, J. Strominger, G. M. Whitesides, *Anal. Chem.* **1996**, *68*, 490.
[17] K. Länge, S. Grimm, M. Rapp, *Sensors and Actuators B* **2007**, *125*, 441.
[18] K. Länge, M. Rapp, *Anal. Biochem.* **2008**, *377*, 170.
[19] N. Barié, M. Rapp, *Biosens. Bioelectron.* **2001**, *16*, 979.
[20] J. Piehler, A. Brecht, T. Giersch, B. Hock, G. Gauglitz, *J. Immunol. Methods* **1997**, *201*, 189.
[21] P. B. Luppa, L. J. Sokoll, D. W. Chan, *Clin. Chim. Acta* **2001**, *314*, 1.
[22] E. M. D. Barcelo, C. B. G. Gauglitz, R. Abuknesha, *Trends. Anal. Chem.* **2001**, *20*, 124.
[23] N. Miura, M. Sasaki, K. V. Gobi, C. Kataoka, Y. Shoyama, *Biosens. Bioelectron.* **2003**, *18*, 953.
[24] R. M. Pemberton, J. P. Hart, T. T. Mottram, *Biosens. Bioelectron.* **2001**, *16*, 715.
[25] A. Aulasevich, R. F. Roskamp, U. Jonas, B. Menges, J. Dostalek, W. Knoll, *Macromolecular Rapid Communications* **2009**, *30*, 872.
[26] Y. Wang, J. Dostálek, W. Knoll, *Biosensors and Bioelectronics* **2009**, *24*, 2264.
[27] K. R. Rogers, *Anal. Chim. Acta* **2006**, *568*, 222.
[28] D. R. Shankaran, K. V. Gobi, N. Miura, *Sensors and Actuators B* **2007**, *121*, 158.
[29] M. Yemini, M. Reches, E. Gazit, J. Rishpon, *Anal. Chem.* **2005**, *77*, 5155.
[30] O. Brandt, J. D. Hoheisel, *Trends in Biotechnology* **2004**, *22*, 617.
[31] T. G. Drummond, M. G. Hill, J. K. Barton, *Nat. Biotechnol.* **2003**, *21*, 1192.
[32] P. A. E. Piunno, U. J. Krull, *Anal. Bioanal. Chem.* **2005**, *381*, 1004.
[33] S. Subrahamanyam, S. A. Piletsky, A. P. F. Turner, *Anal. Chem.* **2002**, *74*, 3942.
[34] S. Kumbhat, D. R. Shankaran, S. J. Kim, K. V. Gobi, V. Joshi, N. Miura, *Chem. Lett.* **2006**, *35*, 678.
[35] J. J. Pancrazio, J. P. Whelan, D. A. Borkholder, W. Ma, D. A. Stenger, *Ann. Biomed. Eng.* **1999**, *27*, 697.
[36] K. M. L. May, Y. Wang, L. G. Bachas, K. W. Anderson, *Anal. Chem.* **2004**, *76*, 4156.
[37] C. J. Taylor, L. A. Bain, D. J. Richardson, S. Spiro, D. A. Russell, *Anal. Biochem.* **2004**, *328*, 60.
[38] J. Lahiri, L. Isaacs, J. Tien, G. M. Whitesides, *Anal. Chem.* **1999**, *71*, 777.
[39] J. Turkova, *J. Chromatrogr. B* **1999**, *722*, 11.
[40] P. W. Beines, I. Klosterkamp, B. Menges, U. Jonas, W. Knoll, *Langmuir* **2007**, *23*, 2231.
[41] Y. Qiu, K. Park, *Advanced Drug Delivery Reviews* **2001**, *53*, 321.
[42] S. Y. Song, H. G. Choi, J. W. Hong, B. W. Kim, S. J. Sim, H. C. Yoon, *colloids and Surfaces A: Physicochem. Eng. Aspects* **2008**, *313-314*, 504.
[43] I. Chaiken, S. Rose, R. Karlsson, *Anal. Biochem.* **1992**, *201*, 197.
[44] H.-S. Ro, B. H. Koh, S. O. Jung, H. K. Park, Y.-B. Shin, M.-G. Kim, B. H. Chung, *Proteomics* **2006**, *6*, 2108.
[45] C. Cao, J. P. Kim, B. W. Kim, H. Chae, H. C. Yoon, S. S. Yang, S. J. Sim, *Biosens. Bioelectron.* **2006**, *21*, 2106.
[46] L. Huang, G. Reekmans, D. Saerens, J. M. Friedt, F. Frederix, L. Francis, S. Muyldermans, A. Campitelli, C. Van Hoof, *Biosens. Bioelectron.* **2005**, *21*, 483.
[47] D. Habauzit, J. Chopineau, B. Roig, *Anal. Bioanal. Chem.* **2007**, *387*, 1215.
[48] S. Kumbhat, D. R. Shankaran, S. J. Kim, K. V. Gobi, V. Joshi, N. Miura, *Biosensors and Bioelectronics* **2007**, *23*, 421.
[49] W. Huber, F. Mueller, *Current Pharmaceutical Design* **2006**, *12*, 3999.
[50] E. Stenberg, B. Persson, H. Roos, C. Urbaniczky, *Journal of Colloid and Interface Science* **1991**, *143*, 513.
[51] P. Bjurling, G. A. Baxter, M. Caselunghe, c. Jonson, M. O'Connor, B. Persson, C. T. Elliot, *Analyst* **2000**, *125*, 1771.
[52] L. M. Bonanno, L. A. DeLouise, *Biosensors and Bioelectronics* **2007**, *23*, 444.

[53] C. Campagnolo, K. J. Meyers, T. Ryan, R. C. Atkinson, Y.-T. Chen, M. J. Scanlan, G. Ritter, L. J. Old, C. A. Batt, *J. Biochem. Biophys. Methods* **2004**, *61*, 283.

[54] A. Sternesjö, C. Mellgren, L. Björck, *Anal. Biochem.* **1995**, *226*, 175.

[55] J.-F. Masson, T. M. Battaglia, P. Khairallah, S. Beaudoin, K. S. Booksh, *Anal. Chem.* **2007**, *79*, 612.

[56] R. Pei, X. Cui, X. Yang, E. Wang, *Talanta* **2000**, *53*, 481.

[57] W. Knoll, *Annu. Rev. Phys. Chem* **1998**, *49*, 569.

[58] H. V. Hsieh, J. E. Gestwicki, J. B. Pitner, *Proc. Spie.* **2002**, *4624*, 81.

[59] M. P. Kreuzer, R. Quidant, G. Badenes, M.-P. Marco, *Biosensors and Bioelectronics* **2006**, *21*, 1345.

[60] A. W. Wark, H. J. Lee, A. J. Qavi, R. M. Corn, *Anal. Chem.* **2007**, *79*, 6697.

[61] H. J. Lee, A. W. Wark, R. M. Corn, *Analyst* **2008**, *133*, 596.

[62] J. S. Mitchell, Y. Q. Wu, C. J. Cook, L. Main, *Anal. Biochem.* **2005**, *343*, 125.

[63] L. He, M. D. Musick, S. R. Nicewarner, F. G. Salinas, S. J. Benkovic, M. J. Natan, C. D. Keating, *J. Am. Chem. Soc.* **2000**, *122*, 9071.

[64] J. S. Mitchell, Y. Wu, C. J. Cook, L. Main, *Analytical Biochemistry* **2005**, *343*, 125.

[65] A. W. Wark, H. J. Lee, A. J. Qavi, R. M. Corn, *Anal. Chem.* **2007**, *79*, 6697.

[66] H. J. Lee, A. W. Wark, R. M. Corn, *Analyst* **2008**, *133*, 596.

[67] L. He, M. D. Musick, S. R. Nicewarner, G. S. Frank, S. J. Benkovic, M. J. Natan, C. D. Keating, *J. Am. Chem. Soc.* **2000**, *122*, 9071.

[68] X. Yao, X. Li, F. Toledo, C. Zurita-Lopez, M. Gutova, J. Mamand, F. Zhou, *Analytical Biochemistry* **2006**, *354*, 220.

[69] T. T. Goodrich, H. J. Lee, R. M. Corn, *J. Am. Chem. Soc.* **2004**, *126*, 4086.

[70] T. T. Goodrich, H. J. Lee, R. M. Corn, *J. Am. Chem. Soc.* **2004**, *126*, 4086.

[71] J. S. Mitchell, Y. Wu, C. J. Cook, L. Main, *Steroids* **2006**, *71*, 618.

[72] H. Aizawa, M. Tozuka, S. Kurosawa, K. Kobayashi, S. M. Reddy, M. Higuchi, *Analytica Chimica Acta* **2007**, *591*, 191.

[73] J. Wang, F. Wang, X. Zou, Z. Xu, S. Dong, *Electrochemistry Communications* **2007**, *9*, 343.

[74] J. Dostalek, W. Knoll, *Biointerphases* **2008**, *3*, FD12.

[75] T. Neumann, M. L. Johansson, D. Kambhampati, W. Knoll, *Adv. Funct. Mater.* **2002**, *12*, 575.

[76] J. Dostalek, W. Knoll, *Biointerphases* **2008**, *3*, FD12.

[77] T. Neumann, M. L. Johansson, D. Kambhampati, W. Knoll, *Adv. Funct. Mater.* **2002**, *12*, 575.

[78] K. Vasilev, W. Knoll, M. Kreiter, *J. Chem. Phys.* **2004**, *120*, 3439.

[79] T. Liebermann, W. Knoll, *Colloids Surf. A: Physicochem. Eng. Aspects* **2000**, *171*, 115.

[80] T. Liebermann, W. Knoll, *Colloids and Surfaces A: Physicochemical and Engineering Aspects* **2000**, *171*, 115.

[81] E. Matveeva, Z. Gryczynski, I. Gryczynski, J. Malicka, J. R. Lakowicz, *Anal. Chem.* **2004**, *76*, 6287.

[82] E. Mateeva, Z. Gryczynski, I. Gryczynski, J. Malicka, J. R. Lakowicz, *Anal. Chem.* **2004**, *76*, 6287.

[83] F. Yu, B. Persson, S. Lofas, W. Knoll, *J. Am. Chem. Soc.* **2004**, *126*, 8902.

[84] F. Yu, B. Persson, S. Löfas, W. Knoll, *J. Am. Chem. Soc.* **2004**, *126*, 8902.

[85] K. S. Phillips, Q. Cheng, *Anal Bioanal Chem* **2007**, *387*, 1831.

[86] R. L. Rich, D. G. Myszka, *Current opinion in Biotechnology* **2000**, *11*, 54.

[87] X. D. Hoa, A. G. Kirk, M. Tabrizian, *Biosensors and Bioelectronics* **2007**, *23*, 151.

[88] R. L. Rich, D. G. Myszka, *Journal of Molecular Recognition* **2005**, *18*, 431.

[89] R. L. Rich, D. G. Myszka, *Journal of Molecular Recognition* **2006**, *19*, 478.

[90] E. Gizeli, N. J. Goddard, C. R. Lowe, A. C. Stevenson, *Sens. Actuators B Chem.* **1992**, *6*, 131.

[91] G. McHale, M. I. Newton, F. Martin, E. Gizeli, K. A. Melzak, *Appl. Phys. Lett.* **2001**, *79*, 3542.

[92] M. Weisser, B. Menges, S. Mittler-Neher, *Sensors and Actuators B* **1999**, *56*, 189.

[93] N. Skivesen, R. Horvath, S. Thinggaard, N. B. Larsen, H. C. Pedersen, *Biosensors and Bioelectronics* **2007**, *22*, 1282.

[94] A. Minardo, R. Bernini, F. Mottola, L. Zeni, *Opt. Express* **2006**, *14*, 3512.

[95] R. E. Kunz, K. Cottier, *Anal. Bioanal. Chem.* **2006**, *384*, 180.

[96] Y. Zong, K. Tawa, B. Menges, J. Ruehe, W. Knoll, *Langmuir* **2005**, *21*, 7036.

[97] M. Zourob, A. Simonian, J. Wild, S. Mohr, X. Fan, I. Abdulhalim, N. J. Goddard, *The Analyst* **2007**, *132*, 114.

[98] A. Sato, B. Menges, W. Knoll, *J. Appl. Phys.* **2009**, *105*, 014701.

[99] B. Menges, A. Sato, W. Knoll, *Proc. SPIE* **2007**, *6556*, 65560G.

[100] M. Dürr, B. Menges, W. Knoll, A. Yasuda, G. Nelles, *Appl. Phys. Lett.* **2007**, *91*, 021113.

[101] P. C. Mathias, N. Ganesh, W. Zhang, B. T. Cunningham, *J. Appl. Phys.* **2008**, *103*, 094320.

[102] A. Kasry, W. Knoll, *Appl. Phys. Lett.* **2006**, *89*, 101106.

[103] J. Dostálek, A. Kasry, W. Knoll, *Plasmonics* **2007**, *2*, 97.

[104] Y. Wang, J. Dostalek, W. Knoll, *Biosens. Bioelectron.* **2009**, *24*, 2264.

[105] D. Sarid, *Phys. Rev. Lett.* **1981**, *47*, 1927.

[106] A. Kasry, J. Dostalek, W. Knoll, Wiley-VCH, Weinheim, **2009**.

[107] W. Knoll, A. Karsy, F. Yu, Y. Wang, A. Brunsen, J. Dostálek, *Journal of Nonlinear Optical Physics & Materials* **2008**, *17*, 121.

[108] V. Nanduri, A. K. Bhunia, S.-I. Tu, G. C. Paoli, J. D. Brewster, *Biosensors and Bioelectronics* **2007**, *23*, 248.

[109] M. Wilchek, E. A. Bayer, O. Livnah, *Immunology Letters* **2006**, *103*, 27.

[110] P. Vermette, T. Gengenbach, U. Divisekera, P. A. Kamouris, H. J. Griesser, L. Meagher, *J. Colloid and Interface Sci.* **2003**, *259*, 13.

[111] P. C. Weber, D. H. Ohlendorf, J. J. Wndoloski, F. R. Salemme, *Science* **1989**, *243*, 85.

[112] J. DeChancie, K. N. Houk, *J. Am. Chem. Soc.* **2007**, *129*, 5419.

[113] P. May, E. May, *Oncogene* **1999**, *18*, 7621.

[114] A. J. Giaccia, M. B. KAstan, *Genes Dev.* **1998**, *12*, 2973.

[115] E. Appella, C. W. Anderson, *Pathol. Biol.* **2000**, *48*, 227.

[116] Y. Cho, S. Gorina, P. D. Jeffrey, N. P. Pavletich, *Science* **1994**, *265*, 346.

[117] S. Friend, *Science* **1994**, *265*, 334.

[118] S. Brandau, A. Boehle, *Eur. Urol.* **2001**, *39*, 491.

[119] V. Leblanc, V. r. Delaunay, J. C. Lelong, F. Gas, G. r. Mathis, J. Grassi, E. May, *Analytical Biochemistry* **2002**, *308*, 247.

[120] S. H. Kroft, R. Oyasu, *Lab Invest* **1994**, *71*, 158.

[121] C. A. Reznikoff, C. D. Belair, R. R. Yeager, e. al., *Semin Oncol* **1996**, *23*, 571.

[122] B. J. Schmitz-Dräger, P. J. Goebell, T. Ebert, Y. Fradet, *Eur. Urol.* **2001**.

[123] Y. Yamaguchi, H. Watanabe, S. r. Yrdiran, K. Ohtsubo, Y. Motoo, T. Okai, N. Sawabu, *Clinical Cancer Research* **1999**, *5*, 1147.

[124] E. Jagelska´, V. Bra´zda, S. Pospisilova´, B. Vojtesek, E. Palacek, *Journal of Immunological Methods* **2002**, *267*, 227.

[125] T. Soussi, *Cancer Research* **2000**, *60*, 1777.

[126] T. R. Hupp, D. W. Meek, C. A. Midgley, D. P. Lane, *Cell* **1992**, *71*, 875.

[127] M. Behn, M. Schuermann, *Nucleic Acids Research* **1998**, *26*, 1356.

[128] C. Kuhn, F. Muller, C. Melle, H. P. Nasheuer, F. Janus, W. Deppert, F. Grosse, *Oncogene* **1999**, *769-774*.

[129] D. R. Hall, D. J. Winzor, *J. Chromatrogr. B* **1998**, *715*, 163.

[130] R. Karlsson, A. Faelt, *J. Immunol. Methods* **1997**, *200*, 121.

[131] M. Malmqvist, *Nature* **1993**, *361*, 186.

[132] E. Maillart, K. Brengel-Pesce, D. Capela, A. Roget, T. Livache, M. Canva, Y. Levy, T. Soussi, *Oncogene* **2004**, *23*, 5543.

[133] P. K. Wilson, T. Jiang, M. E. Minunni, A. P. F. Turner, M. Mascini, *Biosensors and Bioelectronics* **2005**, *20*, 2310.

[134] T. Jiang, M. Minunni, P. Wilson, J. Zhang, A. P. F. Turner, M. Mascini, *Biosensors and Bioelectronics* **2005**, *20*, 1939.

[135] A. M. Davidoff, J. D. Igelhart, J. R. Marks, *Proc. Natl. Acad. Sci. USA* **1992**, *89*, 3439.

[136] M. Reuschenbach, M. v. K. Doebritz, N. Wentzensen, *Cancer Immunol Immunother* **2009**, *58*, 1535.

[137] M. C. v. Breven, M. C. Hollstein, H. M. Cawley, e. al., *Cancer Res.* **1996**, *56*, 4917.

[138] C. M. Wu, R. Tang, J. R. Chen, e. al., *Oncol. Rep.* **2004**, *12*, 1045.

[139] C. P. Wild, M. Ridanapaa, A. Anttila, e. al., *Int. J. Cancer* **1995**, *64*, 176.

[140] Y. Shibata, H. Kotanagi, H. Andoh, K. Koyama, H. Itoh, S. Kudo, *Dis Colon Rectum* **1996**, *39*, 1269.

[141] H. Wunderlich, W. Hindermann, M. Huller, e. al., *Urol. Int.* **2000**, *64*, 13.

[142] R. Tang, C. Y. Yeh, J.-Y. Wang, C. R. Changchien, J.-S. Chen, L. L. Hsieh, *Ann. Surg. Oncol.* **2009**, *16*, 2516.

[143] R. P. Tang, C. Y. Yeh, J. Y. Wang, C. R. Changchien, J. S. Chen, L. L. Hsieh, *Annals of Surgical Oncology* **2009**, *16*, 2516.

[144] J. P. Peyrat, J. Bonneterre, R. Lubin, L. Vanlemmens, J. Fournier, T. Soussi, *Lancet.* **1995**, *345*, 621.

[145] G. Zalcman, J. Tredaniel, B. Schichtholz, e. al., *Int. J. Cancer* **2000**, *89*, 81.

[146] R. N. Saigner, M. H.Shah, A. A. Desai, e. al., *Tumori* **2006**, *92*, 134.

[147] M. R. Rosenfeld, N. Malats, L. Schramm, e. al., *J. Natl Cancer Inst.* **1997**, *89*, 381.

[148] T. Morita, N. Tachikawa, T. Kumamaru, e. al., *Eur. Urol.* **2000**, *37*, 79.

[149] T. Nozoe, M. Yasuda, M.Honda, S. Inutsuka, D. Korenaga, *Hepatogastroenterology* **2007**, *54*, 1422.

[150] G. Zalcman, B. Schlichtholz, J. Tredaniel, T. Urban, R. Lubin, I. Dubois, B. Milleron, A. Hirsch, T. Soussi, *Clinical Cancer Research* **1998**, *4*, 1359.

[151] J. M. Brown, B. G. Wouters, *Cancer Res.* **1999**, *59*, 1391.

[152] S. Löfas, B. Johnsson, A. Edstrom, G. Hansson, G. Linquist, R. Müller, L. Stigh, *Biosens. Bioelectron.* **1995**, *10*, 813.

[153] B. Liedberg, I. Lundström, E. Stenberg, *Sensors and Actuators B* **1993**, *11*, 63.

[154] S. Löfas, *Pure & Appl. Chem.* **1995**, *67*, 829.

[155] Y. Wang, A. Brunsen, U. Jonas, J. Dostalek, W. Knoll, *Analytical Chemistry* **2009**, *81*, 9625.

[156] S. L. McGurk, R. J. Green, G. H. W. Sanders, M. C. Davies, C. J. Roberts, S. J. B. Tendler, P. M. Williams, *Langmuir* **1999**, *15*, 5136.

[157] M. Malmsten, *Colloid. Surface A* **1999**, *159*, 77.

[158] V. Silin, H. Weetall, D. J. Vanderah, *Colloid. Surface A* **1997**, *185*, 94.

[159] R. J. Green, J. Davies, M. C. Davies, C. J. Roberts, S. J. B. Tendler, *Biomaterials* **1997**, *18*, 405.

[160] G. Brink, H. Sigl, E. Sackmann, *Sens. Actuat. B* **1995**, *25*, 756.

[161] J. Andrade, *Surface and interfacial aspects of biomedical polymers*, Plenum, New York, **1985**.

[162] F. Xu, B. Persson, S. Löfas, W. Knoll, *Langmuir* **2006**, *22*, 3352.

[163] A. Kasry, W. Knoll, *Appl. Phys. Lett.* **2006**, *89*, 101106.

[164] J. Dostalek, A. Kasry, W. Knoll, *Plasmonics* **2007**, *2*, 97.

[165] Y. Wang, J. Dostalek, W. Knoll, *Biosens. Bioelectron.* **2009**, *24*, 2264.

[166] A. Kasry, J. Dostalek, W. Knoll, in *Advanced surface design for biomaterial and life science applications* (Eds.: A. T. A. Jenkins, R. Foersch, H. Schoenherr), Wiley-VCH, Weinheim, **2009**, pp. 447.

[167] A. Aulasevich, R. F. Roskamp, U. Jonas, B. Menges, D. J., W. Knoll, *Macromol. Rapid Commun.* **2009**, *30*, 872.

[168] P. W. Beines, I. Klosterkamp, B. Menges, U. Jonas, W. Knoll, *Langmuir* **2007**, *23*, 2231.

[169] W. Knoll, A. Kasry, F. Yu, Y. Wang, A. Brunsen, J. Dostalek, *J. Nonlinear Opt. Phys. Mater.* **2008**, *17*, 121.

[170] D. Sarid, *Phys. Rev. Lett.* **1981**, *47*, 1927.

[171] K. W. L. Watt, P. J.; M'Timkulu, T.; Chan, W. P.; Loor, R., *Proc. Nati. Acad. Sci. USA* **1986**, *83*, 3166.

[172] B. Acevedo, Y. Perera, M. Ruiz, G. Rojas, J. Benitez, M. Ayala, J. Gavilondo, *Clin. Chim. Acta* **2002**, *317*, 55.

[173] S. Radowicki, M. Kunicki, E. Bandurska-Stankiewicz, *Eur. J. Obstet. Gynecol. Reprod. Biol.* **2008**, *138*, 212.

[174] A. P. Doherty, M. Bower, G. L. Smith, R. Miano, E. M. Mannion, H. Mitchell, T. J. Christmas, *Br. J. Cancer* **2000**, *83*, 1432.

[175] E. D. Johnson, T. M. Kotowski, *J. Forensic Sci.* **1993**, *38*, 250.

[176] K. Lind, M. Kubista, *J. Immunol. Meth.* **2005**, *304*, 107.

[177] J. M. Nam, C. S. Thaxton, C. A. Mirkin, *Science* **2003**, *301*, 1884.

[178] D. S. Grubisha, R. J. Lipert, H. Y. Park, J. Driskell, M. D. Porter, *Anal. Chem.* **2003**, *75*, 5936.

[179] F. Yu, B. Persson, S. Lofas, W. Knoll, *Anal. Chem.* **2004**, *76*, 6765.

[180] D. E. Aspnes, *Thin Solid Films* **1982**, *89*, 249.

[181] J. Piehler, A. Brecht, K. Hehl, G. Gauglitz, *Colloids Surf. B* **1999**, *13*, 325.

[182] S. Lofas, B. Johnsson, A. Edstrom, G. Hansson, G. Linquist, R. Muller, L. Stigh, *Biosens. Bioelectron.* **1995**, *10*, 813.

[183] P. Schuck, *Annu. Rev. Biophys. Biomol. Struct.* **1997**, *26*, 541.

[184] C. J. Huang, U. Jonas, J. Dostalek, W. Knoll, *Proc. SPIE* **2009**, *7356*, 735625.

4.3 Electroresponsivity of a Ferrocene-Modified Hydrogel Matrix

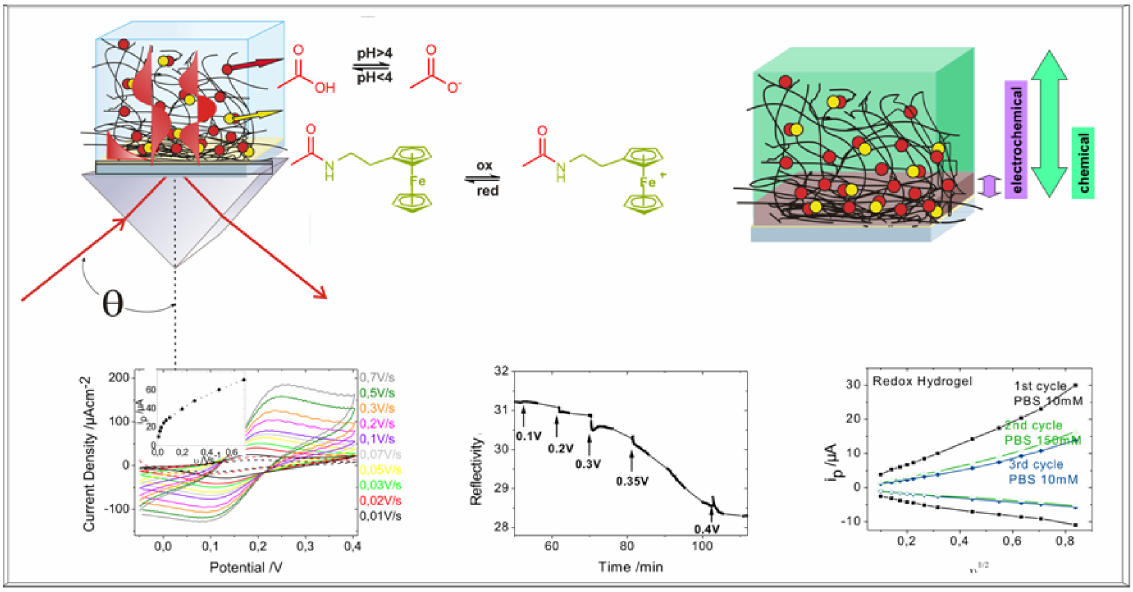

Efficient external charge manipulation of a hydrogel matrix would open fascinating possibilities for example in the field of sensors or separation. Hydrogels containing redox centers might be candidates for this kind of application. For this purpose, a dextran-based hydrogel modified with redox centers was synthesized and the response upon oxidation and reduction of the ferrocene redox moieties is presented. In order to characterize the electrochemical properties and the film morphological changes simultaneous SPR/OWS spectroscopy and cyclic voltammetry as well as the application of permanent potentials were carried out.

4.3.1 Introduction

Redox stimuli responsive, electroactive polymers have been developed for the last decades due to their potential use in electrocatalysis[1-3], biofuel cells,[4, 5] photoelectrochemistry[6], biosensing,[7-10] drug delivery[11-14] and actuators.[15-17] Besides hydrogel based systems[18-21] mainly discussed here donor-acceptor systems,[22] responsive monolayers,[23] polymer brushes[24, 25] and dendrimers[26] are currently under investigation. For a monolayer of poly(ferrocenyldimethylsilanes) investigated with surface plasmon resonance spectroscopy, atomic force microscopy and ellipsometry a reversible thicknes increase over 10% was found upon oxidation assuming a constant refractive index.[23] Hydrogels are potential systems because of their biocompatiblility and their three-dimensional polymeric network which can carry large amounts of fluid and resemble biological tissue. Electrical stimuli allow a precise control of charge and responsive behavior with respect to the magnitude of current, duration of electric pulses and intervals between the pulses for example. Upon applying an electrical field , electroresponsive hydrogels generally change their swelling state[27-29] or bend,[30, 31] depending on their composition, shape and relative position to the electrodes. Bending occurs for polyelectrolyte hydrogels with the main axis located parallel to the electrode without touching it. Hydrogels with their main axis perpendicular to the electrode usually deswell upon electrical stimuli.[13, 32]

The influence of various parameters like pH and charge density on the mechanoelastic behavior of electric sensitive hydrogels was simulated by several groups and found to be in agreement with experimental data.[33-35] Applying an electric field above a certain threshold value, polyelectrolyte hydrogels without any redox functionalization can deswell, swell or erode depending on the gel itself and the experimental set-up.[18] Generally they shrink because water is syneresed from the hydrogel. This contraction occurs relatively slowly and anisotropic due to the diffusion control and cationic gels shrink at the cathode, anionic hydrogels at the anode.[36-38] Contraction increases with increasing magnitude of the electrical field applied and saturates at a certain value depending on the amount of charges transported through the hydrogel.[18, 39-41] It doesn't have to occur along the whole hydrogel but can be partially close to the electrode as well.[17, 36, 42] Usually, the contraction can be reversed by switching off the electrical field. The magnitude of the response as well as the reversibility often decreases with increasing number of electrical cycles. The response of the hydrogel depends on a plethora of factors such as the experimental set-up, the gel's structural parameters like hydrophilicity, charge density, swelling degree, and crosslinks. Three main mechanisms of electrically induced polyelectrolyte hydrogel deswelling have been described:

- the establishment of a stress gradient along the gel axis due to an induced force upon the charges of the hydrogel and the mobile counterions[36]
- local pH-changes close to the electrode due to electrolysis of water[43]
- electroosmosis of water combined with electrophoresis due to migration of the hydrated counterions to the oppositely charged electrode.[43, 44]

In redox functionalized polymers the electric field induced response is based on electron transport by self exchange or electron hopping.[45-47] Electron hopping requires a dense distribution of redox functions like in a conjugated electrically conducting backbone. For redox functionalized hydrogels self exchange resulting from Marcus-type collisional electron transfer[48] prevails and electron conduction is therefore diffusion controlled. If the hopping mechanism dominates, a distance increase between redox centers upon swelling would decrease the conductivity. In the literature the opposite effect is reported for functionalized polymers because of increasing segmential mobility favouring the self-exchange of electrons that cannot traverse by tunneling in the rigid state due to the large distances.[18] Electron conduction in redox hydrogels takes place between the redox functions tethered to backbones of crosslinked polymer networks. Electron diffusion reaches the maximum value for equal distribution of oxidized and reduced centers and saturates for high potentials in case the majority of redox centers is reduced or oxidized respectively.[49] The induced response of a functionalized redox active hydrogel film fixed at an electrode is determined by its segmential mobility or polymer flexibility, its degree of functional density and its ability of hydration. Although a certain flexibility of the redox centers is required the rate of self-exchange of electrons decays exponentially with the distance. An optimal response is reported for redox functions that are tethered to the polymer backbone with spacers of 8-15 atoms (1-3 nm) and a redox center concentration of 0.1-1M in the swollen gel.[18, 50] Nevertheless, the electron diffusion coefficients are reported to be usually less than 10^{-12} cm^2s^{-1} in contrast to hydrogels containing electron conducting backbones.[18, 51] The segmential mobility determining the electron diffusion generally increases with increasing hydration and decreases with increasing crosslinking.[45] Furthermore, the reversibility of the swelling and deswelling processes upon oxidation or reduction are of critical importance for any application. Possible altering effects can be the susceptibility of Fe^+ towards nucleophilic attack[52, 53] which can be prevented by using non-nucleophilic electrolytes like ClO_4^-.[52, 54] Another altering effect is the irreversible swelling due to disentanglement of polymer chains in a crosslinked film or loss of material upon swelling. This effect should be preliminary until an equilibrium state is achieved as long as no irreversible effects interfere. For thick hydrogel layers of several micrometers the oxidation occurs under diffusional control. The cyclic voltammograms show diffusional shape with a peak current proportional to $\nu^{1/2}$.[19] The oxidation of ferrocene for example producing ferrocenium ions results in water and counterion uptake and thus in film swelling. The electrolyte inside is diluted and the viscosity reduced.[19, 55, 56] This swelling was observed for layer-by-layer deposited films with osmium as redox center, too. The changes in thickness and refractive index are reported to be proportional to the fraction of oxidized redox centers.[55] The swelling takes place until the osmotic and the elastic forces are in equilibrium. Thereby, the redox switching strongly depends on the nature of the anions under anion Donnan permselectivity conditions. For thin films a Nernstian behavior for different electrolytes is reported whereas for thicker films diffusion becomes more important. A thermodynamic explanation to this phenomenon has been proposed based on the different contributions to the osmotic pressure and the slow solvent flux compared to electrical charge induction.[56]

Different systems investigating these effects are reported in the literature. A ferrocene modified poly(ethyleneimine) with current densities between 240 and 480 µA/cm² is reported by Merchant et al..[54] The effect of nucleophilic and non-nucleophilic electrolytes, of phosphate containing electrolytes as well as the effect of crosslinking is investigated and the function as molecular wires for enzyme detection with glucose oxidase is proofed.[54] Polyelectrolyte poly(methacryloyloxy)ethyl-trimethyl-ammonium chloride brushes with the redox active counterion ($[Fe(CN)_6]^{3-}$ as redox probes was investigated by Choi et al.. The responsive behavior of these polyelectrolyte brushes is determined by electrostatic interactions and osmotic pressure and thus depends on the polymer length and grafting density and with the osmotic pressure on[54] the charge density of the polymer.[24, 57] The dependence of the electroactivity on the layer thickness was interpreted as a loss of “direct communication” of the redox probes with the electrode with a certain distance from the electrode or an ion movement towards the solution.[57]

A further redox functionalized hydrogel based on poly(4-vinylpyridine) as polymer backbone and an osmium complex as redox center was introduced by Heller and co-workers.[18, 50] The redox centers are coupled to the backbone via 8-15 atom long spacers to facilitate electron conduction as discussed above and the system was tested towards applications in sensors and fuel cells.[4] Besides covalent coupling of redox centers ferrocene has been coupled by host-guest interaction with cyclodextrin.[58]

Regarding its high swelling degrees (Chapter 4.1) and thus the high segmential mobility a ferrocene modified dextran based hydrogel should be a promising candidate for electrically induced switching of swelling.

4.3.2 Electrochemical Characterization of a Ferrocene-Modified Dextran-Based Hydrogel Film

If the ferrocene moieties are introduced by reacting a crosslinked hydrogel film on a substrate or by pre-synthesizing a ferrocene modified dextran based hydrogel the synthetically introduced film functional groups are identical. The hydrogel film consists of a hydrophilic dextran based backbone, benzophenone moieties as photo-crosslinking units, free carboxyl functionalities neutralized by counterions and ferrocene moieties (Figure. 4.3.1).

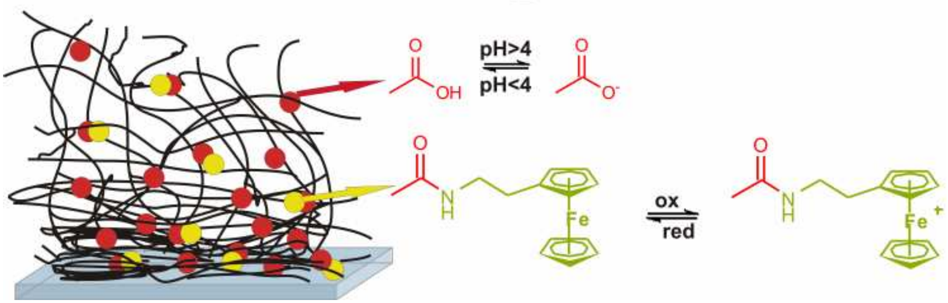

Figure 4.3.1: *Schematic representation of the dextran based redox hydrogel as a photo-crosslinked film.*

While increasing the potential, ferrocenes are oxidized as soon as their oxidation potential is applied. Furthermore, charge neutrality is maintained in any volume element a counterion diffuses upon electron transfer to neutralize the induced charge.[69] Besides, upon oxidation positively charged ferrocene redox centers, pH sensitive negatively charged carboxyl functionalities are present in the hydrogel. In order to investigate the hydrogel film's electroresponsive behavior, cyclic voltammograms and SPR/OWS measurements (Chapter 2.1) were carried out simultaneously. Thereby, kinetic measurements are recorded at a fixed angle in the linear part of the surface plasmon resonance. Due to the penetration depth of the surface plasmon of approximately 200 nm[70] the refractive index variations close to the gold interface are displayed by following the surface plasmon. A decrease of the reflectivity resembles a shift of the surface plasmon resonance to lower angles and thus indicates a decrease of the refractive index. An increase of the refractive index resembles increased water content in the hydrogel film and thus a swelling of the redox hydrogel film. In order to obtain information about the entire hydrogel film angular scans are carried out (Chapter 2.1, 2.3) Typical cyclic voltammograms with increasing scan rate between 0.01 and 0.7 V/s and the corresponding SPR kinetic measurement are shown in Figure 4.3.2.

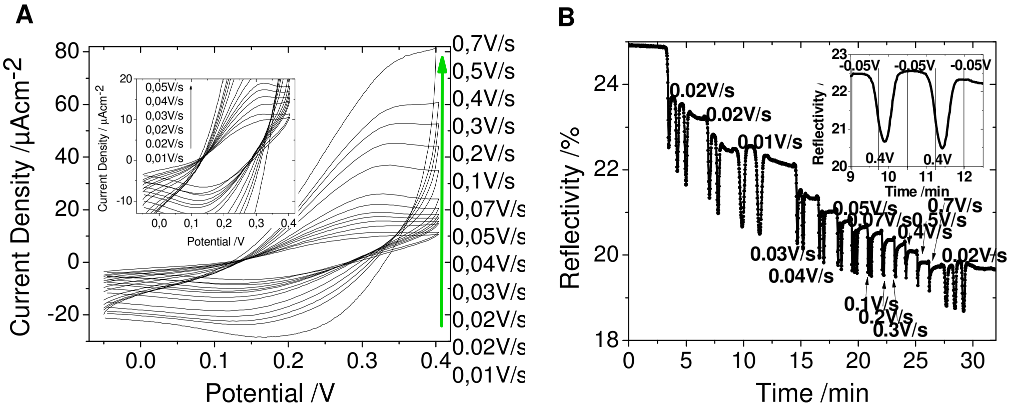

Figure 4.3.2: *A) Representative cyclic voltammograms with increasing scan rates of a ~18 µm thick ferrocene modified photo-crosslinked PCMD hydrogel (swelling degree in 10mM PBS =16 without external stimuli) film (d_s(benzophenone) = 0.04, d_s(carboxymethylation) = 0.16) in 10 mM PBS.* ***B)*** *The corresponding SPR response recorded at a fixed angle in the surface plasmon.*

The cyclic voltammograms show a broad oxidation potential that increases with increasing scan rate while the peak potential separation between the oxidation and the reduction peak increases. Thereby, the oxidation peak shifts to higher potentials and the reduction peak shows a small shift to lower potentials. This effect is displayed in simultaneously recorded kinetic measurement of the surface plasmon resonance signal, too. The surface plasmon response upon screening the potentials with a certain scan rate indicates three main effects. First, the signal variation upon potential screening (Figure 4.3.2 B inset) indicates a swelling upon oxidation followed by a deswelling upon reduction. This potential response might be attributed to an excess of positive charges upon oxidation or increased hydrophilicity leading to water rearrangement and counterion attraction. Second, the amplitude of the change decreases with increasing scan rate indicating a lower number of ferrocene molecules being oxidized. The third effect is a total refractive index decrease while screening potentials resembling a water uptake possibly due to counterion uptake upon charge generation by oxidation.

Pre-Synthesized Redox-Hydrogels versus Ferrocene Binding after Crosslinking

Generally, modification of a hydrogel film with ferrocene moieties after film formation on the substrate (Chapter 3.2) results in comparable structural modification than obtained by pre-synthesizing a ferrocene modified polymer. The challenge for the reaction on the substrate lies in the cleaning without destroying the highly swelling fragile hydrogel film and to ensure the entire removal of non-bound ferrocene. Cyclic voltammograms, SPR kinetic response, and peak current dependence on the scan rate for a typical pre-synthesized and a substrate modified film in PBS 150 mM are compared in Figure 4.3.3.

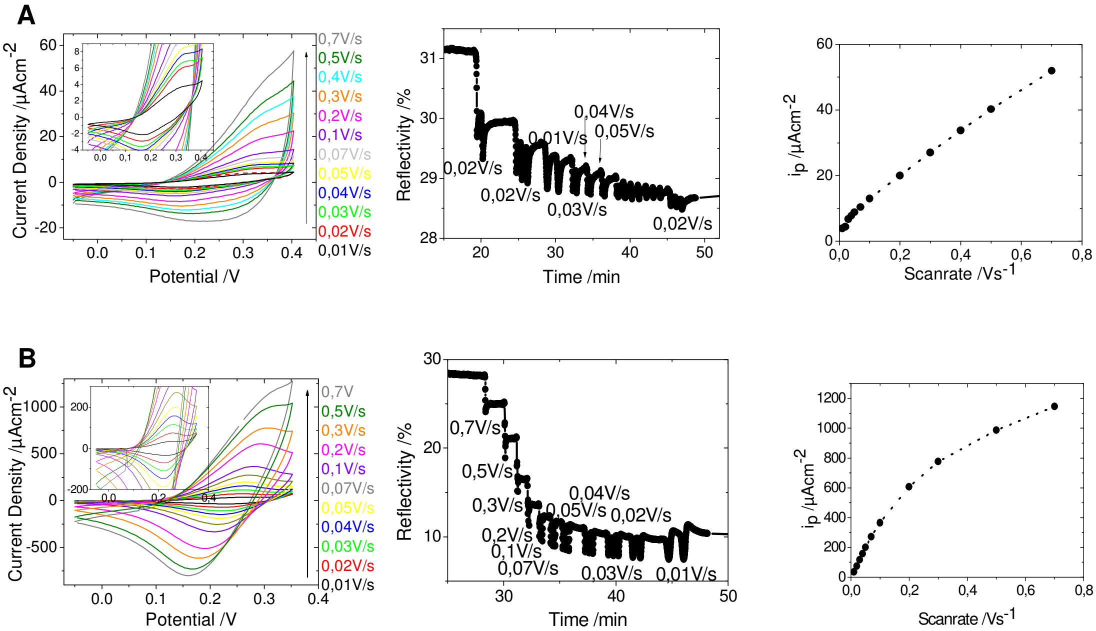

Figure 4.3.3: *Exemplary cyclic voltammograms and SPR response upon screening potentials with varying scan rates for* ***A)*** *a pre-synthesized redox hydrogel film (d = 18µm, d_s(benzophenone) = 0.04, d_s(carboxymethyl) = 0.16, ds(ferrocene) ~ 0.03, crosslinking 254 nm, 30 min, swelling medium = PBS 150mM) and* ***B)*** *a redox hydrogel film modified on the substrate (4µm, d_s(benzophenone) = 0.03, d_s(carboxymethyl) = 0.28, PBS 150mM). The last plot shows the corresponding relation of the peak potential and the scan rate.*

The cyclic voltammograms show a comparable behavior for both types of redox hydrogel films with respect to peak separation and scan rate. The lower peak current for the pre-synthesized film might be attributed to a lower amount of oxidized ferrocene. The shifted peak position can depend on several factors like film morphology along the z-axis, swelling degree, or ferrocene distribution and could not be clearly related to one factor. The oxidation peak potentials vary between 0.18 V and 0.30 V for a scan rate of 10 mV/s. In all cases the peak separation increases with increasing scan rate from approximately 0.1 V for a scan rate of 0.01 V/s to approximately 0.2 V for a scan rate of 0.7 V/s. The peak separation indicates the hindrance of the electron transfer inside the hydrogel film because the scan rate is comparable, or even higher, than the rate of electron transfer corresponding to the redox sites. The electron transfer inside the hydrogel is determined by the segmential mobility and thus by the swelling degree and spacer length as well as by the redox center density or concentration.[24] Therefore, the lower peak separation for the redox hydrogel film in Figure 4.3.3 B (inset) compared to the redox hydrogel film of Figure 4.3.3 A for low scan rates might be due to the higher ferrocene amount that is detected with cyclic voltammetry. The thinner film thickness might have an influence, too.

The SPR response shows comparable characteristics regarding the swelling upon oxidation, the smaller amplitude for higher scan rates and the overall swelling. The magnitude of the overall signal decrease is about much higher for the redox hydrogel film depicted in Figure 4.3.3. B, which correlates to the higher amount of ferrocene as indicated by the cyclic voltammograms. The detected amount of ferrocene (peak current) as well as the swelling effect dramatically decreases with subsequent screening cycles (data not shown). The peak current and the scan rate do not show a linear relation. A linear relation is expected if electron hopping is the dominating mechanism for electron conduction[47] and if no free unbound redox centers are present. This is the case for very thin electrode attached redox centers or redox centers that are very close to eachother. For highly swollen redox center containing hydrogel films diffusion-controlled electron conduction is expected, as discussed below.[18, 71-74]

To make sure the observed effects are due to the ferrocene redox centers the corresponding hydrogel films without redox centers were measured under identical conditions. No oxidation peak between 0.2 V/s and 0.3 V/s was detected. The maximum in the cyclic voltammogramm was extracted and plotted against the scan rate. The peak currents are much lower than measured for redox center containing films and they are comparable for different films. The results are discussed below (Figure 4.3.5 B). The SPR response shows a swelling effect visible in a signal decrease of about 1% in the reflectivity which is much lower than the signal decrease for redox modified films as well.

Redox Hydrogel Morphology Changes upon Potential Screening

If the overall refractive index-decrease upon potential screening is related to counterion and water uptake this should affect the entire hydrogel film. Information about the entire hydrogel film profile were obtained by performing angular scans before and after potential screening and subsequent data analysis by applying the WKB-approximation (Chapter 2.3). The redox hydrogel profile changes upon potential scanning corresponding to the cyclic voltammograms and the kinetic measurement of Figure 4.3.2 are presented in Figure 4.3.4. The refractive index decrease for the entire film is clearly visible. The corresponding thickness increase is not visible for the thick pre-synthesized film (Figure 4.3.4 A, B) due to the low refractive index of the hydrogel at the hydrogel solution interface and the resulting low contrast.

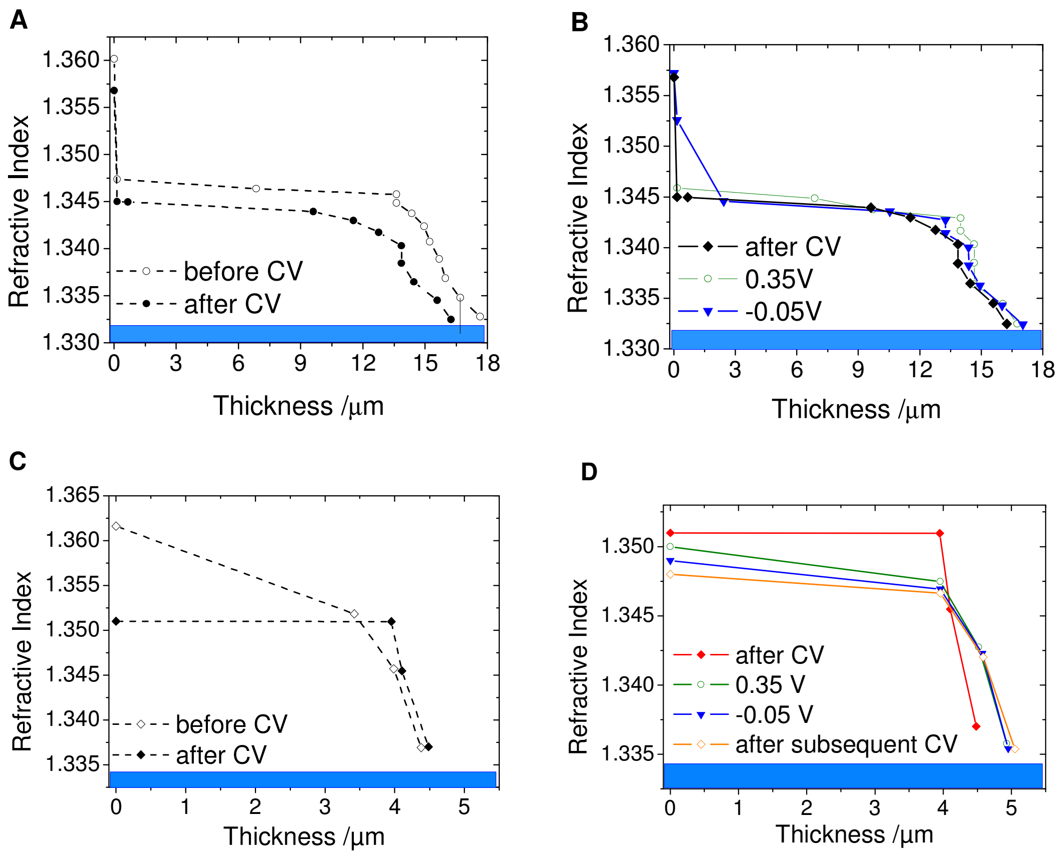

Figure 4.3.4: *Redox hydrogel film refractive index-thickness profiles and the influence of potential screening for two different films discussed above. The pre-synthesized redox hydrogel film is shown in* ***(A)*** *and* ***(B)*** *and the one reacted with ferrocene on the substrate in* ***(C)*** *and* ***(D).*** *The swelling upon performing cyclic voltammetry is shown in A and C and the change upon applying the oxidation (+0.35 V) and reduction (-0.05 V) potential for a longer time is shown in B and D respectively. The swelling upon potential screening is clearly visisble for both films. Whereas the response of the thicker pre-synthesized film to a permanent potential is neglectable the thinner film modified with ferrocene on the substrate continuously swells upon oxidation and subsequent cyclic voltammetry.*

The huge water uptake is indicated as well by the decreasing coupling efficiency of the optical waveguide modes in the angular scan (data not shown). Due to the decreasing contrast especially at the hydrogel gold interface the coupling of optical waveguide modes is lower and the loss of coupled light due to scattering effects for example increases. These effects consequently result in a “vanishing” waveguide structure. The decrease in the refractive index was determined to be 0.0034 at the hydrogel gold interface and 0.0025 in the center of the hydrogel film (Figure 4.3.4 A). The higher refractive index change at the surface might result from the initially denser hydrogel network at the substrate surface. The results for the redox film reacted at the substrate (Figure 4.3.4 C, D) are comparable with the only difference in the response to the permanent oxidation potential, which is much higher. The film is swelling upon oxidation in agreement with the response in the cyclic voltammetry. These data suggest a swelling mechanism upon oxidation divided into a reversible response on a short timescale and an irreversible change on a longer timescale. The immediate response is related to the charge generation and removal upon oxidation and reduction and the irreversible on a long timescale is due to counterion and osmotic water uptake upon oxidation. This water uptake results in an increased swelling and is not reversible, maybe because of the hydrophilic dextran backbone and disentanglement effects. Redox hydrogels with reported viscoelastic changes upon applying a potential are for example N-isopropyacrylamide-vinylferrocene,[75] poly(pyrrole)-tetrafluoroborate[76] and a ferrocene derivatized poly(allylamine).[65]

After recording the cyclic voltammograms for all scan rates a permanent potential was applied for several minutes and the surface plasmon signal records the refractive index changes close to the electrode interface in real time. Two different types of response were observed in several experiments (Figure 4.3.5). One, showing a swelling upon oxidation (+0.35 V) and a de-swelling upon subsequent reduction (-0.05 V) reaching an equilibrium state relatively fast (Figure 4.3.5.A). The second differs in the behavior upon oxidation showing a swelling that converts into a deswelling after a certain period (Figure 4.3.5.B). The origin of the two different kinetic responses could not clearly be identified but the oxidation potential seems to be the most important influence. In case the applied potential is close to the oxidation potential response comparable to Figure 4.3.5 B is observed. Both types of real time responses are observed for a stepwise increase of the applied potential (Figure 4.3.9 A). The swelling degree as well as the PBS concentration (10 mM, 150 mM) and the amount of coupled ferrocene could not exclusively be identified as trigger.

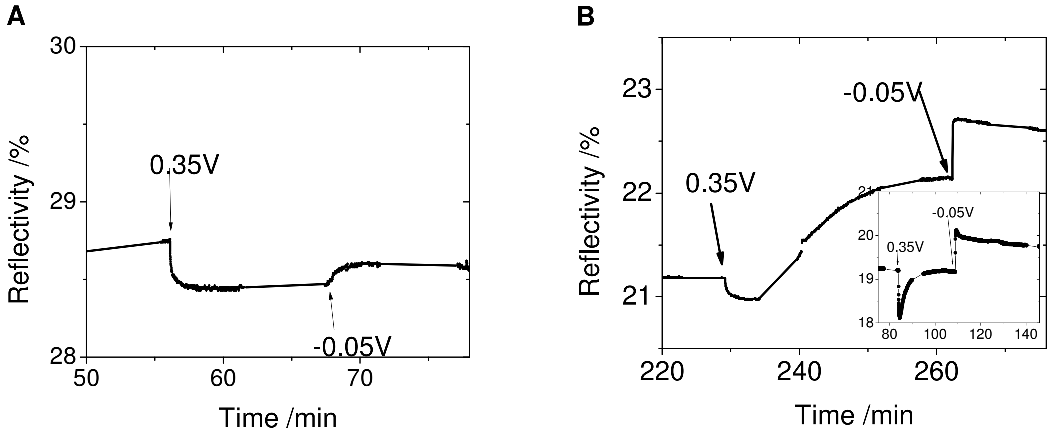

Figure 4.3.5: *The two types* ***(A, B)*** *of surface plasmon resonance kinetic signal upon applying an oxidation potential of +0.35 V and followed by a reduction potential of -0.05V for ferrocene modified carboxymethyl dextran hydrogel films in PBS 150 mM.*

In common for all hydrogel films is the change of the swelling state on the entire length of the film in z-direction upon applying a potential. The constant potential is applied after potential screening at different scan rates. The change of the swelling state extracted from the WKB thickness-refractive index profiles is neglectable (Figure 4.3.4B). This indicates on one hand that the direct influence of the potential is located close to the electrode surface and on the other hand that the swelling upon potential screening can be mainly assigned to a swelling upon water uptake and disentanglement effects.

From the potential screening with varying scan rates information about the electron conduction can be obtained. In case of surface-confined redox couple, a linear relation between the scan rate (υ) and the peak current (i_p) is expected (equation 4.3.1).

$$i_p = \frac{n^2 F^2}{4RT} \nu \Gamma_0 \qquad (4.3.1)$$

Conversely, in case of a diffusion dominated electron conduction a $\upsilon^{1/2}$ dependence is expected. The measured relation is depicted in Figure 4.3.6 A for a 18 µm thick redox hydrogel. The corresponding relation for two different "pure" hydrogels without ferrocene redox centers is shown in Figure 4.3.6 B. It is remarkable that two different hydrogel films with different composition and different thickness show approximately the same response to potential screening. A $\upsilon^{1/2}$ dependence of the peak potential (i_p) is observed indicating a diffusion limited electron conduction inside the redox hydrogel film. This diffusion is mainly determined by the segmential mobility[18] and is based on the Randles-Sevcˇik equation.[71, 77]

The swelling degrees without applying any potential are summarized in Chapter 3.2. After potential screening with cyclic voltammetry a 16.5 nm thick hydrogel with a refractive index of 1.3568 at the gold hydrogel interface and 1.3475 in the center of the gel increase its swelling state to 17 nm and a refractive index of 1.3572 at the gold interface and 1.345 in the center.

The change of the swelling state can be expressed as a change of the surface mass density (Γ) using the following equation (4.3.2)

$$\Gamma = \left(n_h - n_b\right) d_h \frac{\partial c}{\partial n_h} \qquad (4.3.2)$$

n_h resembling the refractive index of the hydrogel and n_b the refractive index of the bulk solution. The hydrogel film thickness is represented by d_h and $\partial n/\partial c \approx 0.2$ µL×mg^{-1}[78]. The results are summarized in Table 4.3.1. The highest change is observed with the first cycle of potential screening by cyclic voltammetry. The surface mass density is thereby reduced about 10% at the gold-hydrogel interface and in the center of the hydrogel film.

***Tab. 4.3.1**: Exemplified surface mass density in ng/cm^2, calculated for the gold-hydrogel interface deduced from the surface plasmon and in the center of the hydrogel film(3-10 µm) using the WKB approximation.*

PBS 10mM	***Swollen hydrogel***	***After cyclic voltammograms***	***Oxidation +0.35V***	***Reduction -0.05V***
Surface (SP) ***PBS 10 mM***	101	89	89	91
Center (3-10µm) ***PBS 10 mM***	52	47	46	45

The change of surface mass density upon applying a potential is negligible compared to the change upon screening cyclic voltamograms with increasing scan rate between 0.01 V/s and 0.7 V/s. The loss of surface mass density as well as the overall swelling observed upon performing cyclic voltammograms seems to be related to irreversible ferrocene related effects inside the hydrogel matrix. A pure hydrogel without ferrocene units does not show this overall swelling upon potential screening.

This altering effect possibly results from a water and counterion uptake upon oxidation leading to a swelling of the hydrogel. Additionally, disentanglement and structure rearrangement effects and the hydrophilicity of the dextran backbone may support the irreversible swelling and loss of material.

Altering Effects on a Longer Timescale

Investigating the redox hydrogel behavior on a larger timescale the refractive index decrease during potential screening was already discussed above. This refractive index decrease indicates a swelling of the hydrogel film resulting in a higher water-content and thus a larger distance of the redox centers with every screening cycle. Only the ferrocene molecules within a certain distance from the gold interface seem to be wired to the electrode. Therefore, an increasing swelling leads to a reduced number of ferrocene redox centers oxidized while applying a potential. In agreement with this observation the cyclic voltammograms show a decrease of the peak potential until an equilibrium state which is usually reached after two or three cycles (Figure 4.3.6 A, 4.3.7 A). This equilibrium state seems to represent the fully extended state of the hydrogel film. Exemplarily, the CV's are shown at different times of the experiment at a scan rate of 20 mV/s are shown in Figure 4.3.7 A. The decrease of the peak potential in dependence of $\upsilon^{1/2}$ is depicted in Figure 4.3.6 A. The corresponding blind experiment performed with an identical hydrogel layer in the absence of ferrocene is depicted in Figure 4.3.6 B. The effect without ferrocene moieties present is significantly lower and a comparable response for a different film (Figure 4.3.6 B (red symbols) was observed.

The effect observed without the presence of redox centers might be attributed to double layer charging or to impurities in the electrode.

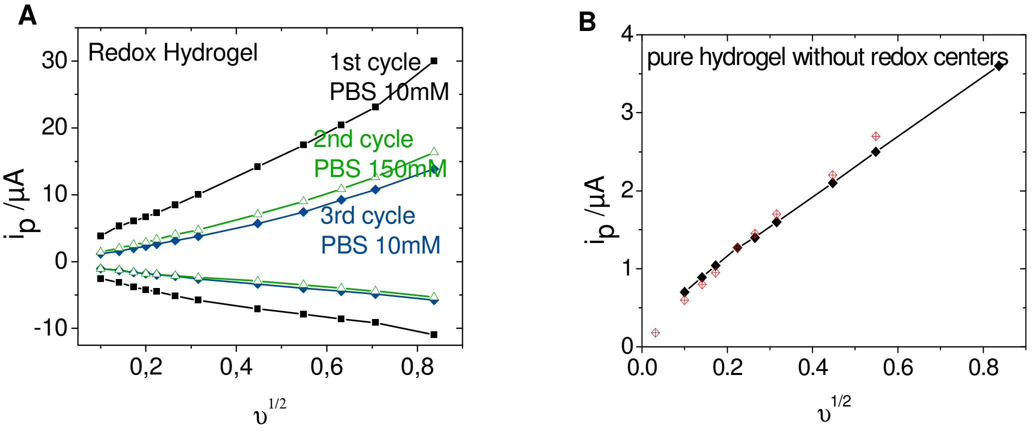

Figure 4.3.6: ***A)*** *$\upsilon^{1/2}$ dependence of the oxidation and reduction peak current for three subsequent potential screening cycles of 18 nm thick (PBS 10mM) redox hydrogel film and the change for increasing number of screening cycles.* ***B)*** *Corresponding blind experiment with two different redox center free hydrogel films (~1 µm nm, (black), PBS 150 mM; ~8 µm red, PBS 10 mm d_s(benzophenone = 0.04, d_s(carboxymethyl) = 0.16)). The redox center free hydrogels show an identical behavior and a linear $\upsilon^{1/2}$ dependence showing the solvent ion diffusion effect.*

A second effect that might influence the potential response of the redox hydrogel matrix is the reported instability of the ferrocinium-ion towards nucleophiles like chloride, which is present in PBS as well.[54] The corresponding cyclic voltammograms for a scan rate of 0.02 V/s at different moments of the experiment are plotted in Figure 4.3.7 A. The decrease of the peak current is clearly visible. The charge density, derived from the integration of the oxidation peak, shows a fast decrease with increasing scan rate until a constant value is reached.

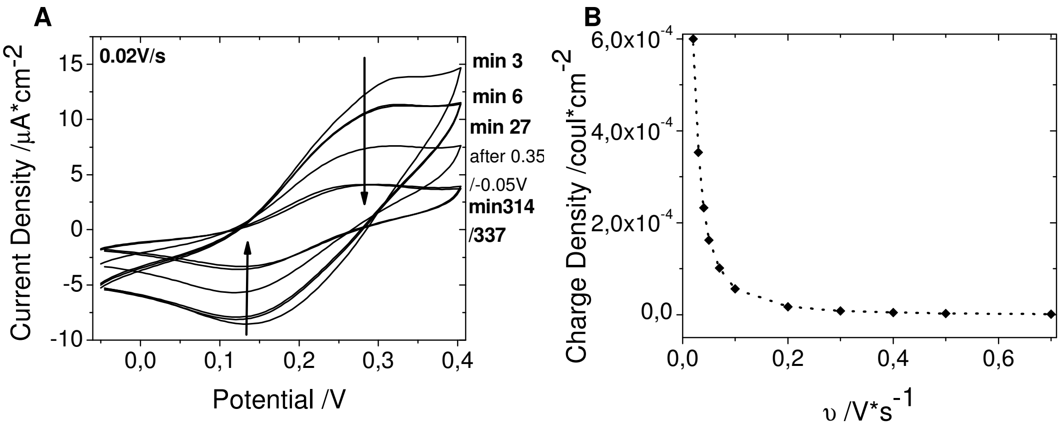

Figure 4.3.7: *Time dependent change of the cyclic voltammograms for a scan rate of 0.02 V/s* ***(A)*** *corresponding to the Figure 4.3.5 A. The development of the charge density with increasing scan rate is shown in* ***(B)****. The charge density is derived by integration of the oxidation peak in the cyclic voltammograms.*

Chemical Switching of the Redox State

In order to achieve a full oxidation and reduction along the entire film length the redox centers were oxidized and reduced chemically. Before doing so the hydrogel film behavior upon applying a potential was characterized by cyclic voltammetry and stepwise increasing potentials. The corresponding cyclic voltammograms for increasing scan rates are shown in Figure 4.3.8 and the related kinetic response of the surface plasmon in Figure 4.3.8 B. The response of the redox hydrogel towards cyclic voltammetric potential screening is comparable to the results discussed above. The coupling of ferrocenethyleneamine was performed on the substrate as described in Chapter 3.2.

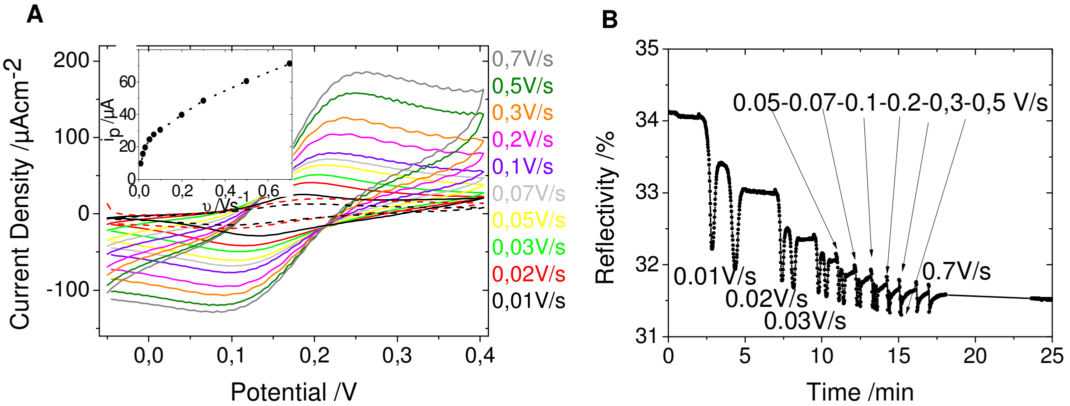

Figure 4.3.8: *Redox hydrogel characteristics upon electrochemical potential screening. The cyclic voltammograms for increasing scan rates are plotted* ***(A)****. The corresponding dependence of the peak current on the scan rate is shown in the inset showing ferrocene diffusion.* ***B)*** *Refractive index decrease at the hydrogel-gold interface is depicted from the decreasing reflectivity of surface plasmon signal corresponding to an angular shift to lower angles.*

After recording the cyclic voltammograms stepwise increasing oxidation potentials were applied to investigate the oxidation behavior. The redox hydrogel response is followed at the hydrogel –gold interface by following the surface plasmon angular shift. A shift to smaller angles is reflected by a decrease in reflectivity corresponding to a decrease in the refractive index. A slight refractive index decrease at the hydrogel-gold interface is observed upon applying 0.3 V. The biggest effect is achieved upon applying 0.35 V (Figure 4.3.9) corresponding to a full oxidation of ferrocene as can be deduced from the cyclic voltammograms (Figure 4.3.8 A). A further increase of the potential does not induce a remarkable change because no further oxidation occurs. By simulating the simultaneously recorded angular SPR/OWS spectra with a one box model the thickness of the hydrogel matrix is obtained. Due to the relatively low film thickness of 2.3 µm only two optical waveguide modes were guided inside the film, not allowing for a precise WKB analysis.

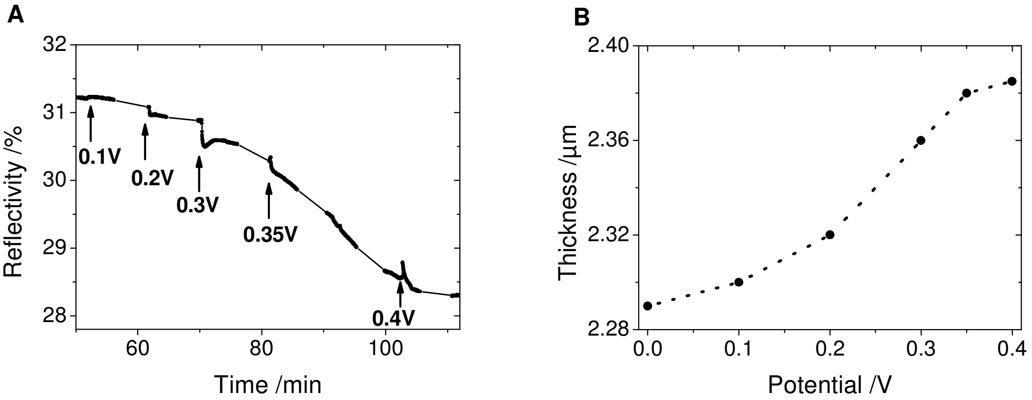

Figure 4.3.9: *A) Time resolved surface plasmon response upon stepwise increase of the oxidation potential. The refractive index decrease of the redox hydrogel matrix upon passing the oxidation potential (0.35 V) is clearly visible by the decreasing reflectivity.**B)** Thickness increase reflecting the corresponding swelling of the matrix upon oxidation.*

The observed swelling is relatively small compared to swelling effects known from pH changes through the entire hydrogel film for example. For an oxidation of the redox centers along the entire thickness of the hydrogel film a bigger effect is expected.

In order to oxidize all redox centers chemically a water soluble oxidation reagent and reduction reagent are required. The hydrogel matrix was incubated with a solution of 0.1 M $FeCl_3$ in 0.1 M KCl solution for 20 minutes for oxidation, followed by rinsing with the swelling medium (PBS). The subsequent reduction was performed by incubation with a 0.1 M hydroquinone solution of 0.1 M KCl for 15 minutes as well followed by rinsing with PBS. As a comparison the experiment was carried out with a redox center free hydrogel film.

The chemical oxidation of the redox hydrogel induces a shrinking from 2350 nm to 1900 nm and the subsequent reduction a re-swelling to 2150 nm. The magnitude of deswelling and swelling mainly depends on the crosslinking density and the number of charges (Chapter 4.1). To be able to discuss the magnitude of the deswelling and swelling in detail it has to be investigated in dependence of these factors. At first, a shrinking of the hydrogel film upon oxidation of ferrocene is observed, in contrast to the observation upon electrochemical oxidation. Second the re-swelling is incomplete and the former swelling level is not reached again. The shrinking upon chemical oxidation of the ferrocene redox centers might be due to an attractive charge interaction between the negatively charged carboxyl groups and the oxidized ferrocene moieties. Thus, the shrinking should be tuneable by the ratio of carboxyl groups to redox centers and, more easily, by varying the pH. Consequently, the concept of combining pH-sensitive carboxyl groups and redox active groups allows to swell or to deswell the hydrogel matrix upon oxidation depending on the charge of the carboxyl groups and with this on the pH.

Obviously two different effects are present for the electrochemical and the chemical oxidation mainly due to the localized oxidation close to the gold electrode in case of electrochemical charge switching as indicated in Figure 4.3.10.

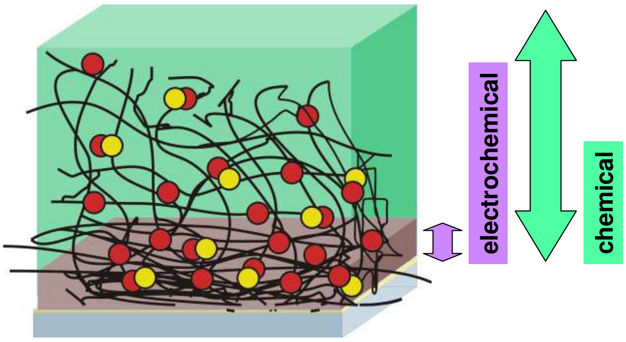

Figure 4.3.10: *Schematic description of the effect of the electrochemical versus the chemical redox switching in a hydrogel film with a thickness of several micrometers.*

4.3.3 Conclusion and Outlook

The characterization of redox center containing dextran-based hydrogel films were presented and the conformational changes of the hydrogel matrix detected by SPR/OWS spectroscopy were discussed. The electrochemical redox switching revealed a direct response of the hydrogel matrix to potential screening close to the electrode interface. An overall swelling along the entire thickness of the hydrogel matrix can most likely be ascribed to an osmotic effect. The data suggest a redox switching upon electrochemical stimulus only occurring close to the hydrogel-electrode interface. In contrast to the electrochemical switching the SPR/OWS scans upon chemical switching with $FeCl_3$ and hydroquinone indicate a shrinking upon oxidation and an incomplete re-swelling upon reduction. Furthermore, the effect is more pronounced than for the electrochemical oxidation. The shrinking might be assigned to an attractive charge interaction of the deprotonated carboxyl groups and the oxidized ferrocene moieties. The swelling upon electrochemical oxidation is most likely due to an osmotic effect. To validate the origin of the different responses further experiments investigating the oxidation and reduction behavior at different pH values with protonated and deprotonated carboxyl groups might be useful. The variation of the degree of crosslinking to fix a higher number of ferrocene centers close to the electrode interface would be versatile as well. To improve the effective range of the electrochemical redox switching, longer spacers allowing Marcus collision transfer in such a swollen matrix might be promising, as well as the synthetic introduction of charge conducting molecular units. Increasing spacer length should result in a continuous shift of the oxidation potential of the ferrocene units. This might be attractive for further charge switching, opening the possibility of electrochemical titration of positive charges inside the hydrogel matrix.

4.3.4 Experimental

SPR-CV Measurements: Surface plasmon resonance-, optical waveguide mode and fluorescence spectroscopy were performed in the Kretschmann configuration[79] as already described in Chapter 4.1.7.
The sample glass slide (LaSFN9 glass, Hellma Optik GmbH Jena, refractive index n = 1.8449) is put onto a custom made teflon flow cell (area = 0.385 cm^2) and at the backside is optically matched to the base of the glass prism (refractive index n = 1.8449, corresponding to $\varepsilon = 1.3583$). Monochromatic and linear, transverse-magnetic polarized (Glan-Thompson polarizer, Owis) laser light (He/Ne laser, Uniphase, $\lambda = 632.8$ nm) is directed through the prism onto the sample slide. By variation of the angle of incidence (θ) (two cycle goniometer, resolution 0.005°, Huber) and detecting the intensity of the reflected laser light $I(\theta)$ with a photodiode (BPW 34B silicon photodiode, Siemens) an angular dependent spectrum is recorded. The laser intensity was adjusted to 100 % reflectivity for all SPR/OWS experiments. This corresponds to 145 µW.
SPR/ OWS Data Treatment: To model the measured spectra the Fresnel equations are solved by a transfer algorithm[58] for a planar multilayer system consisting of the LaSFN9 glass, chromium, gold, a self assembled monolayer as adhesion promoter, the hydrogel and the swelling solvent. For every layer a value for the thickness (d) and the dielectric constant (ε) consisting of a real part (ε') and the imaginary part (ε'') have to be defined.
To determine the parameters for the sample without hydrogel first a slide only coated with chromium and gold was measured. To define the adhesion promoter values a slide with chromium, gold and *S*-3-(4-benzoylphenoxy)propyl ethanthiol as the adhesion promoter was measured and the recorded spectra were simulated with the above mentioned model assuming all other values as fixed.
To simulate the SPR/OWS spectra in the above mentioned model an average refractive index for every layer is assumed (box model). As the hydrogel films are thicker and acting as waveguide the reversed Wentzel-Kramers-Brillouin (WKB) approximation can be used to model the refractive index profile perpendicular to the substrate surface of these films[59]. Thereby, the hydrogel film is assumed to be laterally homogeneous (parallel to the substrate surface).
Refractive Index-Thickness Profiles: The reversed Wentzel-Kramers-Brillouin approximation was used to extract the refractive index-thickness profiles from the angular SPR/OWS spectra. Details are described in Chapter 2.3 and Chapter 4.1.7.
This refractive index value for the gold hydrogel interface (z = 0) was extracted from the box-model simulation of the measured spectrum by simulating the refractive index of the surface plasmon after modeling the waveguide modes and keeping the thickness constant. The accuracy of the refractive index versus thickness profile increases with increasing number of optical waveguide modes. The thickness of the hydrogel film, extracted from the WKB-profile, was determined from the calculated value at maximum thickness.
The Cyclic Voltammetric Measurements and the applying of potentials were performed simultaneously with the SPR/OWS measurements. The gold layer of the sample was

used as working electrode. An Ag/AgCl electrode was connected as reference electrode and a platinium wire was introduced into the flow cell as counter electrode. A potentiostate (Metrohm, Autolab) was used for potential control.

Chemical Redox Reaction: The chemical oxidation was performed by incubation with a 0.1 M $FeCl_3$ (Sigma Aldrich)/ 0.1 M KCl solution in destilled water. For the chemical reduction a 0.1 M hydroquinone (Sigma Aldrich)/ 0.1 M KCl solution in bi-destilled water (milli Q, 18 MΩ) was applied.

4.3.5 Bibliography

[1] C. P. Andrieux, O. Haas, J. M. Saveant, *J. Am. Chem. Soc.* **1986**, *108*, 8175.
[2] S. C. Barton, H. H. Kim, G. Binyamin, Y. C. Zhang, A. Heller, *J. Phys. Chem. B.* **2001**, *105*, 11917.
[3] S. C. Barton, H. H. Kim, G. Binyamin, Y. C. Zhang, A. Heller, *J. Am. Chem. Soc.* **2001**, *123*, 5802.
[4] A. Heller, *Phys. Chem. Chem. Phys.* **2004**, *6*, 209.
[5] I. Willner, Y.-M. Yan, B. Willner, R. Tel-Vered, *Fuel Cells* **2009**, *9*, 7.
[6] I. Willner, Y. Eichen, A. J. Frank, M. A. Fox, *J. Phys. Chem.* **1993**, *97*, 7264.
[7] B. Gregg, A. Heller, *Anal. Chem.* **1990**, *62*, 258.
[8] K. Sirkar, M. V. Pishko, *Anal. Chem.* **1998**, *70*, 2888.
[9] E. J. Calvo, A. Wolosiuk, *Chem. Phys. Chem.* **2005**, *6*, 43.
[10] W. Schuhmann, T. J. Ohara, H.-L. Schmidt, A. Heller, *J. Am. Chem. Soc.* **1991**, *113*, 1394.
[11] J. M. Pernaut, J. R. Reynolds, *J. Phys. Chem. B.* **2000**, *104*, 4080.
[12] I. M. Low, S. Seetharaman, K. He, M. Madou, *J. Sens. Actuators* **2000**, *67*, 149.
[13] S. Murdan, *J. Contr. Release* **2003**, *92*, 1.
[14] J. F. Mano, *Advanced Engineering Materials* **2008**, *10*, 515.
[15] T. F. Otero, J. M. Sansinena, *Adv. Mater.* **1998**, *10*, 491.
[16] Y. Osada, J.-P. Gong, *Adv. Mater.* **1998**, *10*, 827.
[17] Y. Osada, M. Hasebe, *Chem. Lett.* **1985**, *9*, 1285.
[18] A. Heller, *Current Opinion in Chemical Biology* **2006**, *10*, 664.
[19] R. A. Etchenique, E. J. Calvo, *Anal. Chem.* **1997**, *69*, 4833.
[20] G. Liu, X. Zhao, *Jounal of Macromolecular Science Part A* **2006**, *43*, 345.
[21] T. Tanaka, I. Nishio, S.-T. Sun, S. Ueno-Nishio, *Science* **1982**, *218*, 467.
[22] Y. Li, N. Wang, X. He, S. Wang, H. Liu, Y. Li, X. Li, J. Zhuang, D. Zhu, *Tetrahedron* **2005**, *61*, 1563.
[23] M. Péter, M. A. Hempenius, E. S. Kooij, T. A. Jenkins, S. J. Roser, W. Knoll, G. J. Vancso, *Langmuir* **2004**, *20*, 891.
[24] E.-Y. Choi, O. Azzaroni, N. Cheng, F. Zhou, T. Kelby, W. T. S. Huck, *Langmuir* **2007**, *23*, 10389.
[25] A. Anne, J. Moiroux, *Macromolecules* **1999**, *32*, 5829.
[26] C. Ornelas, J. Ruiz, C. Belin, D. Astruc, *J. Am. Chem. Soc.* **2009**, *131*, 590.
[27] S. Haider, S.-Y. Park, K. Saeed, B. L. Farmer, *Sensors and Actuators B* **2007**, *124*, 517.
[28] E. J. Calvo, C. Danilowicz, R. Etchenique, *J. Chem. Soc. Faraday Trans.* **1995**, *91*, 4083.
[29] E. J. Calvo, R. Etchenique, C. Danilowicz, L. Diaz, *Anal. Chem.* **1996**, *68*, 4186.
[30] R. X. Li, X. Z. Zhang, J. S. Zhao, J. M. Wu, Y. Guo, J. Guan, *Journal of Applied Polymer Science* **2006**, *101*, 3493.
[31] S. J. Kim, S. R. Shin, S. M. Lee, I. Y. Kim, S. I. Kim, *Smart Materials and Structures* **2004**, *13*, 1036.
[32] C. J. Whiting, A. M. Voice, P. D. Olmstedt, T. C. B. McLeish, *J. Phys. Condens. Matter* **2001**, *13*, 1381.
[33] H. Li, R. Luo, K. Y. Lam, *Journal of Membrane Science* **2007**, *289*, 284.
[34] R. Luo, H. Li, K. Y. Lam, *Anal. Bioanal. Chem.* **2007**, *389*, 863.
[35] H. Li, T. Y. Ng, Y. K. Yew, K. Y. Lam, *Macromol. Chem. Phys.* **2007**, *208*, 1137.
[36] T. Tanaka, I. Nishio, S. T. Sun, S. Ueno-Nishio, *Science* **1982**, *218*, 467.
[37] S. Ramanathan, L. H. Block, *J. Contr. Release* **2001**, *70*, 109.
[38] S. H. Gehrke, *Adv. Polym. Sci.* **1993**, *110*, 81.
[39] J. P. Gong, T. Nitta, Y. Osada, *J. Phys. Chem.* **1994**, *98*, 9583.
[40] T. Budtova, I. Suleimenov, S. Frenkel, *Polym. Gels Networks* **1995**, *3*, 387.

[41] G. Liu, X. Zhao, *J. Macromol. Sci. A* **2006**, *A43*, 345.

[42] S. H. Yuk, S. H. Cho, H. B. Lee, **1992**, *9*, 955.

[43] D. E. D. Rossi, P. Chiarelli, G. Buzzigoli, C. Domenici, L. Lazzeri, *Trans. Am. Soc. Artif. Intern. Organs* **1986**, *32*, 157.

[44] I. C. Kwon, Y. H. Bae, T. Okano, S. W. Kim, *J. Contr. Release* **1991**, *17*, 149.

[45] A. Aoki, A. Heller, *J. Phys. Chem.* **1993**, *97*, 11014.

[46] A. Aoki, R. Rajagopalan, A. Heller, *J. Phys. Chem.* **1995**, *99*, 5102.

[47] D. N. Blauch, J. M. Saveant, *J. Am. Chem. Soc.* **1992**, *114*, 3323.

[48] R. A. Marcus, N. Sutin, *Biochimica et Biophysica Acta. Review on Bioenergetics* **1985**, *811*, 265.

[49] P. G. Pickup, W. Kutner, C. R. Leidner, R. W. Murray, *J. Am. Chem. Soc.* **1984**, *106*, 1991.

[50] F. Mao, N. Mano, A. Heller, *J. Am. Chem. Soc.* **2003**, *125*, 4951.

[51] H. Nagasaka, M. Watanabe, *Synthetic Metals* **1995**, *69*, 557.

[52] R. Prins, A. R. Korswage, A. G. Kortbeek, *J. Organomet. Chem.* **1972**, *39*, 335.

[53] J. Holecek, K. Handlir, J. Klikorka, N. Dinhbang, *Czech Chem. Commun.* **1979**, *44*, 1379.

[54] S. A. Merchant, D. T. Glatzhofer, D. W. Schmidtke, *Langmuir* **2007**, *23*, 11295.

[55] E. S. Forzani, M. A. Pe´rez, M. L. p. Teijelo, E. J. Calvo, *Langmuir* **2002**, *18*, 9867.

[56] M. Tagliazucchi, D. Grumelli, E. J. Calvo, *Phys. Chem. Chem. Phys.* **2006**, *8*, 5086.

[57] M. Biesalski, D. Johannsmann, J. Rühe, *J. Chem. Phys.* **2004**, *120*, 8807.

[58] I. Tomatsu, A. Hashidzume, A. Harada, *Macromol. Rapid Commun.* **2006**, *27*, 238.

[59] Y. Nishikitani, S. Uchida, T. Asano, M. Minami, S. Oshima, K. Ikai, T. Kubo, *J. Phys. Chem. C* **2008**, *112*, 4372.

[60] J. Huo, L. Wang, T. Chen, L. Deng, H. J. Yu, Q. H. Tan, *Designed Monomers and Polymers* **2007**, *10*, 389.

[61] H. Z. Bu, S. R. Mikkelsen, A. M. English, *Anal. Chem.* **1995**, *67*, 4071.

[62] K. Uosaki, Y. Sato, H. Kita, *Langmuir* **1991**, *7*, 1510.

[63] F. Goujon, C. Bonal, B. Limoges, P. Malfreyt, *Langmuir* **2009**, *25*, 9164.

[64] J. Redepenning, H. M. Tunison, H. O. Finklea, *Langmuir* **1993**, *9*, 1404.

[65] E. J. Calvo, C. Danilowicz, R. Etchenique, *J. Chem. Soc., Fraday Trans.* **1995**, *91*, 4083.

[66] L. L. Norman, A. Badia, *J. Am. Chem. Soc.* **2009**, *131*, 2328.

[67] K. Uosaki, Y. Sato, H. Kita, *Langmuir* **1991**, *7*, 1510.

[68] K. Sutani, I. Kaetsu, K. Uchida, *Radiat. Phys. Chem.* **2001**, *61*, 69.

[69] C. P. Andrieux, J. M. Saveant, *J. Phys. Chem.* **1988**, *92*, 6761.

[70] E. Stenberg, B. Persson, H. Roos, C. Urbaniczky, *Journal of Colloid and Interface Science* **1991**, *143*, 513.

[71] B. Steiger, C. Padeste, A. Grubelnik, L. Tiefenauer, *Electrochimica Acta* **2002**, *48*, 761.

[72] A. S. Kumar, K. C. Pillai, *J. Solid State Electrochem.* **1997**, *4*, 408.

[73] S. Koide, K. Yokoyama, *J. Electroanal. Chem.* **1999**, *468*, 193.

[74] R. J. Forster, J. G. Vos, *J. Inorg. Organometallic Polym.* **1991**, *1*, 67.

[75] N. Oyama, T. Tatsuma, K. Takahashi, *J. Phys. Chem.* **1993**, *97*, 10504.

[76] M. A. M. Noel, P. Topart, *Anal. Chem.* **1994**, *66*, 484.

[77] A. J. Bard, L. R. Faulkner, *Electrochemical Methods, Vol. p. 218*, Wiley, New York, **1980**.

[78] B. Liedberg, I. Lundström, E. Stenberg, *Sensors and Actuators B* **1993**, *11*, 63.

[79] W. Knoll, *Annu. Rev. Phys. Chem* **1998**, *49*, 569.

[80] M. Weisser, F. Thoma, B. Menges, U. Langbein, S. Mittler-Neher, *Opt. Commun.* **1998**, *153*, 27.

4.4 Composit Dextran-Hydrogels with Embedded Magnetic Nanoparticles

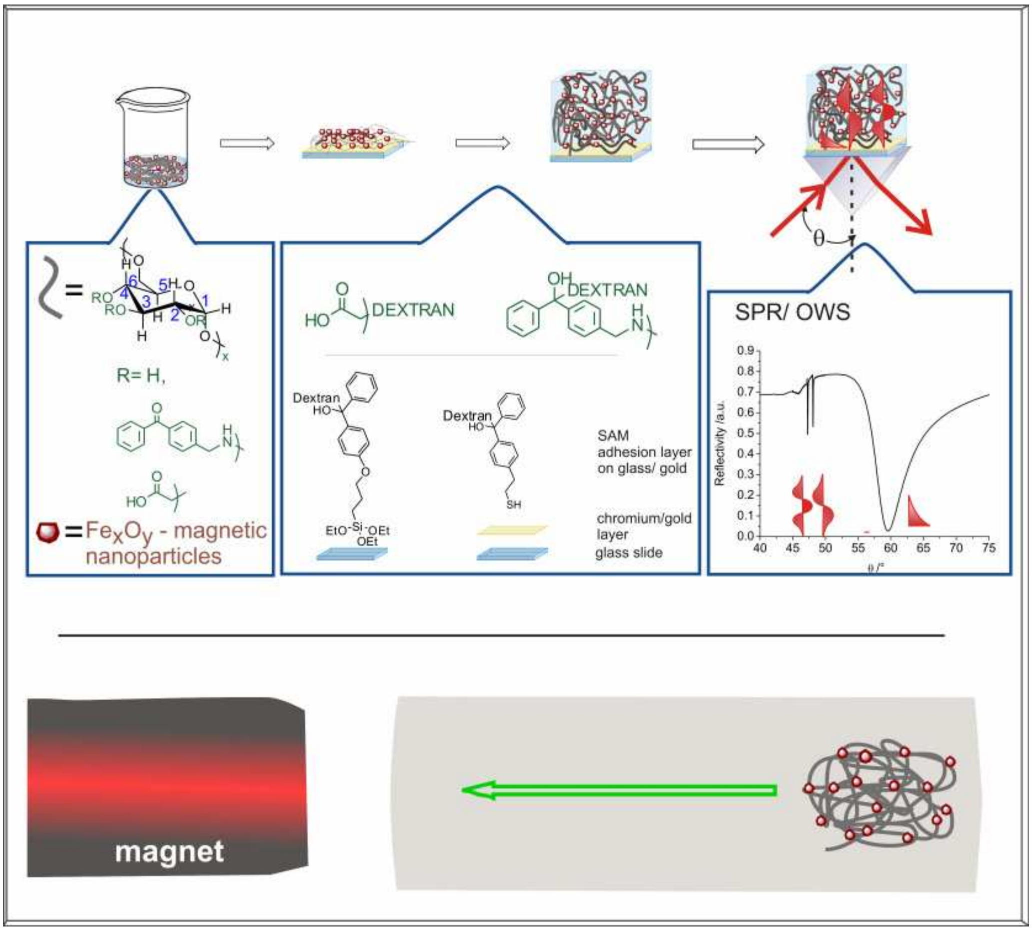

Composite magnetic nanoparticle materials are potential candidates for various applications from medicine to mechanics. Their characteristics are extensively investigated, especially their behaviour in a magnetic field. In this Chapter, the photo-crosslinkable carboxymethylated dextran-based iron oxide nanoparticle composites, which were introduced in Chapter 3.3, are characterized towards their swelling and magnetic characteristics and anticipated applications in this Chapter.

4.4.1 Introduction

The combination of magnetic and elastic properties like in dextran-nanoparticle composite materials opens a broad variety of possible applications due to their responsiveness to magnetic fields. Magnetic resonance imaging[1, 2], inductive heating[3-5], magnetic swelling, hyperthermia,[6, 7] catalysis,[8] magnetically guided drug delivery,[9-12] and magnetic separation,[4, 13-18] and sensing[18, 19] are the most important ones. Most common systems are iron oxide nanoparticles, which show a very low cytotoxicity, integrated into crosslinked poly(vinyl alcohol) (PVA) hydrogels[20, 21], poly(dimethylsiloxane) (PDMS)[22, 23], silicone matrices,[24] polystyrene[21], poly-(2-hydroxyethyl methacrylate)[25] or poly(NIPAAm) [3, 26]. Interpenetrating networks (IPN) of PNIPAAm and PVA for example have also been useful for this because of their enhanced tensile strength compared to pure PNIPAAm.[27]

In the production of magnetic composite hydrogels, the stability of the magnetic nanoparticles inside the hydrogel structure is a very important characteristic. Different strategies of particle immobilization like electrostatic binding, mechanical entrapment or covalent binding using a functionalized core are used (Chapter 3.3). If the coupling forces are too weak, loss of material becomes a critical parameter as reported by Fuhrer et al. for non-covalently fixed magnetic nanoparticles into poly-(2-hydroxyethyl methacrylate) and by Luechinger and co-workers while using composite materials as actuators.[28] This loss of material can be prevented by using covalently coupled core-shell particles.[25]

Chemically stable composites have to be characterized towards their magnetic properties. In the absence of a magnetic field the magnetic moments are randomly distributed and no magnetization is experienced. In a magnetic field the interplay of two types of interactions, the field-particle and the particle-particle interaction, is important.[29-31]

In a uniform magnetic field, i.e. without a field gradient, no attractive or repulsive field-particle interactions are present and the particle-particle interactions are dominant. The external magnetic field induces a magnetic dipole in each particle. Mutual particle interaction occurs if the particles are close enough resulting in attractive forces if the particles are aligned end to end and repelling forces if they are located side-by-side. The alignment of magnetic nanoparticles in a uniform magnetic field is used to generate structured, mechanically and magnetically anisotropic composite materials, called magnetostrictive, magnetorheological or magneto-active materials. Patterns like chains, sheets, honeycombs, or networks can be achieved.[23, 26, 32-39] Theoretically, the deformation of spheroidal ferrogel bodies in a uniform magnetic field was investigated by Morozow and co-workers. They show two competitive mechanisms, magnetistatic and magnetistrictive, being responsible for the deformation of ferrogel bodies.[40]

A non-uniform magnetic field, i.e possessing a magnetic field gradient, is needed to induce movement of magnetic nanoparticles and composite hydrogels. In a magnetic field gradient the field-particle interactions are dominating compared to the particle-particle interactions. The particles experience a magnetophoretic force and are attracted to stronger field intensities. During this process changes in the molecular conformation induce macroscopic shape distortion in case the composite hydrogel is fixed to a surface. If the magnetic material can move freely, the whole composite material accelerates towards the magnet, due to a collective movement of the dispersing liquid, the particles and the crosslinked polymer network until an equilibrium state in which magnetic and elastic forces are balanced.[41]

The magnetization of a ferrogel (M) in an external field is proportional to the concentration of the magnetic nanoparticles and the saturation magnetization (M_s), described by the Langevin function (equation 4.4.1) assuming the magnetization of individual particle to be equal to the saturation magnetization:

$$M = \Phi_m M_s \Lambda(\xi) = \Phi_m M_s \left(\coth \xi - \frac{1}{\xi} \right) \tag{4.4.1}$$

where M represents the bulk magnetic moment, Φ_m the volume fraction of the magnetic particles in the gel, ξ the Langevin function and ξ is defined as:

$$\xi = \frac{\mu_0 mH}{k_B T} \tag{4.4.2}$$

where H stands for the strength of the applied external magnetic field, μ_0 for the magnetic permeability of the vacuum, m for the magnetic moment of the sub-domain ferromagnetic particle, k_B for the Boltzmann constant and T denotes the temperature. This relation is valid for diluted superparamagnetic systems, where the particle-particle interactions are negligible and where the particles are rigidly fixed inside the gel with energy barriers between easy axes for spin alignment being smaller than the thermal energy or with the direction of magnetization within the particles being fixed but rotation of particles in the gel being allowed.[36, 42] Metallic cobalt[43, 44] and metallic iron[45] would combine high saturation magnetization and high density but their instability towards oxidation has promoted the predominant use of the iron oxides magnetite (Fe_3O_4) and maghemite (γ-Fe_2O_3).[11] Aging phenomena in ferrofluids and magnetic beads used for biosensor applications was described by Strömberg and co-workers and mainly related to aggregation effects.[46]

The force-density response for the movement of a magnetic composite gel is mainly determined by the magnetization (M) and the magnetic field gradient (∇H). Considering a homogeneous movement and a linear relationship between magnetization (M) and the magnetic field strength, the force density can be described as follows equation 4.4.3. It is assumed, that the Gaussian theory of rubber elasticity can be used as an approximation, indicating that nonlinear effects resulting from a finite chain extensibility and restricted chain mobility (fluctuation of junction points) due to entanglement are negligible.

$$f_m = \mu_0 (M\nabla) H \tag{4.4.3}$$

with μ_0 resembling the magnetic permeability in vacuum, M the magnetization, and ∇H the magnetic field gradient. In case of non-Gaussian behaviour other theories like the Van der Waals approach have to be used[47]. The orientation of the force density is parallel to the direction of the magnetic field.The force density either leads to an acceleration of the gel towards the magnet surface is reached or to a shape distortion until the network elasticity balances the magnetic stress. According to equation 4.4.3 a magnetic gel moves towards a stronger magnetic field.[20, 21].

In summary, the attraction towards a magnet in a non-uniform magnetic field depends on the magnetic particle content (mass per volume fraction) and the saturation magnetization (force per mass particles).[25, 41, 42] The response is shown to take place instantaneously in hundreds of seconds.[41, 42]

4.4.2 Characteristics and Applications of a Bulk Composite Gel

The magnetic iron oxide nanoparticle photo-crosslinkable carboxymethylated dextran based composite materials presented in this work (Chapter 3.3) can be crosslinked by irradiation of UV-light, resulting in a stable magnetic composite hydrogel network. The magnetic properties of the bulk composite material can be shown by placing the swollen hydrogel close to a magnet. Due to the magnetic field gradient the magnetic hydrogel accelerates towards the stronger field. The movement starts instantaneously and a distance of several centimeters is covered in a few seconds depending on the magnetic field strength and the composite hydrogel properties like weight or nanoparticle content. In the example shown in Figure 4.4.1 it takes eight seconds to move the composite hydrogel over a distance of 4 cm towards the magnet. At the beginning of the movement towards the magnet the gel is stretched because a part of the gel is already attracted, while the rest is still sticking to the bottom of the vial (0-5 seconds).

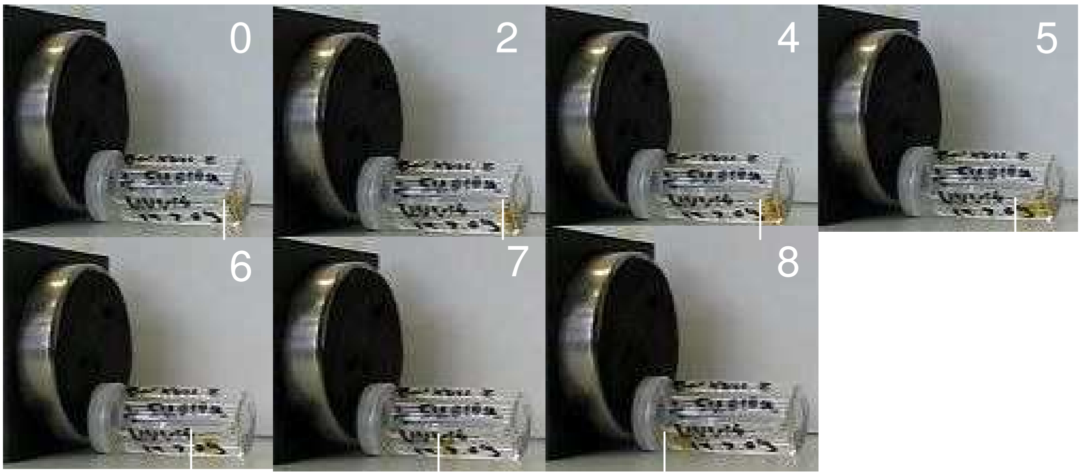

Figure 4.4.1: *Snapshots at 0, 2, 4, 5, 6, 7, and 8 seconds after placing the magnetic composite hydrogel into the magnetic field (0,7 Tesla at the surface of the magnet). The composite hydrogel contains benzophenone groups as photo-crosslinking unit (d_s(benzophenone) = 0.04) and carboxymethyl functionalities (d_s(carboxymethyl) = 0.16) as potential analyte binding points and for the electrostatical coupling of the iron oxide nanoparticles. The nanoparticle content (Fe_xO_y-I) was adjusted to 20 % by mixing. The glass vial has a length of 4 cm.*

The nanoparticles are stable inside the gel for repeated cycles of magnet attraction. No phase separation could be observed. Even at pH 3 the particles are stable inside the gel as already shown by UV-VIS (Chapter 3.3), too. The bulk hydrogel presented in Figure 4.4.1 was swollen in water for 8 month also showing the stability of these materials. The most straight forward application for this magnetic hydrogel can be envisaged in magnetic separation. The ability of biomolecule-binding is proved in Chapter 4.2 and different strategies are known from the literature, too.[48-50] Adopting amino functionalities for example would allow the separation of the iron oxide nanoparticle coupling points from the analyte binding preferably leading to enhanced analyte coupling.

Dextran can be degraded by hydrolysis and cleaved enzymatically by using dextranase.[51-55]

4.4.3 Characteristics and Applications of Composite Hydrogel Films

To investigate the swelling properties and the magnetic response of the magnetic composite hydrogel films, the polymer blend is spincoated onto a gold surface. A self-assembled monolayer of *S*-3-(4-benzoylphenoxy)propyl ethanthiol is serving as adhesion promoter. As described in Chapter 3.1, the polymer composite material is crosslinked and fixed to the surface in one step by UV-light irradiation. The swelling state was monitored by SPR/OWS spectroscopy. From the SPR/OWS spectra the thickness and refractive index profile can be extracted (Chapter 2.3) and the swelling degree (swollen thickness divided by dry thickness after swelling experiment) can be calculated, if the dry thickness after the swelling experiment is known. The swelling degree plotted against the sodium chloride concentration in ultrapure water is displayed in Figure 4.4.2 for a dextran based hydrogel with a benzophenone content of $d_s = 0.04$ and a degree of carboxymethylation of d_s~0.17 related to the amount of repeating units.

The dependence of the swelling degree on the salt concentration shows a comparable tendency for all magnetic composite material types. For sodium chloride concentrations higher than 0.2 M, no significant thickness change is observed, whereas the swelling degree increases for concentrations lower than 0.1 M due to electrostatical repulsion of the free carboxyl groups that are not blocked by sodium ions in accordance with the behaviour of the pristine hydrogel. In contrast to the pristine dextran-based hydrogel, the change in swelling degree upon reducing the sodium chloride concentration is less pronounced for the composite materials, clearly indicating a blocking of carboxyl functionalities. This reflects their coupling to the iron oxide nanoparticles. Furthermore, the swelling degree decreases with increasing particle content as seen in Figure 4.4.2 A. This observation can be attributed to two effects: crosslinking effect and the charge blocking of the magnetic iron oxide nanoparticles due to their ability of attracting more than one carboxyl group. For the composite materials with 12.5-15 % nanoparticle contents almost no change in swelling can be detected between 0.1 M and 0.2 M sodium chloride: in contrast to the pure hydrogel, the material is only swelling in sodium chloride concentrations below 0.1 M. These observations indicate that the screening of carboxyl groups takes place for sodium chloride concentrations up to 0.1 or 0.2 M, showing the free carboxyl groups to be still present in the composite material. The reduced swelling indicates a reduced amount of free carboxyl groups as expected after iron oxide nanoparticle introduction.

Besides the nanoparticle content the nanoparticle size seems to influence the swelling of the magnetic composite dextran hydrogels. Theoretically, based on the assumption of an increased number of carboxyl functionalities per nanoparticle with increasing volume, increasing surface respectively, a reduced swelling upon increasing nanoparticle volume is expected. The difference in swelling degree for varying types of iron oxide nanoparticles is more pronounced for a 12.5-15 % than for a 5 % nanoparticle content as seen in

Figure 4.4.2 B, C and as anticipated the swelling degree decreases with increasing size of the iron oxide nanoparticles.

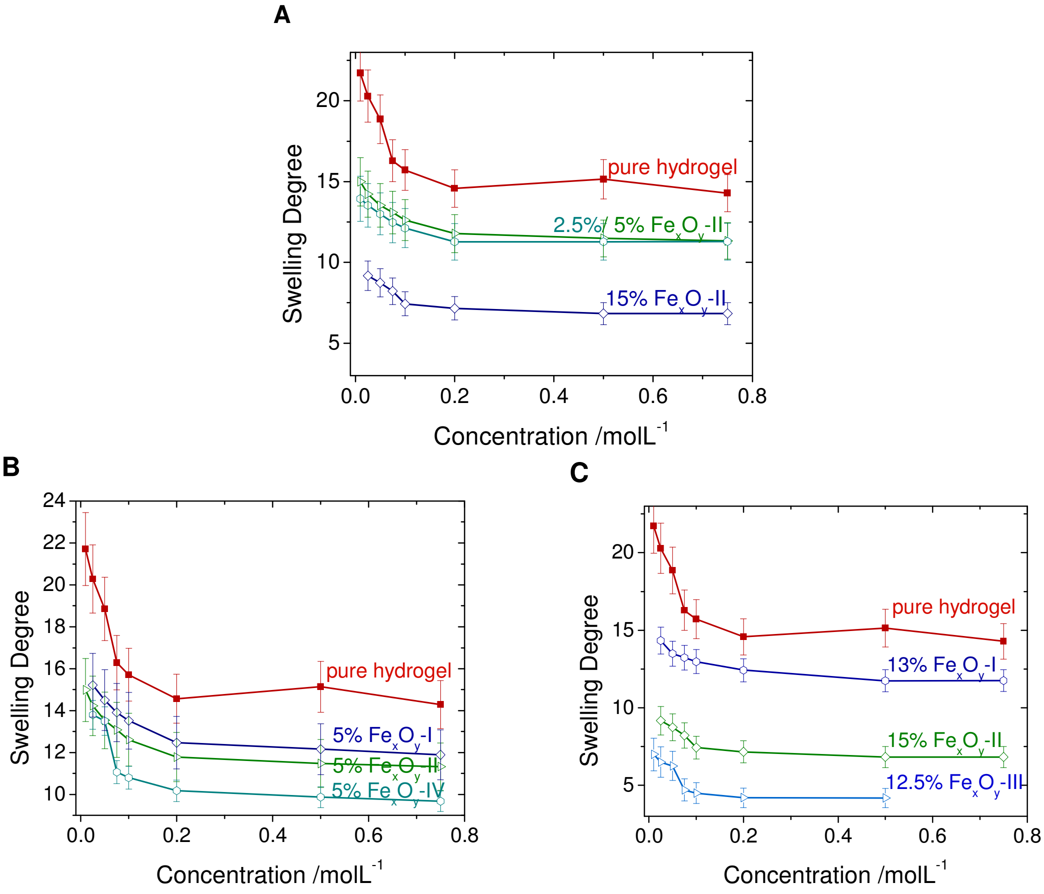

Figure 4.4.2: *Investigating the swelling degree of composite iron oxide dextran-based hydrogel materials with varying type* ***(B, C)*** *and load* ***(A)*** *of magnetic nanoparticles in 10 -20 μm thick swollen composite films. The swelling degree clearly depends on the amount of particles inside the composite gel and on the size of the magnetic nanoparticles. The crosslinking conditions were kept constant with an irradiation wavelength of 254 nm and an irradiation time of 20 minutes, corresponding to an irradiation energy of 4 Jcm^{-2}.*

Another remarkable change occurs for very low salt concentrations, predominantly for concentrations around or below 10 mM. For these low concentrations at pH values above the ionization point of the carboxyl functionalities the swelling degree increases that much that the optical waveguide modes disappear and the hydrogel matrix partly detaches from the surface. This phenomenon is seen as well for the composite hydrogel matrices of course depending on the thickness and the degree of crosslinking as discussed in Chapter 4.1 for pristine hydrogels.

Repeating the ion-concentration dependent swelling experiments while applying a magnetic field gradient (permanent magnet, cylindrical shape, 0.7 T at surface) no swelling effect clearly related to the magnetic field could be observed. The magnetic field gradient for a 1 cm distance from the cylindrical magnet is determined to be 0.2 mT for a 10 μm composite film thickness. The calculation was performed by Núria Queraltó with the software FEMLAB.[56] This gradient is probably too small to induce remarkable swelling. Nevertheless, the swelling degrees are relatively high, providing large pores affording the diffusion of biomolecules opening a broad variety of possible applications to these magnetic composite hydrogels.

4.4.4 Conclusion and Outlook

By mixing a dextran-based photo-crosslinkable polymer with magnetic iron oxide nanoparticles and subsequently crosslinking by UV-light, a magnetic hydrogel with a biocompatible backbone was prepared and the magnetic characteristics were presented in this Chapter. The bulk magnetic dextran-based hydrogel was proofed to accelerate towards a magnet in a non-uniform magnetic field. This attribute combined with the capability of coupling biomolecules, as shown in Chapter 4.2, enables the use of this hydrogel material for magnetic separation applications. Therefore, a tuning of the carboxyl group and magnetic nanoparticle content is necessary to offer a sufficient amount of magnetic nanoparticles but preserve as many carboxyl functionalities for analyte binding as possible. Another strategy could be the decoupling of nanoparticle binding from the analyte binding points by either coupling the particles via a functionalized shell with different functionalities to the hydroxyl groups of the dextran backbone or to modify the strategy of analyte coupling.

Furthermore, the swelling behavior of composite dextran-based hydrogel films was investigated and related to the pristine hydrogel films. A reduced swelling was observed showing a crosslinking effect of the magnetic iron oxide nanoparticles due to multiple carboxyl group binding to one particle. This effect depends on the amount and size of the iron oxide nanoparticles. Nevertheless, the swelling degree is still high allowing biomolecule diffusion.

4.4.5 Experimental

Profiler: The hydrogel film surface topography and the film thickness in the dry state were characterized with a profiler (KLA Tencor, P-15 Profiler) with a vertical measuring range of up to 1 mm and a resolution of ~7,5 Å.

Magnet: To create a magnetic field gradient a cylindrical permanent magnet with a magnetic field of 0.7T at the surface was used.

SPR/ OWS Measurements: Surface plasmon resonance/ optical waveguide mode spectroscopy was performed in the Kretschmann configuration[57] as described in chapter 4.1.7.

The sample glass slide (LaSFN9 glass, Hellma Optik GmbH Jena, refractive index n = 1.8449, corresponding to ε = 1.3583) is put onto a homemade glass flow cell and at the backside is optically matched to the base of the glass prism (refractive index n = 1.8449, corresponding to ε = 1.3583). Monochromatic and linear, transverse-magnetic polarized (Glan-Thompson polarizer, Owis) laser light (He/Ne laser, Uniphase, λ = 632.8 nm) is directed through the prism onto the sample slide. The laser intensity was adjusted to 100 % reflectivity for all SPR/OWS experiments. This corresponds to 145 µW. By variation of the angle of incidence (θ) (two cycle goniometer, resolution 0,005°, Huber) and detecting the intensity of the reflected laser light I(θ) with a photodiode (BPW 34B silicon photodiode, Siemens) an angular spectrum is recorded.

SPR/ OWS Data Treatment: To model the measured spectra the Fresnel equations are solved by a transfer algorithm[58] for a planar multilayer system consisting of the LaSFN9 glass, chromium, gold, a self assembled monolayer as adhesion promoter, the hydrogel and the swelling solvent. For every layer a value for the thickness (d) and the dielectric constant (ε) consisting of a real part (ε') and the imaginary part (ε'') have to be defined.

To determine the parameters for the sample without hydrogel first a slide only coated with chromium and gold was measured. To define the adhesion promoter values a slide with chromium, gold and *S*-3-(4-benzoylphenoxy)propyl ethanthiol as the adhesion promoter was measured and the recorded spectra were simulated with the above mentioned model assuming all other values as fixed.

To simulate the SPR/OWS spectra in the above mentioned model an average refractive index for every layer is assumed (box model). As the hydrogel films are thicker and acting as waveguide the reversed Wentzel-Kramers-Brillouin (WKB) approximation can be used to model the refractive index profile perpendicular to the substrate surface of these films[59]. Thereby, the hydrogel film is assumed to be laterally homogeneous (parallel to the substrate surface).

Refractive Index-Thickness Profiles: The reversed Wentzel-Kramers-Brillouin approximation was used to extract the refractive index-thickness profiles from the angular SPR/OWS spectra. Details are described in Chapter 2.3 and Chapter 4.1.7.

This refractive index value for the gold hydrogel interface (z = 0) was extracted from the box-model simulation of the measured spectrum by simulating the refractive index of the surface plasmon after modeling the waveguide modes and keeping the thickness constant. The accuracy of the refractive index versus thickness profile increases with increasing number of optical waveguide modes. The thickness of the hydrogel film, extracted from the WKB-profile, was determined from the calculated value at maximum thickness.

Sodium Chloride Solutions: The screening of sodium chloride concentrations was carried out with custom made sodium chloride (Sigma Aldrich) solutions in destilled water.

4.4.6 Bibliography

[1] M. Baghi, M. G. Mack, M. Hambeck, J. Rieger, T. Vogl, W. Gstoettner, R. Knecht, *Anticancer Res.* **2005**, *25*, 3665.

[2] D. E. Sosnovik, R. Weissleder, *Current Opinion in Biotechnology* **2007**, *18*, 4.

[3] N. S. Satarkar, J. Z. Hilt, *Acta Biomaterialia* **2008**, *4*, 11.

[4] D. Horák, M. Babic, H. Maková, M. J. Benes, *J. Sep. Sci.* **2007**, *30*, 1751.

[5] S. Ghosh, C. Yang, T. Cai, Z. Hu, A. Neogi, *Journal of Physics D-Applied Physics* **2009**, *42*, 135501.
[6] A. K. Gupta, M. Gupta, *Biomaterials* **2005**, *26*, 3995.
[7] A. Ito, Y. Kuga, H. Honda, H. Kikkawa, A. Horiuchi, Y. Watanabe, T. Kobayashi, *Cancer Lett.* **2004**, *212*, 167.
[8] T. Gelbrich, M. Feyen, A. M. Schmidt, *Macromolecules* **2006**, *39*, 3469.
[9] N. Kohler, C. Sun, J. Wang, M. Zhang, *Langmuir* **2005**, *21*, 8858.
[10] A. K. Gupta, A. S. Curtis, *J. Mater. Sci. Mater. Med.* **2004**, *15*, 493.
[11] S. Bhattacharya, F. Eckert, V. Boyko, A. Pich, *Small* **2007**, *3*, 650.
[12] J. K. Oh, R. Drumright, D. J. Siegwart, K. Matyjaszewski, *Prog. Polym. Sci.* **2008**, *33*, 448.
[13] D. H. Wang, N. Rosenzweig, Z. Rosenzweig, *Nano Lett.* **2004**, *4*, 409.
[14] D. W. Inglis, R. Riehn, R. H. Austin, J. C. Sturm, *Appl. Phys. Lett.* **2004**, *85*, 5093.
[15] A. H. Latham, M. E. Williams, *Accounts of Chemical Research* **2008**, *41*, 411.
[16] Y.-Y. Liang, L.-M. Zhang, W. Jiang, W. Li, *Chem. Phys. Chem* **2007**, *8*, 2367.
[17] V. Thomas, M. Namedo, Y. M. Mohan, S. K. Bajbai, M. Bajpai, *J. Macromol. Sci. A* **2008**, *45*, 107.
[18] H. Kuramitz, *Anal. Bioanal. Chem.* **2009**, *394*, 61.
[19] N. Jaffrezic-Renault, C. Martelet, Y. Chevolot, J.-P. Cloarec, *Sensors* **2007**, *7*, 589.
[20] M. Zrínyi, L. Barsi, D. Szabó, H.-G. Kilian, *J. Chem. Phys.* **1997**, *106*, 5685.
[21] M. Zrinyi, D. Szabo, L. Barsi, *J. Intell. Mater. Syst. Struct.* **1998**, *9*, 667.
[22] Z. Varga, G. Filipcsei, M. Zrínyi, *Polymer* **2006**, *47*, 227.
[23] Z. Varga, G. Filipcsei, M. Zrínyi, *Polymer* **2005**, *46*, 7779.
[24] T. Shiga, A. Okada, T. Kurauchi, *J. Appl. Polym Sci.* **1995**, *58*, 787.
[25] R. Fuhrer, E. K. Athanassiou, N. A. Luechinger, W. J. Stark, *Small* **2009**, *5*, 383.
[26] M. Zrínyi, *Colloid Polym. Sci.* **2000**, *278*, 98.
[27] A. Mitwalli, S. Leeb, T. Tanaka, U. Sinha, *Universities Power Engineering Conference* **1994**, *September*, 871.
[28] N. A. Luechinger, N. Booth, G. Heness, S. Bandyopadhyay, R. N. Grass, W. J. Stark, *Adv. Mater.* **2008**, *20*, 3044.
[29] R. E. Rosenzweig, *Ferrohydrodynamics*, Cambridge University Press, Cambridge, **1985**.
[30] T. B. Jones, *Electromechanics of particles*, Cambridge University Press, Cambridge, **1995**.
[31] B. Berkovski, V. Bashtovoy, *Magnetic fluids and applications handbook*, Begell House, New York, **1996**.
[32] J. E. Martin, R. A. Anderson, D. Read, G. Gulley, *Phys. Rev. E* **2006**, *74*, 051507.
[33] S. Ahn, R. M. Kasi, S.-C. Kim, N. Sharma, Y. Zhou, *Soft Matter* **2008**, *4*, 1151.
[34] M. Farshad, M. L. Roux, *Polym. Test.* **2005**, *24*, 163.
[35] G. Y. Zhou, J. R. Li, *Smart Mater. Struct.* **2003**, *12*, 859.
[36] G. Filipcsei, I. Csetneki, A. Szilagyi, M. Zrinyi, *Adv. Polym. Sci.* **2007**, *206*, 137.
[37] A. M. Schmidt, *J. Magn. Magn. Mater.* **2005**, *289*, 5.
[38] A. M. Schmidt, *Macromol. Rapid Commun.* **2006**, *27*, 1168.
[39] T. Mitsumata, e. al., *INternational Journal of Modern Physics* **2002**, *16*, 2419.
[40] K. Morozov, M. Shliomis, H. Yamaguchi, *Phys. Rev. E* **2009**, *79*, 040801(R).
[41] M. Zrínyi, L. Barsi, A. Büki, *J. Chem. Phys.* **1996**, *104*, 8750.
[42] M. Zrínyi, L. Barsi, A. Büki, *Polymer Gels and Networks* **1997**, *5*, 415.
[43] H. Bonnemann, W. Brijoux, R. Brinkmann, N. Matoussevitch, N. Waldofner, N. Palina, H. Modrow, *Inorg. Chim. Acta* **2003**, *350*, 617.
[44] A. H. Lu, E. L. Salabas, F. Schuth, *Angew. Chem. Int. Ed.* **2007**, *46*, 1222.
[45] J. L. Wilson, P. Poddar, N. A. Frey, H. Srikanth, K. Mohomed, J. P. Harmon, S. Kotha, J. Wachsmuth, *J. Appl. Phys.* **2004**, *95*, 1439.
[46] M. Strömberg, K. Gunnarson, S. Valizadeh, P. Svedlindh, M. Stromme, *JOURNAL OF APPLIED PHYSICS* **2007**, *101*, 023911.
[47] H.-G. Kilian, *Colloid Polym. Sci.* **1987**, *265*, 410.
[48] A. Aulasevich, R. F. Roskamp, U. Jonas, B. Menges, J. Dostalek, W. Knoll, *Macromolecular Rapid Communications* **2009**, *30*, 872.
[49] B. Johnsson, S. Löfas, G. Lindquist, *Anal. Biochem.* **1991**, *198*, 268.
[50] K. Länge, M. Rapp, *Anal. Biochem.* **2008**, *377*, 170.
[51] H. Basan, M. Gümüşderelioğlu, M. T. Orbey, *European Journal of Pharmaceutics Biopharmaceutics* **2007**, *65*, 39.
[52] W. E. Hennink, C. F. v. Nostrum, *Adv. Drug Delivery Rev.* **2002**, *54*, 13.
[53] O. Franssen, L. Vandervennet, P. Roders, W. E. Hennink, *J. Control. Release* **1999**, *60*, 211.

[54] C. J. d. Groot, M. J. A. Luyn, W. N. E. Dijk-Wolthuis, J. A. Cadee, J. A. Plantinga, W. Otter, e. al., *Biomaterials* **2001**, *22*, 1197.

[55] J. A. Cadee, C. J. d. Groot, W. Jiskoot, W. Otter, W. E. Hennink, *J. Control. Release* **2002**, *78*, 1.

[56] COMSOL, *FEMLAB Mulit Physics Software* **2000**, http://www.nasatech.com/NEWS/May00/ntbprod_0500.html

[57] W. Knoll, *Annu. Rev. Phys. Chem* **1998**, *49*, 569.

[58] M. Born, E. Wolf, in *Principles of Optics, 7th ed.*, Cambridge University Press, Cambridge, U.K., **1999**.

[59] M. Weisser, F. Thoma, B. Menges, U. Langbein, S. Mittler-Neher, *Opt. Commun.* **1998**, *153*, 27.

4.5 Swelling and Cell Growth in a Dextran-Based Composite Hydrogel

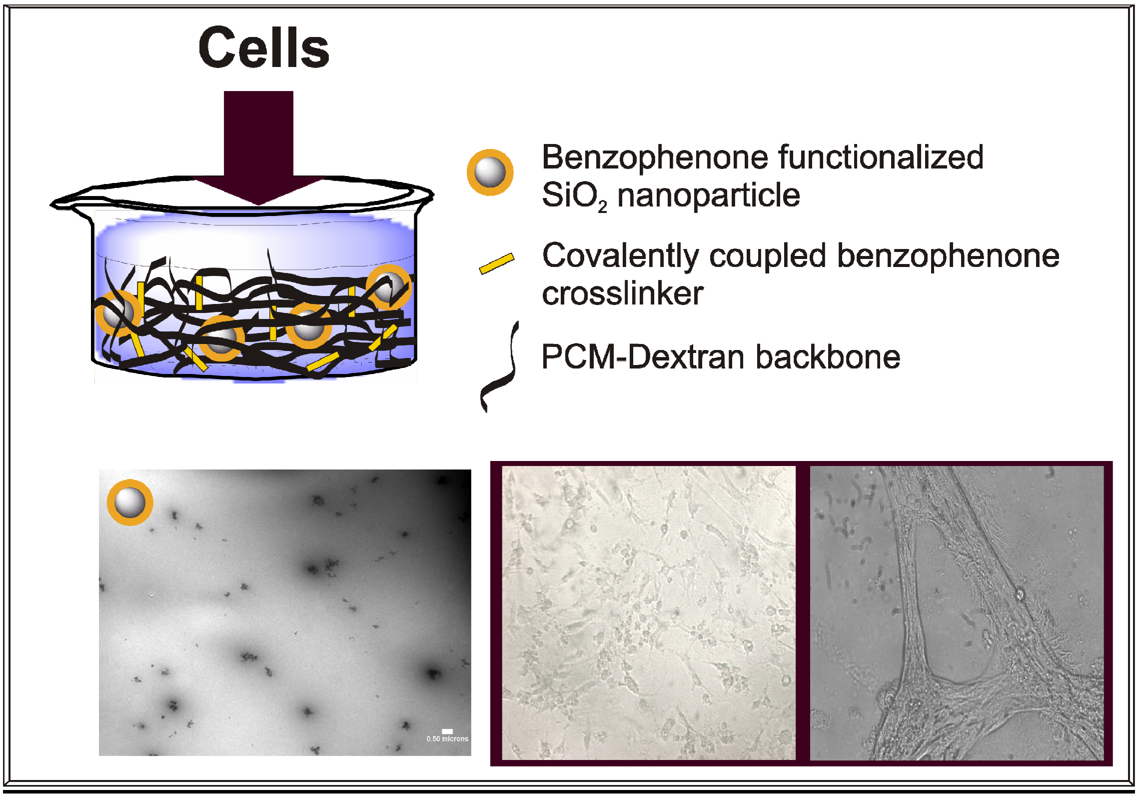

Hydrogels are suitable scaffolds for cell adhesion and cell growth. They enable cell attachment, can be structured to direct cell growth, and exist in a broad variety of chemical compositions. Simultaneously, they allow the proliferation of small molecules like nutrients or gasses which are obligatory for cell growth and can even induce specific cell growth. In this Chapter, the cell response of osteoblasts and endothelial cells to the photo-crosslinkable, carboxymethylated dextran based hydrogel scaffold is described. The influence of a higher degree of crosslinking and the introduction of gelatin as spacer material is discussed as well as the mechanical structuring on a scale of micrometers and millimeters.

4.5.1 Introduction

Cell adhesion and cell growth on and in hydrogel matrices is a promising tool for medical applications such as bone regeneration, wound healing, and tissue engineering.[1-6]

As already briefly mentioned in Chapter 3.4 the interaction of cells with polymers is determined by a variety of factors, including biophysical (degree of hydrophilicity and hydration), chemical (functional groups), topographical, and mechanical properties including the surface to volume ratio.[2, 7-9] Consequently, the system properties can be tuned by optimizing these parameters.

Tissue engineering requires a 3D matrix that ideally guides cell formation and simultaneously provides adequate transport of nutrients and growth factors. Hydrogels permit this exchange of oxygen and nutrients obligatory for cell growth.[10] Different approaches have been followed to create pores for cell growth and to pattern materials to direct cell growth.[1, 11, 12] A versatile approach is the crosslinking and patterning by photopolymerization. Photopolymerized hydrogels have been used to successfully encapsulate various types of cells including pancreatic islets,[13] smooth muscle cells,[14] osteoblasts for bone regeneration,[15] or labeled HepG2 cells into PEG hydrogels for example.[16]

To induce cell growth inside a 3D hydrogel matrix the most common procedure is the mixing of cells with the polymer prior to hydrogel formation. In this method the cells themselves create their space by their presence during the crosslinking process.[17]

Examples for hydrogels used for cell attachment and cell growth are 2-hydroxyethyl methacrylate (HEMA),[18] poly(ethyleneglycol) (PEG),[19] polyacrylamides, or poly(N-isopropyl acrylamide) (PNIPAAm).[1] An overview of the materials used, their potential for cell growth, and their advantages and limitations can be found in a review by Hynd *et al.*[3] For example Arcaute *et al.* have demonstrated the use of stereolithography to fabricate complex, bioactive, 3D PEG-based hydrogel structures with internal channels of various orientation as templates for cell encapsulation.[20] Another example is the encapsulation of cells in photo-crosslinked polydimethylsiloxane micro-molded hydrogel constructs. By controlling the feature sizes on the elastomeric stamp, the size as well as the shape of the molded hydrogels could be controlled.[21] Furthermore, highly interconnected macroporous PEG hydrogels, suitable for applications as tissue-engineering scaffolds, have been designed by combining the photo-crosslinking reaction with a foaming process. Thereby, pore dimensions, as well as the swelling rate, were modulated by polymer concentrations and foaming agent composition in the precursor solution.[22] An advanced idea is the development of a 3D scaffold that contains multiple cell types in which the spatial arrangement of the cells is controlled by a pre-designed pattern.[23]

Functionalized dextran-based hydrogels are known to enable derivation of vascular cells in particular of endothelial cells which makes them good candidates for application in tissue engineering and regenerative medicine.[24] Thereby, a correlation between the degree of carboxymethyl-, benzylamide, and sulfation substitution for dextran-based systems was reported.[25]

In this Chapter the potential of a modified dextran-based hydrogel for application as scaffold for cell growth is discussed. For this purpose dextran-based hydrogel matrices were prepared and optimized in terms of swelling, chemical composition and patterning (Chapter 3.4). The swelling properties of the hydrogel matrix were investigated by surface plasmon resonance (SPR) and optical waveguide mode spectroscopy (OWS). Cell adhesion and cell growth experiments of endothelial cells and osteoblasts were performed in cooperation with Dr. U. Ritz and Dr. A. Hofmann at the University Medical Center in Mainz.

4.5.2 Swelling Characteristics of Composite Hydrogels

Because the swelling of a hydrogel matrix determines the mechanical properties and the pore size it is important to optimize the swelling characteristics for cell growth experiments. To increase the mechanical strength super-crosslinking benzophenone-functionnalized SiO_2-nanoparticels were introduced into the photo-crosslinkable, carboxymethylated dextran (PCMD) (Chapter 3.4, Figure 4.5.1). The swelling of this composite PCMD hydrogel material (Chapter 3.4) depends on the pH and the ion concentration due to the free carboxyl groups (Figure 4.5.1) and on the crosslinking density. To investigate the charge dependent electrostatical responsiveness in dependence of the super-crosslinker content swelling experiments with varying sodium chloride concentrations were performed. Films were produced by spin-coating the PCMD-based polymer composite on a chromium/gold-covered glass slide. As adhesion promoter, a self-assembled monolayer of *S*-3-(4-benzoylphenoxy)propyl ethanethiol was chemisorped onto the gold before spincoating. The subsequent irradiation at 254 nm resulted in a photo-crosslinked and surface-bound hydrogel film in one step as described in Chapter 3.1.3. The swelling properties of these films were subsequently characterized by SPR/OWS spectroscopy applying the WKB approximation (Chapter 2.1, 2.3) and compared to the swelling behavior of pure PCMD films. The composite matrices were swollen in a 0.05 M sodium chloride solution over night followed by a screening of sodium chloride concentrations between 10 mM and 1 M at a neutral pH. A schematic view of the polymer-nanoparticle material is shown in Figure 4.5.1.

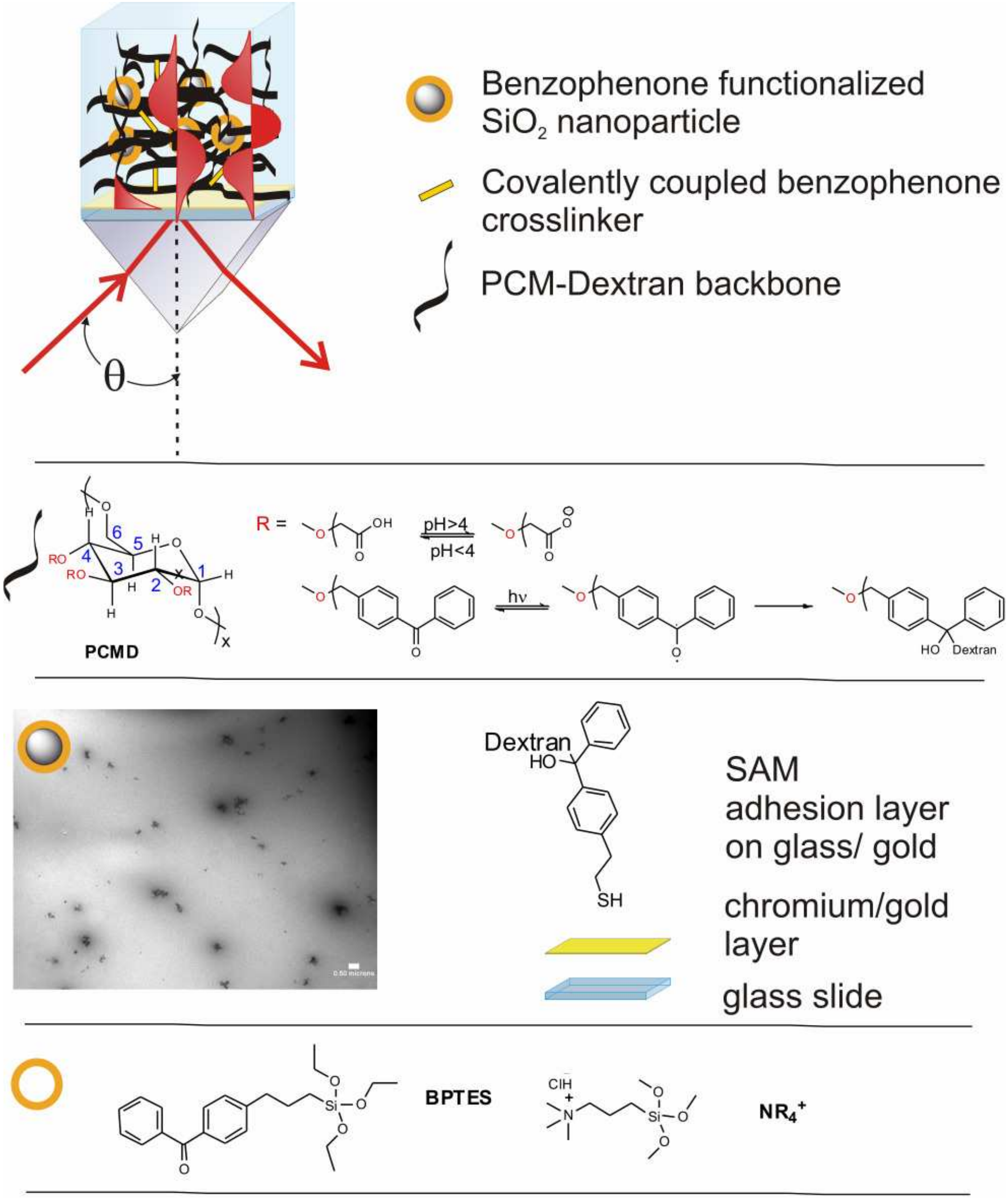

Figure 4.5.1: *Scheme of the composite hydrogel containing benzophenone functionalized silica nanoparticles as crosslinking centers and the chemical structure of the PCMD backbone.*

To investigate the variation of the swelling in the entire hydrogel film the WKB profile derived from the angular position of the optical waveguide modes and the surface plasmon (Chapter 2.3) were derived (Figure 4.5.2 A, B). The response up to a concentration of 0.1 M is comparable for a SiO_2-nanoparticle content of 5 and 20 wt%. For higher ion concentrations the hydrogel matrix with a nanoparticle content of 20 wt% shows a more pronounced shrinking.

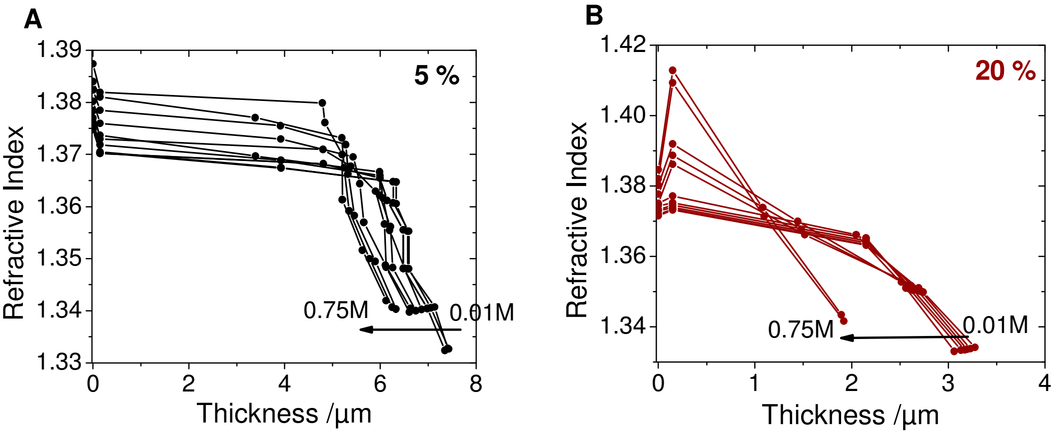

Figure 4.5.2: *Swelling behavior of the hydrogel film containing benzophenone functionalized SiO_2-nanoparticles as multiple crosslinking units with a content of 5 and 20 %. The WKB refractive index-thickness profiles extracted from the angular scans are presented:* ***A)*** *5 wt% super-crosslinking nanoparticles,* ***B)*** *20 wt% supercrosslinking nanoparticles. The different responses to high ion concentrations are remarkable.*

In Figure 4.5.3 the swelling degrees depending on the sodium chloride concentration are compared for samples with increasing amounts of benzophenone-functionalized silica nanoparticles. Thereby, the swelling degrees were calculated by dividing the film thickness in the swollen state extracted from the WKB profile by the film thickness in the dry state after swelling and drying.

As expected the hydrogel matrices modified with nanoparticle super-crosslinkers show a reduced swelling compared to the pure hydrogel. The number of free carboxyl groups and with this the swelling due to the carboxyl group deprotonation is preserved. Consequently, the benzophenone-carrying silica nanoparticles, serving as multiple-crosslinking centers, affect the crosslinking density and thus lead to a reduction of the swelling degree.

The benzophenone-functionalized nanoparticles increase the degree of crosslinking and thus the stability of the hydrogel due to structural reinforcement upon multiple crosslinking units per particle. A gradual swelling at concentrations below 0.2 M is related to the protonation-deprotonation equilibrium of the carboxyl functionalities and exists in all carboxymethylated dextran hydrogel matrices (compare Chapter 4.1). If the number of carboxyl groups is reduced the magnitude of swelling and the magnitude of the change in swelling decreases for identical crosslinked films. The overall swelling and the response of the hydrogel to decreasing ion concentration is reduced in case of enhanced crosslinking and rigidity of the matrix as well as for reduced amount of charges. A reduced swelling due to the reduction of free carboxyl groups was already observed in sensing applications (Chapter 4.2) and for the coupling of iron oxide nanoparticles to the carboxyl groups (Chapter 4.4). The concentration of the maximum hydrogel matrix response to varying ion concentrations depends on the amount of free carboxyl groups present in the hydrogel film. The hydrogels presented here (d_s(carboxymethyl) = 0.3) show a maximum in the swelling response at concentrations below 0.2 mM (Figure 4.5.3).

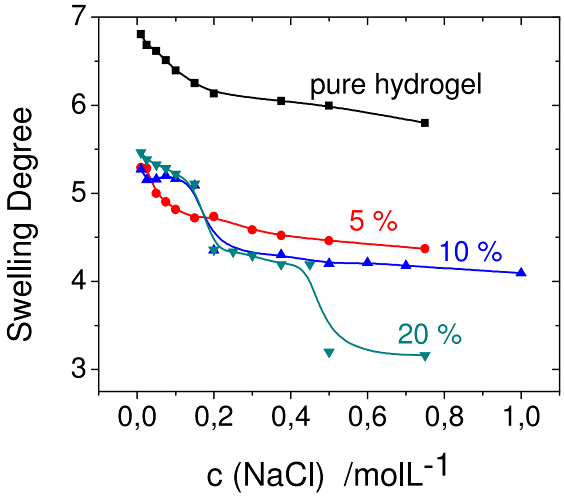

Figure 4.5.3: *The swelling degree in dependence of the NaCl concentration for different contents of benzophenone-functionalized* SiO_2*-nanoparticles as multiple crosslinking units. The swelling degree was calculated from the WKB profile thickness in the swollen state related to the thickness in the dry state after swelling and drying.*

Surprisingly, not only the shrinking due to charge screening of the deprotonated carboxyl groups is detected. For a silica particle content of 20 % a second additional swelling response at higher ion concentrations appears. This additional swelling response seems to be related to the presence of the silica nanoparticles because it does not appear for pure hydrogels and at low SiO_2 nanoparticle concentrations. This second transition is observed for different samples but the magnitude of the change varies and the concentrations for which the swelling step occurs shift between 0.25 M and 0.4 M. Even at different positions on one substrate the response varies. In Figure 4.5.3 the response for a 20 % content is relatively high compared to the average responses whereas the response for a SiO_2-nanoparticle content of 10 % is relatively low. A possible reason for this inconsistency might be a locally changing concentration of silica particles which can be induced by the presence of nanoparticle aggregates or nanoparticle accumulation in the sample preparation process. Increasing nanoparticle aggregation with increasing nanoparticle content was observed in TEM studies of the composite material (Chapter 3.4). Furthermore, the SiO_2 nanoparticles are not only functionalized with benzophenone terminated silanes but as well with *N*-(trimethoxysilylpropyl)-*N*,*N*,*N*-trimethylammonium chloride (NR_4^+) to keep them dispersed in water. The local screening of these positive charges might be a reason for the second transition as well. Further detailed investigation of the nanoparticle influence on the swelling behavior of the PCMD hydrogel is needed but outside the scope of this work. The super-crosslinker containing hydrogel matrices were used for cell growth experiments.

4.5.3 Cell Growth and Dextran-Based Hydrogels

In a cooperation project with Dr. A Hofmann and Dr. U. Ritz in the Center for musculosceletal Trauma Surgery of Prof. P. M. Rommens at the University Hospital in Mainz the hydrogel matrices were investigated as scaffolds for cell growth. Endothelial cells and osteoblasts transduced with red fluorescent protein and green fluorescent protein respectively were adhered to the modified PCMD hydrogel. The pure unmodified PCMD hydrogels, the composite SiO_2-nanoparticle PCMD hydrogels and the composite hydrogels with added gelatin were investigated with respect to their applicability for cell growth. Furthermore, the effect of patterning the matrix was investigated. A scheme of the matrix for cell growth experiments is depicted in Figure 4.5.4.

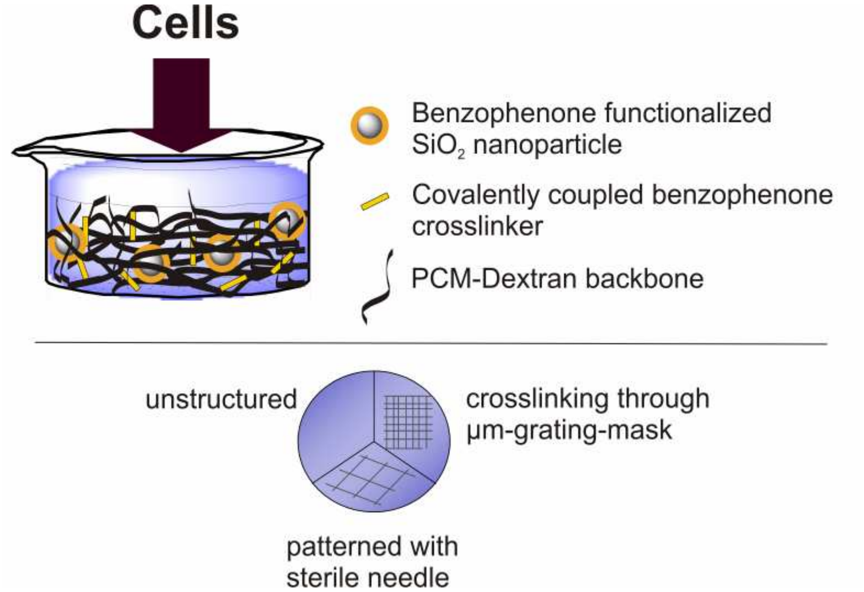

Figure 4.5.4: *Scheme of the hydrogel matrix for cell growth experiments.*

Pure hydrogels

First, the pure PCMD hydrogel matrices were tested for cell adhesion. The corresponding polymer solution was dropcast into a petri dish, dried over night and crosslinked at 254 nm for 90 minutes. With these highly swelling hydrogel matrices no reproducible cell adhesion and cell growth could be achieved. The unmodified hydrogel matrices seemed to swell too much to present a suitable scaffold for cells to attach and to grow. Consequently, the mechanical strength has to be improved which is usually achieved by increased crosslinking. Simultaneously, the pore size has to be maximized to present space for cells to penetrate into the hydrogel matrix.

Composite hydrogels

The crosslinking density of a hydrogel scaffold is known to have a great influence on the ability to serve as matrix for cell growth.[3] Cell metabolism, gene expression and cell morphology are reported to be influenced by the crosslinking density.[26-28] Typically, increasing crosslinking density leads to an inhibition of cell proliferation due to a reduced pore size. For the pure PCMD-hydrogel matrix, the crosslinking density seems to be too low and thus the water uptake too high to be suitable for cell adhesion. The mechanical strength has to be increased. Increased crosslinking thereby results in a reduced pore size which is disadvantageous for cells to penetrate into the hydrogel matrix. These adverse effects have to be balanced to achieve successful cell growth.

In order to increase the mechanical strength of the hydrogel and supposedly facilitate cell adhesion and cell growth, super-crosslinking units were introduced as described in Chapter 3.4. The aim was to achieve an enhancement of the mechanical strength but simultaneously preserve a pore size as big as possible. Using super-crosslinkers, such as benzophenone-functionalized nanoparticles, seems to be the most promising approach to balance mechanical stability and pore size of the hydrogel matrix. With this strategy structural reinforcement and an increased mechanical stability were achieved. The composite PCMD hydrogel matrices were divided into a non-structured and two differently structured parts as described in Chapter 3.4. The structuring was performed through a µm-grating mask while crosslinking and after crosslinking with a sterile needle. Subsequent cell adhesion and cell growth experiments were carried out successfully. Selected graphs of endothelial cells and osteoblasts growing on such a hydrogel matrix with a super-crosslinker content of 10 wt% are depicted in Figure 4.5.5. The cells clearly adhere to the hydrogel matrix. Monocultures of endothelial cells usually survive for only a few days. Co-cultures of osteoblasts and endothelial cells were growing on composite PCMD matrices with 10 wt% as well as on matrices with 20 wt% SiO_2-nanoparticle content. A clear influence of the matrix structuring could not be observed. The cells were growing on and inside the hydrogel matrices in the structured and in the non-structured parts. The fact that the cells penetrate inside the hydrogel scaffold is deduced from difficulties of focusing the microscope pictures. This indicates that the cells are not growing in one plane but on different height levels inside the hydrogel matrix.

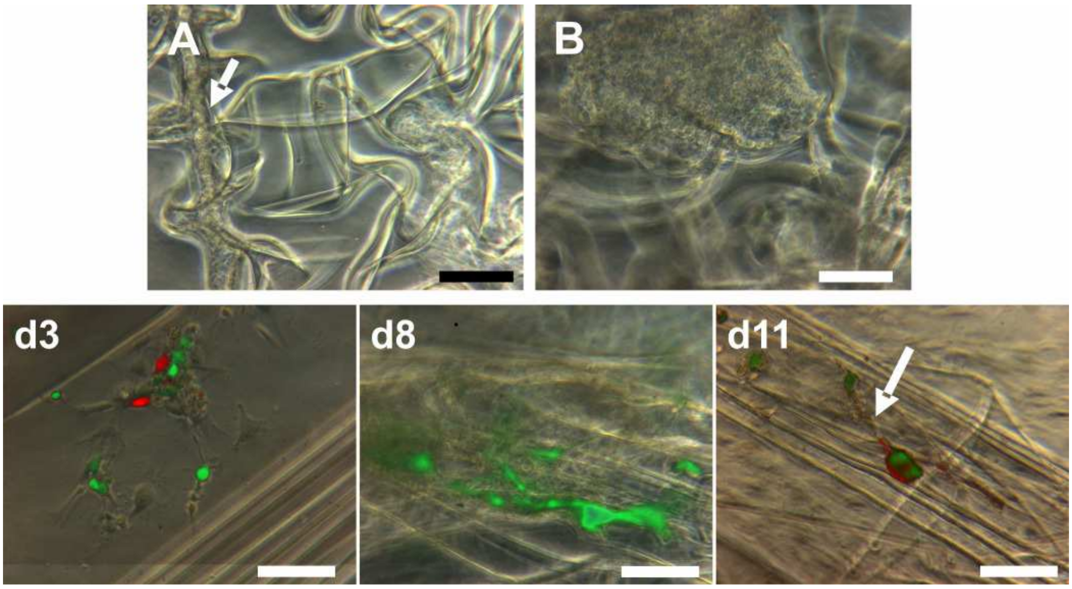

Figure 4.5.5: *Representative microscope graphs for a composite PCMD hydrogel matrix with a super-crosslinker content of 10 wt%:* ***A, B)*** *pure matrix without cells (d0). In (A) the structure induced by a sterile needle is visible (white arrow). d3, d8, d11 show endothelial cells (red) and osteoblasts (green) seeded on the composite PCMD scaffold and the cell growth after 3 (d3), 8 (d8), and 11 (d11) days. After 8 days the development of 3D structures and after 11 days the spheroid formation and outgrowth of neovessel-like structures (white arrow) is visible. The scalebar indicates a length of 100 µm.*

The cell growth was followed for up to 14 days. After approximately one week the cells started to build spheroidal 3Dimensional structures containing both cell types (Figure 4.5.5, d8).

Influence of Gelatin

With the aim to facilitate cell growth inside the hydrogel scaffolds gelatin as a third component was added. Gelatin was selected because of two reasons: first, it attracts cells because it can be digested and second, gelatin particles can serve as spacer material inside the dextran matrix. The gelatin was added to the polymer solution as pestled powder with a particle size of up to 100 µm or as polydisperse nanoparticle suspension as described in Chapter 3.4. With this strategy, cell adhesion and cell growth on top and inside the hydrogel matrix was improved. Typical microscope images showing the cell growth of a co-culture of endothelial cells and osteoblasts are depicted in Figure 4.5.7. A remarkable observation was the increased lifetime of endothelial cells in a mono-culture on a composite PCMD matrix with 10 wt% of super-crosslinking SiO_2-nanoparticles and 10 or 20 wt% gelatin. The endothelial cells were growing on the matrix containing the gelatin as nanoparticles and on the one with pestled gelatin. They stayed in a round shape and no differentiation was observed for a period of 7 days. In Figure 4.5.6 the microscope images of the pure hydrogel matrix and the microscope images after 3 days for a hydrogel matrix with gelatin nanoparticles as well as with pestled gelatin are shown. After a period of 7 days the cells show a comparable structure.

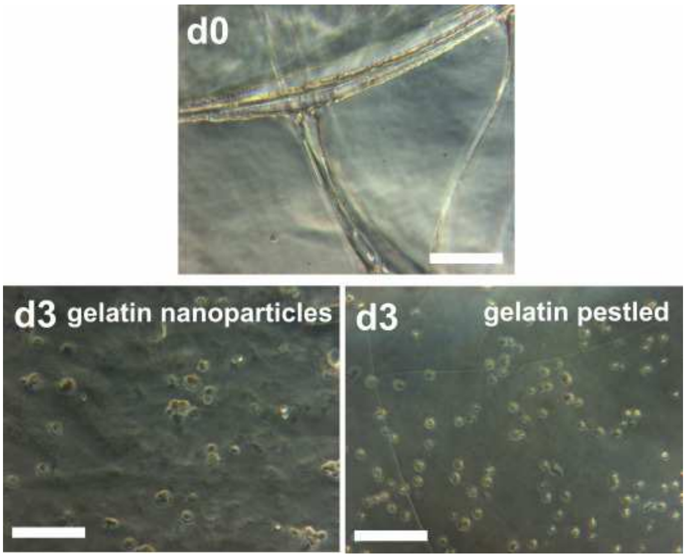

Figure 4.5.6: *Cell growth of a monoculture of endothelial cells on a gelatin containing (10 wt%)composite PCMD hydrogel (10 wt% SiO2-crosslinking nanoparticles). The pure hydrogel matrix (d0) before cell growth is shown for comparison. No difference between the cell growth with the gelatin introduced as nanoparticles or as pestled powder was observed. The scalebar represents 100 µm.*

The observations of cell growth of co-cultures of endothelial cells and osteoblasts growing on gelatin containing super-crosslinker containing PCMD hydrogels were comparable to the above described composite hydrogels. The best results were observed for the matrices containing 10 wt% of super-crosslinking SiO_2-nanoparticles and 10 wt% of gelatin (Figure 4.5.7).

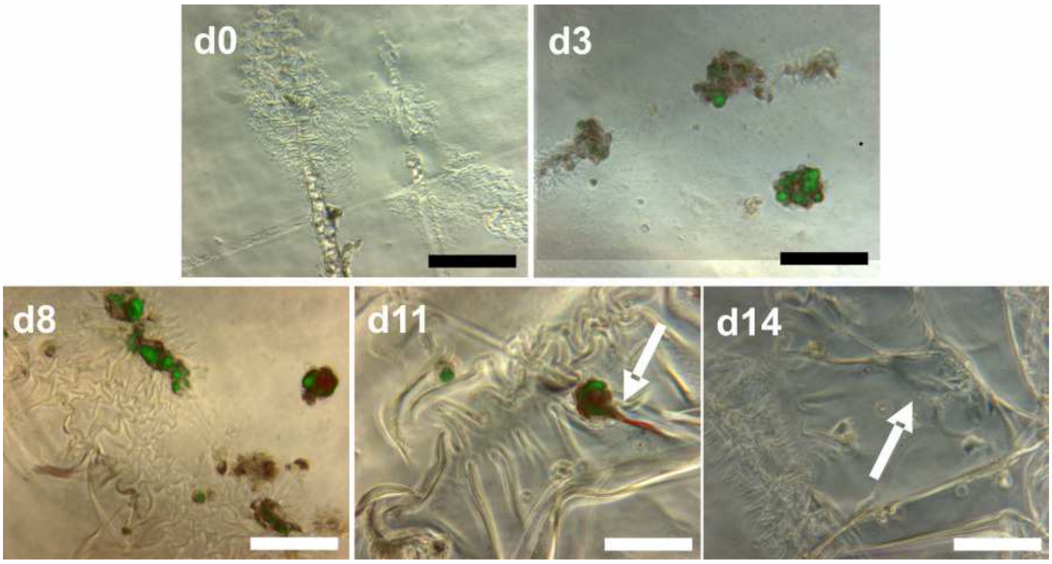

Figure 4.5.7: *Cell growth of co-cultured endothelial cells (red) and osteoblasts (green) on a gelatin containing (10 wt%, gelatin nanoparticles)) composite (10 wt% super-crosslinking SiO2-nanoparticles) PCMD hydrogel. The pure hydrogel (d0) is shown for comparison. Again the structures introduced by a sterile needle are visible. Cell growth is depicted after 3 (d3), 8 (d8), 11 (d11), and 14 (d14) days. The image after14 days was recorded without fluorescence. The scalebar represents 100 µm.*

Thereby, the gelatin conformation, nanoparticles or pestled gelatin, didn't seem to have a remarkable influence. In addition the matrices with 10 wt% super-crosslinker and 20 wt% gelatin (pestled) showed comparable results. After approximately one week, the cells started to form spheroids (Figure 4.5.7, d8) followed by the formation of neo-vessel like structures (Figure 4.5.7, d11). These cell structures are developing and after two weeks cell structures are covering the hydrogel matrix. The cells are penetrating into the hydrogel matrix which is visible by the difficulties in focusing a cell structure. By focusing on one cell other cells or other parts of the cell are located above or below the focus. This becomes clear by comparing the two images after two weeks of cell growth in Figure 4.5.8. The two images are recorded at one position by focusing on different height levels.

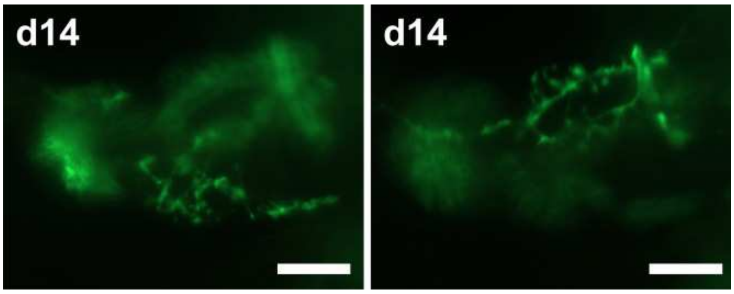

Figure 4.5.8: *Two images at one position with focusing on two different height levels. A co-culture of endothelial cells (red) and osteoblasts (green) at a gelatin containing composite PCMD matrix (10% super-crosslinking* SiO_2*-nanoparticles and /20% pestled gelatin) afte r14 days of cell growth. The scalebar represents 100 µm.*

The influence of the matrix structuring on the cell adhesion can not clearly be stated. For the entire PCMD matrices structuring with a µm-grating mask (Figure 3.4.10) during the crosslinking process can not be resolved in the microscope images of the swollen hydrogel matrix. A reason for this might be the swelling of the hydrogel that does not preserve the µm-structure. Furthermore, scattering effects at the mask due to the unfocused irradiation might prevent a clear border between irradiated and dark areas on the hydrogel film. This effect is increased because the dry hydrogel films are thick compared to the irradiation wavelength. In contrast, structuring with a sterile needle introduces patterns, which can be resolved with the microscope and which are preserved while swelling the matrix. The cells adhere to these structures as well as to the non-structured parts of the hydrogel matrices. The chemical composition and the crosslinking density seem to be more crucial for cell adhesion than the structuring in this case. For the higher swelling PCMD matrices without super-crosslinking SiO_2-nanoparticles no cell adhesion and cell growth was achieved even if gelatine was added. Consequently, the crosslinking density is the crucial characteristic to enable cell adhesion to these PCMD hydrogel scaffolds.

4.5.4 Conclusion and Outlook

The photo-crosslinkable carboxymethylated dextran-based hydrogel matrix was successfully modified to serve as scaffold for cell growth of osteoblasts and endothelial cells. This was achieved by increasing the crosslinking density by super-crosslinking nanoparticles. Furthermore, gelatin was successfully incorporated as digestable spacer for cell penetration. Cell adhesion, cell growth, and the development of cell structures was observed for higher crosslinked PCMD matrices as well as for gelatin modified matrices. Besides this chemical modification, a mechanical structuring on a scale of millimeters presented a suitable environment for cell proliferation. The optimization of the composition and the further development of the 3D structuring of the hydrogel matrix are expected to result in a potential hydrogel matrix for medical applications. In further experiments cellular analysis such as RNA expression and protein expression of cell proliferation and various cell markers will be studied. A further promising development would be the incorporation of growth factors which should be possible without additional chemical modifications by using active ester chemistry to couple amines to the present carboxyl groups.

4.5.5 Experimental

Dextran-Based Hydrogel Scaffolds: For the hydrogel synthesis the commercially available dextran (Sigma Aldrich, $M_r = 2.000.000$) was used and modified as described in Chapter 3.1 and 3.4.

Sample Preparation: The polymer solution or the corresponding composite solutions were used as prepared with a concentration of 0.1-0.2 g/mL. The polystyrene petri dishes with a diameter of 3.5 cm (cellstar, Greiner bio-one) were treated with oxygen plasma (60-70 W, 0.2 mbar, Technics Plasma GmbH, 200-G Plasma System) for 5 minutes to create a more hydrophilic surface. Immediately after the plasma treatment 0.15-0.3 mL of the polymer solutions were dropcast onto the petri dishes. The polymer solution was left at room temperature in a dark environment over night for drying and subsequently crosslinked at 254 nm for 60 minutes. The surface was divided into three parts. One part was crosslinked as prepared, one part was crosslinked through a μm-grating-mask and the last part was structured with a sterile needle.

SPR/OWS: SPR/OWS measurements and subsequent data treatment using the WKB approximation were performed as described in Chapter 2.1, 2.3, 4.1.7. The sodium chloride solutions were prepared with commercially available NaCl (Sigma Aldrich) in ultrapure water (MilliQ). The laser intensity was adjusted to 100 % reflectivity for all SPR/OWS experiments. This corresponds to 145 µW.

Osteoblasts were extracted from human bone tissue and cultivated at 37 °C in DMEM with 10 % fetal calf serum and 1% penicillin/streptomycin. As specific cell markers alkaline phosphatase and mineralization were determined to ensure the osteoblastic cell type.

Endothelial Cells (HUVEC - human umbilical vein endothelial cells) were used as purchased (Promocell) and cultivated in EBM-2-Media (Lonza, USA).

Transduction of the Cells with eGFP or RFP was achieved with a lentiviral eGFP/RFP-virus from transformed human kidney cells (HEK293). The gene for the eGFP and the RFP was introduced into the genome of the osteoblasts or the endothelial HUVEC cells. The efficiency of the transduction was determined by fluorescence microscopy or flow cytometry to be 60-95 %. The advantage of this method can be seen in the stable fluorescence of the cells.

Hydrogel Scaffolds were swollen in PBS for approximately 30 minutes and rinsed at least 6 x with PBS to remove all non-bound material. Subsequently, 100.000 cells per hydrogel sample were seeded either as HUVEC-c-monoculture (Promocell, Heidelberg, Germany) or as HUVEC and osteoblast co-culture with the same amount (50.000) of each cell type. The analysis of cell growth was performed with a fluorescence microscope (Wilovert AFL 30, Hund, Wetzlar, Germany).

4.5.6 Bibliography

[1] B. D. Ratner, S. J. Bryant, *Annu. Rev. Biomed. Eng.* **2004**, *6*, 41.
[2] H. C. H. Ko, B. K. Milthorpe, C. D. McFarland, *European Cells and Materials* **2007**, *14*, 1.
[3] M. R. Hynd, J. N. Turner, W. Shain, *J. Biomater. Sci. Polymer Edn.* **2007**, *18*, 1223.
[4] J. L. Ifkovits, J. A. Burdick, *Tissue Engineering* **2007**, *13*, 2369.
[5] M. Risbud, A. Hardikar, R. Bhonde, *J. Biosici.* **2000**, *25*, 25.
[6] M. Ishihara, K. Ono, M. Sato, K. Nakanishi, Y. Saito, H. Yura, T. Matsui, H. Hattori, M. Fujita, M. Kikuchi, A. Kurita, *Wound Repair Regen.* **2001**, *9*, 513.
[7] A. I. Teixeira, J. K. Duckworth, O. Hermanson, *Cell Res.* **2007**, *17*, 56.
[8] Y. Cao, G. Mitchell, A. Messina, L. Price, E. Thompson, A. Penington, W. Morrison, A. O'Connor, G. Stevens, J. Cooper-White, *Biomaterials* **2006**, *27*, 2854.
[9] M. Mastrogiacomo, S. Scaglione, R. Martinetti, L. Dolcini, F. Beltrame, R. Cancedda, R. Quarto, *Biomaterials* **2006**, *27*, 3230.
[10] A. K. A. Silva, C. Richard, M. Bessodes, D. Scherman, O.-W. Merten, *Biomacromolecules* **2009**, *10*, 9.
[11] J. M. Taboas, R. D. Maddox, P. H. Krebsbach, S. J. Hollister, *Biomaterials* **2003**, *24*, 181.
[12] D. W. Hutmacher, *Biomaterials* **2000**, *24*, 2529.
[13] G. M. Cruise, O. D. Hegre, F. V. Lamberti, S. R. Hager, R. Hill, e. al., *Cell Transplant* **1999**, *8*, 293.
[14] B. K. Mann, R. H. Schmedlen, J. L. West, *Biomaterials* **2001**, *22*, 439.
[15] J. A. Burdick, K. S. Anseth, *Biomaterials* **2002**, *23*, 4315.
[16] V. A. Liu, S. N. Bhatia, *Biomed. Microdevices* **2002**, *4*, 257.
[17] G. D. Nicodemus, S. J. Bryant, *Tissue Engineering: B* **2008**, *14*, 149.
[18] T. V. Chirila, I. J. Constable, G. J. Crawford, S. Vijayasekaran, D. E. Thompson, Y.-C. Chen, W. A. Fletcher, B. J. Griffin, *Biomaterials* **1993**, *14*, 26.
[19] D. L. Elbert, J. A. Hubbell, *Annu. Rev. Mater. Sci.* **1996**, *26*, 365.
[20] K. Arcaute, B. K. Mann, R. B. Wicker, *Ann. Biomed. Eng.* **2006**, *34*, 1429.
[21] J. Yeh, Y. Ling, J. M. Karp, J. Gantz, A. Chandawarkar, G. Eng, J. Blumling, R. Langer, A. Khademhosseini, *Biomaterials* **2006**, *27*, 5391.
[22] A. Sannino, P. A. Netti, M. Madaghiele, V. Coccoli, A. Luciani, A. Maffezzoli, L. Nicolais, *J. Biomed. Mater. Res. A* **2006**, *79*, 229.
[23] W. Tan, T. A. Desai, *Tissue Eng.* **2003**, *9*, 255.

[24] L. S. Ferreira, S. Gerecht, J. Fuller, H. F. Shieh, G. Vuniak-Novakovic, R. Langer, *Biomaterials* **2007**, *28*, 2706.
[25] P. Mestries, C. Borchiellini, C. Barbaud, A. Duchesnay, Q. Escartin, D. Barritault, J. P. Caruelle, P. Kern, *?? Wiley vch* **1998**, *?*, 286.
[26] S. J. Bryant, J. A. Arthur, K. S. Anseth, *Acta Biomater.* **2005**, *19*, 1781.
[27] S. J. Bryant, T. T. Chowdhury, D. A. Lee, D. L. Bader, K. S. Anseth, *Ann. Biomed. Eng.* **2004**, *32*, 407.
[28] S. J. Bryant, K. S. Anseth, D. A. Lee, D. L. Bader, *J. Orthop. Res.* **2004**, *22*, 1143.

5 Summary and Outlook

Towards the aim of creating a dextran-based hydrogel matrix suitable for optical biosensing with waveguide modes and for biomedical applications, projects from hydrogel synthesis to optical waveguide mode fluorescence spectroscopy were performed. An overview about the projects presented in this thesis is depicted in Figure 5.1.1.

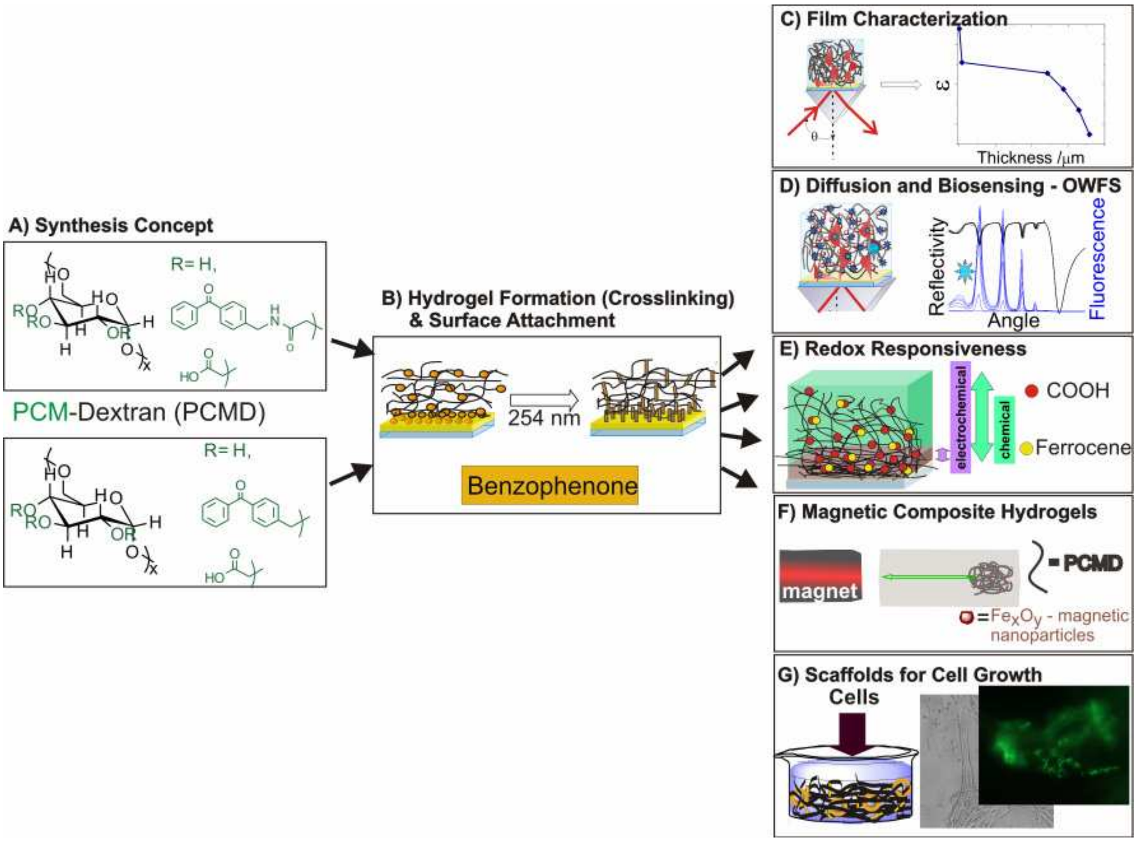

Figure 5.1: *Schematic overview about the projects presented in this thesis.*

Synthesis Concept and Hydrogel Film Formation

A synthesis concept built on the modification of a commercially available dextran backbone with benzophenone groups as photo-crosslinking units and carboxymethyl groups, serving as analyte binding points, was developed (Figure 5.1.1 A). Thereby, the carboxyl groups were selected because they can be modified with almost any molecule carrying a primary amino group even under aqueous conditions by using active ester chemistry. By photo-crosslinking it was possible to accurately control the degree of crosslinking and thus the degree of swelling of the hydrogel matrix by tuning the irradiation energy dose. Furthermore, the swelling was adjusted by regulating the chemical composition and the pH according to the pKa value of the carboxyl groups. By modifying gold or glass surfaces with benzophenone-terminated thiols or silanes respectively, the PCMD polymer was not only photo-crosslinked but simultaneously attached to the substrate surface (Figure 5.1.1 B). Mechanically stable, surface attached PCMD hydrogel films in the range of up to 20 µm in the swollen state were prepared. The ratio of benzophenone and carboxyl groups was determined to be crucial for the degree of swelling and thus for the mechanical properties and the stability of the hydrogel films. Future developments could aim for different surface functionalization strategies. For example plasma surface treatment could lead to improved surface stability for macroscopic hydrogel scaffolds and to new routes of combining various substrate materials with the PCMD hydrogel matrix. A versatile approach for biomedical applications could be the functionalization of PEEK as implant material with a PCMD hydrogel.

Film Characterization

The chemical, mechanical, and optical characterization of the PCMD hydrogel films was required for the optimization of the hydrogel matrix towards high swelling degrees and waveguiding properties. High swelling degrees are necessary for biosensor applications because the mobility of analytes is limited by the pore size. The pore size is determined to a large extend by the swelling degree and the charge of the hydrogel. The PCMD hydrogels revealed high, pH-dependent swelling degrees between 10 and almost 50 and a refractive index gradient in one dimension perpendicular to the substrate surface. This was determied by surface plasmon resonance (SPR) and optical waveguide mode spectroscopy (OWS) and subsequent data treatment by using the Wentzel-Kramers-Brillouin approximation (WKB). The high swelling degrees and the resulting enormous water content was affirmed by neutron scattering experiments as well as by diffusion experiments with fluorescence correlation spectroscopy (FCS). Thus, a hydrogel matrix was developed which serves as waveguide and simultaneously allows the diffusion of analytes due to its high swelling degrees. However, a more detailed characterization especially with FCS is required for an improved understanding of the pore structure and the diffusion properties of analytes inside the swollen hydrogel matrix. The structural characterization of a swollen hydrogel structure is still challenging.

Diffusion and Biosensing – OWFS

A biosensor concept based on using thick hydrogel matrices in combination with optical read out mechanisms was developed. Sensor matrices with a swollen thickness of several micrometers are able to capture a higher number of analytes and thus increase the detected signal. Simultaneously, they can serve as waveguide allowing fluorescence excitation of molecules that are loated inside the hydrogel matrix. Two different optical techniques were applied: the combination of SPR and OWS as well as long range surface plasmon spectroscopy (LRSP). In a sandwich assay the fluorescence of labeled analytes such as streptavidin-Cy5 or secondary labeled antibodies was excited by the evanescent field of the surface plasmon (SPFS) and simultaneously by the electromagnetic field of the leaky optical waveguide modes (OWFS) (Figure 5.1 D). The enhanced electromagnetical field of the optical waveguide modes as compared to the evanescent electromagnetic field of the surface plasmon and the increased number of analytes due to the thicker analyte capturing matrix resulted in a 2-3 orders of magnitude higher OWFS signal as compared to the SPFS signal an improved signal to noise ratios. Although, the sensor concept was successfully applied the sensitivity can still be optimized by tuning the coupling efficiency of the optical waveguide modes. This could be achieved by reducing the gold layer or by optimizing the waveguiding properties of the hydrogel matrix. In addition, the amount of analyte capturing units as well as the analyte distribution perpendicular to the substrate can be optimized. For thick, swollen sensor matrices in the range of 15-20 µm a gradient in the analyte distribution perpendicular to the substrate was determined by applying the theory of the relative photon density. Nevertheless, the advantages of a thick hydrogel matrix in the range of micrometers could be shown. In addition, the applicability of the developed sensor matrix for clinically relevant samples was proofed by the detection of prostate specific antigen (PSA) in blood serum by LR-SPFS in a cooperation project with Y. Wang and J. Dostálek.

Functionalization - Redox Responsive and Magnetic Hydrogels

Further functionalization of the PCMD aimed towards external manipulation of the hydrogel response and the charge of the biosensor matrix. External manipulation of the hydrogel matrix response is especially interesting for biosensing as well as for other biomedical applications. The modulation of a hydrogel response to pH, ion concentration, electrochemical switching, or a magnetic force was investigated. The external generation of charges for example can facilitate diffusion of charged analytes. Biomolecules such as proteins are usually charged at the optimal pH to perform the coupling reaction. If the matrix can be externally charged the swelling degree can be manipulated and the matrix can be electrostatically loaded with a charged analyte of interest. As electrochemically sensitive unit ferrocene molecules were covalently bound into the hydrogel film (Figure 5.1 E). The electrochemical switching resulted in an oxidation and reduction of the ferrocene units close to the electrode surface whereas a chemical oxidation and reduction in water seems to address the ferrocene molecules through the entire hydrogel film. The disadvantage of chemical switching is the possible incompatibility of the oxidation and reduction agent with biomolecules. Future optimization should aim for a configuration which increases the distance from the electrode that can be addressed electrochemically to allow reversible electrochemical switching of the entire hydrogel layer. A further optimization would be the introduction of molecules with varying oxidation potential to be able to titrate the charge. For one certain molecule such as ferrocene a shift of the oxidation potential can be achieved by increasing the spacer length, for example. Furthermore, a magnetic hydrogel was prepared by the introduction of magnetic nanoparticles into the PCMD matrix simply by mixing of the PCMD and the nanoparticles (Figure 5.1 F). A hydrogel responding to a magnetic field with the possibility of coupling biomolecules might be interesting for applications such as magnetic separation as well.

Scaffolds for Cell Growth

Apart from the bio-related application in the field of sensing, thick dextran-based hydrogel matrices are versatile materials for the adhesion and growth of cells and can be designed for applications in bone regeneration. In cooperation with Dr. U. Ritz and Dr. A. Hofmann at the Center for Musculoskeletal Trauma Surgery in Mainz a scaffold for cell growth of endothelial cells and osteoblasts was designed. The swelling characteristics and the chemical composition were optimized for cell growth by introducing super-crosslinking nanoparticles and gelatin as sacrificial spacer material. With this a scaffold suitable for the growth of endothelial cells and osteoblasts was prepared (Figure 5.1 G). Future optimization aims for the introduction of cell growth factors or drugs for example and to optimize the chemical structure towards biodegradation. The ultimate goal would be the preparation of a biodegradable dextran-based hydrogel scaffold for bone regeneration in the human body.

ACKNOWLEDGEMENTS

First of all, I want to thank my supervisor for giving me the opportunity to do my PhD in his group at the Max Planck Institute for Polymer Research in Mainz and for supporting all my scientific ideas as well as all my additional activities concerning fellowships, summer schools and soft skill trainings. It was a really inspiring experience to get to know so many people from so many different countries and with so diverse background in this huge group.

Second; I want thank the Professor from the University of Mainz that he kindly agreed to be my second supervisor and spent his time for my thesis.

All Professors thanks for agreeing to be part of the committee in my defense.

The most important person for scientific discussions, brainstorming and feedback was my project leader. At my first day of my PhD everything started with him. He always had thousands of ideas if inspiration was needed. Although he moved to Crete he kept the contact maybe even closer than before and was available for any kind of discussion from science to politics. Thank you for everything and sorry for sentences with more than four lines.

Besides him, I want to thank two other project leaders who helped me a lot with any question and tricks related to biosensors and optical waveguide mode spectroscopy. Especially thanks for bringing me into contact with WKB and WKB profiles and for discussing the corresponding results. Special thanks for being so patient with my still growing knowledge about SPR/OWS, fluorescence, and sensing at the beginning of my PhD and for broadening the horizon concerning optical sensing by introducing new SPR techniques in our group. Furthermore, thanks to you and your PhD student for the productive cooperation which continued even as you left to Vienna.

In this context I want to say thank you as well to the postdoc of the Bio-Group who was open for any discussion about biological issues at any time. Especially thank you for the Western Blots. As well, thanks to the project leader who brought me into contact with the University Medical Center, to the PhD student in our group who was a great help for calculations with “ATSOS” and to the one who helped me with the microscope images.

During my PhD I started to work a little bit with electrochemistry. This would not have been so easily possible without the help of two postdocs in our group. Thank you so much for helping me with this and for hours together in the lab.

In addition to my own projects I was able to start various cooperations: because of the magnetic nanoparticles from a PhD student in the chemistry department at the University of Mainz and her help I was able to prepare a magnetic hydrogel. The people from the Medical Center of the University of Mainz contributed their competence in cell growth experiments resulting in a very productive cooperation. A PhD student at the Max Planck Institute of Polymer Research added his knowledge about FCS and data fitting to study the diffusion inside my hydrogel matrices which led to useful additional information. Another sub-group measured the swollen hydrogel surfaces with neutron reflectivity to complete the structural knowledge. Thank you all for the productive, successful, and hopefully continuing cooperation.

Not only cooperating but as well discussing all kinds of subjects with or without a coffee or a friday afternoon beer is a main source of ideas. For this I want to thank all the PhDs and postdocs who were frequent pools of ideas, help, or supply of synthesis products such as nanoparticles or silanes for self-assemby.

The infrastructure at the MPIP is excellent. Thanks to the mechanical and the electrical workshop, the supermarkets and the glassblower for the support in all small and bigger problems. Especially, I want to thank all the people I was in closer contact with for their support with analytical measurements or synthesis from AFM, cryo-SEM, NMR, or GPC to molecular synthesis, or for keeping labs in shape.

In addition to the open and international environment at the MPIP I remember many moments that would not have been possible without the IMPRS and its coordinator. Thanks for organizing all these amazing summer schools, seminars, and for giving me the opportunity to present my work at the 11th Pacific Polymer Conference in Australia. This was a very inspiring experience, scientifically and personally. Thanks to all the IMPRS members for the enjoyable atmosphere in all the schools and seminars.

Another very inspiring experience was the exchange with students and PhD students of completely different departments and universities. This was only possible so intensively due to the support of the Studienstiftung des Deutschen Volkes. I greatly appreciated not only the financial support but as well the opportunity of participating in the huge program offering summer schools, language courses, PhD-, and soft skill seminars. Thanks to our “Vertrauensdozent” and all members of our group for the various events and inspiring discussions.

My thesis was proof read by many people. All of you thanks a lot for your help with that.

No PhD would be such an exciting experience without friends to share the time with. So many people here at the MPIP shared a period with me. Thank you for all the interesting time we spend together. Many thanks to all the people I shared the office 2.504, the lab 2.417, the lab 2.422, and the lab 2.507 with. I had an interesting time there and with you it was never boring. Thanks to all friends that spent a part of their time for organizing special events such as a bus-tour through the Netherlands, a tour to Edinburgh, holidays in Sardegna, or that simply shared a room with me in one or another seminar and conference. I really enjoyed all the informative and funny coffee corner breaks. The “Mensa Group” leaving at 11:30 sharp always was a relaxing part of the day and thanks to the last surviving friends and colleagues we manage to keep the tradition until the end. Thanks as well to the “Kicker Community”. Furthermore, thanks to the international MPIP community especially to the “Spanish-speaking community” for the Salsa evenings and all the other events. My Spanish improved a lot in the last year not only because of the language courses but as well because of the tandem and the spanish-german lunch. Thanks for that! Last but not least I discovered the fun of playing football in a women’s team. Thanks to all members of our team participating in our fridays trainings sessions and especially to our coach for organising it.

Beyond the colleagues and friends from the MPIP I want to thank my three flatmates for the exciting time we spent in our WG. Thanks for all the discussions and ideas. I will really miss this exchange between chemistry, medicine, law, politics, and other diverse subjects of discussion.

I want to express my thanks to all my friends that keep in contact since several years being there for me, having an open ear even if the distance increases and the number of meetings is reduced. Thanks to my best friend for keeping such a close contact between

Berlin and Mainz. A special thought goes to my Marburg-housemate and friend. Thanks for all the time we spent together.

The most constant support during all this time was my family. I really want to say thank you for sharing all happy and sad moments and for always being there if I needed a silent period at home. Without you I would not have come so far. Thank you so much.

PUBLICATIONS & PRESENTATIONS

ANNETTE BRUNSEN

ARTICLES

W. Knoll, A. Kasry, F. Yu, Y. Wang, A. Brunsen, J. Dostalek, *New concepts with surface plasmons and nano-biointerfaces*, Journal of Nonlinear Optical Physics and Materials, 17, (2), 121-129, **2008**.

Y. Wang, A. Brunsen, U. Jonas, J. Dostalek, W. Knoll, Anal. Chem., *Prostate Specific Antigen Biosensor Based on Long Range Surface Plasmon-Enhanced Fluorescence Spectroscopy and Dextran Hydrogel Binding Matrix*, Analytical Chemistry, 81, (23), 9625-9632, **2009**.

A. Brunsen, U. Jonas, J. Dostalek, B. Menges, W. Knoll, *Synthesis and Characterization of a Photo-Crosslinkable Hydrogel as Biosensor Matrix,* in preparation (Chapter 3.1, 4.1, 4.2).

A. Brunsen, S. Utech, M. Maskos, U. Jonas, W. Knoll, *Magnetic Dextran-Based Hydrogels for Biomedical Applications*, in preparation (Chapter 3.3, 4.4).

CONFERENCES

Presentations

A. Brunsen, B. Yameen, R. Roskamp, W. Knoll, U. Jonas, *Chemical Surface Modification of PEEK with Polymer Layers*, European Conference on Biomaterials, Lausanne, September 2009.

A. Brunsen, Y. Wang, B. Menges, J. Dostalek, U. Jonas, W. Knoll, *Photocrosslinkable Dextran-Based Hydrogel Films as Biosensor Binding Matrix,* 11th Pacific Polymer Conference, Cairns, Australia, December 2009.

Poster Contributions

A. Brunsen, T. Buckup, T. Klar, L.-O. Essen, M. Motzkus, *Femtosecond Transient Absorption Studies on the Photolyase of Thermus thermophilus and their Chromophores FMN and FAD*, DPG Tagung, Düsseldorf, MO 26.4, March 2007.

A. Brunsen, U. Jonas, W. Knoll, *Dextran-Based Functional Hydrogels for Biosensing*, Biointerface, Kerkrade, Netherlands, June 2008.

Contributions from Cooperations

Presentations

J. Dostalek, Y. Wang, A. Brunsen, R. Roskamp, W. Knoll, *Biosensor based on long range surface plasmon-enhanced fluorescence spectroscopy*, Europtrode IX, Dublin, Book of abstracts 66, March 30th 2008.

J. Dostalek, Y. Wang, C.J. Huang, R. Chulia-Jordan, A. Aulasevich, R. Roskamp, A. Brunsen, W. Knoll, *Advanced biosensing based on surface plasmon-enhanced fluorescence spectroscopy*, Nanosens, Vienna, Book of abstracts, September 29-30th 2008.

R. Raccis, R. Roskamp, A. Brunsen, B. Menges, U. Jonas, W. Knoll, G. Fytas, Diffusion of molecular probes and proteins in hydrogels, APS March Meeting, Session X18: Elastomers and Gels I, Pittsburgh, Pennsylvania, USA, X18.00015, March 2009

J. Dostalek, Y. Wang, C.J. Huang, A. Aulasevich, R. Roskamp, A. Brunsen, W. Knoll, *Surface plasmon mediated fluorescence for biosensing*, 4th International Symposium on Medical, Bio- and Nano-Electronics, Sendai, Book of abstracts pp. 21, March 5-6, 2009.

J. Dostalek, Y. Wang, C.J. Huang, R. Chulia-Jordan, A. Aulasevich, R. Roskamp, A. Brunsen, W. Knoll, *Advanced biosensing based on surface plasmon-enhanced fluorescence spectroscopy*, Optics and Optoelectronics 2009, Prague, Czech Republic, Book of abstracts 7356, April 20-23, 2009.